Investigations of Graphene and Inorganic Graphene Analogues

A Thesis

Submitted for the Degree of

Doctor of Philosophy

by

H. S. S. Ramakrishna Matte

Chemistry and Physics of Materials Unit

Jawaharlal Nehru Centre for Advanced Scientific Research

BANGALORE-560064, INDIA

November 2012

Dedicated to Amma, Daddy and Annayya

DECLARATION

I hereby declare that the matter embodied in the thesis entitled **"Investigations of graphene and inorganic graphene analogues"** is the result of investigations carried out by me at Chemistry and Physics of Materials Unit, Jawaharlal Nehru Centre for Advanced Scientific Research, Bangalore, India under the supervision of Prof. C.N.R. Rao F.R.S and it has not been submitted elsewhere for the award of any degree or diploma.

In keeping with the general practice in reporting scientific observations, due acknowledgment has been made whenever the work described is based on the findings of other investigators.

.

_____

H. S. S. Ramakrishna Matte

CERTIFICATE

I hereby certify that the matter embodied in this thesis entitled **"Investigations of graphene and inorganic graphene analogues"** has been carried out by Mr. H. S. S. Ramakrishna Matte at Chemistry and Physics of Materials Unit, Jawaharlal Nehru Centre for Advanced Scientific Research, Bangalore, India under my supervision and it has not been submitted elsewhere for the award of any degree or diploma.

Prof. C. N. R. Rao

(Research Supervisor)

ACKNOWLEDGEMENTS

PREFACE

The thesis consists of two parts. Part 1 describes the investigations of graphene. In this Part, Section 1.1 provides a brief overview of graphene. Section 1.2 deals with nanocarbons and their composites formed at the liquid-liquid interface. Magnetic properties of graphenes are discussed in Section 1.3. Section 1.4 presents the interaction of graphene with electron donor organic molecules. Interaction of graphene with $FeCl_3$ and $CuCl_2$ is discussed in Section 1.5.

Investigations of inorganic graphene analogues are presented in Part 2. Section 2.1 gives an introduction to inorganic graphene analogues. Synthesis and characterization of metal chalcogenide based graphene analogues are discussed in Section 2.2, while Section 2.3 deals with the synthesis and characterization of nanoscrolls of metal chalcogenides. Magnetic properties of metal chalcogenides-based graphene analogues are discussed in Section 2.4. In a Appendix to section 2.4, field-effect transistor based on mechanically exfoliated MoS_2, GaS and GaSe are described. In Section 2.5, a study of the layer-dependent resonant Raman scattering of molybdenum sulphide is presented. Superior infrared detection properties of few-layer molybdenum selenide have been discussed in Section 2.6. Section 2.7 gives a preliminary account of the superconducting properties of graphene analogues of $NbSe_2$.

A summary of the research work on metal-organic frameworks carried out by the candidate for the Master's degree has been given at the end of the thesis.

Contents

x

PART 1

Investigations of graphene

1.1: Brief overview of graphene

1.1.1: Introduction

Carbon nanotubes and graphene are the two most studied materials today. Two-dimensional graphene has specially attracted a lot of attention because of its unique electrical properties such as very high carrier mobility, quantum Hall effect at room temperature, ambipolar electric field effect along with ballistic transport of charge carriers.[1-3] Some other properties of graphene that are equally interesting include its unexpectedly broad absorption of light,[4] high elasticity,[5] unusual magnetic properties,[6] high surface area,[7] gas adsorption[8] and charge transfer interaction with molecules.[9] While graphene normally refers to a single-layer of sp^2 bonded carbon atoms, there are important investigations on bi- and few- layer graphenes as well. In the very first experimental study on graphene carried out by Novoselov et al.[1a] in 2004 was obtained using micromechanical cleavage from graphite. Since then, there has been much progress in the synthesis of graphene and a number of methods have been devised to prepare high quality single- and few-layer graphenes.

1.1.2: Stability of graphene

Graphene is the two-dimensional counterpart of three-dimensional graphite, exhibiting high crystal quality and ballistic conduction. But according to some earlier reports, perfect two-dimensional crystals cannot exist in free state.[10] But surprisingly, individual graphene sheets freely suspended on a micro fabricated scaffold in vacuum or in air have also been reported.[1a]

1.1: Brief overview of graphene

More than 70 years ago, Peierls [10b] and Landau[11] raised questions about the existence of a strictly two-dimensional (2D) crystal. They showed that in the standard harmonic approximation,[10b] thermal fluctuations destroy the long-range order leading to the melting of the 2D lattice at any finite temperature. Indeed, a detailed analysis of the 2D crystal problem beyond the harmonic approximation has led to the conclusion[12] that interaction between the bending and the stretching long-wavelength phonons could in principle stabilize atomically thin membranes through their deformation in the third dimension.[13]

1.1.3: Characterization

Characterization of graphene is an important part of graphene research and involves measurements based on various microscopic and spectroscopic techniques. Characterization involves the determination of the number of layers and purity of the sample in terms of the absence or the presence of defects. Optical contrast of graphene layers on different substrates is the most simple and effective method for identifying the number of layers. It is based on the contrast arising from the interference of the reflected light beam at the air-to-graphene, graphene-to-dielectric and (in the case of thin dielectric films) dielectric-to-substrate interfaces.[14] Single-, bi-, and multiple-layer (<10 layers) graphenes on Si substrates with a 285 nm SiO_2 are differentiated by using contrast spectra, generated from the reflected light of a white light source (see Figure 1(A)).[15] A total color difference (TCD) method, based on a combination of reflection spectrum calculation and International Commission on Illumination (CIE) color space is also used to quantitatively investigate the effect of light source and substrate on the optical imaging of graphene for determining the thickness of the flakes. It is found that 72 nm thick Al_2O_3 film is much better for characterizing graphene than the graphene deposited on SiO_2 and Si_3N_4 films.[1f]
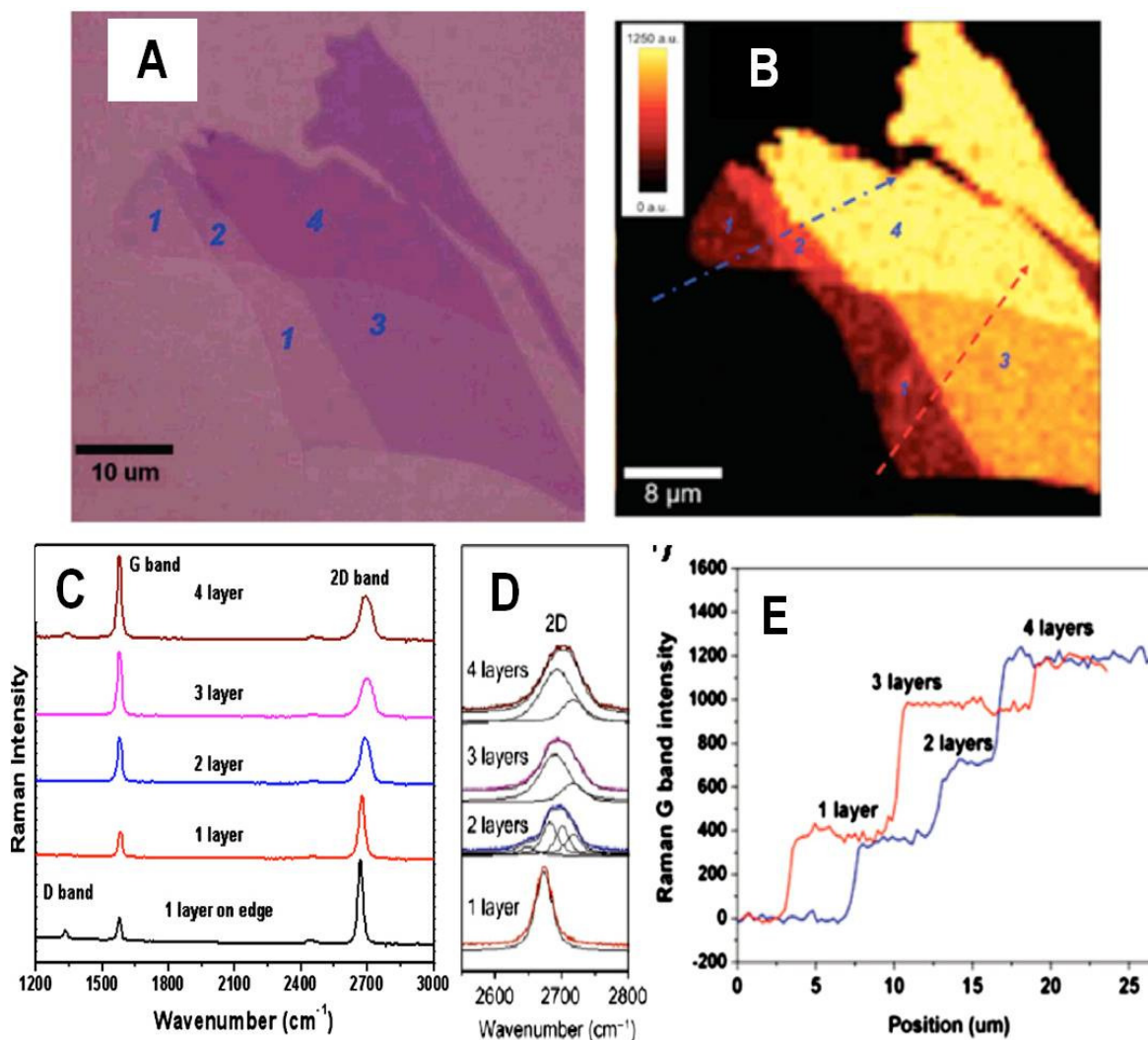
Figure 1: (A) Optical image of graphene with one, two, three, and four layers, (B) Raman image plotted by the intensity of G band, (C) Raman spectra as a function of number of layers, (D) Zoom-in view of the Raman 2D band, (E) The cross section of Raman image, which corresponds to the dash lines and the cross section of the Raman image, which corresponds to the dashed lines in (B) (from ref [1f]).

Contrast in scanning electron microscope (SEM) images is another way to determine the number of layers. The secondary electron intensity from the sample operating at low electron acceleration voltage has a linear relationship with the number of graphene layers (see Figure 2(A)).[1g] A quantitative estimation of the layer thicknesses is obtained by using attenuated secondary electrons emitted from the substrate with an in-column low-energy electron

3

detector.[16] Transmission electron microscopy (TEM) can be directly used to observe the number of layers on viewing the edges of the sample, each layers corresponding to a dark line. Gass et al.[17] observed the individual atoms in graphene by high-angle annular dark-field (HAADF) in aberration-corrected STEM mode at an operation voltage of 100 kV. Direct visualization of defects in the graphene lattice like Stone-Wales defect have been possible with aberration corrected TEM with monochromator (see Figure 2 (B)).[3] Electron diffraction can be used for differentiating the single-layer with multiple-layers of graphene. In single-layer graphene (SLG), there is only zero-order Laue zone in the reciprocal space and the intensities of diffraction peaks do not therefore, change much with the incidence angle. In contrast, bi-layer graphene exhibits changes in total intensity with different incidence angles. Thus, the weak monotonic variation in diffraction intensities with tilt angle is a reliable way to identify monolayer graphene.[18] From the relative intensities of the electron diffraction pattern from the {2110} and {1100} planes can be used to determine the number of layers. If $I_{\{1100\}}/ I_{\{2110\}}$ is greater than one it is identified as SLG and if the ratio is < 1 it is multi-layer graphene. Thickness of graphene layers can be directly probed by atomic force microscopy (AFM) in tapping mode. Based on the interlayer distance of 3.5 Å in graphite, the thickness of a graphene flake or the number of layers is determined as shown in Figure 2(C).[1c] Scanning tunneling microscopy (STM) also provides high resolution images of graphene.

Raman spectroscopy has been extensively used as a non destructive tool to probe structural and electronic characteristics of graphene.[1c] Figure 1(C) shows typical Raman spectra of one-, two-, three- and four-layer graphene prepared using micromechanical cleavage technique and placed on SiO_2/Si substrate. The Raman spectrum of graphene has three major bands. The D-band located around 1300 cm^{-1} is a defect-induced band. The G-band is

around 1580 cm^{-1} and is due to in-plane vibrations of the sp^2 carbon atoms. The 2D band around

2700 cm^{-1} results from a second-order process. The appearance of the D- and 2D- bands is

related to the double resonance Raman scattering process and with increasing the number of

layers the 2D band gets broadened and blue-shifted.[19] A sharp and symmetric 2D band is found
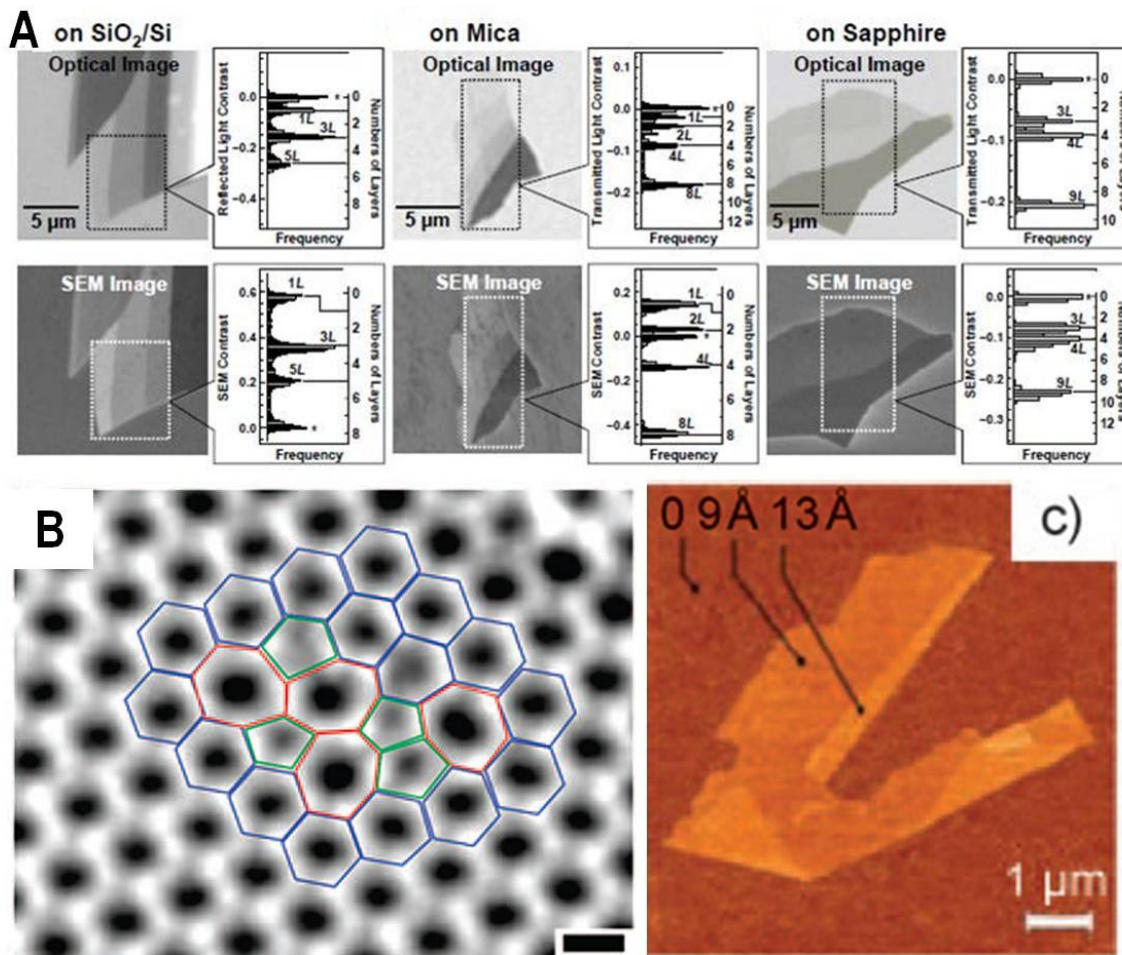
Figure 2: (A) Comparison of the counting of layers by optical microscopy and by SEM for graphene on SiO$_2$/Si, mica and sapphire. For each figure is shown a histogram of the distribution of graphene layers within the rectangular area indicated by a dotted line,((Reprinted with permission from[1d]) (B) High resolution transmission electron microscopic image showing Stone Wales defects in graphene (Reprinted with permission from [3]) and (C) Atomic Force microscopic image of single layer graphene. Folded edge shows a height increase of 4Å indicating single layer graphene (from ref [1c]).

in the case of SLG as shown in Figure 1(D). A Raman image obtained from the intensity of the G band is shown in Figure 1(B). A linear increase in the intensity profile of the G band with the increase in the number of layers along the dashed line is shown in Figure 1(E).[15]

1.1.4: Synthesis of single- and few-layer graphenes

Single- and few-layer graphenes have been synthesized by several methods. We have listed some of the important methods. The synthetic methods includes exfoliation, ultrsonication, chemical vapor deposition, arc discharge and reduction of graphene oxide.

Mechanical Exfoliation and Ultrasonication: Stacking of sheets in graphite is the result of overlap of partially filled p_z or π orbitals perpendicular to the plane of the sheet (involving van der Waals forces). Due to the weak bonding in the perpendicular direction compared to the stronger bonding in the in-plane, it has been attempted to synthesize graphene sheets through exfoliation of graphite. Graphene sheets of different thickness can indeed be obtained through mechanical exfoliation, or peeling off layers from graphitic materials such as highly ordered pyrolytic graphite (HOPG), single crystal graphite or natural graphite. Peeling and manipulation of graphene sheets have been achieved through AFM and STM tips.[20] Greater control over folding and unfolding could be achieved by modulating the distance or bias voltage between the tip and the sample.[20f] Zhang et al.[21] obtained 10-100 nm thick graphene sheets by using graphite island attached to tip of micro-machined Si cantilever to scan over SiO$_2$/Si surface.

Novoselov et al.[1b] pressed patterned HOPG square meshes on a photo resist spun over a glass substrate followed by repeated peeling using scotch tape and then the flakes so obtained were released in acetone. Some flakes got captured on to SiO$_2$/Si wafer when dipped in the acetone. By using this method atomically thin graphene sheets were obtained. This method was

simplified to just peeling off of one- or few-sheets of graphene using scotch tape and depositing them on SiO_2 (300 nm)/Si substrates. Though mechanical exfoliation produces graphene of the highest quality (with least defects), the method is limited by low productivity. Chemical exfoliation, on the other hand, possesses advantages of bulk scale production.

Solution-phase exfoliation of graphite in an organic solvent such as N-methylpyrrolidone (NMP) yields single-layer graphene in high yields.[18] In this case, the energy required to exfoliate graphene is balanced by the solvent–graphene interaction. Such solvent graphene interactions are also used to disperse graphene in perfluorinated aromatic solvents[22], orthodichloro benzene[23] and even in low-boiling solvents such as chloroform and isopropanol.[24] Hernandez et al.[25] carried out detailed study on dispersibility of graphene in 40 different solvents and proposed that good solvents for graphene are characterized based on Hildebrand and Hansen solubility parameters. More than 63% of observed flakes had less than 5 layers in most solvents.

Exfoliation: Chemical exfoliation is a two-step process. The first step is to increase the interlayer spacing, thereby reducing the interlayer van der Waals forces. This is achieved by intercalating graphene to prepare graphene intercalated compounds (GIC). The GICs are then exfoliated into graphene with single- to few-layers by rapid heating or sonication.[26] A classic example of chemical exfoliation is the generation of single-layer graphene oxide (SGO) prepared from graphite oxide by ultrasonication.[27] Graphite oxide (GO) is prepared by Hummers method or modified Hummers method involving the oxidation of graphite with strong oxidizing agents like $KMnO_4$ and $NaNO_3$ in H_2SO_4/H_3PO_4.[28] On oxidation, the interlayer spacing increases from 3.7 Å to 9.5 Å which on exfoliation with simple ultrasonication in a DMF:water (9:1) mixture gives rise to single-layer graphene. The SGO so prepared has a high density of functional groups

and reduction needs to be carried out to obtain graphene-like properties. Chemical reduction has been achieved with hydrazine monohydrate to obtain well dispersed single layer graphene sheets generally called as reduced graphene oxide.[28b, 29]

Rapid heating to 1050 °C also breaks up functionalized GO into individual sheets through evolution of CO_2.[30] A statistical analysis by atomic force microscopy has shown that 80% of the observed flakes are single sheets.[30b] Exfoliation of commercial expandable graphite has also been carried out by heating at 1000 ºC in forming gas for 60 sec.[31] Guoqing et al.[32] used microwave to give a thermal shock to acid intercalated graphite oxide in order to carry out the exfoliation. Liang et al.[33] patterned few-layer graphene on SiO_2/Si substrates using the electrostatic force of attraction between HOPG and the Si substrate. Laser exfoliation of HOPG has also been employed to prepare few-layer graphene, using a pulsed neodymium-doped yttrium aluminum garnet (Nd:YAG) laser.[34] The product depends on laser fluence, a fluence of ~ 5.0 Jcm^{-2} yeilded high quality graphene with ultrathin morphology.

Viculis et al.[26] prepared K-, Cs-, and NaK_2-intercalated graphite by reacting alkali metals with acid intercalated exfoliated graphite in pyrex sealed tubes. GICs were treated with ethanol causing a vigorous reaction to yield exfoliated few-layer graphene. A schematic representation of the reaction is presented in Figure 3(A). K-intercalated GICs have also been prepared using the ternary potassium salt to obtain $K(THF)_xC_{24}$ and they get readily exfoliated in N-methyl pyrrolidone yielding a dispersion of negatively charged single layer graphene which can then be deposited onto any substrate.[35]

Direct exfoliation along with noncovalent functionalization and solubilization of graphene in water is achieved by employing the potassium salt of coronenetetracarboxylic acid (CS) to yield monolayer graphene-CS composites (see Figure 3(B)).[36] Stable high-concentration
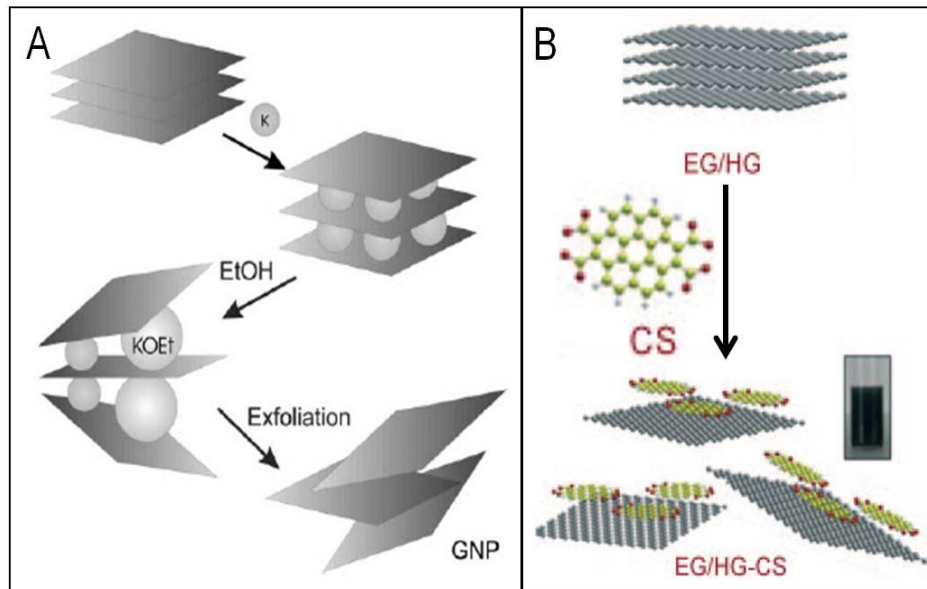
Figure 3: (A) Schematic diagram showing the intercalation of potassium between layers followed by violent reaction with alcohol to produce exfoliated ~30 layers thin slabs of graphite. (Reprinted with permission from [22]) and (B) a schematic illustration of the exfoliation of few-layer graphene with Coronene tetracarboxylate (CS) to yield monolayer graphene–CS composites (from ref [36]).

suspensions of few-layer graphene was obtained by direct sonication in ionic liquids.[37] Exfoliation-reintercalation-expansion of graphite yields highly conducting graphene sheets suspended in organic solvents.[31]

Chemical Vapor Deposition: The most promising, inexpensive and readily accessible approach for the deposition of reasonably high quality graphene is chemical vapor deposition (CVD) onto transition metal substrates such as Ni[38] Pd,[39]Ru,[40]Ir[41]or Cu.[1c] The process is based on the carbon-saturation of a transition metal upon exposure to a hydrocarbon gas at high temperature. While cooling the substrate, the solubility of carbon in the transition metal decreases and a thin film of carbon precipitates from the surface.[42] Different hydrocarbons such as methane, ethylene, acetylene and benzene were decomposed on various transition metal substrates like Ni, Cu, Co, Au and Ru.[42]

A radio frequency plasma enhanced chemical vapor deposition (PECVD) system has been used to synthesize graphene on a variety of substrates such as Si, W, Mo, Zr, Ti, Hf, Nb, Ta, Cr, 304 stainless steel, SiO_2 and Al_2O_3. This method reduces energy consumption and prevents the formation of amorphous carbon or other types of unwanted products.[43] Graphene layers have been deposited on different transition metal substrates by decomposing hydrocarbons such as methane, ethylene, acetylene and benzene. CVD with various hydrocarbons on different metal catalysts gave the conclusion that the growth of graphene film, depends on the
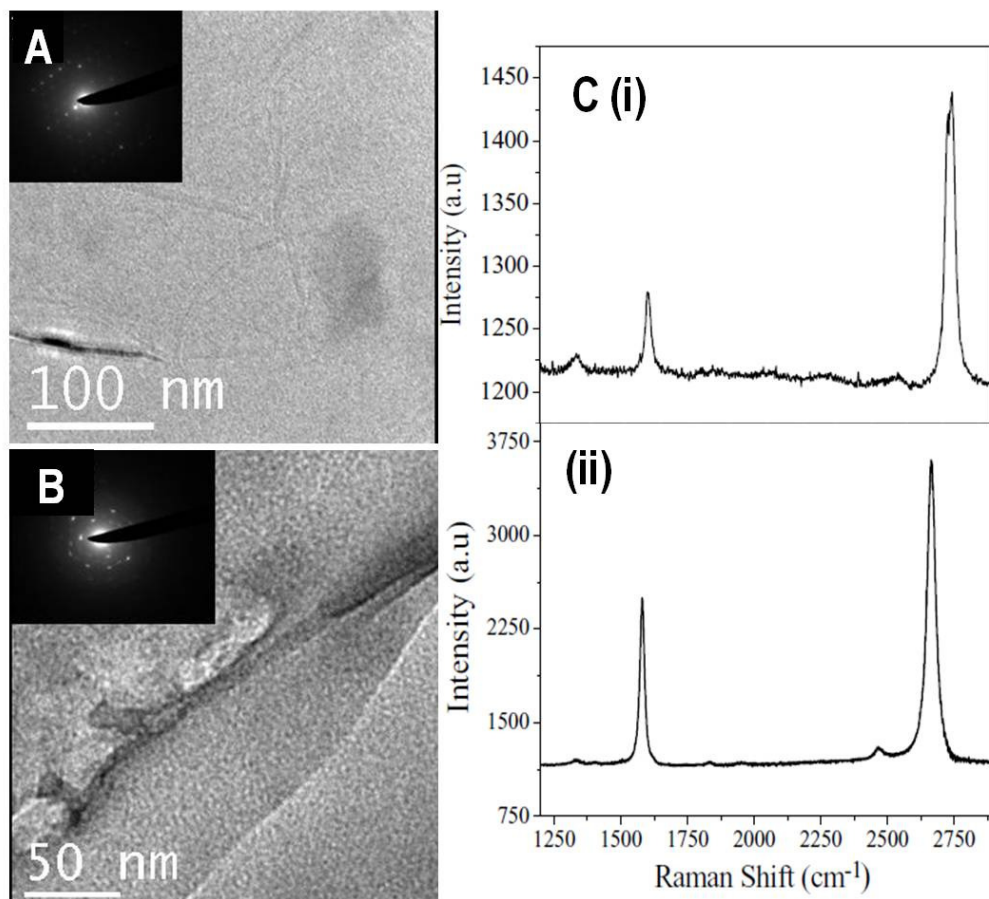
Figure 4: TEM images of graphene prepared by the thermal decomposition of (A) methane (70 sccm) at 1000 °C, (B) benzene (Ar passed through benzene with flow rate of 200 sccm) at 1000 °C on a nickel sheet. Insets show electron diffraction pattern from the corresponding graphene sheets and (C) Raman spectra of graphene prepared from the thermal decomposition of (i) methane and (ii) benzene (from ref [1e]).

hydrocarbon source and the reaction conditions. On a nickel foil, CVD of methane (60–70 sccm) or ethylene (4–8 sccm) diluted with hydrogen (500 sccm) at 1000 °C for 5–10 min yielded SLG. In the case of benzene, vapors diluted with argon and hydrogen were decomposed at 1000 °C for 5 min. On a cobalt foil, acetylene (4 sccm) and methane (65 sccm) diluted with hydrogen (500 sccm) were decomposed at 800 and 1000 °C respectively. Figure 4 shows the TEM images and the Raman spectra of graphene sheets obtained by CVD method. The narrow line width (30-40 cm^{-1}) and relatively high intensity of the 2D band (~ 2670 cm^{-1}) indicate that these graphene samples predominantly contain single-layer.[1e] The narrow line width and relatively high intensity of 2D band in Raman spectra confirm the formation of graphenes having 1-2 layers.[42] Graphene obtained using CVD process can be transferred to other substrates by etching of the underlying transition metal and can be transferred in to any arbitrary substrate.

Arc Discharge: Synthesis of graphene by the arc evaporation of graphite in the presence of hydrogen has been reported.[44] This procedure yields graphene (HG) sheets with 2-3 layers having flake size of 100-200 nm. This makes use of the knowledge that the presence of H_2 during arc-discharge process terminates the dangling carbon bonds with hydrogen and prevents the formation of closed structures. The conditions that are favorable for obtaining graphene in the inner walls are the high current (above 100 A), the high voltage (>50 V), and the high pressure of hydrogen (above 200 torr). This method has been conveniently employed to dope graphene with boron and nitrogen.[45] To prepare boron and nitrogen doped graphene (B-HG and N-HG) the discharge is carried out in the presence of H_2+diborane and H_2+(pyridine or ammonia) respectively. Based on these observations with some minor modifications in the synthetic conditions, resulted few-layer graphene samples in bulk scale. Cheng et al.[46] employed hydrogen arc discharge process as a rapid heating method to prepare graphene from

GO. Graphene nanosheets are prepared by arc discharge in an air atmosphere resulted in graphene nanosheets of ~100–200 nm wide predominantly with 2–layers.The yield depends strongly on the initial air pressure.[47] Li et al.[48] have synthesized N-doped multi-layer graphene in He and NH_3 atmosphere using arc-discharge method. Arc-discharge carried out in a helium atmosphere has been explored to obtain graphene sheets with different number of layers by regulating gas pressures and currents.[49]

Reduction of graphite oxide: Chemical reduction of graphite oxide is one of the established procedures to prepare graphene in large quantities.[28c] Graphite oxide when ultra sonicated in water forms a homogenous colloidal dispersion of predominantly single layer graphene oxide in water. Reduced graphene oxide with properties similar to that of graphene is prepared through chemical, thermal, or electrochemical reduction pathways.[27] While most strong reductants have slight to strong reactivity with water, where hydrazine monohydrate does not, making it an attractive option for reducing aqueous dispersions of graphene oxide.[27] Large excess of $NaBH_4$ has also been used as a reducing agent.[50] Other reducing agents used include phenyl hydrazine[51], hydroxylamine,[52] glucose,[53] ascorbic acid,[54] hydroquinone,[55] alkaline solutions,[56] pyrrole[57] etc. Electrochemical reduction is another means to synthesize graphene in large scale. The reduction initiates at -0.8 V and is completed by -1.5 V with formation of black precipitate on the bare graphite electrode.[58] Zhou et al.[59] coupled electrochemical reduction with a spray coating technique to prepare large-area and patterned RGO films with thicknesses ranging from a single-layer to several microns on various conductive and insulating substrates.

1.1: Brief overview of graphene

Photothermal and photochemical reduction of GO is a rapid, clean, and versatile way to obtain RGO. Ding et al.[60] reduced GO using UV irradiation to obtain single- to few-layer graphene sheets without the use of any photocatalyst. Cote et al.[61] prepared RGO by photothermal reduction of GO using Xenon flash at ambient conditions and patterned GO or GO/polymer films using photomask. Nanosecond laser pulses of KrF excimer laser or 335 nm and 532 nm were shown to effectively reduce dispersions of GO to thermally and chemically stable graphene.[62]
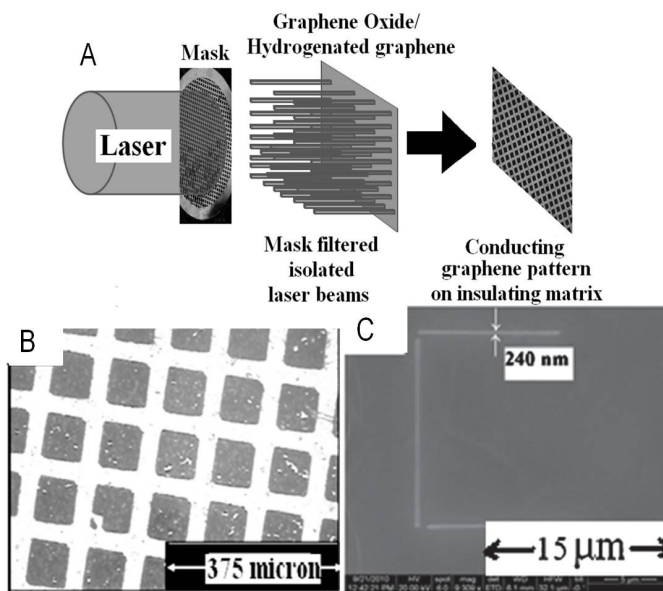
Figure 5: (A) Schematic diagram illustrating masked laser patterning, (Reprinted with permission from [63(a)]) (B) Optical microscopic image of the pattern achieved after excimer laser reduction of graphene oxide, (C) Electron-beam pattern with 250 nm wide lines of RGO on GO films (from ref [63a]).

High quality RGO has been prepared by irradiating GO with sunlight, ultraviolet light and KrF excimer laser.[63] The reduction of GO to graphene by excimer laser irradiation results in the change of color of the solid GO film from brownish yellow to black.

Photochemical reduction of GO and single layer graphene oxide (SGO) to graphene has also been exploited for pattering. For this purpose GO films deposited on Si substrates were subjected to excimer laser radiation (Lambda Physik KrF excimer laser, 248 nm wavelength, 30 ns life time, 300 mJ laser energy, 5 Hz repetition rate, 200 shots), after inserting a TEM grid as

the mask and covering them with a quartz plate. Figure 5(A) shows a schematic representation of the process of laser patterning using TEM grid as mask and Figure 5(B) shows the optical microscopic image of the pattern achieved after excimer laser reduction of graphene oxide respectively. Electron beam induced reduction of GO has been reported.[64] Electron-beam patterning of GO films has been used to obtain patterns of RGO as thin as 250 nm as shown in Figure 5(C).[63a]

1.1.5: Properties and applications of graphene

Surface area and gas adsorption: Single-layer graphene is theoretically predicted to have a large surface area of 2600 m^2/g[7] while that for few-layer graphene is 270-1550 m^2/g.[8a] Patchkovskii et al.[65] carried out computations and suggested that H$_2$ adsorption capacities on graphene can approach the values set by the US Department of Energy (DOE) (6.5 wt% and 62 kg of H$_2$ per m^3). H$_2$ adsorption studies on few-layer graphene samples prepared by the EG and DG by Ghosh et al. has revealed a H$_2$ uptake value of 1.7 wt% at atmospheric pressure and 77 K. A maximum adsorption of 3 wt% was achieved at 298 K and 100 atm for EG. Adsorption of H$_2$ was found to be directly proportional to the surface area of the samples as can be seen in Figure 6 (A)).[8b]
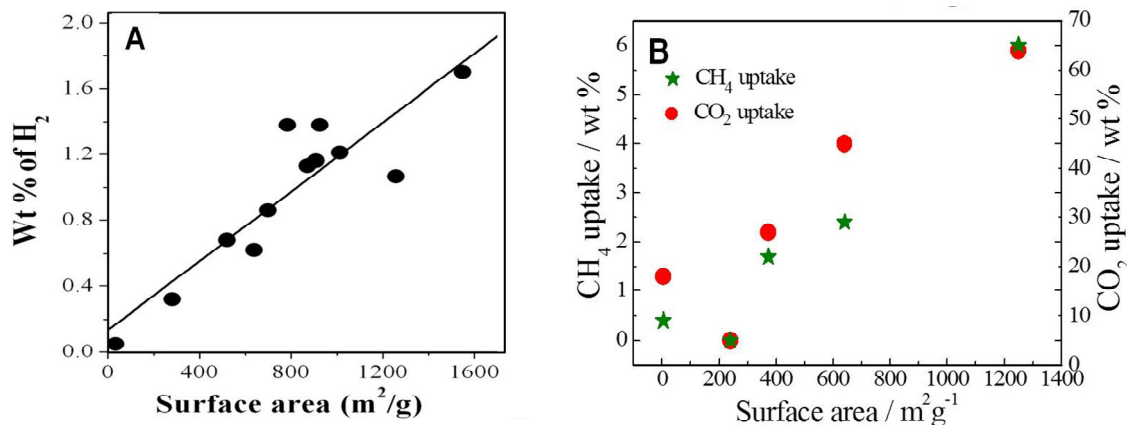
Figure 6: (A) Linear relationship between the BET surface area and weight percentage of hydrogen uptake at 1 atm pressure and 77 K for various graphene samples(Reprinted with permission from [8b]) and (B) Plot of weight% of CO$_2$ uptake (at 195K and 1 atm) and methane uptake (at 298K and 5MPa) versus surface area for different graphene samples (from ref [8b]).

1.1: Brief overview of graphene

Adsorption depended on surface areas of the studied samples with EG showing the highest surface area (640 m^2/g) and SGO, the lowest (5 m^2/g) while activated charcoal had a surface area of 1250 m^2/g. Activated charcoal showed 64 wt % uptake of CO_2 at 195 K and 1 atm while uptake of CO_2 by EG at 298 K and 50 bar was 51 %. The uptake values varied between 5 and 45 wt % in the case of graphene samples at 195K and 0.1MPa with EG exhibiting the highest uptake. However, all the graphenes exhibit smaller uptake capacity for CO_2 compared to activated charcoal which also has a huge number of surface functional groups. Adsorption of methane on the graphenes and activated charcoal was measured at 273 K and 298 K. The weight uptake of methane by activated charcoal is 7 and 6 wt % at 273 K and 298 K and 5 MPa respectively. The CH_4 uptake of the graphene samples varies between 0 and 3 wt % at 273 K and 5MPa. Figure 6 (B) shows the CO_2 and methane uptake of graphene samples as well as activated charcoal against their surface areas.

Molecular Charge-Transfer: Interaction of carbon nanostructures with electron-donor and electron-acceptor molecules causes marked changes in their electronic structure and properties. C_{60} is known to exhibit charge-transfer interaction with electron donating molecules such as organic amines both in the ground and excited states.[9a]

Electron donors such as aniline and tetrathiafulvalene (TTF) soften (i.e. shift to lower frequency) the G-band of few-layer graphene progressively with the increasing concentration while electron-acceptors such as nitrobenzene and tetracyanoethylene (TCNE) stiffen (i.e. shift to higher frequency) the G band as can be seen from Figures 7(A) and 7(B).[9] Both electron-donors and –acceptors broaden the G-band. The intensity of the 2D-band decreases markedly with the concentration of either donor or acceptor molecule. The ratio of intensities of the 2D and G bands, $I_{(2D)}/I_{(G)}$, is a sensitive probe to examine doping of graphene by electron-donor and

-acceptor molecules. Dong et al.[66] have studied the adsorption of various aromatic molecules on single-layer graphene films which cause stiffening or softening of the G-band frequencies.
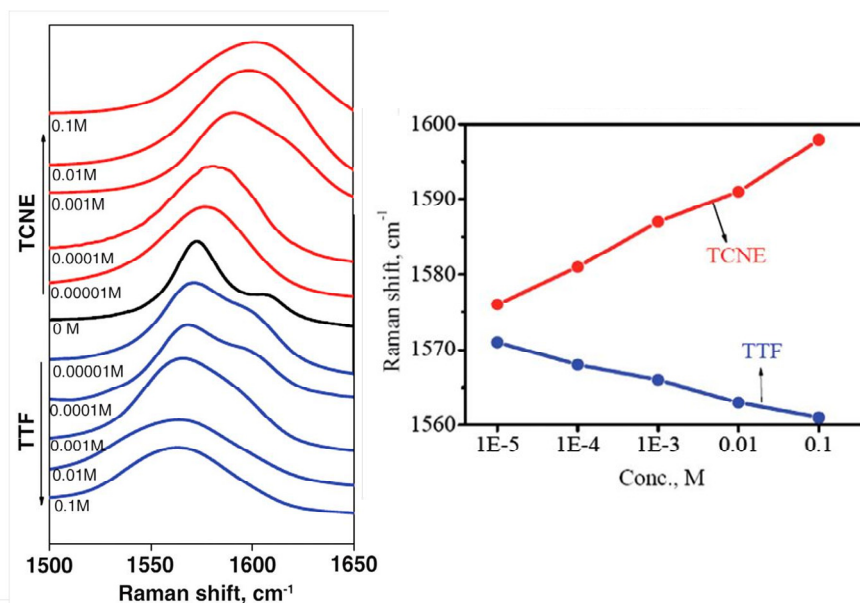
Figure 7: (A) Shifts of the Raman G-band of graphene caused by interaction with varying concentrations of TTF and TCNE, (B)Variation in the Raman G-band position of graphene on interaction with varying concentrations of electron-donor (TTF) and electron-acceptor (TCNE) molecules. (from ref [9])

Investigations of charge-transfer doping of few-layer graphene (one-layer (1 L) to four-layer (4 L)) with Br_2 and I_2 vapors have shown that charge-transfer effects are greater on single- and bi–layer graphenes compared to three- and four–layer graphenes.[67] Detailed studies of the interaction of halogen molecules with graphene have been carried out.[68] Stiffening of the Raman G-bands on treating with the different halogen molecules and the emergence of new bands in the electronic absorption spectra, both point to the fact that the halogen molecules are involved in molecular charge-transfer with the nanocarbons. The magnitude of molecular charge transfer between the halogens and the nanocarbons generally varies in the order ICl>Br_2>IBr>I_2 which is consistent with the expected order of electron affinities.[68] The occurrence of charge-

transfer doping in few-layer graphene covered with electron acceptor (TCNE) and donor (TTF) molecule is also evidenced in the electronic absorption spectra and X-ray photoelectron spectroscopy (XPS).[69] Quantitative estimates of the extent of charge transfer in these complexes have been obtained from XPS. Electrical resistivity of graphene films with and without charge transfer interactions show the expected changes. For example, the resistance is lowest in the presence of nitrobenzene and highest in the presence of aniline. There is a systematic dependence of resistance with the electron -donating and -withdrawing power of the substituents. The magnitude of interaction between graphene and donor/acceptor molecules seems to depend on the surface area of the graphene sample.[9a] DFT calculations confirm the occurrence of charge-transfer induced changes in graphene giving rise to mid-gap molecular levels with tuning of band gap region near the Dirac point and show how they are different from the effects of electrochemical doping.[70] It has been shown that n-type and p-type graphenes result from charge-transfer interaction of graphene with donor- and acceptor-molecules respectively. It is also predicted that the extent doping depends on the coverage of organic molecules.

Decoration with metal and oxide nanoparticles: Nanocarbons have been used as support materials for the dispersion and stabilization of metal nanoparticles due to their large chemically active surface area and stability at high temperatures. Decoration with metal nanoparticles result in changing the electronic structure of nanocarbons through Columbic charge-transfer.[71] Combinations of these two materials may lead to a successful integration of their properties in hybrid materials with possible use in catalysis, nanoelectronics, optics and nanobiotechnology.[72]

Palladium nanoparticle–graphene hybrids were used as an efficient catalysts for the Suzuki reaction.[73] Three-dimensional Pt-on-Pd bimetallic nanodendrites supported on graphene

nanosheets were used as an advanced nanoelectrocatalysts for methanol oxidation.[74] Composites of positively charged gold nanoparticles (GNPs) and pyrene functionalized graphene (PFG) showed strong electrocatalytic activity and high electrochemical stability.[75] Au films deposited on SLG are used for surface enhanced Raman scattering (SERS) substrates for the characterization of rhodamine R6G molecules.[76] Silver-decorated graphene oxide (Ag–GO) can be used as an antibacterial material, with a superior antibacterial activity towards Escherichia coli (E. coli).[77]

Graphene has been decorated with metal nanoparticles such as Au, Ag, Pt, Pd and Co employing different chemical methods.[78] The influence of metal nanoparticles on the electronic structure of graphene has been examined by microscopic and spectroscopic techniques along with
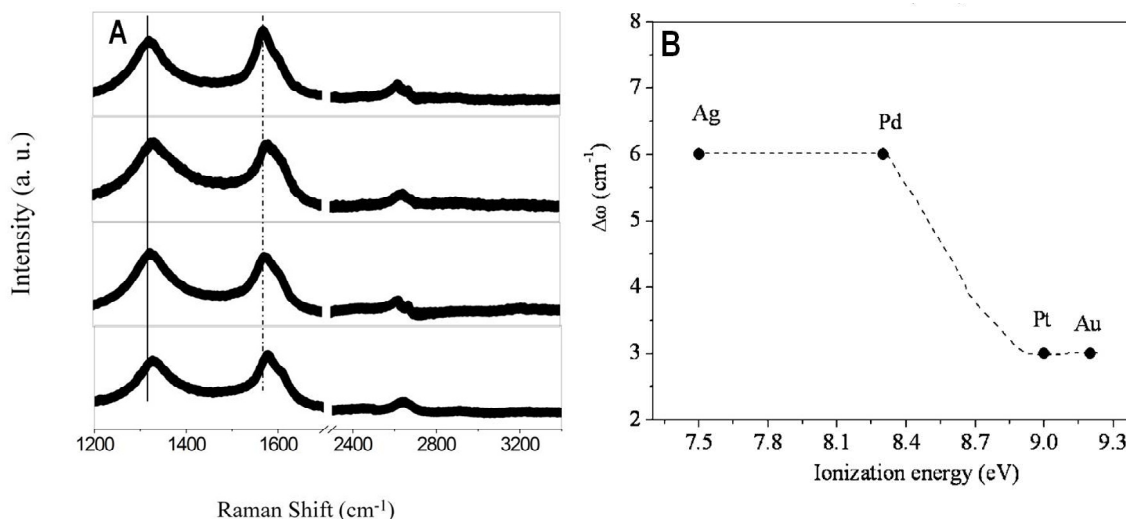
Figure 8: (A) Raman spectra of EG, EG-Ag, EG-Pt and EG-Au. (B) Variation in the position of the G-band with the ionization energy of the metal. The broken curves given as a guide to the eye (from ref [71]).

the first-principles calculations.[71] There is stiffening in the position of G-band, and the relative intensity of the 2D band to the G band decreases (Figure 8(A)). The shifts in the G- band show meaningful trends with the ionization energies of the metals as well as the charge-transfer energies. Figure 8(B) shows the frequency shifts of the G band of EG against the ionization

energy (IE) of the metal. Interestingly, the magnitude of the band shifts generally decreases with increase in ionization energy of the metal.

Graphene oxide (GO) is known to interact with NPs of semiconducting oxides such as ZnO and TiO_2 through excited-state electron transfer.[79] A study of the magnetic properties of graphene composites with nanoparticles of ZnO, TiO_2, Fe_3O_4, $CoFe_2O_4$, and Ni has been carried out.[80] These composites also yield higher values saturation magnetization compared to the individual particles or their mechanical mixtures with graphene. First principles DFT calculations reveal that the weak charge transfer interaction and the magnetic coupling are directly linked to the ionization energy and electron affinity of the deposited NPs.

Mechanical properties: Lee et al.[5] measured the elastic properties and intrinsic breaking strength of free-standing monolayer graphene membranes by nanoindentation and found that it possess a excellent echanical properties such as an elastic modulus of ~1 TPa, a strength of
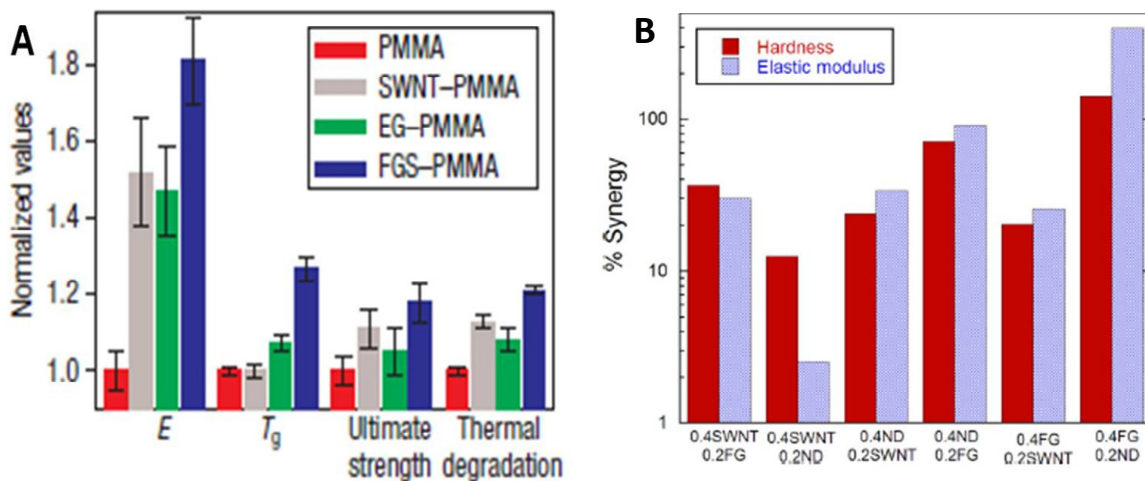
Figure 9: (A) Summary of thermo-mechanical property improvements for 1 wt% single layer functionalized graphene–PMMA compared to SWNT–PMMA and EG–PMMA composites with all property values normalized to the values for neat PMMA(from ref [83]) and (B) Percentage synergy in mechanical properties of different binary mixtures of nanodiamond (ND), single walled nanotubes (SWNTs) and few layer graphene (FG) (from ref [85]).

~130 GPa and a breaking strength of 42Nm^{-1}. This has led to the exploration of graphene-reinforced polymer matrix composites.[81] Ramanathan et al.[82] have reported that just ~1 wt% addition of graphene to PMMA leads to increases of 80% in elastic modulus and 20% in ultimate tensile strength compared to other nanofillers (see Figure 9(A)). A combined effect of nanoscale surface roughness results in enhancing mechanical interlocking along with the functionalized graphene sheets which enhances the interaction with the polymer matrix to transfer load between matrix and the fiber which is responsible for the enhanced mechanical properties. A significant increase of 35% and 45% respectively in the elastic modulus and hardness was observed on addition of just 0.6 wt% of graphene to PVA.[83] Rafie et al.[84] compared the mechanical properties of epoxy composites of 0.1 wt% of graphene with that of CNTs and found that graphene composites showed much greater increase in Young's modulus (by 31%), tensile strength (by 40%) and fracture toughness by 53% with nanotube-epoxy composites. Planar geometry of graphene and better matrix adhesion and interlocking arising from their wrinkled surface is presumed to be the cause of better mechanical properties of graphene composites.[84]

Detailed studies of the mechanical properties of binary combinations of nanodiamond (ND), few-layer graphene (FG), and single-walled nanotubes (SWNT) in PVA matrices have been carried out. The mechanical properties of the resulting composites, evaluated by the nanoindentation technique, showed extraordinary synergy with improvement by as much as 400% in stiffness and hardness compared to those obtained with single nanocarbon reinforcements. The synergistic effect was dramatic in the ND plus FG composites (PVA-0.4FG-0.2ND) with 4- and 1.5-fold increases in E and H, respectively (see Figure 9(B)). Variation in the percent crystallinity (%) of the PMCs with the two nanocarbons is around 2%, suggesting that increase in crystallinity was not the cause of the observed synergy.[85]

1.1: Brief overview of graphene

Field effect transistors: Experiments with field-effect transistors (FETs) on micromechanically cleaved graphene by Novoselov et al.[1a] have revealed that the sheet resistivity (ρ) depends on the gate voltage (V_g) exhibiting a sharp peak to a value of several kilo ohms and decays back to 100 ohms on increasing V_g (see Figure 10(A)). At the same V_g where ρ had its peak, the Hall coefficient showed a sharp reversal of its sign thus revealing ambipolar character (see Figure 10(B)). Micromechanically cleaved graphene showed extremely high mobilities of ~15,000 cm^2/V.s at room temperature with electron and hole FET concentrations of 10^{13} cm^2 with ballistic transport up to sub micrometer distances.[1a] Characteristics of EG, DG, HG, N-HG (nitrogen doped HG) and B-HG (boron doped HG) have been investigated by us in comparison with RGO. RGO showed ambipolar transfer characteristics on sweeping the V_{gs} between -20 to +20 V and V_{ds} = 1V, while all the few-layer graphenes showed n-type behavior. The highest mobility was found with HG possessing 2-3 layers and with the least defects. FETs based on boron and nitrogen doped graphene show n-type and p-type behaviour respectively.[86] Different factors such as the average number of layers, surface functionality and concentration of defects are found to be responsible for observing different characteristics in the different samples. HG with the smallest number of layers exhibits the highest mobility. It is remarkable that transistor characteristics are found even in few-layer samples with defects. Hwang et al.[87] theoretically calculated the phonon scattering limited extrinsic electron mobility in graphene to be a function of temperature and carrier density with the room-temperature intrinsic mobility reaching the values of above 105 cm^2/V.s. Chen et al.[1d] have shown that electro-acoustic phonon scattering in graphene is independent of the carrier density and contributes just 30 Ω to room temperature resistivity of graphene with intrinsic mobility of graphene being 200,000 cm^2/V.s. The actual mobility, is however, dependent on scattering by various extrinsic factors

21

like surface phonons,[88] charged impurities on top of graphene or in the underlying substrate [89] and ripples and corrugation in the graphene sheet.[90] Dramatically reduced carrier scattering was reported in suspended graphene devices by Du et al.[91] allowing the observation of a very high mobility of 120,000 cm^2/V.s near room temperature (T~240 K).
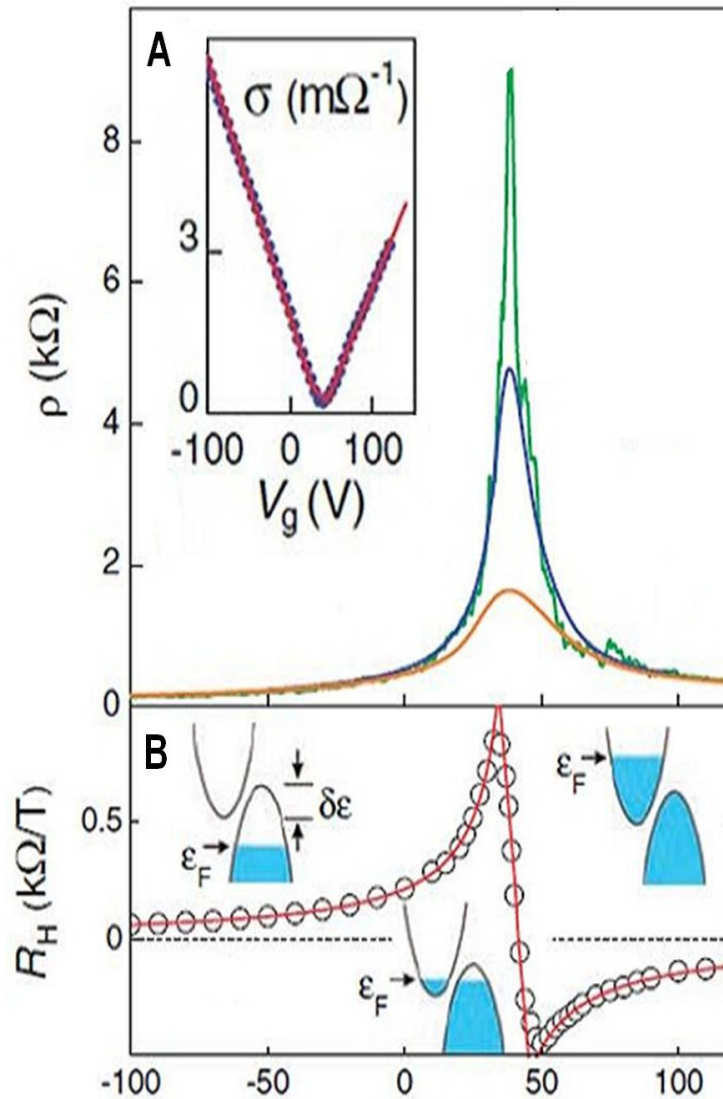
Figure 10: (A) Resistivity ρ of few-layer graphene on gate voltage (V$_g$) for different temperatures (T = 5, 70, and 300 K from top to bottom) with inset showing the change in conductivity σ = 1/ρ (at 70 K) and (B) Hall coefficient R$_H$ versus V$_g$ for the same at 5 K (from ref [1a]).

1.1: Brief overview of graphene

Since the bandgap of graphene is zero, devices with channels made of large-area graphenes cannot be switched off and therefore are not suitable for logic applications. However, the band structure of graphene can be modified, to open a bandgap by constraining large-area graphene in one dimension to form graphene nanoribbons. Chen et al.[92] have fabricated graphene nano ribbons (GNR) FETs with 20-40 nm width and measured FET characteristics with high ON/OFF ratios. FETs with sub-10 nm nanoribbons prepared by Wang et al.[93] showed much greater I_{ON}/I_{OFF} of 10^5 at room temperature. The device had 20 times higher current density and 100 times higher transconductance per μm, due to larger band gaps and high GNR quality with better edge smoothness.

Supercapacitors: Vivekchand et al.[94] prepared the electrochemical supercapacitors with different graphene samples as electrode material in aq. H_2SO_4 as well as in an ionic liquid (N-butyl-N-methylpyrrolidiniumbis(trifluoromethanesulfonyl)imide, PYR14TFSI) as electrolytes. Exfoliated graphene (EG) and diamond graphene (DG) exhibit high specific
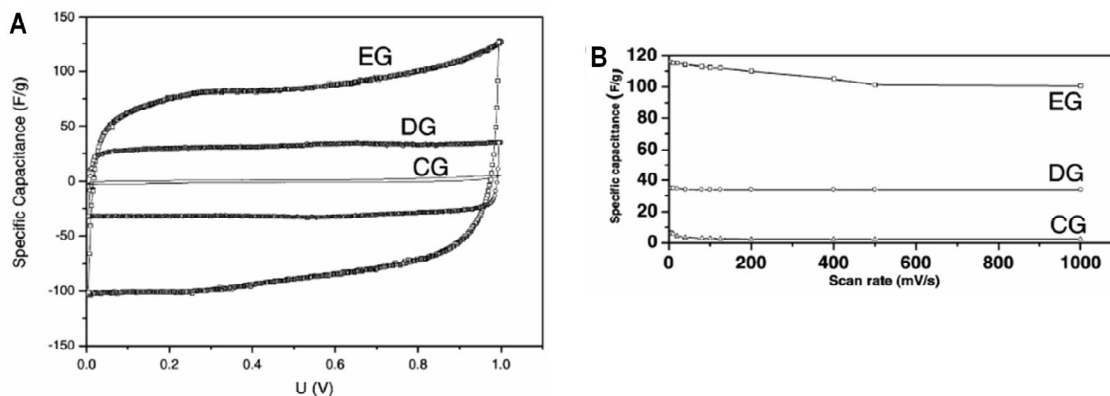
Figure 11: (A) Voltammetric characteristics of a capacitor built from different graphene electrodes (5 mg each) at a scan rate of 100 mVs^{-1} in aqueous H_2SO_4 (1m) and (B) specific capacitance as a function of scan rate (from ref [94]).

capacitance in aq. H_2SO_4, the value reaching up to 117 and 35 F/g respectively. Voltammetric characteristics of a capacitor built from graphene electrodes (5 mg each), at a scan rate of 100 mV/s using aqueous H_2SO_4 (1 M) shown in Figure 11(A). Figure 11(B) shows specific capacitance as a function of scan rate for different graphene samples. By using an ionic liquid, the operating voltage has been extended to 3.5 V (instead of 1 V in the case of aq. H_2SO_4), the specific capacitance values being 75 and 40 F/g for EG and DG respectively. High surface area graphite prepared by ball-milling showed a large specific capacitance of 33 $\mu F\ cm^{-2}$ in aqueous medium, which might be due to high open surface area, lattice defects, and oxygen functional groups presented in the sample.[95]

Chemically modified graphene sheets obtained by the reduction of graphene oxide with hydrazine when used as electrode material in supercapacitors gave specific capacitances of 135 and 99 F/g in aqueous and organic electrolytes, respectively.[96] 3D CNT/graphene sandwich structures with CNT pillars grown in between the graphene layers have been used as high-performance electrode materials for supercapacitors and a maximum specific capacitance of 385 F/g could be obtained at a scan rate of 10 mV/s in 6 M KOH aqueous solution.[97] Graphene/polyaniline composites with an appropriate weight ratio prepared using in-situ polymerization exhibited a higher specific capacitance of 1046 F /g at a scan rate of 1 mV/s due to the synergistic effect between graphene and polyaniline.[98] Graphene–$Co(OH)_2$ nanocomposite shows a capacitance as high as 972.5 F /g, leading to a significant improvement.[99]

1.1: Brief overview of graphene

Field emission and blue light emission: There have been several attempts to investigate the field emission properties of graphene films recently.[100] To take advantage of the high field enhancement, graphene sheets would have to stand on their edges and not lay laterally flat on the substrate. A spin-coated graphene-polystyrene composite film was reported to exhibit a threshold field of 4V/µm (at 10^{-8} A/cm^2) with a field enhancement factor of 1200.[100a] Malesevic et al.[100b] grew vertically aligned few-layer graphene films by CVD and found these films to exhibit favorable turn-on field but decays after five cycles.

Field emission properties of undoped arc-discharge graphene (HG), as well as boron- and nitrogen-doped graphenes have been studied. Electrophoretic deposition was employed for
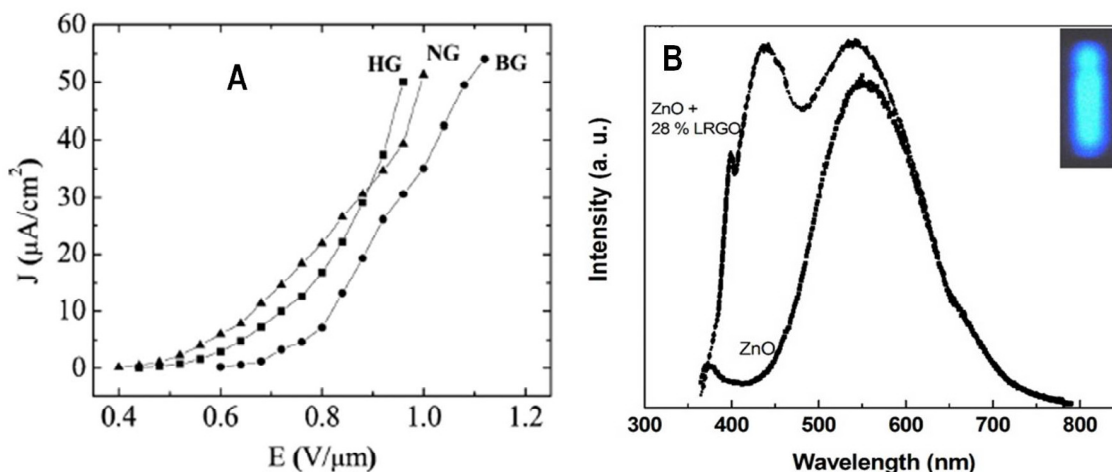
Figure 12: (A) Current density (j) of undoped HG, boron-doped BG, and nitrogen-doped NG graphenes as a function of electric field (from ref [101]) (B) White light emission from ZnO-LRGO nanocomposites (from ref [103]).

depositing vertically oriented graphene sheets.[101] N-doped graphene showed the lowest turn-on field of 0.6 V/µm with an emission current density of 10 µA/cm^2 (see Figure 12(A)).

Aqueous solutions of acid treated graphene or reduced graphene oxide shows blue emission centered at 440nm on being excited by UV of 325 nm.[102] On mixing the blue light emitting graphene sample with yellow emitting zinc oxide nanoparticles it is possible to get bluish white

1.1: Brief overview of graphene

light as can be seen in Figure 12(B).[103] A plausible cause of the blue photoluminescence in reduced graphene oxide (RGO) is the radiative recombination of electron-hole (e-h) pairs generated within localized states. The energy gap between the π and π^* states generally depends on the size[104] of the sp^2 clusters or conjugation length.[105] Interaction between nanometer-sized sp^2 clusters and finite-sized molecular sp^2 domains could play a role in optimizing the blue emission in RGO. The presence of isolated sp^2 clusters in a carbon-oxygen sp^3 matrix can lead to the localization of e-h pairs, facilitating radiative recombination of small clusters.

Chemical storage of hydrogen and halogens: Hydrogenation of graphene has been carried out with hydrogen plasma and also from molecular H_2 by catalytic hydrogenation.[106] Elias et al.[107] have reported the reversible hydrogenation of graphene films prepared by micromechanical cleavage of graphite. Hydrogenation was obtained with cold hydrogen plasma containing hydrogen-argon mixture (10 % H_2). The hydrogenated sample showed the evidence of metallic to insulator transition. Zheng et al. [106] have adopted the catalytic hydrogenation of graphene using Radio frequency catalytic chemical vapor deposition (rf-cCVD) in which they used Ni (8 wt %) in Al_2O_3 as catalyst. Hydrogenation was confirmed by the appearance of peaks at 2920 cm^{-1} and 2853 cm^{-1} in (C-H stretching modes) in IR spectra and an increase in the intensity of D-band in Raman spectrum of hydrogenated samples. Chemical hydrogenation of various graphene samples (EG and HG) by Birch reduction has been performed.[108] Evidence of hydrogenation were obtained from appearance of C-H stretching modes in the IR spectra of hydrogenated samples as can be seen from Figure 13(A). An increase in the intensity of D-band relative to G-band in the Raman spectrum of hydrogenated EG and HG (EGH and HGH) samples reflects an increase in the sp^3 character. Elemental analysis of reduced graphene samples
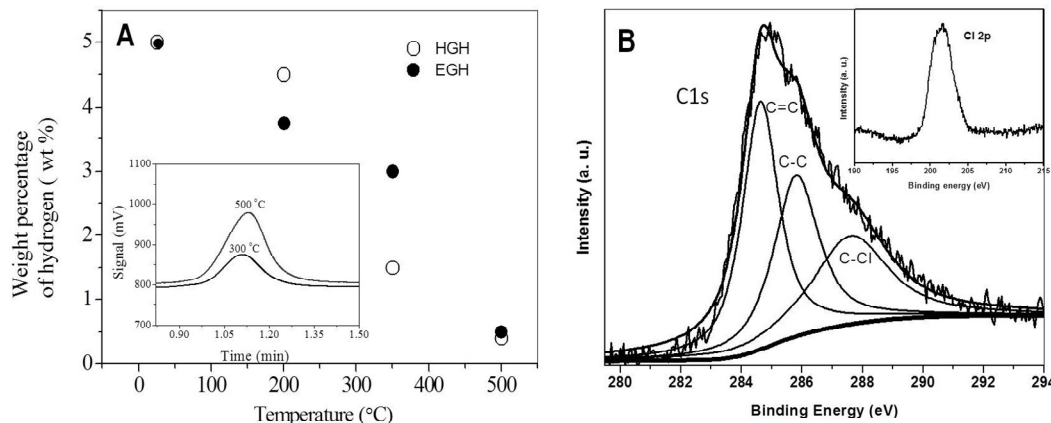
Figure 13: (A) Change in weight percentage of hydrogen released from EGH and HGH with temperature. In inset is shown the evolution of hydrogen as recorded by a gas chromatograph (Reprinted with permission from [108]) and (B) C1s core level XP spectrum of photo-chlorinated graphene. Inset shows the Cl 2p signal in XPS (Reprinted with permission from [109]).

showed the hydrogen content to be around 5 wt %. Thermal analysis of EGH and HGH showed that these samples were stable at room temperature for prolonged time. Almost all the H_2 was lost by 500 ºC and the sample regained its original properties. Dehydrogenation could also be obtained by irradiation of the hydrogenated samples with UV radiation or with a KrF excimer laser. On dehydrogenation the sample regains all its properties and becomes graphene like. Birch reduction of graphene nanoribbons (GNR) prepared by oxidative unzipping of carbon nanotubes showed the H_2 uptake of 3 wt%. Thermal analysis of the sample showed H_2 loss initiating at 300ºC and completing by 600 ºC with release of 3.05 wt % H_2 during this period. Chlorination of graphene (HG and EG) by irradiation with UV light in liquid chlorine medium giving rise to chlorination of 56 wt. % has been reported (Figure 13(B)).[109]

1.1.6: References

[1]   a)K. S. Novoselov, A. K. Geim, S. V. Morozov, D. Jiang, Y. Zhang, S. V. Dubonos, I. V. Grigorieva, A. A. Firsov, *Science* **2004**, *306*, 666; b)K. S. Novoselov, A. K. Geim, S. V. Morozov, D. Jiang, M. I. Katsnelson, I. V. Grigorieva, S. V. Dubonos, A. A. Firsov, *Nature* **2005**, *438*, 197; c)C. N. R. Rao, A. K. Sood, K. S. Subrahmanyam, A. Govindaraj, *Angew. Chem. Int. Ed.* **2009**, *48*, 7752; d)J.-H. Chen, C. Jang, S. Xiao, M. Ishigami, M. S. Fuhrer, *Nat. Nanotechnol.* **2008**, *3*, 206; e)C. N. R. Rao, K. S. Subrahmanyam, H. S. S. Ramakrishna Matte, B. Abdulhakeem, A. Govindaraj, B. Das, P. Kumar, A. Ghosh, D. J. Late, *Sci. Tech. Adv. Mater.* **2010**, *11*, 054502; f)L. Gao, W. Ren, F. Li, H.-M. Cheng, *ACS Nano* **2008**, *2*, 1625; g)H.Hiura, H.Miyazaki, K.Tsukagoshi, *Appl. Phys. Exp.* **2010**, *3* 095101

[2]   M. Y. Han, Ouml, B. zyilmaz, Y. Zhang, P. Kim, *Phys. Rev. Lett.* **2007**, *98*, 206805.

[3]   J. C. Meyer, C. Kisielowski, R. Erni, M. D. Rossell, M. F. Crommie, A. Zettl, *Nano Lett.* **2008**, *8*, 3582.

[4]   R. R. Nair, P. Blake, A. N. Grigorenko, K. S. Novoselov, T. J. Booth, T. Stauber, N. M. R. Peres, A. K. Geim, *Science* **2008**, *320*, 1308.

[5]   C. Lee, X. Wei, J. W. Kysar, J. Hone, *Science* **2008**, *321*, 385.

[6]   Y. Wang, Y. Huang, Y. Song, X. Y. Zhang, Y. F. Ma, J. J. Liang, Y. S. Chen, *Nano Lett.* **2009**, *9*, 220.

[7]   A. Peigney, C. Laurent, E. Flahaut, R. R. Bacsa, A. Rousset, *Carbon* **2001**, *39*, 507.

[8]   a)C. N. R. Rao, A. K. Sood, R. Voggu, K. S. Subrahmanyam, *J. Phys. Chem. Lett.* **2010**, *1*, 572; b)A. Ghosh, K. S. Subrahmanyam, K. S. Krishna, S. Datta, A. Govindaraj, S. K. Pati, C. N. R. Rao, *J. Phys. Chem. C* **2008**, *112*, 15704.

[9]   a)C. N. R. Rao, R. Voggu, *Mater. Today* **2010**, *13*, 34; b)B. Das, R. Voggu, C. S. Rout, C. N. R. Rao, *Chem. Comm.* **2008**, 5155; c)R. Voggu, B. Das, C. S. Rout, C. N. R. Rao, *J. Phys.-Condes. Matter* **2008**, *20*, 472204.

[10]   a)K. H. M. Born, *Dynamical Theory of Crystal Lattices, Clarendon, Oxford,* **1954**; b)R. E. Peierls, *Ann. Inst. Henri Poincare* **1935**, *5*, 177.

[11]   L. D. Landau, *Phys. Z. Sowjetunion* **1937** *11*, 26.

[12]   M. Zinke-Allmang, L.C. Feldman, M.H. Grabow, *Surf. Sci. Rep.* **1992**, *16*, 377.

[13]   D. R. Nelson, T. Piran, S. Weinberg, *Statistical Mechanics of Membranes and Surfaces, World Scientific, Singapore,* **2004.**

[14]   D. S. L. Abergel, A. Russell, V. I. Falko, *Appl. Phys. Lett.* **2007**, *91*, 063125.

[15]   Z. H. Ni, H. M. Wang, J. Kasim, H. M. Fan, T. Yu, Y. H. Wu, Y. P. Feng, Z. X. Shen, *Nano Lett.* **2007**, *7*, 2758.

[16]   V. Kochat, A. Nath Pal, E. S. Sneha, A. Sampathkumar, A. Gairola, S. A. Shivashankar, S. Raghavan, A. Ghosh, *J. Appl. Phys.* **2011**, *110*, 014315.

[17]   M. H. Gass, U. Bangert, A. L. Bleloch, P. Wang, R. R. Nair, A. K. Geim, *Nat Nano* **2008**, *3*, 676.

[18]   Y. Hernandez, V. Nicolosi, M. Lotya, F. M. Blighe, Z. Sun, S. De, I. T. McGovern, B. Holland, M. Byrne, Y. K. Gun'Ko, J. J. Boland, P. Niraj, G. Duesberg, S. Krishnamurthy, R. Goodhue, J. Hutchison, V. Scardaci, A. C. Ferrari, J. N. Coleman, *Nat. Nanotechnol* **2008**, *3*, 563.

[19]   A. K. Geim, K. S. Novoselov, *Nat. Mater.* **2007**, *6*, 183.

[20]   a)H. Hiura, T. W. Ebbesen, J. Fujita, K. Tanigaki, T. Takada, *Nature* **1994**, *367*, 148; b)T. W. Ebbesen, H. Hiura, *Adv. Mater.* **1995**, *7*, 582; c)T. M. Bernhardt, B. Kaiser, K.

Rademann, *Surf. Sci.* **1998**, *408*, 86; d)H. Roy, *J. Appl. Phys.* **1998**, *83*, 4695; e)X. Lu, M. Yu, H. Huang, R. S. Ruoff, *Nanotechnol.* **1999**, *10*, 269; f)H. V. Roy, C. Kallinger, K. Sattler, *Surf. Sci.* **1998**, *407*, 1.

[21]   Y. Zhang, *Appl. Phys. Lett.* **2005**, *86*, 073104.

[22]   A. B. Bourlinos, V. Georgakilas, R. Zboril, T. A. Steriotis, A. K. Stubos, *Small* **2009**, *5*, 1841.

[23]   C. E. Hamilton, J. R. Lomeda, Z. Sun, J. M. Tour, A. R. Barron, *Nano. Lett.* **2009**, *9*, 3460.

[24]   A. ONeill, U. Khan, P. N. Nirmalraj, J. Boland, J. N. Coleman, *J. Phys. Chem. C* **2011**, *115*, 5422.

[25]   Y. Hernandez, M. Lotya, D. Rickard, S. D. Bergin, J. N. Coleman, *Langmuir* **2009**, *26*, 3208.

[26]   L. M. Viculis, J. J. Mack, O. M. Mayer, H. T. Hahn, R. B. Kaner, *J. Mater. Chem.* **2005**, *15*, 974.

[27]   D. R. Dreyer, S. Park, C. W. Bielawski, R. S. Ruoff, *Chem. Soc. Rev.* **2010**, *39*, 228.

[28]   a)D. C. Marcano, D. V. Kosynkin, J. M. Berlin, A. Sinitskii, Z. Sun, A. Slesarev, L. B. Alemany, W. Lu, J. M. Tour, *ACS Nano* **2010**, *4*, 4806; b)S. Park, J. An, I. Jung, R. D. Piner, S. J. An, X. Li, A. Velamakanni, R. S. Ruoff, *Nano Lett.* **2009**, *9*, 1593; c)W. S. Hummers, R. E. Offeman, *J. Am. Chem. Soc.* **1958**, *80*, 1339.

[29]   V. C. Tung, M. J. Allen, Y. Yang, R. B. Kaner, *Nat. Nanotechnol.* **2009**, *4*, 25.

[30]   a)H. C. Schniepp, J.-L. Li, M. J. McAllister, H. Sai, M. Herrera-Alonso, D. H. Adamson, R. K. Prud'homme, R. Car, D. A. Saville, I. A. Aksay, *J. Phys. Chem. B* **2006**, *110*, 8535; b)M. J. McAllister, J.-L. Li, D. H. Adamson, H. C. Schniepp, A. A. Abdala, J. Liu, M.

Herrera-Alonso, D. L. Milius, R. Car, R. K. Prud'homme, I. A. Aksay, *Chem. Mater.* **2007**, *19*, 4396.

[31]   X. Li, G. Zhang, X. Bai, X. Sun, X. Wang, E. Wang, H. Dai, *Nat. Nanotechnol.* **2008**, *3*, 538.

[32]   X. Guoqing, H. Wontae, K. Namhun, M. C. Sung, C. Heeyeop, *Nanotechnol.* **2010**, *21*, 405201.

[33]   X. Liang, A. S. P. Chang, Y. Zhang, B. D. Harteneck, H. Choo, D. L. Olynick, S. Cabrini, *Nano Lett.* **2008**, *9*, 467.

[34]   M. Qian, *Appl. Phys. Lett.* **2011**, *98*, 173108.

[35]   C. Valleİs, C. Drummond, H. Saadaoui, C. A. Furtado, M. He, O. Roubeau, L. Ortolani, M. Monthioux, A. Peİ nicaud, *J. Am. Chem. Soc.* **2008**, *130*, 15802.

[36]   A. Ghosh, K. V. Rao, S. J. George, C. N. R. Rao, *Chem.–Eur. J.* **2010**, *16*, 2700.

[37]   X. Wang, P. F. Fulvio, G. A. Baker, G. M. Veith, R. R. Unocic, S. M. Mahurin, M. Chi, S. Dai, *Chem. Comm.* **2010**, *46*, 4487.

[38]   K. S. Kim, Y. Zhao, H. Jang, S. Y. Lee, J. M. Kim, K. S. Kim, J.-H. Ahn, P. Kim, J.-Y. Choi, B. H. Hong, *Nature* **2009**, *457*, 706.

[39]   S.-Y. Kwon, C. V. Ciobanu, V. Petrova, V. B. Shenoy, J. Bareno, V. Gambin, I. Petrov, S. Kodambaka, *Nano Lett.* **2009**, *9*, 3985.

[40]   P. W. Sutter, J.-I. Flege, E. A. Sutter, *Nat. Mater.* **2008**, *7*, 406.

[41]   J. Coraux, A. T. N`Diaye, C. Busse, T. Michely, *Nano Lett.* **2008**, *8*, 565.

[42]   A. Reina, X. Jia, J. Ho, D. Nezich, H. Son, V. Bulovic, M. S. Dresselhaus, J. Kong, *Nano. Lett.* **2008**, *9*, 30.

[43]   a)J. J. Wang, M. Y. Zhu, R. A. Outlaw, X. Zhao, D. M. Manos, B. C. Holloway, V. P. Mammana, *Appl. Phys. Lett* **2004**, *85*, 1265; b)J. Wang, M. Zhu, R. A. Outlaw, X. Zhao, D. M. Manos, B. C. Holloway, *Carbon* **2004**, *42*, 2867; c)M. Zhu, J. Wang, B. C. Holloway, R. A. Outlaw, X. Zhao, K. Hou, V. Shutthanandan, D. M. Manos, *Carbon* **2007**, *45*, 2229.

[44]   K. S. Subrahmanyam, L. S. Panchakarla, A. Govindaraj, C. N. R. Rao, *J. Phys. Chem. C* **2009**, *113*, 4257.

[45]   L. S. Panchakarla, A. Govindaraj, C. N. R. Rao, *Inorg. Chim. Acta* **2009**, *363*, 4163.

[46]   Z.-S. Wu, W. Ren, L. Gao, J. Zhao, Z. Chen, B. Liu, D. Tang, B. Yu, C. Jiang, H.-M. Cheng, *ACS Nano* **2009**, *3*, 411.

[47]   W. Zhiyong, L. Nan, S. Zujin, G. Zhennan, *Nanotechnol* **2010**, *21*, 175602.

[48]   N. Li, Z. Wang, K. Zhao, Z. Shi, Z. Gu, S. Xu, *Carbon* **2010**, *48*, 255.

[49]   C. Wu, G. Dong, L. Guan, *Physica E* **2010**, *42*, 1267.

[50]   H.-J. Shin, K. K. Kim, A. Benayad, S.-M. Yoon, H. K. Park, I.-S. Jung, M. H. Jin, H.-K. Jeong, J. M. Kim, J.-Y. Choi, Y. H. Lee, *Adv. Funct. Mater.* **2009**, *19*, 1987.

[51]   V. H. Pham, T. V. Cuong, T.-D. Nguyen-Phan, H. D. Pham, E. J. Kim, S. H. Hur, E. W. Shin, S. Kim, J. S. Chung, *Chem. Comm.* **2010**, *46*, 4375.

[52]   X. Zhou, J. Zhang, H. Wu, H. Yang, J. Zhang, S. Guo, *J. Phys. Chem. C* **2011**, *115*, 11957.

[53]   C. Zhu, S. Guo, Y. Fang, S. Dong, *ACS Nano* **2010**, *4*, 2429.

[54]   J. Zhang, H. Yang, G. Shen, P. Cheng, J. Zhang, S. Guo, *Chem. Commun.* **2010**, *46*, 1112.

[55]   G. Wang, J. Yang, J. Park, X. Gou, B. Wang, H. Liu, J. Yao, *J. Phys. Chem.* **2008**, *112*, 8192.

[56]   X. Fan, W. Peng, Y. Li, X. Li, S. Wang, G. Zhang, F. Zhang, *Adv. Mater.* **2008**, *20*, 4490.

[57]   C. A. Amarnath, C. E. Hong, N. H. Kim, B.-C. Ku, T. Kuila, J. H. Lee, *Carbon* **2011**, *49*, 3497.

[58]   a)H.-L. Guo, X.-F. Wang, Q.-Y. Qian, F.-B. Wang, X.-H. Xia, *ACS Nano* **2009**, *3*, 2653; b)R. S. Sundaram, C. Gómez-Navarro, K. Balasubramanian, M. Burghard, K. Kern, *Adv. Mater.* **2008**, *20*, 3050; c)O. C. Compton, B. Jain, D. A. Dikin, A. Abouimrane, K. Amine, S. T. Nguyen, *ACS Nano* **2011**, *5*, 4380.

[59]   M. Zhou, Y. Wang, Y. Zhai, J. Zhai, W. Ren, F. Wang, S. Dong, *Chem.–Eur. J.* **2009**, *15*, 6116.

[60]   Y. H. Ding, et al., *Nanotechnol.* **2011**, *22*, 215601.

[61]   L. J. Cote, R. Cruz-Silva, J. Huang, *J. Am. Chem. Soc.* **2009**, *131*, 11027.

[62]   V. Abdelsayed, S. Moussa, H. M. Hassan, H. S. Aluri, M. M. Collinson, M. S. El-Shall, *J. Phys. Chem. Lett.* **2010**, *1*, 2804.

[63]   a)P. Kumar, B. Das, B. Chitara, K. S. Subrahmanyam, K. Gopalakrishnan, S. B. Krupanidhi, C. N. R. Rao, *Macromol. Chem. Phys.* **2012**, *213*, 1146; b)P. Kumar, K. S. Subrahmanyam, C. N. R. Rao, *Mater. Exp.* **2011**, *1*, 252.

[64]   M. Baraket, S. G. Walton, Z. Wei, E. H. Lock, J. T. Robinson, P. Sheehan, *Carbon* **2010**, *48*, 3382.

[65]   S. Patchkovskii, J. S. Tse, S. N. Yurchenko, L. Zhechkov, T. Heine, G. Seifert, *Proc Natl Acad. Sc.USA* **2005**, *102*, 10439.

[66]   X. Dong, D. Fu, W. Fang, Y. Shi, P. Chen, L.-J. Li, *Small* **2009**, *5*, 1422.

[67]   N. Jung, N. Kim, S. Jockusch, N. J. Turro, P. Kim, L. Brus, *Nano Lett.* **2009**, *9*, 4133.

[68]   S. Ghosh, S. R. K. Chaitanya Sharma Y, S. K. Pati, C. N. R. Rao, *RSC adv.* **2011**, *2*, 1181.

[69]   D. Choudhury, B. Das, D. D. Sarma, C. N. R. Rao, *Chem. Phys. Lett* **2010**, *497*, 66.

[70]   S. K. Saha, R. C. Chandrakanth, H. R. Krishnamurthy, U. V. Waghmare, *Phys. Rev. B* **2009**, *80*, 6.

[71]   K. S. Subrahmanyam, A. K. Manna, S. K. Pati, C. N. R. Rao, *Chem. Phys. Lett* **2010**, *497*, 70.

[72]   G. G. Wildgoose, C. E. Banks, R. G. Compton, *Small* **2006**, *2*, 182.

[73]   Y. Li, X. Fan, J. Qi, J. Ji, S. Wang, G. Zhang, F. Zhang, *Nano Res.* **2010**, *3*, 429.

[74]   S. Guo, S. Dong, E. Wang, *ACS Nano* **2009**, *4*, 547.

[75]   W. Hong, H. Bai, Y. Xu, Z. Yao, Z. Gu, G. Shi, *J. Phys. Chem. C* **2010**, *114*, 1822.

[76]   Y. Wang, Z. Ni, H. Hu, Y. Hao, C. P. Wong, T. Yu, J. T. L. Thong, Z. X. Shen, *Appl. Phys. Lett* **2010**, *97*, 163111.

[77]   J. Ma, J. Zhang, Z. Xiong, Y. Yong, X. S. Zhao, *J. Mater. Chem* **2010**, *21*, 3350.

[78]   P. V. Kamat, *J. Phys. Chem. Lett.* **2009**, *1*, 520.

[79]   G. Williams, P. V. Kamat, *Langmuir* **2009**, *25*, 13869.

[80]   B. Das, B. Choudhury, A. Gomathi, A. K. Manna, S. K. Pati, C. N. R. Rao, *Chem. Phys. Chem.* **2011**, *12*, 937.

[81]   S. Stankovich, D. A. Dikin, G. H. B. Dommett, K. M. Kohlhaas, E. J. Zimney, E. A. Stach, R. D. Piner, S. T. Nguyen, R. S. Ruoff, *Nature* **2006**, *442*, 282.

[82]   T. Ramanathan, A. A. Abdala, S. Stankovich, D. A. Dikin, M. Herrera Alonso, R. D. Piner, D. H. Adamson, H. C. Schniepp, ChenX, R. S. Ruoff, S. T. Nguyen, I. A. Aksay, R. K. Prud'Homme, L. C. Brinson, *Nat. Nanotechnol.* **2008**, *3*, 327.

[83]   B. Das, K. E. Prasad, U. Ramamurty, C. N. R. Rao, *Nanotechnol.* **2009**, *20*, 125705.

[84]   M. A. Rafiee, J. Rafiee, Z. Wang, H. Song, Z.-Z. Yu, N. Koratkar, *ACS Nano* **2009**, *3*, 3884.

[85]   K. E. Prasad, B. Das, U. Maitra, U. Ramamurty, C. N. R. Rao, *Proc. Natl. Acad. Sci. USA* **2009**, *106*, 13186.

[86]   D. J. Late, A. Ghosh, K. S. Subrahmanyam, L. S. Panchakarla, S. B. Krupanidhi, C. N. R. Rao, *Solid State Commun.* **2010**, *150*, 734.

[87]   E. H. Hwang, S. Das Sarma, *Phys. Rev. B* **2008**, *77*, 115449.

[88]   a)F. T. Vasko, V. Ryzhii, *Phys. Rev. B* **2007**, *76*, 233404; b)E. H. Hwang, S. Adam, S. Das Sarma, *Phys. Rev. Lett.* **2007**, *98*, 186806; c)T. Stauber, N. M. R. Peres, F. Guinea, *Phys. Rev. B* **2007**, *76*, 205423.

[89]   J. H. Chen, C. Jang, S. Adam, M. S. Fuhrer, E. D. Williams, M. Ishigami, *Nat. Phys.* **2008**, *4*, 377.

[90]   S. V. Morozov, K. S. Novoselov, M. I. Katsnelson, F. Schedin, D. C. Elias, J. A. Jaszczak, A. K. Geim, *Phys. Rev. Lett.* **2008**, *100*, 016602.

[91]   X. Du, I. Skachko, A. Barker, E. Y. Andrei, *Nat. Nanotechnol.* **2008**, *3*, 491.

[92]   Z. Chen, Y.-M. Lin, M. J. Rooks, P. Avouris, *Physica E* **2007**, *40*, 228.

[93]   X. Wang, Y. Ouyang, X. Li, H. Wang, J. Guo, H. Dai, *Phys. Rev. Lett.* **2008**, *100*, 206803.

[94]   S. Vivekchand, C. Rout, K. Subrahmanyam, A. Govindaraj, C. Rao, *J. Chem. Sc.* **2008**, *120*, 9.

[95]   H.-Q. Li, Y.-G. Wang, C.-X. Wang, Y.-Y. Xia, *J. Pow. Sour.* **2008**, *185*, 1557.

[96]   M. D. Stoller, S. Park, Y. Zhu, J. An, R. S. Ruoff, *Nano. Lett.* **2008**, *8*, 3498.

[97]   Z. Fan, J. Yan, L. Zhi, Q. Zhang, T. Wei, J. Feng, M. Zhang, W. Qian, F. Wei, *Adv. Mater.* **2010**, *22*, 3723.

[98]   J. Yan, T. Wei, Z. Fan, W. Qian, M. Zhang, X. Shen, F. Wei, *J. Pow. Sour.* **2010**, *195*, 3041.

[99]   E. Yoo, J. Kim, E. Hosono, H.-S. Zhou, T. Kudo, I. Honma, *Nano Lett.* **2008**, *8*, 2277.

[100] a)G. Eda, H. E. Unalan, N. Rupesinghe, G. A. J. Amaratunga, M. Chhowalla, *Appl. Phys. Lett.* **2008**, *93*, 233502; b)A. Malesevic, R. Kemps, A. Vanhulsel, M. P. Chowdhury, A. Volodin, C. Van Haesendonck, *J. Appl. Phys.* **2008**, *104*, 084301; c)S. M. Jung, J. Hahn, H. Y. Jung, J. S. Suh, *Nano Lett.* **2006**, *6*, 1569.

[101] U. A. Palnitkar, R. V. Kashid, M. A. More, D. S. Joag, L. S. Panchakarla, C. N. R. Rao, *Appl. Phys. Lett* **2010**, *97*, 063102.

[102] K. S. Subrahmanyam, P. Kumar, A. Nag, C. N. R. Rao, *Solid State Commun.* **2010**, *150*, 1774.

[103] K. Prashant, L. S. Panchakarla, S. V. Bhat, M. Urmimala, K. S. Subrahmanyam, C. N. R. Rao, *Nanotechnol.* **2010**, *21*, 385701.

[104] J. Robertson, E. P. O'Reilly, *Phys. Rev. B* **1987**, *35*, 2946.

[105] J. L. Bredas, R. Silbey, D. S. Boudreaux, R. R. Chance, *J. Am. Chem. Soc.* **1983**, *105*, 6555.

[106] L. Zheng, Z. Li, S. Bourdo, F. Watanabe, C. C. Ryerson, A. S. Biris, *Chem. Commun.*
2010, *47*, 1213.

[107] D. C. Elias, R. R. Nair, T. M. G. Mohiuddin, S. V. Morozov, P. Blake, M. P. Halsall, A.
C. Ferrari, D. W. Boukhvalov, M. I. Katsnelson, A. K. Geim, K. S. Novoselov, *Science*
2009, *323*, 610.

[108] K. S. Subrahmanyam, P. Kumar, U. Maitra, A. Govindaraj, K. Hembram, U. V.
Waghmare, C. N. R. Rao, *Proc. Natl. Acad. Sci. USA* **2011**, *108*, 2674.

[109] K. Gopalakrishnan, K. S. Subrahmanyam, P. Kumar, A. Govindaraj, C. N. R. Rao, *RSC
Adv.* **2012**, *2*, 1605.

1.2: Self-assembly of nanocarbons and their composites at the liquid-liquid interface

Summary[*]

Self-assembly of C_{60}, single-walled carbon nanotubes (SWNTs) and few-layer graphene and their binary composites at the toluene-water interface has been investigated, starting with different concentrations of the nanocarbons in the organic phase. The films of the composites and their pristine counterparts formed at the liquid-liquid interface have been characterized by electron microscopy. Raman spectroscopy and electronic absorption spectroscopy of these films reveal the occurrence of charge-transfer interaction between few-layer graphene and C_{60}.

Few-layer graphene-CdSe nanoparticle composites have been synthesized at the organic-aqueous interface. The nanocomposites have been examined by electron microscopy, electronic absorption and photoluminescence spectroscopies as well as Raman spectroscopy. Electron microscopy reveals that the nanoparticles are well dispersed on the graphene surface. Raman spectra show the presence of definitive electronic interaction between the nanoparticles and graphene.

1.2: Nanocarbons and their composites at the liquid-liquid interface

1.2.1: Introduction

Zero-, one-, and two- dimensional nanocarbons have become materials of great scientific and technological importance. While zero-dimensional C_{60} and one-dimensional carbon nanotubes have been active areas of research for two decades, two-dimensional graphene is of recent origin.[1] It is of considerable interest to investigate the self-assembly of these nanocarbons of different dimensionalities to form continuous films for their use in the device fabrication. Various approaches have been reported for the self assembly of the nanocarbons. Recently, molecular templates [2] and direct chemical vapor deposition[3] have been employed to obtain graphene-based or graphene-oxide-based films on selected substrates. A major challenge remaining is the lack of a simple, fast, low-cost and efficient method of obtaining graphene films. Recent efforts based on spin-coating,[4] vacuum filtration,[5] layer-by-layer technique [6] Langmuir–Blodgett (LB) technique,[7] and interfacial self-assembly[8] have shown the feasibility of wet-chemical methods. Among these methods our interest is to use interfacial assembly not only for obtaining large area graphene films but also for a possibility to prepare graphene-composites of desired property.

The liquid–liquid interface possesses unique thermodynamic properties compared to their bulk counterparts as to their viscosity, density and dielectric constant. A liquid–liquid interface is a nonhomogeneous region having a thickness of the order of a few nanometers. The interface is not sharp, since there is always a little solubility of one phase in the other.[9]

There have been a few studies on the self-assembly of nanocarbons, wherein nanosheets of C_{60} comprising hexagonal, rhombohedral and mixed polygonal aggregates have been obtained by solvent engineering.[10] Size-tunable hexagonal nanosheets have been generated at the liquid-liquid interface.[11] In the case of single-walled carbon nanotubes

(SWNTs), water dispersions containing surfactants mixed with non-polar solvents are reported to give rise to interfacial assemblies.[12] SWNT films can be obtained by spray coating of surfactant-dispersed aqueous solutions.[13] There are reports of composites formed by SWNTs with C_{70} and alkylated C_{60}.[14] C_{60} molecules are known to decorate the surface of functionalized SWNTs.[15]

Platelets of graphene modified by polyacrylic acid have been obtained by using layer-by-layer assembly.[16] Nanosheets of graphene can be generated at the liquid-liquid interface.[8, 17] Membranes of graphene oxide (GO) can be obtained at the liquid-air interface by evaporating the hydrosol of GO.[18] Ropes and bundles of carbon nanotubes have been formed along with the graphene by the reduction of GO admixed with the nanotubes.[19] Nanotube films containing small amounts of graphene are reported to be transparent conductors.[20] Layer-by-layer assembly has been employed for the formation of nanofilms of reduced graphene oxide with multi-walled carbon nanotubes.[21] Reduced graphene oxide (RGO)-wrapped C_{60} wires were prepared via liquid-liquid interfacial precipitation method and it was found that π-π interaction was the driving force for the assembly of RGO sheets and C_{60} wires. The assembly of nanocarbons and the electron transfer at interfaces induces interesting properties like exhibiting p-type behavior in the composite where RGO shows ambipolar and C_{60} has n-type characteristics. Photovoltaic applications have been carried out on these composites and have shown relatively low efficiency.[22] Solar cells made up of composites containing C_{60}/SWNTs/RGO as the active layer and an additional evaporated C_{60} as blocking layer yield a efficiency of 0.21%, which has increased to 0.85% by replacing C_{60} with C_{70}.[23]

1.2: Nanocarbons and their composites at the liquid-liquid interface

Quantum dots (QDs) have been extensively studied in various matrices for their optoelectronic applications. To enhance the photocurrent generated by these systems, it is essential to retard the recombination of the electron-hole pairs. Carbon nanotubes and conductive polymers decorated with semiconductor nanoparticles have been found to possess this desirable property.[24] Graphene, which is of recent inertest because of its high surface area and good conductivity, can be claimed as the ideal 2-D matrix.[1c] Furthermore, graphene can be produced at low cost and in high yields compared to the other nanocarbons. There are few reports on the synthesis of semiconductor-based graphene nanocomposites. CdSe nanoparticles can be attached to reduced graphene oxide (RGO) by adding RGO to the reaction mixture during the process of synthesizing CdSe nanoparticles.[25] Kim et al. have electrochemically deposited CdSe nanocrystal thin films over graphene.[26] A dispersion of graphite oxide in an aqueous solution of Cd^{2+}/Zn^{2+} on treatment with H_2S gas results in the deposition of metal sulphide nanoparticles over graphene sheets.[27] Fluorescent graphene-CdSe composites can be prepared by interaction of graphene with CdSe nanoparticles in the presence of long chain surfactants.[28] Interaction between graphene oxide and CdSe have been studied using life-time measurements and found the rate constants for energy and electron transfer for the CdSe−GO composites as 5.5×10^8 and 6.7×10^8 s^{-1}, respectively. Devices fabricated from CdSe−graphene composites in solar cells displayed a improved photocurrent response of $\sim 150\%$ compared to bare CdSe.[29]

1.2.2: Scope of the present investigations

Self-assembly of C$_{60}$, SWNTs and few-layer graphene and their binary composites:
In view of the importance of recent trends, it would be worthwhile to carry out a systematic study of the self-assembly of pristine C$_{60}$, SWNTs and graphene at the organic-aqueous interface in the absence of any chemical modification or surfactants, and more importantly to investigate the nature of the composite films formed by any of the two nanocarbons at the interface. Such self-assembly at the organic-aqueous interface is facile because owing to unique features of the solvent interfaces. It is known that the organic-aqueous interface favors organized assembly of nanoparticles, and has been used to generate ultrathin nanocrystalline as well as single crystalline films of inorganic materials.[9, 30] We have examined films of few-layer graphene, SWNTs and their composites formed at the organic-aqueous interface as a function of time and concentration by employing electron microscopy. Besides electron microscopic investigation, we have studied the assembly of few-layer graphene with SWNTs by employing Raman spectroscopy and electron microscopy. C$_{60}$ and few-layer graphene films have been obtained by following the same procedure. The present study not only helps to explore the structures formed by the assembly of these nanocarbons and of their binary composites at the interface, but also demonstrates the occurrence of charge-transfer interaction between C$_{60}$ and few-layer graphene in the composites.

Synthesis and characterization of graphene-CdSe composites: In spite of many successful efforts in preparing the graphene composites with semiconductors, there is need to explore simple and better methods of generating composites of CdSe nanoparticles with graphene and related materials, wherein the nanoparticles properly bind to the graphene surface. Having this in mind, we have employed a simple, green, efficient and effective

method for the synthesis of graphene-CdSe composites at room temperature using liquid-liquid interface. Along with the ease of synthesis, this approach also allows to prepare large area graphene films with homogenous distribution of nanoparticles on the surface. We have examined the nanocomposites of graphene-CdSe by Raman spectroscopy and other techniques.

1.2.3: Experimental Section

Self-assembly of C$_{60}$, SWNTs and few-layer graphene and their binary composites:

C$_{60}$ was prepared by the arc evaporation of graphite, following the procedure of Krätschmer et. al.[31] The procedure involved the evaporation of spectroscopic grade graphite rods in an atmosphere of helium in a water cooled stainless steel vacuum chamber resulting in the formation of large quantities of soot, followed by purification using chromatography.[32] SWNTs were prepared by the arc discharge method followed by purification, which involves acid washing and high-temperature hydrogen treatment.[33] Few-layer graphene was prepared by the exfoliation of graphite oxide by employing the literature procedure.[34] Exfoliation of graphite oxide was carried out in a furnace preheated to 1050 ℃ under argon flow for about 30 s. The few-layer graphene sample so obtained (EG) had 3-6 layers with lateral dimensions of 300-700 nm. The few-layer graphene was heated at 800 ℃ for 3 hours in hydrogen atmosphere to remove the amorphous carbon present in the sample.

Toluene (nanocarbons)
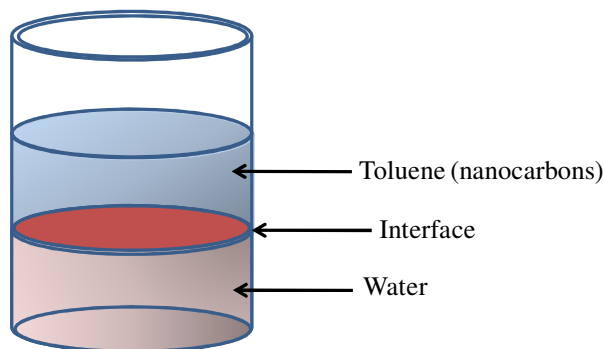
Interface

Water

Scheme 1: Liquid-liquid interface

The nanocarbons were taken in toluene (each one separately) and their dispersions were added very slowly to a beaker containing water to create the interface. Assembly was allowed to occur for a definite amount of time and after that remaining organic phase was gently syringed out without disturbing the film at the interface (see scheme 1). The films were lifted on to a preferred solid substrate for characterization purposes. Self-assembly of the nanocarbons at the organic-aqueous interface was studied at different time intervals and also after complete evaporation of the organic phase containing the nanocarbons (C_{60}/few-layer graphene/ SWNTs). Assembly of two nanocarbons at the interface was carried out by slowly adding toluene solution/dispersions containing the two nanocarbons with known concentrations (C_{60} + few-layer graphene, and SWNT + few-layer graphene) into a beaker containing water. After self assembly for definite time, the organic phase was removed and the film at the interface lifted on a solid substrate based on the requirement for the corresponding characterization.

Synthesis and characterization of graphene-CdSe composites: The liquid-liquid interface, known to be an excellent medium to generate nanocrystalline films of inorganic materials[30], was employed to prepare large-area graphene-CdSe nanoparticle composites. Cadmium cupferronate was used as the cadmium source and 1,1-dimethylselenourea as the selenium source for the preparation of CdSe. Stock solutions of cadmium cupferronate and 1,1-dimethylselenourea were prepared by taking 1 mg of each in 100 ml of toluene and 100 ml of water respectively (1 µg/ml). A few drops of n-octylamine were added to the cadmium cupferronate stock solution to make it completely homogeneous. Then 2 mg of few-layer graphene was added to the cadmium cupferronate solution and subjected to sonication for 1 h at four intervals of 15 min each. For the synthesis of EG-CdSe

nanocomposite, the solution containing cadmium cupferronate and EG was added slowly to 20 ml of 1,1-dimethylselenourea stock solution taken in 100 ml glass beaker. The reaction mixture was left undisturbed for 24 h. After 24 h, a thin black coloured film formed by self - assembly at the toluene-water interface. The toluene in the upper layer was gently removed by syringe without disturbing the film. The film was lifted onto a desirable solid substrate for characterization purposes. This method was employed for the preparation of other nanocomposites as well.

Characterization:

Field emission scanning electron microscopy (FESEM): The morphology of the films was studied by FEI Nova-Nano SEM-600 instrument.

Transmission electron microscopy (TEM): TEM images were recorded with a JEOL TEM 3010 instrument operated with an accelerating voltage of 300 kV.

UV-Absorbtion: UV spectra of the films deposited on a quartz plate and recorded with a Perkin Elmer Lambda 900 UV/VIS spectrophotometer.

Raman spectroscopy: Raman spectra were recorded with a LabRAM HR high resolution Raman spectrometer (Horiba-Jobin Yvon) using a He–Ne laser ($\lambda = 632.8$ nm).

1.2.4: Results and Discussion
Self-assembly of C$_{60}$, SWNTs and few-layer graphene and their binary composites:

In Figure 1, we show FESEM images of the few-layer graphene films formed at the interface with 3.3 µg of few-layer graphene in 10 ml of toluene after 2.5 hours and after complete evaporation. The FESEM image of films obtained at the interface after 2.3 hours of assembly has lateral dimensions in the range of 50-100 µm (Figure 1(a)) along with some sheets which are of 10-15 µm in size (Figure 1(b)). Figure 1(c) shows the image corresponds to the films obtained after the complete evaporation and are relatively thick compared to the
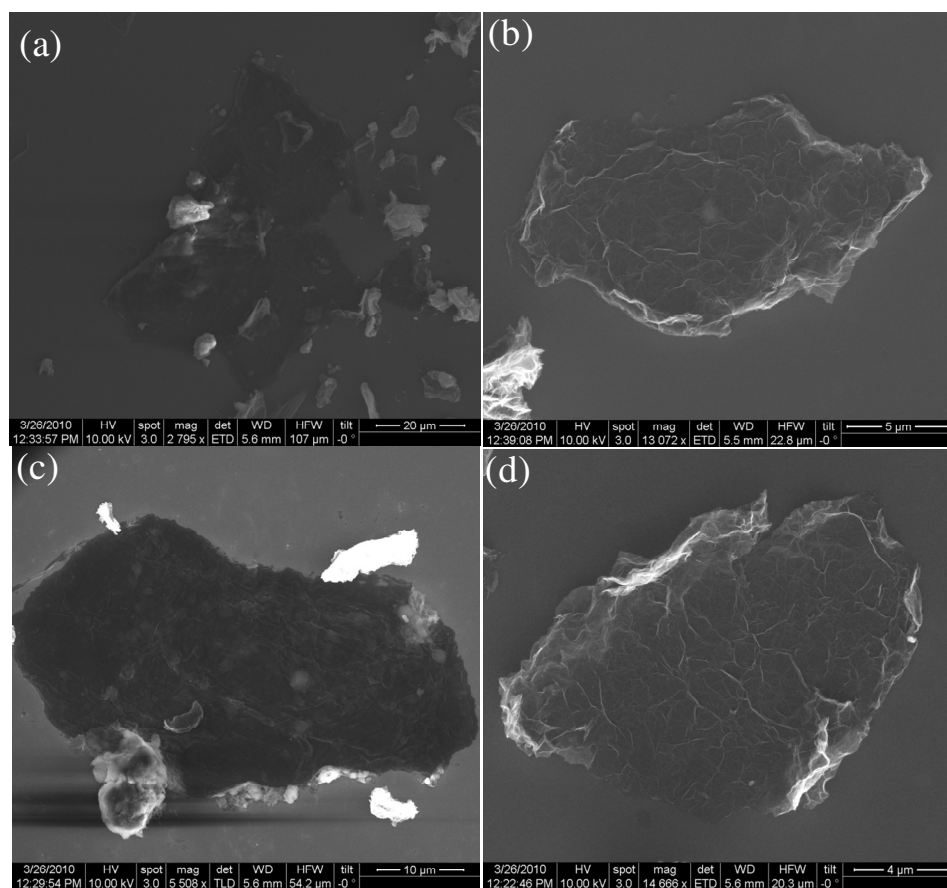
Figure 1: (a), (b) are the FESEM images of graphene films formed after 2.5 hours of assembly and (c), (d) are the FESEM images after complete evaporation.

films obtained after 2.30 hours of assembly. Along with the thick films having lateral dimensions of hundreds of microns, we have also observed the films having 20 µm as shown

47

in Figure 1(d). In Figure 2, we have shown the TEM images of the films formed at the interface at different time intervals. Figure 2(a) shows the films formed after 2.5 hours of assembly where as Figure 2(b) shows the film formed after 12 hours of assembly and the TEM image in Figure 2(c) corresponds to the TEM image obtained after complete evaporation. All these films are extended to several microns and we have not observed much difference in the images with the variation of the time, but the images obtained here are similar to the images obtained from the chemical vapor deposition as reported in the literature.[35]
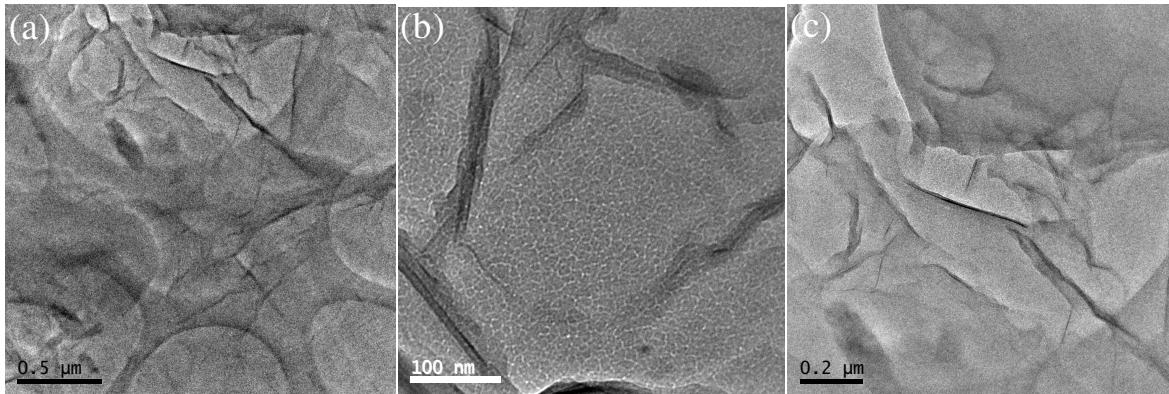
Figure 2: TEM images of graphene films at different time durations (a) 2.5 hours, (b) 12 hours, and (c) after complete evaporation.

We have measured the thickness of the few-layer graphene films formed at the interface after different durations of assembly time by atomic force microscopy. Figures 3 (a), (b) and (c) show the topographic images of the films obtained after 2.5 hours, 12 hours and after complete evaporation respectively. The AFM images were examined by section analysis using nanoscope software and the results are shown in Figures 3 (d), (e) and (f). The section analysis suggested the average layer thickness of graphene sheet was 4-7 nm for 2.3 hours of the assembly, 12-15 nm for 12 hours of assembly and around 40 nm for the complete evaporation. There is an increase in the film thickness with increase in time
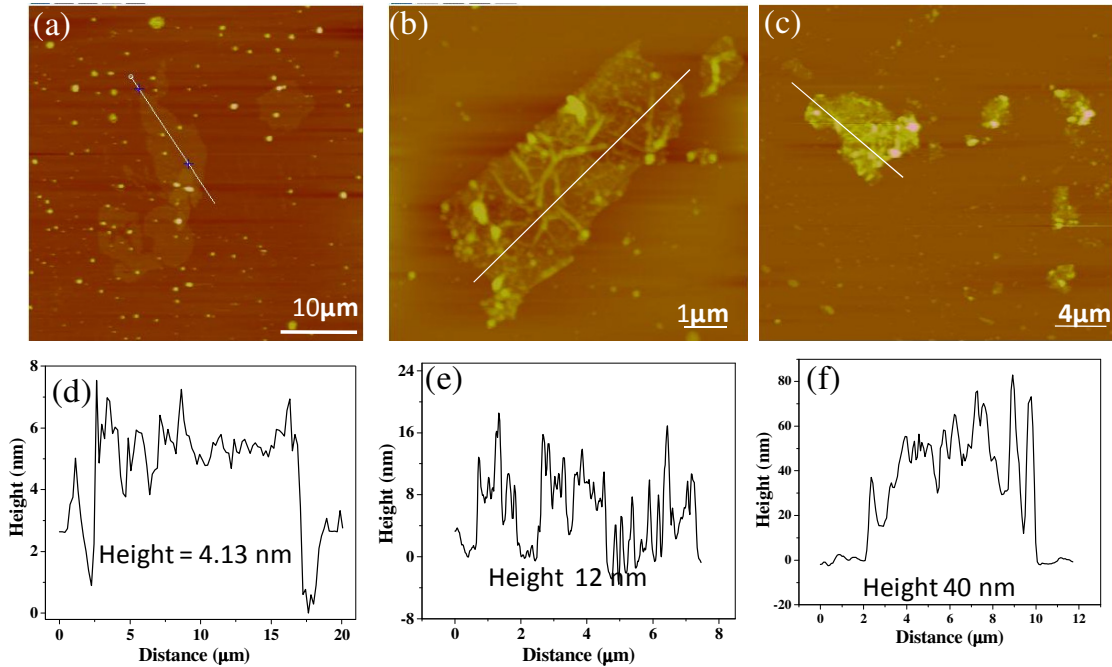
Figure 3: (a), (b), (c) are the Topographic images of the graphene films obtained after (a) 2.3 hours, (b) 12 hours, and (c) complete evaporation and their corresponding height profiles in (d), (e) and (f) respectively.

duration of assembly as expected.
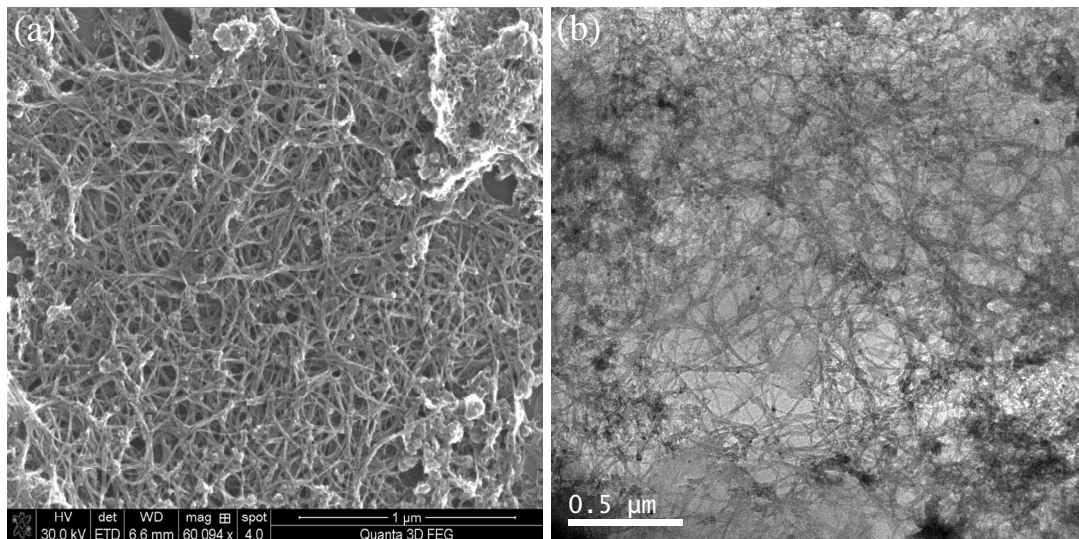
Figure 4: SWNT film formed at the interface for 12 hours of assembly (a) FESEM image for and (b) TEM image

In the similar way, we have also assembled SWNTs at the liquid-liquid interface. Figure 4 (a) shows a FESEM image of the film formed at the interface with a dispersion of a 3.3 µg of SWNTs in 10 ml of toluene after 12 hours of assembly and its TEM image is shown in Figure 4(b). These films show a dense and homogeneous network of SWNTs. Similar films were obtained after different durations of assembly. We have not observed any appreciable changes in their lateral dimensions compared to the films obtained by normal drop casting of SWNTs dispersion.
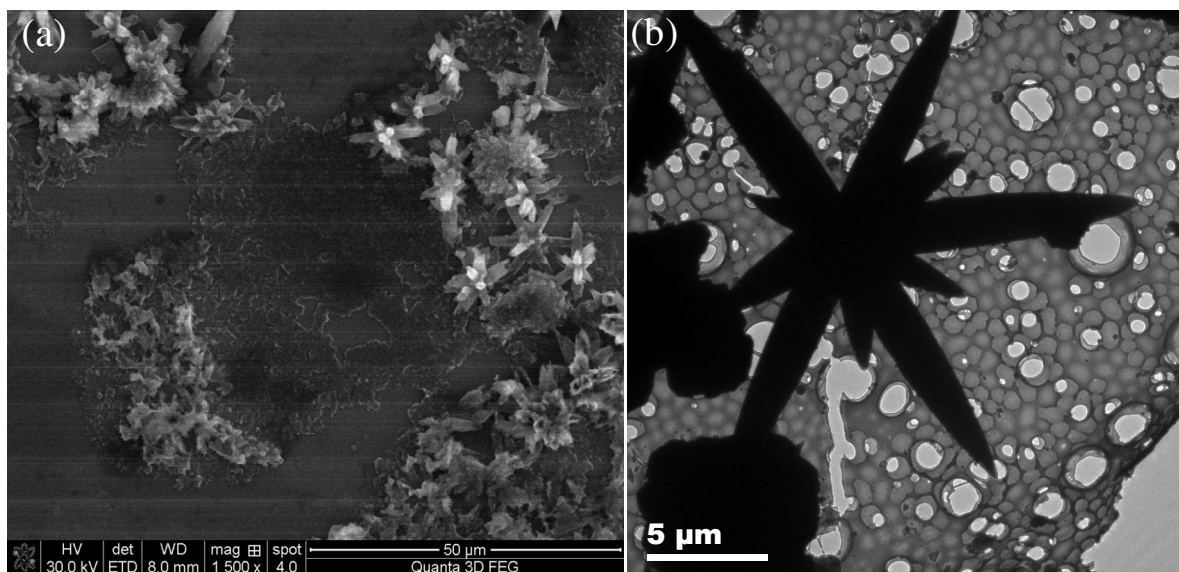
Figure 5: (a) FESEM image and (b) TEM images for composite films of C_{60} and graphene after 12 hours of assembly.

As discussed in the introduction, it is interesting to prepare composites of graphene with C_{60} and SWNTs at the interface because of the possible superior and synergistic properties. In Figure 5 (a), we have shown FESEM image of the composite film of C_{60} (23 µM) and few-layer graphene (3.3 µg in 10 ml) formed at the interface after 12 hours of assembly. It mainly consists of C_{60} films and flower-like structures. The few-layer graphene gets completely covered by the C_{60} structures. Figure 5(b) shows a TEM image showing

flower like structures on the composite film. Since C_{60} is on the surface of graphene, it is difficult to differentiate the two carbons from microscopic images. For this purpose, we have
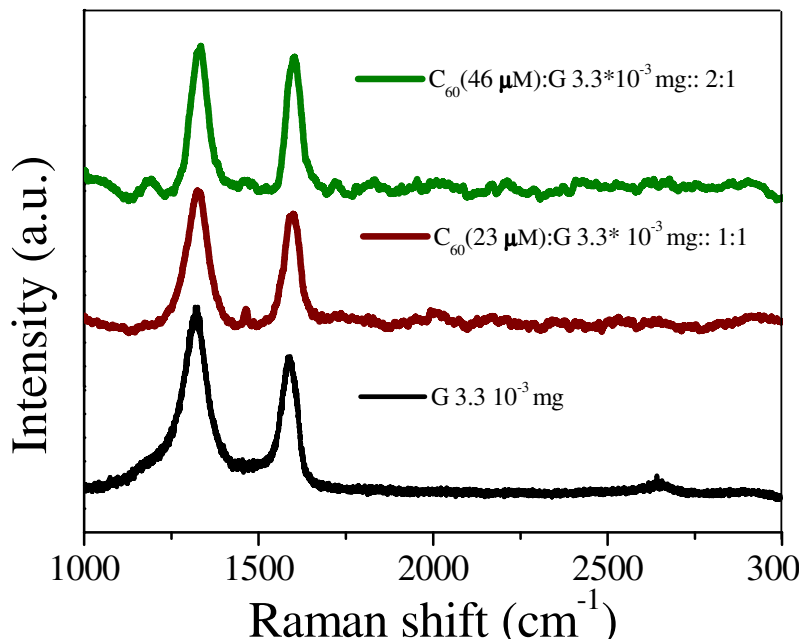
Figure 6: Raman spectra of composite films of C_{60} and graphene (2:1 and 1:1 represents the increase in concentration of C_{60} with the same weight of graphene).

carried out spectroscopic measurements. In Figure 6, we show the Raman G-band of a few-layer graphene film along with the bands in the composites of graphene with C_{60} at different concentrations.
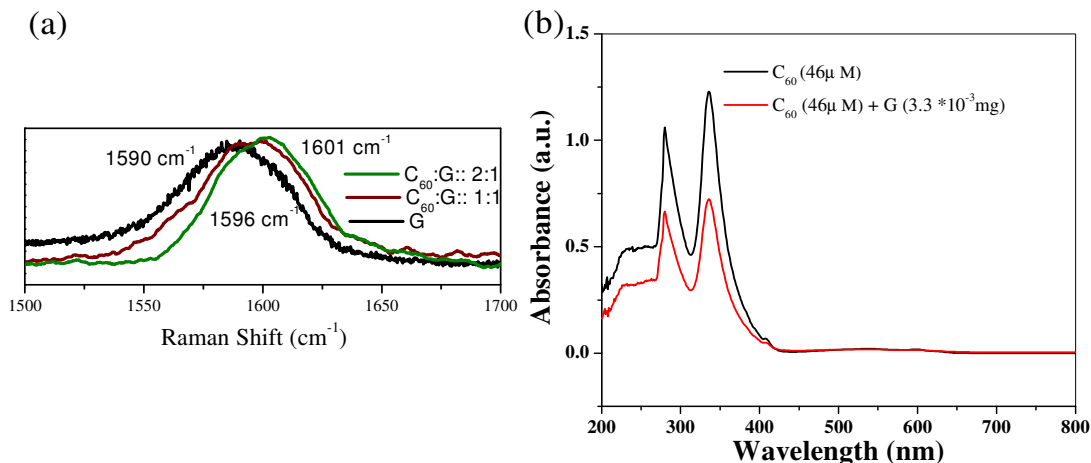
Figure 7: (a) shows stiffening of Raman G-band of graphene. (b) electronic absorption spectra of composite films of C_{60} and graphene(2:1 and 1:1 represents the increase in concentration of C_{60} with the same weight of graphene).

Pure graphene shows the G-band at 1590 cm^{-1} while composites containing C_{60} exhibit stiffening of the G-band. The G-band occurs at 1596 cm^{-1} when the concentration of C_{60} is 23 μM and shifts 1601 cm^{-1} when the C_{60} concentration is 46 μM (Figure 7(a)). These results suggest the occurrence of charge-transfer interaction between C_{60} and few-layer graphene, similar to that found between graphene and electron-acceptor molecules like TCNE and nitrobenzene.[36] We have also examined the UV–visible absorption spectra of the composite films. Figure 7(b) shows the electronic absorption spectrum of C_{60} and the graphene-C_{60} composites. In the composites, we observe a slight reduction in the absorbance because of the adsorption of C_{60} on the graphene surface.
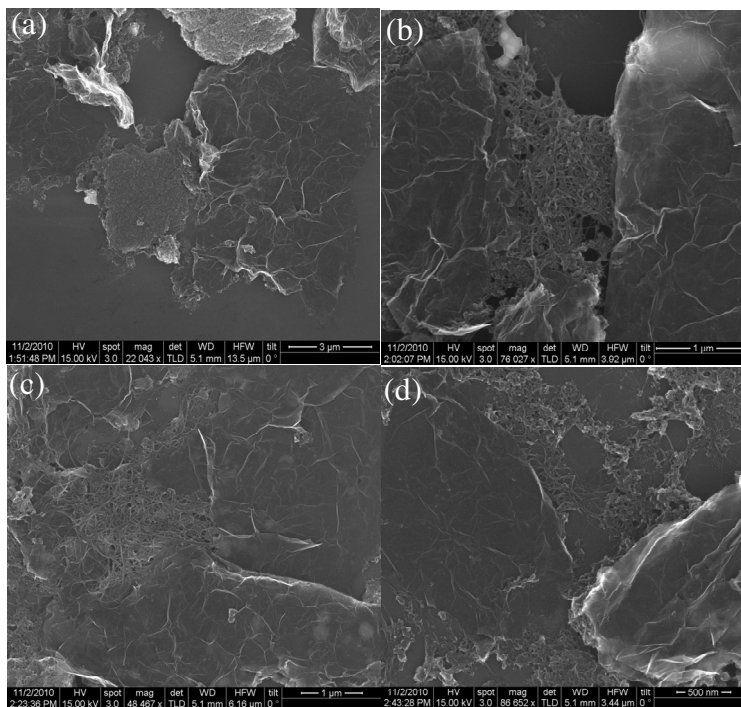
Figure 8: (a), (b), (c) and (d) are the FESEM images of the composite films of graphene with SWNT after time 12 hours of assembly.

In Figure 8, we have shown the FESEM images of the composites of graphene with SWNTs at interface after the assembly of 12 hours. The composites films are prepared with the concentration of SWNTs (3.3 µg in 10 ml) and few-layer graphene (3.3 µg in 10 ml). The overall morphology of the composites is shown in Figure 8. In Figure 8(a), we have shown that graphene flakes are interconnected by the SWNTs like the bridges. This interconnection leads to the formation of continuous films in millimeter range. This type of assemblies enhances the transport properties and can possibly be used in transparent
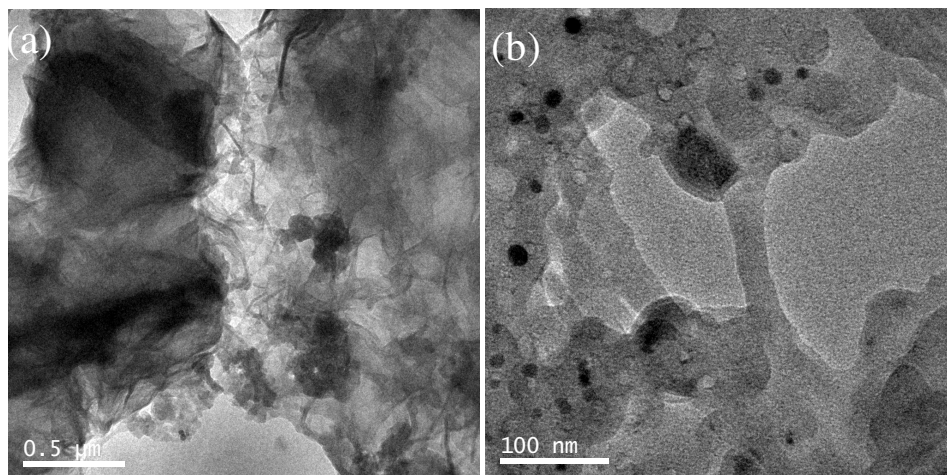
Figure 9: (a) shows the FESEM images and (b) shows the TEM images of the composite films of graphene and SWNT formed after 12 hours of assembly.

conducting electrodes. Figure 8 (b) shows another area which essentially reveals the same information. The SWNTs are completely embedded in the graphene flakes by making a uniform composite (Figures 8(c) and (d)). We have also characterized these composite films using TEM. Figures 9(a) and (b) show the TEM images with signatures of both graphene and SWNTs supporting the FESEM observations.

Along with the microscopic techniques, we have also characterized the composites using Raman spectroscopy. In Figure 10, we have shown the Raman spectra of pure SWNTs along with the graphene-SWNT composite. There are no appreciable interactions in the composites of graphene-SWNTs, as there was no change in the G-band position which is

sensitive to interaction. Raman spectrum of the composites show RBM bands (radial breathing mode) which are fingerprints of SWNTs, increase in the intensity of defect induced D-band and G-band which is a characteristic of sp^2 carbon materials. The analysis from Raman spectroscopy proves the presence of both individual components and uniformity of the composite. Inset of Figure 10 shows the comparison of G-band of pristine SWNT and its composite.
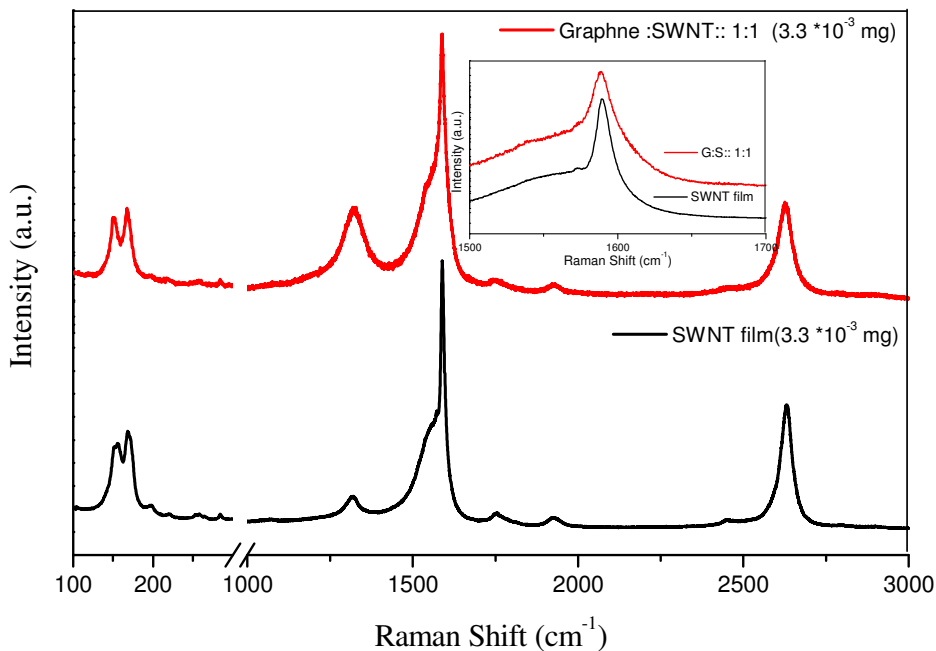
Figure 10: Raman spectra of composite films of graphene and SWNT formed after 12 hours of assembly (1:1 represents the with the weight ration of graphene and SWNTs)

Synthesis and characterization of graphene-CdSe composites: The liquid-liquid interface[9] has been employed by us to prepare large area graphene-semiconductor nanoparticle composites. Figure 11 (a) shows a HREM image of the EG-CdSe composite film. The image shows the presence of lattice fringes in the CdSe nanoparticles of diameter 4-5 nm. FESEM image of EG–CdSe composite film formed at the organic–aqueous interface after 24 hours of reaction is shown in Figure 11(b). The film extends over several micrometers. The FESEM image reveals the decoration of CdSe nanoparticles over the graphene surfaces. Such extended decoration has been possible because of the use of liquid-liquid interface which is otherwise difficult to obtain. Adsorption of cadmium cupferronate on the few-layer graphene helps in more effective reaction of 1,1-dimethyl selenourea at the liquid-liquid interface. Figure 12 (a) shows the electronic absorption and PL spectra of EG–
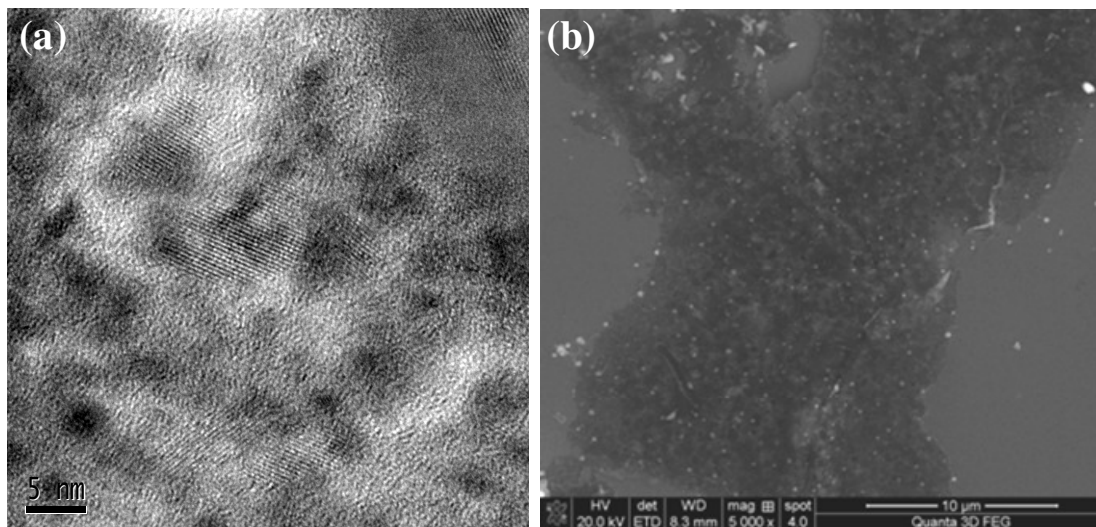
Figure 11: (a) TEM and (b) FESEM images of EG-CdSe prepared at the liquid-liquid interface

CdSe composite film. The absorption spectrum[37] shows an intense band around 480 nm and a broad around 530 nm. The particle size of CdSe nanoparticles calculated from the absorption spectrum is in close agreement with that from TEM. The PL spectrum of the

composites shows an intense signal at around 670 nm making the graphene composite fluorescent. It should be noted that the CdSe particles in the composites prepared at the liquid-liquid interface are not capped strongly by binding reagents.
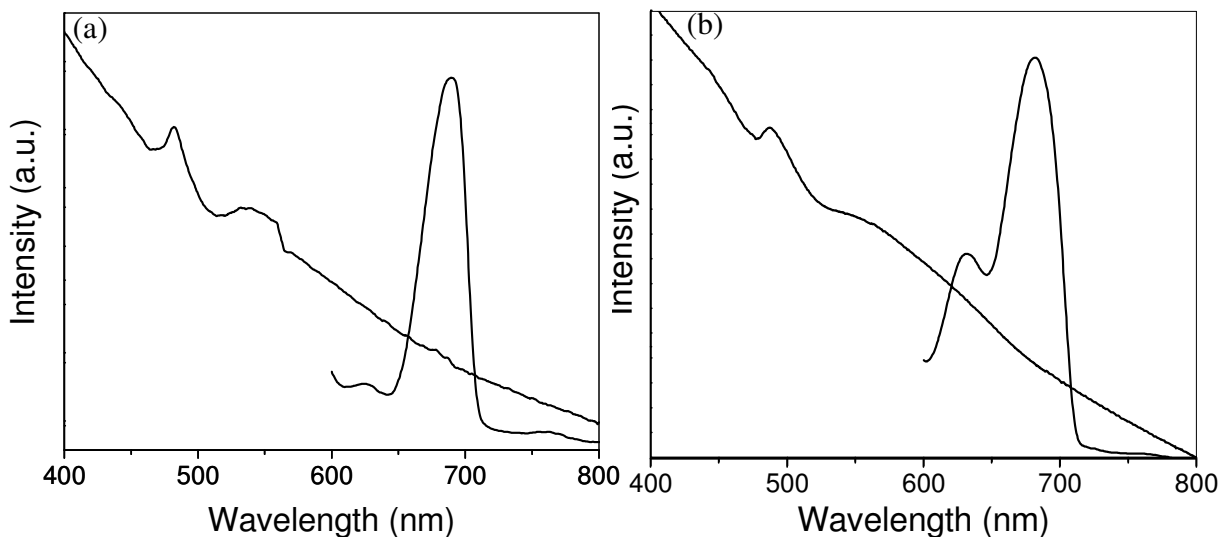
Figure 12: (a) and (b) shows UV, PL of RGO-CdSe and EG-CdSe respectively.

The Raman spectra of EG-CdSe and EG are shown in Figure 13(a). EG shows the G-band at 1586 cm^{-1} whereas the composite of EG and CdSe shows the band at 1584 cm^{-1}, exhibiting softening of the G–band. This result suggest the occurrence of charge transfer interaction between EG and CdSe nanoparticles, similar to that of graphene with electron donor molecules like aniline.[36]
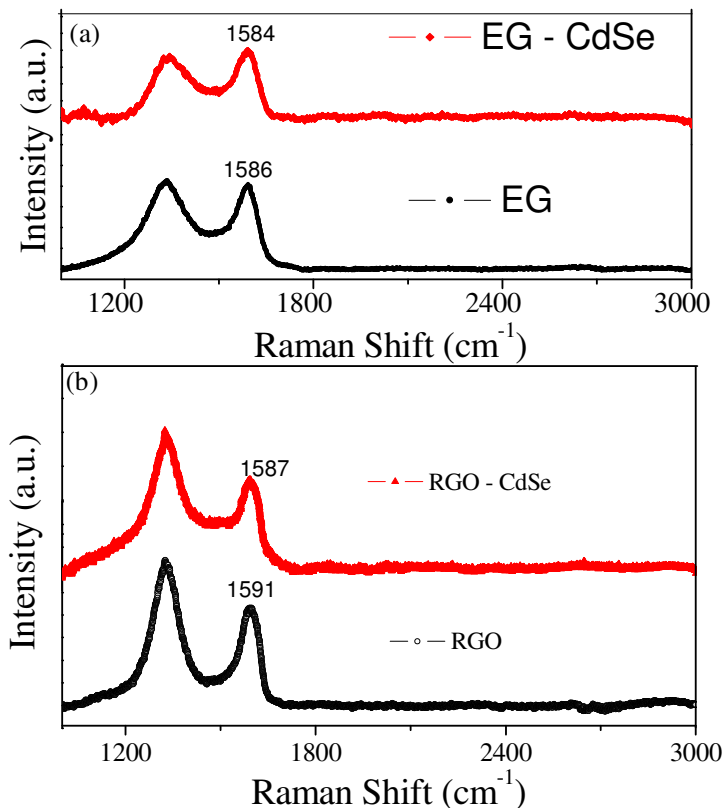
Figure 13: Raman spectra of (a) EG_CdSe and pure EG prepared at
(b) RGO-CdSe and pure RGO prepared at liquid-liquid interface.

We have also employed the liquid-liquid interface method to prepare the RGO-CdSe

nanocomposite. Figure 14(a) shows a FESEM image of a RGO–CdSe composite film

extending over several micrometers. The image shows that CdSe nanoparticles are uniformly

decorated over reduced graphene oxide. Figure 15(b) gives the EDX analysis corresponding

to the FESEM image in Figure 14(a). Figures 14(c) & (d) show the TEM and HREM images

of the RGO-CdSe composite films. The HREM image indicates the presence of lattice

fringes of the CdSe nanoparticles. The inset in Figure 14(d) shows the electron diffraction
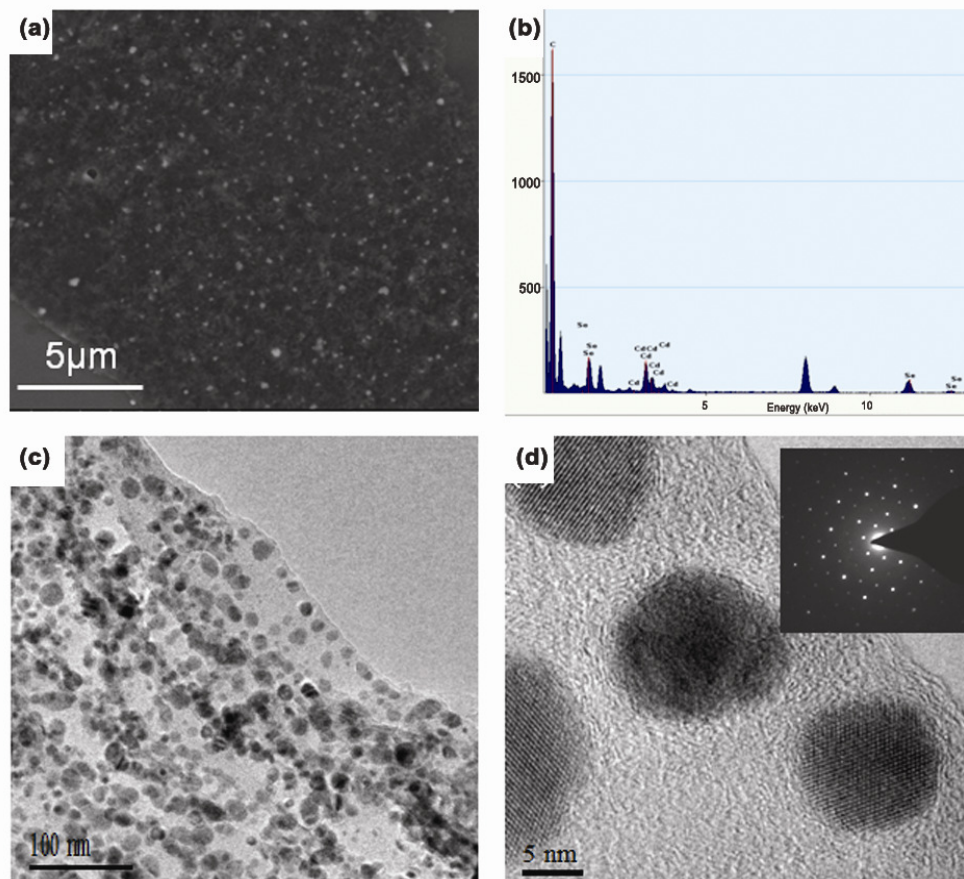
Figure 14: (a) FESEM image and (b) EDX pattern of RGO-CdSe prepared at the liquid-liquid interface. Low (c) and high (d) magnification TEM images of RGO-CdSe.

pattern of the RGO-CdSe composite, which confirms the single crystalline nature of CdSe nanoparticles over RGO.

The Raman spectra of RGO-CdSe and RGO are shown in Figure 13(b). RGO shows the G-band at 1591 cm^{-1} whereas the composite of RGO and CdSe shows the band at 1587 cm^{-1}, exhibiting the softening of G–band. This result suggest the occurrence of charge transfer interaction between RGO and CdSe nanoparticles, similar to that found between graphene and electron donor molecules like aniline.[36]

1.2.5: Conclusions

C$_{60}$, SWNTs and few-layer graphene self-assemble to form large area, continuous films at the organic-aqueous interface. It is noteworthy that the films are well ordered. Formation of good films by the C$_{60}$+few-layer graphene and SWNT+ few-layer graphene composites at the interface is intersting since such films may find use in certain applications. Occurrence of charge-transfer between few-layer graphene and C$_{60}$ is an interesting observation that could have implications for electronic and photovoltaic devices.

We have successfully obtained the composite films of EG-CdSe and RGO-CdSe at the organic-aqueous interface at room temperature. Electron microscopic investigations revealed the decoration of CdSe nanoparticles over the surface of EG and RGO. The composite was found to be fluorescent because of the CdSe nanoparticles attached to it. Raman spectroscopy has suggested the existence of electronic communication between the graphene and the nanoparticles. These composites will find suitable applications in opto-electronic devices and solar cells.

1.2.6: References

[1]   a)C. N. R. Rao, A. Govindaraj, *Nanotubes and Nanowires, Vol. Second Edtion*, The Royal Society of Chemistry, London, **2011**; b)S. K. Pati, T. Enoki, C. N. R. Rao, World Scientific, Singapore, **2011**; c)C. N. R. Rao, A. K. Sood, K. S. Subrahmanyam, A. Govindaraj, *Angew. Chem. Int. Ed.* **2009**, *48*, 7752.

[2]   Z. Wei, D. E. Barlow, P. E. Sheehan, *Nano Lett.* **2008**, *8*, 3141.

[3]   K. S. Kim, Y. Zhao, H. Jang, S. Y. Lee, J. M. Kim, K. S. Kim, J.-H. Ahn, P. Kim, J.-Y. Choi, B. H. Hong, *Nature* **2009**, *457*, 706.

[4]   H. Yamaguchi, G. Eda, C. Mattevi, H. Kim, M. Chhowalla, *ACS Nano* **2010**, *4*, 524.

[5]   G. Eda, G. Fanchini, M. Chhowalla, *Nat Nanotechnol.* **2008**, *3*, 270.

[6]   H. Li, S. Pang, S. Wu, X. Feng, K. Müllen, C. Bubeck, *J. Am. Chem. Soc* **2011**, *133*, 9423.

[7]   X. Li, G. Zhang, X. Bai, X. Sun, X. Wang, E. Wang, H. Dai, *Nat Nanotechnol.* **2008**, *3*, 538.

[8]   S. Biswas, L. T. Drzal, *Nano Lett.* **2008**, *9*, 167.

[9]   C. N. R. Rao, K. P. Kalyanikutty, *Acc. Chem. Res.* **2008**, *41*, 489.

[10]   M. Sathish, K. i. Miyazawa, J. P. Hill, K. Ariga, *J. Am. Chem. Soc* **2009**, *131*, 6372.

[11]   M. Sathish, K. i. Miyazawa, *J. Am. Chem. Soc* **2007**, *129*, 13816.

[12]   P. Asuri, S. S. Karajanagi, J. S. Dordick, R. S. Kane, *J. Am. Chem. Soc* **2006**, *128*, 1046.

[13]   Q. Liu, T. Fujigaya, H.-M. Cheng, N. Nakashima, *J. Am. Chem. Soc* **2010**, *132*, 16581.

[14] a)N. Tezuka, T. Umeyama, S. Seki, Y. Matano, M. Nishi, K. Hirao, H. Imahori, *J. Phys. Chem. C* **2010**, *114*, 3235; b)Y. Shen, A. G. Skirtach, T. Seki, S. Yagai, H. Li, H. Möhwald, T. Nakanishi, *J. Am. Chem. Soc* **2010**, *132*, 8566.

[15] a)T. Umeyama, N. Tezuka, S. Seki, Y. Matano, M. Nishi, K. Hirao, H. Lehtivuori, N. V. Tkachenko, H. Lemmetyinen, Y. Nakao, S. Sakaki, H. Imahori, *Adv. Mater.* **2010**, *22*, 1767; b)T. Umeyama, N. Tezuka, M. Fujita, S. Hayashi, N. Kadota, Y. Matano, H. Imahori, *Chem. Eur. J.* **2008** *14* 4875.

[16] J. Shen, Y. Hu, C. Li, C. Qin, M. Shi, M. Ye, *Langmuir* **2009**, *25*, 6122.

[17] Z. Tang, J. Zhuang, X. Wang, *Langmuir* **2010**, *26*, 9045.

[18] C. Chen, Q.-H. Yang, Y. Yang, W. Lv, Y. Wen, P.-X. Hou, M. Wang, H.-M. Cheng, *Adv. Mater.* **2009**, *21*, 3007.

[19] V. C. Tung, L.-M. Chen, M. J. Allen, J. K. Wassei, K. Nelson, R. B. Kaner, Y. Yang, *Nano Lett.* **2009**, *9*, 1949.

[20] P. J. King, U. Khan, M. Lotya, S. De, J. N. Coleman, *ACS Nano* **2010**, *4*, 4238.

[21] a)Y.-K. Kim, D.-H. Min, *Langmuir* **2009**, *25*, 11302; b)C. N. R. Rao, H. S. S. Ramakrishna Matte, R. Voggu, A. Govindaraj, *Dalton Trans.* **2012**, *41*, 5089.

[22] J. Yang, M. Heo, H. J. Lee, S.-M. Park, J. Y. Kim, H. S. Shin, *ACS Nano* **2011**, *5*, 8365.

[23] V. C. Tung, J.-H. Huang, J. Kim, A. J. Smith, C.-W. Chu, J. Huang, *Ener. Environ. Sci.* **2012**, *5*, 7810.

[24] a)I. Robel, B. A. Bunker, P. V. Kamat, *Adv. Mater.* **2005**, *17*, 2458; b)L. Sheeney-Haj-Ichia, J. Wasserman, I. Willner, *Adv. Mater.* **2002**, *14*, 1323.

[25]   Y. Lin, K. Zhang, W. Chen, Y. Liu, Z. Geng, J. Zeng, N. Pan, L. Yan, X. Wang, J. G. Hou, *ACS Nano* **2010**, *4*, 3033.

[26]   Y.-T. Kim, J. H. Han, B. H. Hong, Y.-U. Kwon, *Adv. Mater.* **2010**, *22*, 515.

[27]   a)C. Nethravathi, T. Nisha, N. Ravishankar, C. Shivakumara, M. Rajamathi, *Carbon* **2009**, *47*, 2054; b)A. Cao, Z. Liu, S. Chu, M. Wu, Z. Ye, Z. Cai, Y. Chang, S. Wang, Q. Gong, Y. Liu, *Adv. Mater.* **2010**, *22*, 103.

[28]   Y. Wang, H.-B. Yao, X.-H. Wang, S.-H. Yu, *J. Mater. Chem.* **2011**, *21*, 562.

[29]   I. V. Lightcap, P. V. Kamat, *J. Am. Chem. Soc* **2012**, *134*, 7109.

[30]   C. N. R. Rao, G. U. Kulkarni, V. V. Agrawal, U. K. Gautam, M. Ghosh, U. Tumkurkar, *J. Colloid Interface Sci.* **2005**, *289*, 305.

[31]   W. Kratschmer, L. D. Lamb, K. Fostiropoulos, D. R. Huffman, *Nature* **1990**, *347*, 354.

[32]   A. Govindaraj, C.N.R. Rao, *Fullerene Sci. Technol.* **1993** *1*, 557.

[33]   S.R.C. Vivekchand, R. Jayakanth, A. Govindaraj, C. N. R. Rao, *Small* **2005**, *1*, 920.

[34]   a)H. C. Schniepp, J.-L. Li, M. J. McAllister, H. Sai, M. Herrera-Alonso, D. H. Adamson, R. K. Prud'homme, R. Car, D. A. Saville, I. A. Aksay, *J. Phys. Chem. B* **2006**, *110*, 8535; b)K. S. Subrahmanyam, S. R. C. Vivekchand, A. Govindaraj, C. N. R. Rao, *J. Mater. Chem.* **2008**, *18*, 1517.

[35]   C. N. R. Rao, K. S. Subrahmanyam, H. S. S. Ramakrishna Matte, B. Abdulhakeem, A. Govindaraj, B. Das, P. Kumar, A. Ghosh, D. J. Late, *Sci. Tech. Adv. Mater.* **2010**, *11*, 054502.

[36]   C. N. R. Rao, R. Voggu, *Mater. Today* **2010**, *13*, 34.

[37]   B. Farrow, P. V. Kamat, *J. Am. Chem. Soc* **2009**, *131*, 11124.

1.3: Magnetic properties of graphenes

Summary[*]

We have investigated the magnetic properties of graphenes prepared by different methods from which we have understood that in all our graphene samples, dominant ferromagnetic interactions coexist along with antiferromagnetic interactions somewhat like in frustrated or phase-separated systems. Thus, all the graphene samples exhibit room-temperature magnetic hysteresis. The magnetic properties depend on the number of layers and the sample area, small values of both favoring larger magnetization. Molecular charge-transfer affects the magnetic properties of graphene, interaction with a donor molecule such as tetrathiafulvalene having greater effect than an electron-withdrawing molecule such as tetracyanoethylene. The value of magnetization increases with hydrogenation of graphene.

1.3: Magnetic properties of graphene

1.3.1 Introduction

Magnetism in carbon nanostructures: Magnetism of carbon materials is of particular interest because of lightweight and cheap magnets could open up new ways to design adaptable and flexible information storage systems. The potential application of carbon-based magnets in spin electronics integrates spin and molecular electronics. These are very encouraging findings in spintronics, where carbon magnetism could play an important role. The phenomenon of ferromagnetism relies on the possibility of aligning unpaired spins. But carbon, with its propensity to utilise all its valence electrons in very strong bonds, is perhaps the last element one would expect to retain unpaired electrons and exhibit ferromagnetism. But, the origin of magnetism in carbon based materials can be understood as follows. The electronic structure of benzene is described with six π-orbitals, which are split into three occupied bonding π and three unoccupied antibonding π*-levels with a finite band gap. Polycyclic condensed aromatic molecules such as naphthalene and anthracene which are formed by fusing benzene rings have a structure similar to that of π -electrons in benzene. In these molecules, the HOMO–LUMO gap decreases with an increase in the number of benzene rings. In the extreme of an infinite size, graphene sheet or 2D graphite has a semi-metallic electronic structure featured with the bonding π and antibonding π*-bands that are touched to each other at EF with no HOMO-LUMO splitting.[1] A group of these condensed polycyclic aromatic hydrocarbons therefore have common electronic properties based on these π-orbitals. However among these, there is a sub-family particularly featured with magnetism. A typical example is phenalenyl-free radical consisting of three benzene rings fused as shown in Figure 1, in which an unpaired electron having localized magnetic moment S = ± ½ exists as a consequence of the presence of a singly-occupied non-bonding π-electron state at E_F in addition to the π - and π*- levels. In general, we can group all the carbon

sites of a condensed polycyclic aromatic hydrocarbon into two subgroups, where the neighboring sites directly bonded to a site belonging a subgroup ("starred" subgroup) belong to another subgroup ("unstarred" subgroup). According to Lieb's theorem, the unpaired electrons are produced when the numbers of sites belonging to these two subgroups are different. Actually, the difference in the numbers corresponds to the number of unpaired electrons. In the case of phenalenyl-free radical, the difference gives one localized spin, resulting in carbon-based magnetism. The issue of starred and unstarred is the same to that in bipartite lattice in physics language. The same theorem is also applicable to nano-sized graphene sheet or nanographene. The zigzag and armchair edge (Figure 1) leads to strikingly different properties of the states near the Fermi level. The ribbons with zigzag edges possess partly flat bands at the Fermi level corresponding to electronic states localized in the near vicinity of the edge. These localized states ''edge states'' correspond to the nonbonding molecular orbital NBMO as can be seen from the analytic solution for semi-infinite graphite with a zigzag edge.[2] In contrast, localized edge states and the corresponding flat bands are completely absent for ribbons with armchair edges. The localized edge states are of special interest in nanographite physics, because of their relatively large contribution to the density of states (DOS) at the Fermi energy.
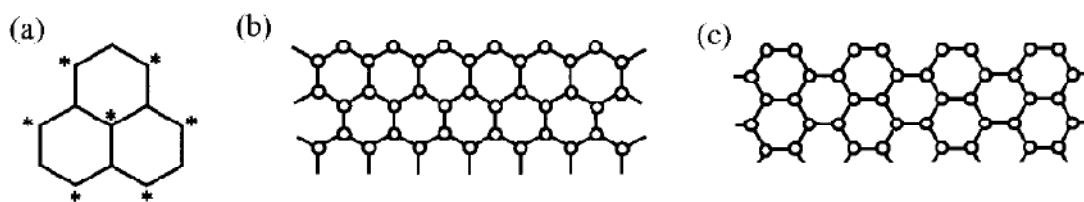
Figure 1: (a) Phenalenyl-free radical where up and down spins are placed on starred and unstarred sites, (b) zigzag edge, (c) armchair edge.

1.3: Magnetic properties of graphene

The observed magnetic susceptibility χ is the sum of four components: 1) localized spin susceptibility χ_{spin}, 2) diamagnetic susceptibility due to the core electrons χ_{core}, 3) pauli paramagnetic susceptibility χ_p, and 4) orbital diamagnetic susceptibility χ_{orb}, due to the cyclotron motion of the itinerant electrons.[3]

χ_{spin} originates from the electron-electron interaction, χ_{core} arises from core electrons of the atoms, it is small and basically temperature independent. χ_p, the Pauli paramagnetic susceptibility is related to the DOS at the Fermi level, which represents an important component in zigzag nanographite ribbons where an enhanced density of states appears at the Fermi level. Note that χ_p, is negligible in armchair ribbons, aromatic molecules, and graphite sheets, because their DOS is suppressed at the Fermi level. χ_p, introduces a very pronounced temperature dependence, which is nearly Curie-like. The width of the peak of DOS at the fermi level has the order of meV, which is comparable to the temperature scale of room temperature. Therefore, it is expected that the Pauli susceptibility of zigzag ribbons might be sensitive to temperature, although the Pauli susceptibility of other usual metals is temperature independent. The χ_{orb}, diamagnetic contribution to the susceptibility is very familiar from the magnetic properties of graphite sheets. It is due to the orbital cyclotron motion of the electrons in a field with a finite component perpendicular to the plane. It is well known that graphite shows a large anisotropic diamagnetic susceptibility, while aromatic molecules show only weak diamagnetism. This fact tells us that the orbital diamagnetic susceptibility is sensitive to the size of graphite fragments.

Occurrence of high-temperature ferromagnetism in graphite-related materials is a topic of considerable interest. Here we review, some of the theoretical reports reported on the magnetism of graphene related materials. Localized unpaired spins arising from topological and bonding defects are suggested to be responsible for ferromagnetism

1.3: Magnetic properties of graphene

observed in such nanomaterials. Nanometer-sized graphenes with triangular and hexagonal shapes terminated by zig-zag edges have been predicted to be magnetic.[4] Yazyev et al.[5] show that magnetism in graphene can be induced by the vacancy defect or by hydrogen chemisorption. Ferromagnetic or antiferromagnetic coupling is observed depending on whether the defects correspond to the same or to different hexagonal sublattices of the graphene lattice. Single-atom defects can induce ferromagnetism in graphene-based materials.[6] Vacancies, substitutional atoms (e.g., B or N) and adatoms could also be responsible for the magnetism of graphene.[7] Some workers suggest that the zig-zag edges are responsible for the magnetic properties of graphene.[8] For example, zig-zag edges, longer than 3-4 repeated units are predicted to be magnetic irrespective of whether the edges are regular or irregular. An interplay between mechanical and magnetic properties can occur in graphene wherein the tensile strain along the zig-zag direction enhances the ferromagnetic stability.[9] The presence of van Hove singularities can also lead to magnetism and such singularities are generated by the rotation between the stacked layers of graphene.[10]

Magnetic properties of nanographite prepared by the conversion of nanodiamond at different temperatures have been investigated in detail by Enoki et al.[11] Inhomogeneous distribution of ferromagnetic structures of nanographene sheets have been observed below 20 K.[12] Magnetism of activated carbon fibres (ACF) heated to different temperatures comprising a disordered network of nanographites has been reported.[13] Microporous carbon exhibits high-temperature ferromagnetism originating from topological disorder associated with curved graphene sheets.[14] The difference between values of ZFC and FC magnetization indicates that the microporus carbon possesses a disordered magnetism similar to diluted magnetic semiconductors [15] and doped rare earth manganites,[16] suggesting a percolative-type transition at low

temperatures.

Room-temperature ferromagnetism has been reported in highly oriented pyrolytic graphite materials. Macroscopic quantities of magnetic graphite (MG) are produced by controlled etching of graphite employing a redox reaction in a closed system.[17] MG exhibits a strong ferromagnetic response at room temperature due to topographic defects as shown by magnetic force microscopy. Susceptibility measurements show two transitions temperatures at 115 K and 315 K associated with the weak coupling between ferromagnetic regions related to defects and to the ferromagnetism inside the defect regions respectively.[18] Nano fluid magnetic graphite prepared by sonication of magnetic graphite in the presence of a cationic surfactant exhibits room-temperature ferromagnetism.[19] Ferromagnetic behavior in highly oriented pyrolytic graphite (HOPG) and Kish graphite samples has been attributed to topological defects and strong coulomb interaction between electrons.[20]

Magnetism has been induced in carbon-related materials by irradiation with different ions. Thus, ferro- or ferri-magnetism is triggered in HOPG by proton irradiation of 2.25 MeV. SQUID and MFM measurements show that that magnetic ordering is stable at room temperature.[21] Irradiation of HOPG by H, C and N ions in the MeV range triggers Curie-type paramagnetism, ferromagnetism or an anomalous paramagnetic state.[22] Room-temperature ferromagnetism in HOPG produced by low-energy carbon-ion implantation can easily be tuned by controlling the implantation dose.[23] On bombarding graphite with protons at low temperatures and low fluences, a significant increase in the magnitude of the magnetic order is observed.[24] Spectromicroscopy study at room temperature of proton-irradiated metal-free carbon using x-ray magnetic circular dichroism reveals that magnetic order arises from the carbon π electron system.[25] Nano sized diamond particles implanted with nitrogen and carbon show ferromagnetic

1.3: Magnetic properties of graphene

hysteresis at room temperature.[26] Ferromagnetic order has been evidenced at defect structures in HOPG using magnetic force microscopy and bulk magnetization measurements at room temperature.[27] Ferromagnetic spots created by protons irradiation on graphite surface has been examined by magnetic force microscopy.[28] Carbon nano-particles produced by a pulsed arc submerged in ethanol show room temperature magnetic hysteresis.[29]

Wang et al.[30] reported room temperature ferromagnetism in a graphene sample prepared by the partial reduction of graphene oxide with hydrazine followed by annealing the samples at different temperatures in an argon atmosphere. These authors suggested long-range coupling of spin units (defects) to be responsible for ferromagnetism.[30] Rout et al.[31] find room-temperature ferromagnetism in graphitic petal arrays grown on Si substrates by microwave plasma chemical vapour deposition without any catalyst. They have shown that upon O_2 annealing, saturation magnetization and corecivity decrease.[31]

Aryl-radical functionalization of epitaxial graphene leads to disordered magnetism in the graphene sheet, due to the presence of a mixture of ferromagnetic, superparamagnetic and antiferromagnetic regions.[32] The functionalization enhances the magnetic properties of the eptaxial graphene. These workers also find that pristine single-layer graphene is inhomogeneous with respect to the number of layers and other features and suggest that the magnetism is confined to the surface of graphene with a distribution of magnetic regions over the surface.[33]

Adsorption of different guest molecules on graphene gives rise to a reversible low-spin/high-spin magnetic switching phenomenon which depends on the nature of the guest species. Adsorption of H_2O,[34] interaction with acids[35] and intercalation with potassium clusters reduce the magnetization of nanographite.[36] The reduction in magnetization has been interpreted as due to the interaction with lone pair orbitals as well

as charge-transfer with graphene sheets. The edge sites participating in host–guest interactions can give rise to magnetic phenomenon. Guest molecules accommodated through physisorption mechanically compress the flexible nanographite domains, leading to a significant reduction in the inter-nanographene-sheet distance. Such a reduction in the intersheet distance could align the magnetic moments anti-parallel and reduce the net magnetic moment.[37]

Graphene-like systems on hydrogenation become semiconducting and the edge structures as well as the electronic properties of these materials get modified by hydrogen adsorption. Hydrogenation of graphene can induce magnetism since the formation of tetrahedral carbons can reduce the connectivity of the π-sheets and the π-π energy gap of the localized double bonds and hence the ring current diamagnetism. Such changes in structure can therefore cause an increase in magnetic susceptibility. [38]

Partial hydrogenation of graphene leads to the formation of unpaired electrons and the remanent delocalized bonding network appears to be responsible for the observed ferromagnetism on epitaxial graphene grown on 4H SiC-(0001).[39] Furthermore at the interface between graphene and graphane, magnetism arising from the edges can be tuned.[40] Semi-hydrogenated graphene is predicted to be a ferromagnetic semiconductor with a small indirect gap and a Curie temperature between 278 K to 417 K.[41] Magnetic properties of graphene with adsorbed hydrogen clusters have been examined.[42] Hydrogen saturation appears to stabilize the vacancy structure and induce magnetic coupling between the defects.[43]

1.3.2: Scope of the present investigations

Magnetic properties of certain carbon materials like HOPG,[57] polymerised fullerenes,[58] nanographite particles[59] and activated carbon fibres[60] have been studied, but those of graphene have not yet been reported. We felt that it would be worthwhile to measure magnetic properties of chemically synthesized graphene samples. For various practical applications the required feature is, the tunability of the magnetic properties. In order to fulfil the requirement, we employed two routes. The first one is adsorption of molecules like tetrathiafulvalene (TTF) and tetracyanoethylene (TCNE) on graphene. The second one is hydrogenation of graphene through Birch reduction. We find that all the graphene samples show evidence for ferromagnetism with well-defined hysteresis, along with antiferromagnetic features. Electron-donating TTF markedly affects the magnetic properties of graphene. Hydrogenation caused the increase in the magnetic moments which is attributed to delocalisation of π-electrons.

1.3.3: Experimental section

We have carried out an experimental study of the magnetic properties of a few-graphene samples (EG, DG and HG) prepared by different methods ensuring that they were devoid of transition metal impurities. The absence of magnetic transition metal impurities was ensured by employing due care during the synthesis of graphenes.

Synthesis of EG

The first method to prepare EG involved the thermal exfoliation of graphitic oxide. Graphitic oxide (GO) was prepared according to the Staudenmaier method. A 250 ml reaction flask containing a magnetic stir bar with sulfuric acid (10 ml) and nitric acid (5 ml) and kept in an ice bath. The acid mixture was stirred and allowed to cool for 15 min,

and graphite (0.5 g) was added slowly under vigorous stirring to avoid agglomeration. After the graphite powder was well dispersed, potassium chlorate (5.5 g) was added slowly over 15 min to avoid sudden increase in temperature. The reaction flask was loosely capped to allow evolution of gas from the reaction mixture and stirred for 96 h at room temperature. On completion of the reaction, the mixture was poured into 0.5 L of deionized water and filtered. The GO was redispersed and washed in a 5% solution of HCl. The GO was then washed repeatedly with deionized water until the pH of the filtrate was neutral. The GO slurry was dried in vacuum at 60°C.

Graphite oxide (0.2 g), prepared as described above where the oxidation step was carried out for 4 days, was placed in an alumina boat and inserted into a 1.3 m long quartz tube that was sealed at one end. The other end of the quartz tube was fixed to a two holed rubber stopper. An argon (Ar) inlet was inserted through one of the holes of the rubber stopper, and the outlet was fixed through the other hole. The sample was purged with Ar for 10 min, and then the quartz tube was quickly inserted into a tube furnace preheated to 1050℃ and held in the furnace for 10 minutes.

Synthesis of DG

DG was prepared by graphitization of nanodiamond powder (particle size 4-6 nm, Tokyo Diamond Tools, Tokyo, Japan) in an inert argon atmosphere. The mean size and the size distribution of the diamond particles checked by transmission electron microscopy were in good agreement with the reported ones (catalogue specifications). In order to avoid contamination with magnetic impurities, we treated nanodiamond particles by soaking in concentrated HCl before use. 50 mg of pristine nanodiamond powder placed in a graphite tube having diameter 0.35 cm, was heat treated in furnace in a helium atmosphere, at 1650°C for 3 hrs.[61]

1.3: Magnetic properties of graphene

Synthesis of HG

To prepare HG, direct current (DC) arc discharge evaporation experiments were carried out in a stainless steel chamber that was filled with hydrogen and helium mixtures without using any catalyst. In typical experiment a graphite rod (6 mm diameter and 50 mm long) was used as an anode and as cathode, a pure graphite rod (having diameter of 13 mm and 60 mm length) was used. The purity of the graphite rod was 99.998%. The discharge current was carried out at 100 A, and the voltage, about 38 V. The arc was maintained by continuously translating the cathode to keep a constant distance (2 mm) between it and the anode. Typical synthesis time was 10 min. Soot materials with web like appearance were formed on the inner walls of the reaction chamber and around the cathode after the evaporation.

Synthesis of RGO, RGO(E) and RGO (W)

To prepare RGO, at first single-layer graphene oxide (SGO) was prepared by ultra-sonication of graphite oxide (GO). The so obtained SGO was reduced employing hydrazine hydrate/ethylene glycol as a reducing agent at refluxing conditions and through hydrothermal routes. These samples are designated as RGO and RGO (E) respectively. [62] In order to ensure that there were no magnetic transition metal impurities, we washed the GO solution with 8-hydroxy-quinoline-5-sulfonic acid prior to the reduction. In this process, 8-hydroxy-quinoline-5-sulfonic acid was added to GO solution in ethanol and the mixture was subjected to sonication followed by stirring for 12 hr. The product obtained by filtration and through washing was employed for reduction. The reduced graphene so obtained by this process is designated as RGO (W).

Hydrogenated Samples

Hydrogenated samples comprising different contents of hydrogen have been prepared by Birch reduction.

1.3: Magnetic properties of graphene

Preparation of TTF adsorbed HG

For the synthesis of TTF adsorbed HG sample, we have dispersed 7 mg of HG sample in each 10 ml of benzene solutions of having 0.120 g and 0.024 g of TTF (0.05 M and 0.01 M) and sonicated for 30 min. The TTF adsorbed HG sample was filtered using anodisc filter paper and then dried at room temperature for 6 hrs.

Preparation of TCNE adsorbed HG

To prepare TCNE adsorbed HG sample, 7 mg of HG sample was dispersed in each 10 ml of benzene solutions of having 0.065 g and 0.013 g of TCNE (0.05 M and 0.01 M) and sonicated for 30 min. The TCNE adsorbed HG sample was filtered using anodisc filter paper and then dried at room temperature for 6 hrs.

Characterization

Physical property measurement system (PPMS)

Magnetic measurements were performed on 6-8 mg of graphene samples by employing a vibrating sample magnetometer (VSM) in physical property measuring system (PPMS)(Quantum Design, USA) from the temperature range of 5 – 300 K.

Electron paramagnetic resonance (EPR)

Electron paramagnetic resonance (EPR) spectra were recorded using a Bruker EMX X-band continuous wave (CW) EPR spectrometer in temperature range of 2.5 K to 300 K. AC suspectibility measurements were carried out in PPMS from the temperature range of 5 K to 300 K for EG , DG and HG Samples. Spin density calculations have been done for all the samples at room temperature in Bruker EMX X-band continuous wave (CW) EPR spectrometer for these three samples.

1.3.4: Results and discussion

The graphene samples prepared by different chemical methods, were characterized by various techniques including AFM, TEM, and Raman spectroscopy.
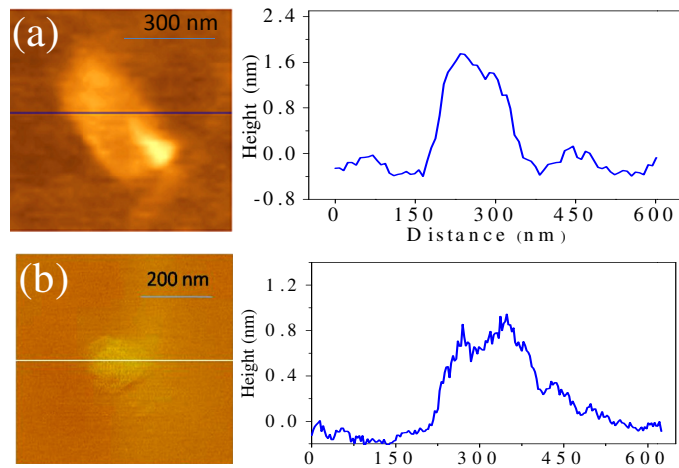
Figure 2: AFM images of (a) EG and (b) HG samples
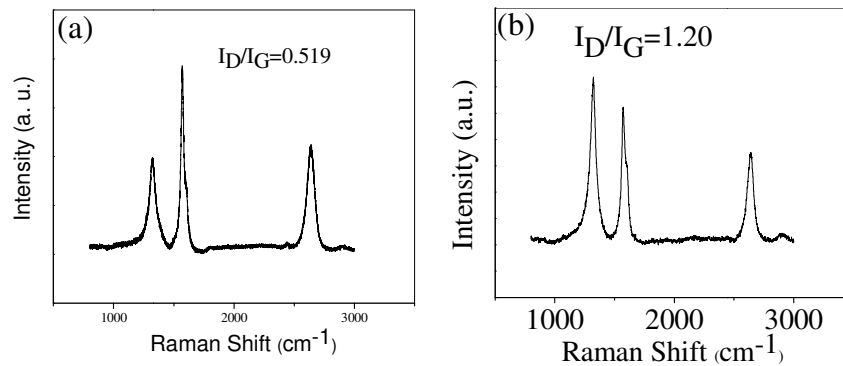
Figure 3: Raman Spectra of (a) EG and (b) HG sample
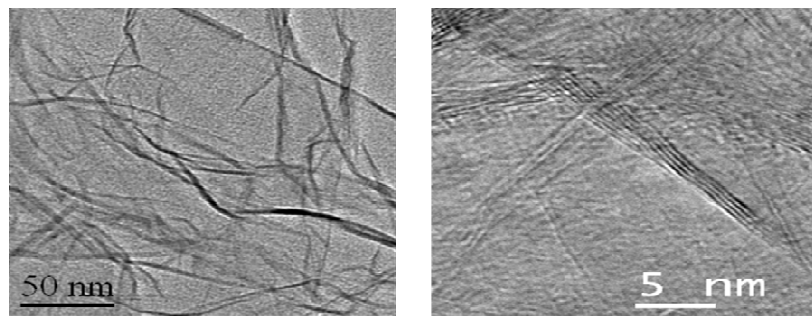
Figure 4: TEM image of (a) EG and (b) HG

1.3: Magnetic properties of graphene

From the AFM measurements, the average number of graphene layers was estimated to be 6-7, 4-5 and 2-3 respectively in EG, DG and HG (Figure 2). Raman spectra show the D-, G-, and 2D bands around 1320, 1570 and 2640 cm^{-1} and the relative intensity of the defect-related D-band is much higher in HG (Figure 3). The BET surface areas of the samples were 826 m^2/g, 781 m^2/g and 680 m^2/g respectively. The areas of the graphene flakes in the EG, DG and HG samples were $65\pm25x10^3$ nm^2, $40\pm20x10^3$ nm^2 and $25\pm15x10^3$ nm^2 respectively. Figure 4 shows the TEM images of EG and HG. Of the three graphene samples, HG had the smallest number of graphene layers and the smallest area.

In Figure 5, we show the temperature-dependence of magnetization of all the graphene samples (EG, DG and HG) measured at 500 Oe and 1 T. Figures 5(a), (c) and (e) show the temperature dependent magnetization data of field-cooled (FC) and zero-field-cooled (ZFC) data at 500 Oe and the Figures 5(b), (d) and (f) shows the FC and ZFC at 1 T. It shows divergence between the FC and ZFC data, starting around 300 K. The divergence nearly disappears on the application of 1 T as can be seen from Figure 5(b). As we can notice from the Figure 5 that, as the temperature increases the magnetic moment increases and there is a sudden increase in magnetic moment at temperature less than 15 K which can be attributed to the curie tail like behaviour which is very common in magnetic material at lower temperatures, and it also may be due to the adsorbed paramagnetic oxygen in the graphene sample. Interestingly, we observe well-defined maxima in the magnetization at low temperatures, the maxima becoming prominent in the data recorded at 1 T (see Figures 5 (b), (d) and (f)). Such magnetic anomalies are found when antiferromagnetic correlations compete with ferromagnetic (FM) order. Application of high fields aligns the FM clusters and decreases the divergence between FC and ZFC data as indeed observed. It is possible that the data correspond to percolation type of situation, where in different types of magnetic states coexist. The FM clusters in such a

case would not be associated with a well-defined global ferromagnetic transition temperature. This behavior is similar to that of microporus carbon and some phase-separated members of the rare earth manganite family, $Ln_{1-x}A_xMnO_3$ (Ln=rare-earth, A=alkaline earth), nanoparticles of antiferromagnetic order shown similar behavior.[61]
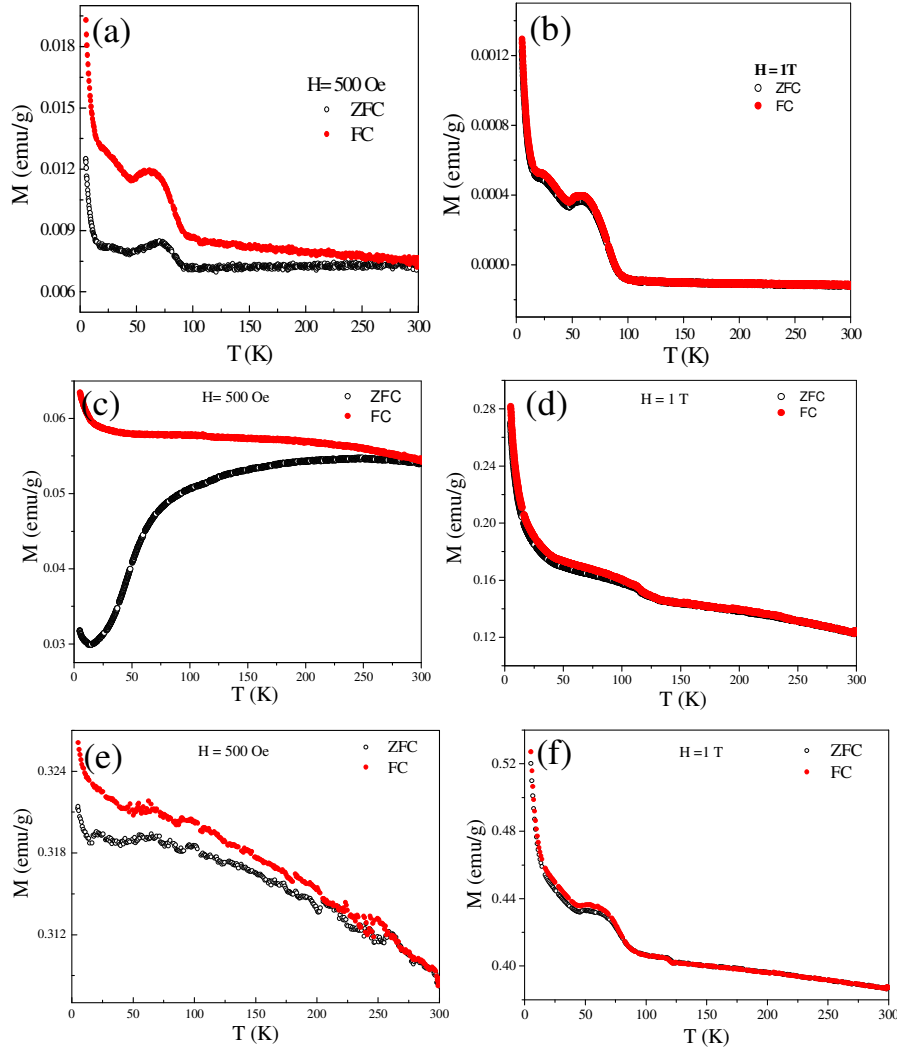
Figure 5: Temperature variation of magnetization of (a) EG (c) DG (e) HG at 500 Oe, (b) EG (e) DG (f) HG showing the ZFC and FC data at 1 T.

The Curie-Weiss temperatures obtained from the high-temperature inverse susceptibility data of field cooled 500 Oe is negative for all the samples, indicating the presence of antiferromagnetic interactions.

1.3: Magnetic properties of graphene

Having done with the FC and ZFC measurements, we have carried out the magnetic hysteresis measurements for all the samples at 5 K and 300 K in the field range of -6 T < H < +6 T (see Figures 6 and 7). For EG sample, saturation of the magnetization values are M_s = 0.07, 0.01 and 0.01 emu/g for 5 K, 100 K and 300 K respectively. The coercive field H_c is 213, 210 and 139 Oe and reminant magnetization is 0.0055, 0.0048 and 0.0032 emu/g at different temperatures 5 K, 100 K, and 300 K respectively. Similarly we have carried hysteresis measurements for DG sample and found M_s = 0.34, 0.16 and 0.14 emu/g for 5 K, 100 K and 300 K respectively with coercive field H_c is 380, 180 and 117 Oe at 5 K, 100 K and 300 K respectively. In the case of HG the M_s = 0.54, 0.41 and 0.32 emu/g for 5 K, 100 K and 300 K respectively with coercive field H_c is 3, 6 and 23 Oe at different temperatures 5 K, 100 K, and 300 K respectively. These results clearly show that the graphene samples have a weak ferromagnetic ordering at room temperature
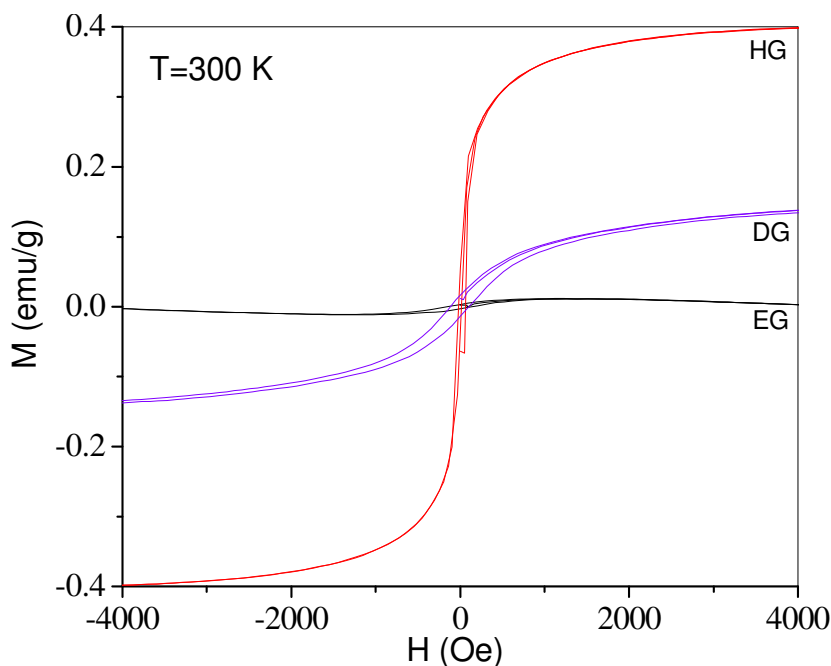
Figure 6: Magnetic hysteresis in EG, DG-1650 °C and HG at 300 K.

1.3: Magnetic properties of graphene
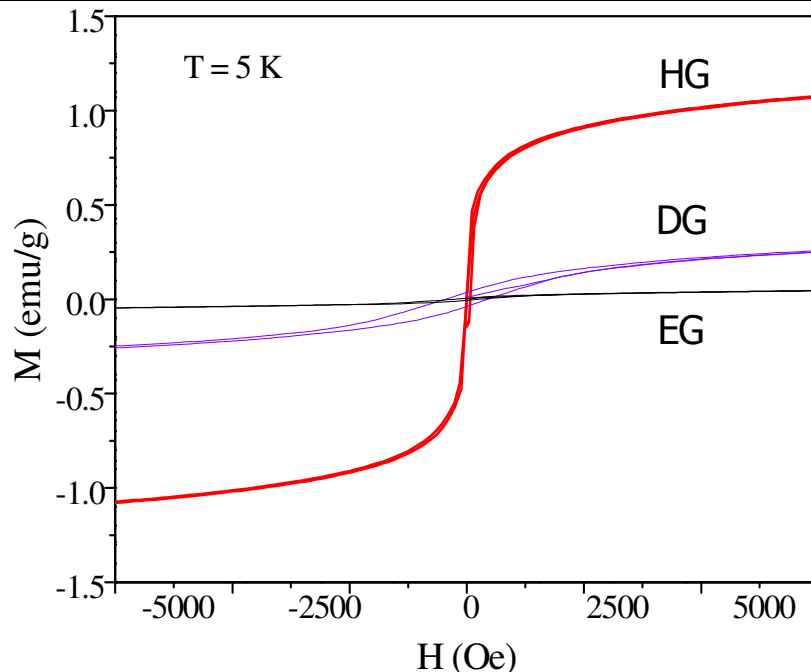
Figure 7: Magnetic hysteresis in EG, DG- and HG at 5 K.

Even though enough care was taken during the preparation of the various graphene samples, in order to ensure that there were no magnetic transition metal impurities, we washed some of the graphene samples with complexing agents. Thus, in the case of RGO, we washed the GO solution with 8-hydroxy-quinoline -5-sulfonic acid prior to the reduction. The graphene so obtained is designated as RGO (W). In Figure 8, we show the temperature-dependence of magnetization of RGO (W) measured at 500 Oe. Inset in the figure shows temperature-dependence of magnetization measured at 3000 Oe. Clearly the basic features of the graphene samples (SGO, RGO, RGO(E) and RGO (W)) described earlier are preserved. In Figure 9, we show the magnetic hysteresis of the samples at room temperature. We see that θ_p, M_R and M_S are highest in case of HG which also shows higher value of magnetization than the other samples at all temperatures. We have plotted the values of the various magnetic properties of the samples in Figure 10(a) to demonstrate how the properties vary as HG > DG > EG. In Figure 10(b), we have shown the variation of the average area and the number of layers in these three samples. It

is noteworthy that both the area and the number of layers decrease in the order of EG> DG> HG. It is likely that the edge effects would be greater in samples with smaller number of layers as well as small areas.
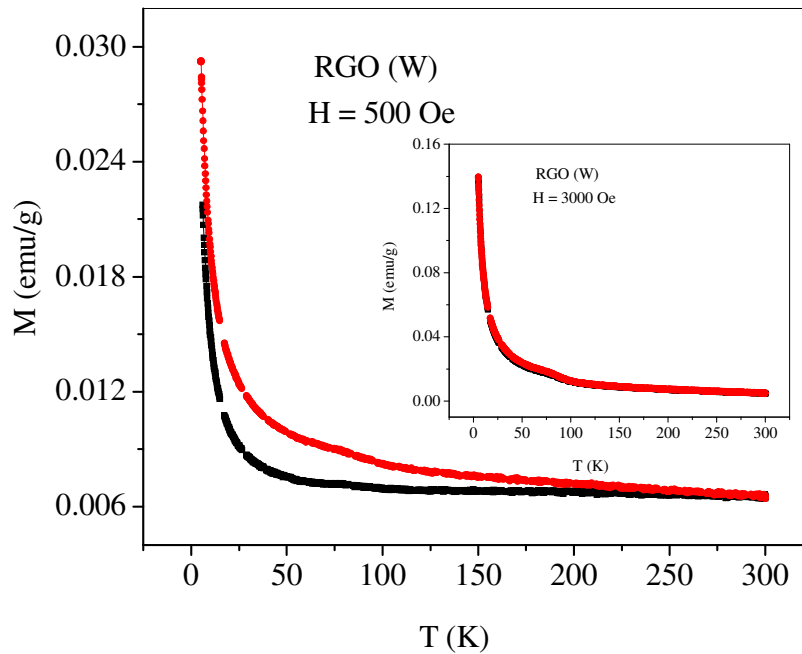
Figure 8: Temperature variation of magnetization of RGO (W) at 500 Oe showing the ZFC and FC data. The insets show the magnetization data at 3000 Oe.
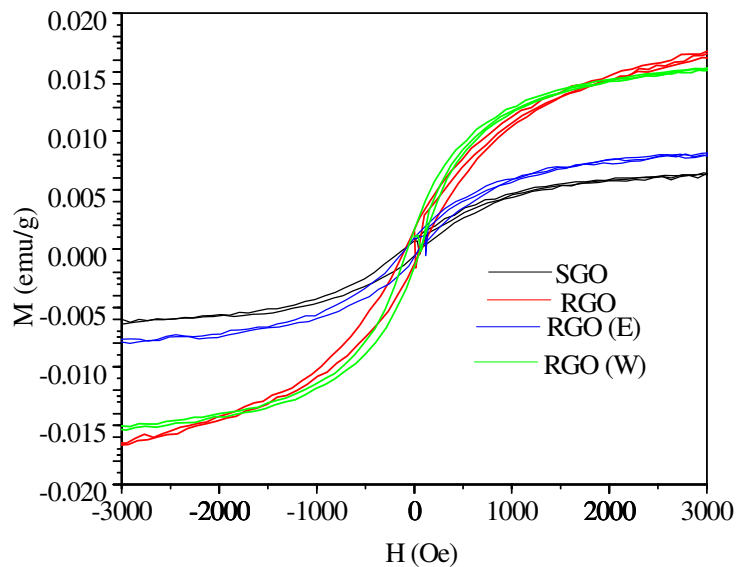
Figure 9: Magnetic hysteresis in SGO, RGO, RGO (E) and RGO (W) at 300 K.

Figure 10: (a) Comparison of the magnetic properties of EG, DG and HG. (b) Variation of the number of layers and sample area.

EPR measurements: Occurrence of intrinsic magnetism in carbon-based materials comprising sp^2 networks has been somewhat a controversial due to doubts raised, whether the ferromagnetic features are due to magnetic impurities such as iron, cobalt and nickel etc. Albeit, special care has been taken during the synthesis of graphene samples, still to confirm further whether there are any detectable impurities are present in the sample, we have investigated the Electron paramagnetic resonance measurements of all samples from the temperature ranging from 2.5 K to 300 K. In Figure 11, we show EPR plots of EG
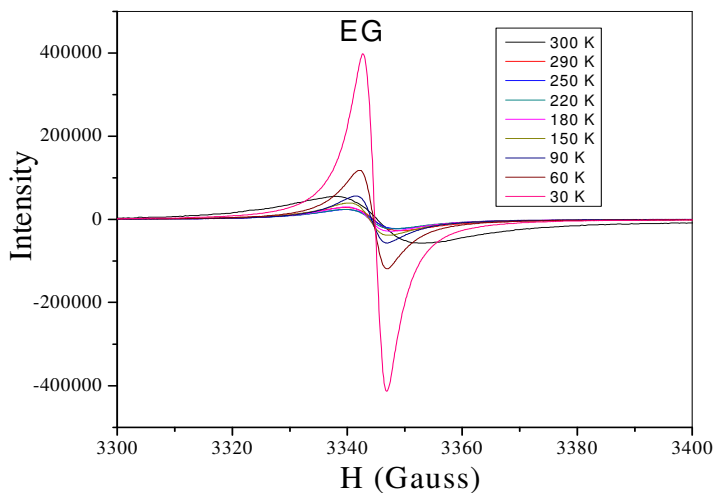
Figure 11: EPR plots of EG sample.

sample. These experiments revealed that graphene samples studied by us did not contain detectable levels of transition metal impurities. Thus the unusual magnetic properties shown by graphene samples here are, therefore, intrinsic to the carbon. In Figure 12, we have plotted the temperature dependence of the Intensity in the EPR signal. The
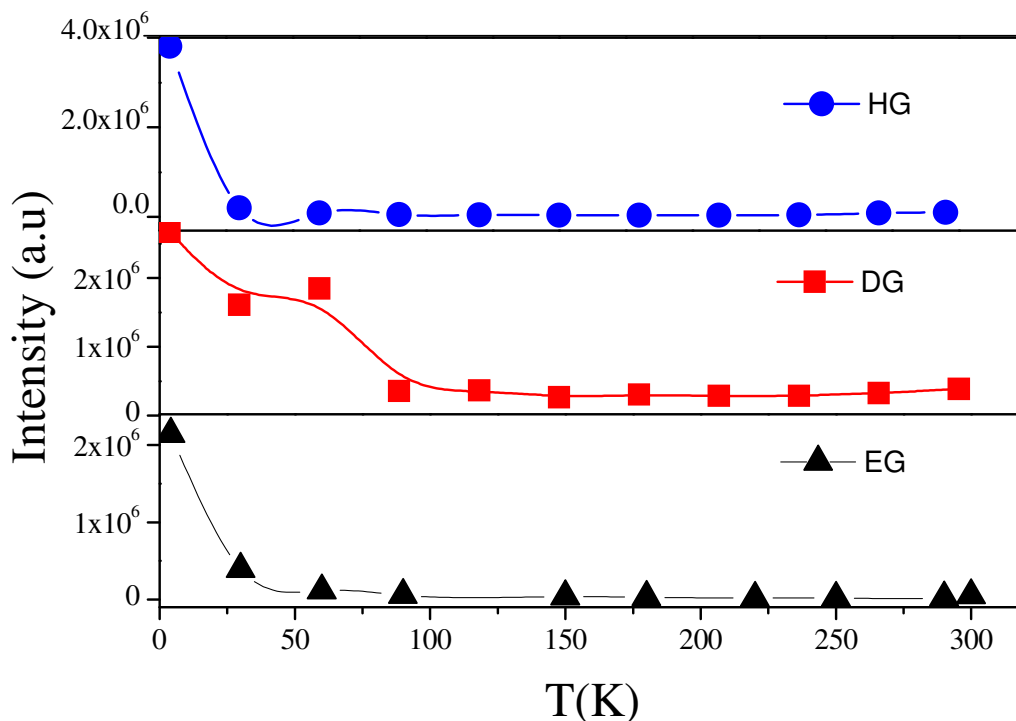
Figure 12: Temperature dependence of the intensity in the EPR spectra of the EG, DG and HG sample.

temperature variation of the EPR intensity is consistent with the magnetization data showing a marked increase at low temperatures.

In Figure 13, we have shown the temperature dependence of the line width ΔH in the EPR signal. As it is clear from the Figure 13, there is a decrease in the linewidth as the temperature decreases. We observe a signal with a line-width of $\Delta H \approx 0.7$-2.9 mT with a g- value is in the 2.006-2.013 range. The small value of the line-width and the small deviation in the g value from the free-electron value suggest that the spins do not originate from transition-metal impurities but from only carbon-inherited spin species in the graphene sheets. We have measured the temperature dependence of ac susceptibility

at different frequencies. We have carried out this experiment since we find the presence of AFM interactions as well as magnetic hysteresis in our graphene samples, a behavior somewhat like that of frustrated magnetic systems. The measurements on DG and HG
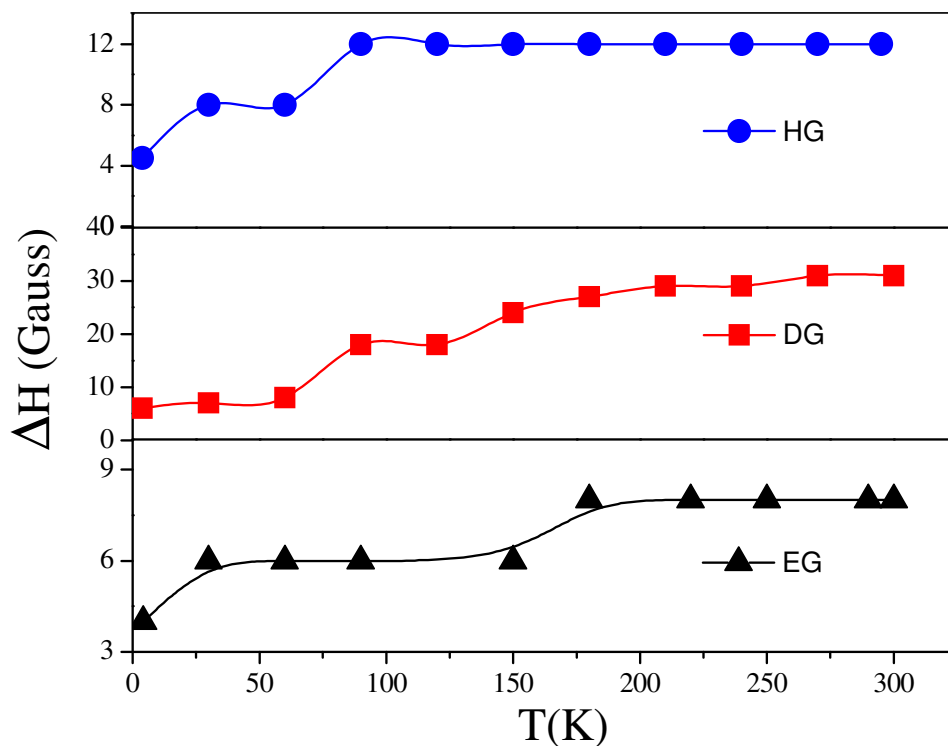
Figure 13: Temperature dependence of the line width ΔH in the EPR signal.

samples in the frequency range from 97 to 9997 Hz did not showed any frequency-dependent features in the temperature range of 3-300 K range, ruling out the observed ferromagnetism is due to spin-glass behavior. We have carried out spin-density measurements on EG, DG and HG samples taking copper sulfate as a reference, gave values of 2.86×10^{12}, 1.48×10^{13} and 2.46×10^{14} spins/mg respectively. This order of magnitude is also consistent with the magnetization values.

Tuning the magnetic properties of HG sample: In order to design more subtle magnetic carbon devices, proper control on the magnetization of these materials essential. For this purpose, we have developed a method for fine-tuning of the magnetization in graphene samples through adsorption of TTF and TCNE.

1.3: Magnetic properties of graphene

Adsorption of benzene solutions of TTF and TCNE has a profound effect on the magnetic properties of graphene. This method is easy to synthesis, reliable and highly reproducible. The large reversible concentration-dependent effects of adsorbing TTF and TCNE on the magnetic properties of graphene lend evidence to the fact that the magnetic properties of the graphene samples observed by us are intrinsic to them. In Figure 14, we show typical results on the effect of adsorbing 0.01 M and 0.05 M solutions of TTF on the magnetic properties of HG. The value of the magnetization drastically decreases on adsorption of TTF and TCNE, although the basic trend in the temperature-variation of magnetization remains the same. Thus, the graphene sample continues to show room-temperature hysteresis. On increasing the concentration of TTF or TCNE, the magnetization value decreases progressively. Interestingly, TTF has a greater effect than TCNE, even though the magnitude of adsorption of TCNE on HG is greater. Magnetic hysteresis of HG persists even after adsorption of TTF and TCNE. On adsorption of 0.01 and 0.05 M TTF on graphene, Ms value at 5 K drops from 0.54 to 0.42 and 0.25 respectively. Hc and Mr also decrease following the same trend. In case of TCNE, the Curie-Weiss temperature, θ_p, also decreases markedly on adsorption of these molecules. Thus, θ_p, of HG becomes -485 K and -83 K after adsorbing 0.05 M TCNE and TTF respectively (compared to -3340 K for pure HG). Clearly, charge-transfer interaction between graphene and TTF (TCNE)[63] is responsible for affecting the magnetic properties. In the literature, there is some evidence to show that adsorption of H_2O[64] and interactions of acids[65] reduce the magnetization of nanographite. Potassium clusters also reduce the magnetization of nanographite.[66] In these cases, the reduction in magnetization has been interpreted as due to the interaction with lonepair orbitals as well as charge-transfer with graphene sheets.
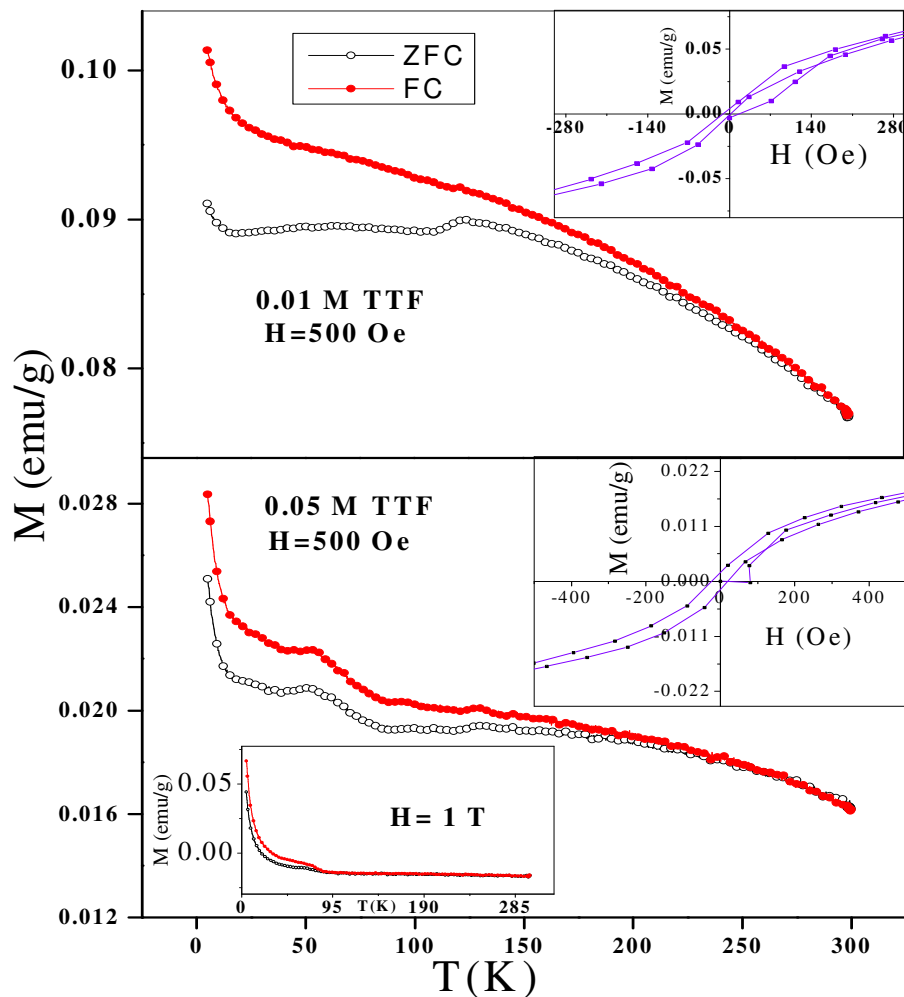
Figure 14: Temperature-variation of the magnetization of HG samples (500 Oe) after adsorption of 0.01 M and 0.05 M TTF solutions. The magnetization data given in the figure are corrected for the weight of adsorbed TTF. Magnetic hysteresis data at 300 K are shown as insets. In the case of 0.05 M TTF-HG, magnetization data is shown at 1 T as an inset. Magnetization data of HG with adsorbed TCNE are similar to those with TTF, except that the decrease in magnetization relative to pure HG is smaller.

Hydrogenation: Graphene-like systems on hydrogenation become semiconducting and the edge structures as well as the electronic properties of these materials get modified by hydrogen adsorption. Hydrogenation of graphene can induce magnetism since the formation of tetrahedral carbons can reduce the connectivity of the π -sheets and the π - π^* energy gap of the localised double bonds and hence the ring current diamagnetism. Such changes in structure can therefore cause an increase in magnetic susceptibility.[38]

1.3: Magnetic properties of graphene

We have carried out the hydrogenation of graphene (HG) employing birch reduction. Hydrogenated graphene samples with varying hydrogen contents of 2 wt%, 3 wt% and 5 wt% were prepared and designated as HGH_1, HGH_2 and HGH_3 respectively. They have been examined for the magnetic properties. We observe a gradual increase in the magnetic moment with increase in the hydrogen content. We also measured dependence of magnetization of HG and HGH_2 at 500 Oe. There is also an anomaly from 50 K to 80 K in the case of ZFC of HGH_2, compared to HG. This anomaly could be due to percolation type of situation arising from different types of magnetic states. It appears that there is a change in the magnetic structure in HGH_2 compared to HG. In Figure 15 we show the remanent magnetization (M_r), saturation magnetization (M_s) and magnetization at 3000 Oe (FC@10 K) of HG with different weight percentages of hydrogen. The values of these properties increase with hydrogen content. On dehydrogenation at 500 °C for 4 hours, the samples exhibit a decrease in the magnetic moment (Table 2).
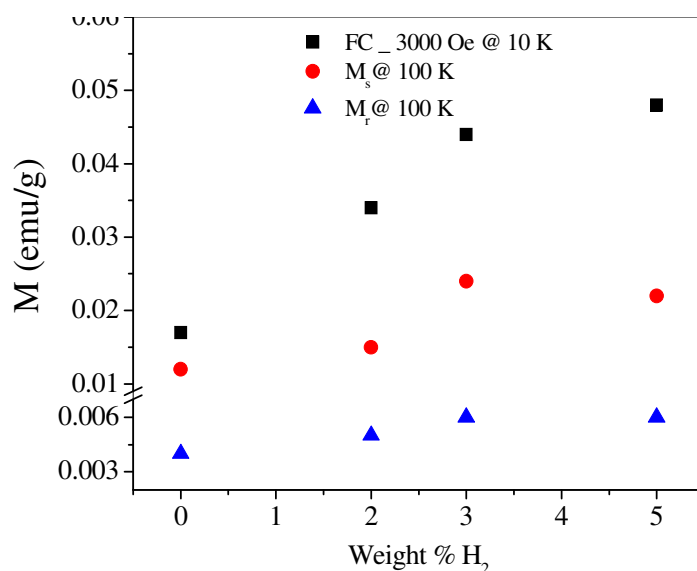
Figure 15: Comparison of the magnetic properties of hydrogenated few-layer graphenes (HGH_1, HGH_2 and HGH_3) with pristine sample (HG).

Table 2. Magnetic properties of the hydrogenated graphene samples.

Sample name	Wt (%) of hydrogen	M (emu/g) (FC @ 10 K)		Saturation magnetization (M_s)	
		3000 Oe	1 T	100 K	300 K
HG		0.017	0.025	0.012	0.01
HGH_1	2	0.034	0.07	0.015	0.012
HGH_2	3	0.044	0.092	0.024	0.02
HGH_3	5	0.048	0.099	0.022	0.016
HGH_2_DH	-	0.038	0.048	0.019	0.015

This observation confirms that the increase in the magnetic properties arises from hydrogenation. On dehydrogenation these properties revert back to those of the starting graphene samples. The large reversible concentration-dependent effects of adsorbing TTF, TCNE and hydrogen on the magnetic properties of graphene lend additional evidence to the fact that the magnetic properties of the graphene samples observed by us are intrinsic to them.

1.3.5: Conclusions

In conclusion, graphene samples prepared by different methods show prominent ferromagnetic features along with the antiferromagnetic characteristics. The value of magnetization as well as the other magnetic properties varies from sample to sample. All the graphene samples exhibit room-temperature magnetic hysteresis. Magnetization of graphene could be tuned by the adsorption of molecules. The value of the magnetization drastically decreases on adsorption of TTF and TCNE, having greater effect in the case of

1.3: Magnetic properties of graphene

TTF. Hydrogenation of graphene, gives rise to an increase in the values of the magnetic

properties with the increase in hydrogen content.

1.3.6 References

[1]   a)T. Enoki, K. Takai, *Dalton Trans.* **2008**, 3773-3781; b)T. Enoki, Y. Kobayashi, K. Fukui, *Int. Rev. Phys. Chem.* **2007**, *26*, 609-645.

[2]   a)K. W. Mitsutaka Fujita, Kyoko Nakada and Koichi Kusakabe, *J. Phys. Soc. Jpn.* **1996**, *65* 1920-1923; b)K. Nakada, M. Fujita, G. Dresselhaus, M. S. Dresselhaus, *Phys. Rev. B* **1996**, *54*, 17954.

[3]   K. Wakabayashi, M. Fujita, H. Ajiki, M. Sigrist, *Phys. Rev. B* **1999**, *59*, 8271-8282.

[4]   J. Fernandez-Rossier, J. J. Palacios, *Phys. Rev. Lett.* **2007**, *99*, 177204.

[5]   O. V. Yazyev, L. Helm, *Phys. Rev. B* **2007**, *75*, 125408.

[6]   O. V. Yazyev, *Phys. Rev. Lett.* **2008**, *101*, 037203.

[7]   a)R. Singh, P. Kroll, *J. Phys.-Condes. Matter* **2009**, *21*, 196002; b)M. M. Ugeda, I. Brihuega, F. Guinea, J. M. Gomez-Rodriguez, *Phys. Rev. Lett.* **2010**, *104*, 096804.

[8]   S. Bhowmick, V. B. Shenoy, *J. Chem. Phys.* **2008**, *128*, 244717.

[9]   L. Z. Kou, C. Tang, W. L. Guo, C. F. Chen, *Acs Nano* **2011**, *5*, 1012.

[10]   G. H. Li, A. Luican, J. dos Santos, A. H. C. Neto, A. Reina, J. Kong, E. Y. Andrei, *Nat. Phys.* **2009**, *6*, 109.

[11]   O. E. Andersson, B. L. V. Prasad, H. Sato, T. Enoki, Y. Hishiyama, Y. Kaburagi, M. Yoshikawa, S. Bandow, *Phys. Rev. B* **1998**, *58*, 16387.

[12]   V. L. J. Joly, K. Takahara, K. Takai, K. Sugihara, T. Enoki, M. Koshino, H. Tanaka, *Phys. Rev. B* **2010**, *81*, 115408.

[13]   Y. Shibayama, H. Sato, T. Enoki, M. Endo, *Physical Review Letters* **2000**, *84*, 1744.

[14]   Y. Kopelevich, R. R. da Silva, J. H. S. Torres, A. Penicaud, T. Kyotani, *Phys. Rev. B* **2003**, *68*, 092408.

[15]   a)N. Theodoropoulou, A. F. Hebard, M. E. Overberg, C. R. Abernathy, S. J. Pearton, S. N. G. Chu, R. G. Wilson, *Phys. Rev. Lett.* **2002**, *89*, 107203; b)S. Chaudhary, M. K. Chattopadhyay, K. J. Singh, S. B. Roy, P. Chaddah, E. V. Sampathkumaran, *Phys. Rev. B* **2002**, *66*, 014424.

[16]   J. Dho, W. S. Kim, N. H. Hur, *Phys. Rev. Lett.* **2002**, *89*, 027202.

[17]   H. Pardo, R. Faccio, F. M. Araújo-Moreira, O. F. de Lima, A. W. Mombrú, *Carbon* **2006**, *44*, 565-569.

[18]   Mombr, uacute, A. W., H. Pardo, R. Faccio, O. F. de Lima, E. R. Leite, G. Zanelatto, A. J. C. Lanfredi, C. A. Cardoso, Ara, F. M. jo-Moreira, *Phys. Rev. B* **2005**, *71*, 100404.

[19]   N. S. Souza, S. Sergeenkov, C. Speglich, V. A. G. Rivera, C. A. Cardoso, H. Pardo, A. W. Mombru, A. D. Rodrigues, O. F. de Lima, F. M. Araujo-Moreira, *Appl. Phys. Lett.* **2009**, *95*, 233120-233123.

[20]   P. Esquinazi, A. Setzer, ouml, R. hne, C. Semmelhack, Y. Kopelevich, D. Spemann, T. Butz, B. Kohlstrunk, M. sche, *Phys. Rev. B* **2002**, *66*, 024429.

[21]   P. Esquinazi, D. Spemann, ouml, R. hne, A. Setzer, K. H. Han, T. Butz, *Phys. Rev. Lett.* **2003**, *91*, 227201.

[22]   M. A. Ramos, J. Barzola-Quiquia, P. Esquinazi, Mu, ntilde, A. oz-Martin, A. Climent-Font, Garc, iacute, H. a, aacute, M. ndez, *Phys. Rev. B*, *81*, 214404.

[23]   H. Xia, W. Li, Y. Song, X. Yang, X. Liu, M. Zhao, Y. Xia, C. Song, T.-W. Wang, D. Zhu, J. Gong, Z. Zhu, *Adv. Mater.* **2008**, *20*, 4679-4683.

[24]   J. Barzola-Quiquia, P. Esquinazi, M. Rothermel, D. Spemann, T. Butz, Garc, iacute, N. a, *Phys. Rev. B* **2007**, *76*, 161403.

[25]   H. Ohldag, T. Tyliszczak, ouml, R. hne, D. Spemann, P. Esquinazi, M. Ungureanu, T. Butz, *Phys. Rev. Lett.* **2007**, *98*, 187204.

[26]   S. Talapatra, P. G. Ganesan, T. Kim, R. Vajtai, M. Huang, M. Shima, G. Ramanath, D. Srivastava, S. C. Deevi, P. M. Ajayan, *Phys. Rev. Lett.* **2005**, *95*, 097201.

[27]   J. Cervenka, M. I. Katsnelson, C. F. J. Flipse, *Nat Phys* **2009**, *5*, 840-844.

[28]   K. h. Han, D. Spemann, P. Esquinazi, R. Höhne, V. Riede, T. Butz, *Adv. Mater.* **2003**, *15*, 1719-1722.

[29]   N. Parkansky, B. Alterkop, R. L. Boxman, G. Leitus, O. Berkh, Z. Barkay, Y. Rosenberg, N. Eliaz, *Carbon* **2008**, *46*, 215-219.

[30]   Y. Wang, Y. Huang, Y. Song, X. Y. Zhang, Y. F. Ma, J. J. Liang, Y. S. Chen, *Nano Lett.* **2009**, *9*, 220.

[31]   C. S. Rout, A. Kumar, N. Kumar, A. Sundaresan, T. S. Fisher, *Nanoscale*, *3*, 900-903.

[32]   J. Hong, S. Niyogi, E. Bekyarova, M. E. Itkis, P. Ramesh, N. Amos, D. Litvinov, C. Berger, W. A. de Heer, S. Khizroev, R. C. Haddon, *Small* **2011**, *7*, 1175.

[33]   S. Niyogi, E. Bekyarova, J. Hong, S. Khizroev, C. Berger, W. de Heer, R. C. Haddon, *J. Phys. Chem. Lett* **2011**, 2487-2498.

[34]   H. Sato, N. Kawatsu, T. Enoki, M. Endo, R. Kobori, S. Maruyama, K. Kaneko, *Solid State Communications* **2003**, *125*, 641-645.

[35]   S. Hao, K. Takai, K. Feiyu, T. Enoki, *Carbon* **2008**, *46*, 110-116.

[36]   K. Takai, S. Eto, M. Inaguma, T. Enoki, H. Ogata, M. Tokita, J. Watanabe, *Phys. Rev. Lett.* **2007**, *98*, 017203.

[37]   T. Enoki, K. Takai, *Dalton Trans.* **2008**, 3773.

[38]   T. Makarova, F. Palacio, *Carbon Based Magnetism (Elsevier, Amsterdam, 2006).*

[39]   L. Xie, X. Wang, J. Lu, Z. Ni, Z. Luo, H. Mao, R. Wang, Y. Wang, H. Huang, D. Qi, R. Liu, T. Yu, Z. Shen, T. Wu, H. Peng, B. Ozyilmaz, K. Loh, A. T. S. Wee, Ariando, W. Chen, *Appl. Phys. Lett.* **2011**, *98*, 193113.

[40]   M. J. Schmidt, D. Loss, *Physical Review B* **2010**, *82*, 13.

[41]   J. Zhou, Q. Wang, Q. Sun, X. S. Chen, Y. Kawazoe, P. Jena, *Nano Lett.* **2009**, *9*, 3867.

[42]   A. Ranjbar, M. S. Bahramy, M. Khazaei, H. Mizuseki, Y. Kawazoe, *Phys. Rev. B* **2010**, *82*, 165446.

[43]   W. F. Li, M. W. Zhao, X. A. Zhao, Y. Y. Xia, Y. G. Mu, *Phys. Chem. Chem. Phys.* **2010**, *12*, 13699.

[44]   E. H. Hwang, S. Das Sarma, *Phys. Rev. B* **2009**, *80*, 5.

[45]   J. F. Zou, G. J. Jin, Y. Q. Ma, *J. Phys.-Condes. Matter* **2009**, *21*, 6.

[46]   M. Nishioka, A. M. Goldman, *Appl. Phys. Lett.* **2007**, *90*, 252505-252505-252503.

[47]   W. Han, W. H. Wang, K. Pi, K. M. McCreary, W. Bao, Y. Li, F. Miao, C. N. Lau, R. K. Kawakami, *Phys. Rev. Lett.* **2009**, *102*, 4.

[48]   W. Han, K. Pi, K. M. McCreary, Y. Li, J. J. I. Wong, A. G. Swartz, R. K. Kawakami, *Phys. Rev. Lett.* **2010**, *105*, 4.

[49]   B. E. Feldman, J. Martin, A. Yacoby, *Nat. Phys.* **2009**, *5*, 889-893.

[50]   A. L. Friedman, J. L. Tedesco, P. M. Campbell, J. C. Culbertson, E. Aifer, F. K. Perkins, R. L. Myers-Ward, J. K. Hite, C. R. Eddy, G. G. Jernigan, D. K. Gaskill, *Nano Lett.* **2010**, *10*, 3962-3965.

[51]   X. Hong, S. H. Cheng, C. Herding, J. Zhu, *Phys. Rev. B* **2011**, *83*, 5.

[52]   S. Pisana, P. M. Braganca, E. E. Marinero, B. A. Gurney, *Nano Lett.* **2009**, *10*, 341-346.

[53]   S. K. Saha, M. Baskey, D. Majumdar, *Adv. Mater.* **2010**, *22*, 5531-5536.

[54]   M. G. Zeng, Y. P. Feng, G. C. Liang, *Nano Lett.* **2011**, *11*, 1369-1373.

[55]   F. Munoz-Rojas, J. Fernandez-Rossier, J. J. Palacios, *Phys. Rev. Lett.* **2009**, *102*, 4.

[56]   J. W. Bai, R. Cheng, F. X. Xiu, L. Liao, M. S. Wang, A. Shailos, K. L. Wang, Y. Huang, X. F. Duan, *Nat. Nanotechnol.* **2010**, *5*, 655-659.

[57]   Y. Kopelevich, P. Esquinazi, J. H. S. Torres, S. Moehlecke, *Journ. Low Temp.Phys.* **2000**, *119*, 691.

[58]   aT. L. Makarova, B. Sundqvist, R. Hohne, P. Esquinazi, Y. Kopelevich, P. Scharff, V. A. Davydov, L. S. Kashevarova, A. V. Rakhmanina, *Nature* **2001**, *413*, 716-718; bT. L. Makarova, K. H. Han, P. Esquinazi, R. R. d. Silva, Y. Kopelevich, I. B. Zakharova, *Carbon* **2003**, *41*, 1575.

[59]   T. Enoki, N. Kawatsu, Y. Shibayama, H. Sato, R. Kobori, S. Maruyama, K. Kaneko, *Polyhedron* **2001**, *20*, 1311-1315.

[60]   Y. Shibayama, H. Sato, T. Enoki, M. Endo, *Phys. Rev. Lett.* **2000**, *84*, 1744.

[61]   O. E. Andersson, B. L. V. Prasad, H. Sato, T. Enoki, Y. Hishiyama, Y. Kaburagi, M. Yoshikawa, S. Bandow, *Physical Review B* **1998**, *58*, 16387.

[62]   S. Stankovich, D. A. Dikin, R. D. Piner, K. A. Kohlhaas, A. Kleinhammes, Y. Jia, Y. Wu, S. T. Nguyen, R. S. Ruoff, *Carbon* **2007**, *45*, 1558-1565.

[63]   R. Voggu, B. Das, C. S. Rout, C. N. R. Rao, *J. Phys.: Condens. Matter* **2008**, *20*, 472204.

[64]   H. Sata, N. Kawatsu, T. Enoki, M. Endo, R. Kobori, S. Maruyama, K. Kaneko, *Solid State Commun.* **2003**, *125*, 641.

[65]   S. Hao, K. Takai, F. Kang, T. Enoki, *Carbon* **2008**, *46*, 110.

[66]   K. Takai, S. Eto, M. Inaguma, T. Enoki, H. Ogata, M. Tokita, J. Watanabe, *Phys. Rev. Lett.* **2007**, *98*, 017203.

1.4: Interaction of graphene with electron donor organic molecules

Summary[*]

Investigations of quenching of fluorescence of organic donor molecules by graphene have been carried out with pyrene butanoic acid succinimidyl ester (**PyBS, I**) and oligo (*p*-phenylenevinylene) methyl ester (**OPV-ester, II**). Absorption and photoluminescence spectra of **I** and **II** recorded in mixture with increasing the concentrations of graphene showed no change in the former, but remarkable quenching of fluorescence in the latter. On the basis of fluorescence decay and time-resolved transient absorption spectroscopic measurements quenching of fluorescence of these two aromatic molecules by graphene is found to be associated with photo-induced electron transfer.

Covalent functionalization of graphene with an organic donor, oligo (phenylenevinylene) (OPV) has been examined. We present morphological proof for the unprecedented self-organization of these hybrids into higher order assemblies, with a periodic spacing of ~2.3 nm, intercalated with OPV molecules. After systematic characterization of the resulting hybrid material, we provide unequivocal proof for possible electronic communication between the donor OPV molecules and the graphene sheets. The extent of functionalization and degree of fluorescence quenching were determined by hydrolyzing the **EG-OPV** hybrid. We also discuss the formation of head-to-tail cyclo-addition dimer of OPV molecules possibly due to the topochemical constraint set by the assembled **EG-OPV**.

1.4: Interaction of graphene with electron donor organic molecules

1.4.1: Introduction

Graphene has generated great sensation in the last few-years because of its fascinating properties and potential applications.[1] Apart from the interesting and rich physics in graphene, its chemical and other properties are also equally interesting.[1a, 1b, 1d] As discussed in the introduction to graphene, its mechanical, optical and electronic properties are of significant importance. In many of these investigations, it becomes necessary to prepare dispersions of graphene in organic or aqueous media.[2] For this purpose, different approaches have been successfully employed for few-layer graphene. The two main approaches for obtaining is either covalent functionalization or by non-covalent interactions. There has been some recent effort to carry out covalent and non-covalent functionalization of graphene with aromatic molecules, which helps to modify its electronic properties, exfoliate and stabilize the individual graphene sheets.[3] Here is the review of some of the important approaches used in the literature.

Non-covalent functionalization of graphene is interesting, as it does not affect the electronic structure and planarity of this 2D material. Stable aqueous dispersions of polymer-coated graphitic nanoplatelets can be prepared through an exfoliation and *in situ* reduction of graphite oxide in the presence of poly(sodium 4-styrenesulfonate).[4] Graphene can be functionalized through noncovalent modification by different methods such as wrapping with PEG and other surfactants. Wrapping with PEG gives water-soluble graphene. Rao et al. reported the noncovalent functionalization and solubilization of graphene by employing several reagents, such as different surfactants and large aromatic molecules. By employing a variety of surfactants, in particular Igepal CO-890 [polyoxyethylene (40) nonylphenyl ether] (IGP), solubilization of few-layer graphene in water has been accomplished. By using 1-

pyrenebutanoic acid succinimidyl ester, PYBS, one large aromatic system, solubilization of graphene has been induced in dimethylformamide through π–π interactions.[3f] Recently, interaction of electron-donor and -acceptor molecules with graphenes has been exploited to modify the electronic properties of graphene through ground-state charge-transfer.[5]

Haddon and coworkers[6] functionalized graphene with long chain hydrocarbons. Oxidative treatment of microcrystalline graphite with nitric and sulfuric acid produce oxidized graphite, which contain –OH and –COOH groups and readily soluble in water. Treatment with $SOCl_2$ converts these acidic functionalities to –COCl groups. Further treatment with octadecylamine (ODA) provides a way to introduce long hydrocarbon chains as graphene–ODA is soluble in polar solvents. Rao and coworkers [3f, 7] have studied this method of functionalization with different graphene samples. The wet chemical exfoliation of graphite in association with an in situ covalent functionalization of intermediately generated graphene was accomplished by coupling reductive graphite activation with oxidative arylation by organic aryldiazonium salts in a one-pot reaction.[8] These covalent functionalization gives the solubility alone, if we can attach another functional molecule to the graphene leads to hybrid materials. Hybrid materials of graphene have the advantage of multifunctionality comprising properties of both graphene and the functionalizing agent.[2b, 3i, 9] Organic-solution-processable functionalized-graphene hybrid material with porphyrins has been synthesized and studied for its, photophysical and optical-limiting properties.[9a] Covalent functionalization of graphene with porphyrin and fullerene enhanced the non-linear optical (NLO) performance in the nanosecond regime.[9b] Aryl radical functionalization of epitaxial graphene has opened the band gap of graphene and also show disorder induced

magnetism in the graphene sheet with antiferromagnetic regions mixed with superparamagnetic and ferromagnetic clusters.[2a]

1.4.2: Scope of the Present Investigations

Quenching of fluorescence of aromatic molecules by graphene due to electron transfer: Fluorescence quenching is one of the important property of graphene to be studied and has been made use for the selective detection of biomolecules[10], in sensors and for other purposes.[11] Excited-state photophysical processes between nanocarbons such as SWNTs and fullerenes with donor and acceptor molecules have been of immense interest, because of their relevance to photovoltaics.[12] Adducts of SWNTs with pyrene and porphyrin are shown to exhibit fast electron transfer leading to long-lived charge separated states.[13] Polycyclic aromatic molecules such as perylene and coronene are known to interact with graphene enabling non-covalent functionalization of graphene[3a, 3f], but photophysical aspects of such systems have not been explored. Quenching of the fluorescence of porphyrin by graphene and photophysical properties of porphyrin-graphene complexes have been reported [14], but the mechanism of quenching of fluorescence by graphene has not been examined adequately, although it is believed that electron or energy transfer between graphene and the aromatic molecule would be responsible for the phenomenon. Theoretical studies show that long-range energy transfer is operative in the fluorescence quenching of a dye molecule in the presence of graphene.[15] The quenching of the green emission of ZnO nanoparticles accompanying the photoreduction of graphene oxide is, however caused by electron transfer from ZnO. Electron transfer has been similarly invoked in the case of TiO_2-graphene oxide.[11b] We were interested in investigating the mechanism of quenching the

fluorescence of aromatic molecules by graphene to find out whether it occurs via electron or energy transfer. With this purpose, we have investigated the quenching of fluorescence of two aromatic molecules by non-covalent interaction with graphene and demonstrated the occurrence of intermolecular photo-induced electron transfer. Specifically, we have examined the interaction of graphene with pyrene-butanaoic acid succinimidyl ester, (PyBS), I , and oligo(*p*-phenylenevinylene) methyl ester (OPV-ester), II ,shown in scheme 1 with a graphene derivative, EGA, which is soluble in chloroform and dimethylformamide (DMF).

Covalently Linked Graphene-Oligo(phenylenevinylene) Adduct: Molecular functionalization of graphene, resulting in its solubilization and assembly, plays a crucial role in exploring applications in nano-electronic devices and other areas. Excited-state processes involving graphene and chromophoric electron donors such as oligo(phenylenevinylene) (OPV) [3b, 3g, 16] and porphyrin and the concomitant photo-induced electron transfer process from the chromophore to graphene have also been reported, which could be of value in the design of photovoltaics,.[3b-e] We consider it worthwhile to carry out the covalent functionalization of graphene with electron donor molecules using reaction protocols similar to those established in the case of carbon nanotubes,[2a, 8, 14a, 17] and examine the structural and spectroscopic aspects of the resulting hybrid materials. We report a novel hybrid obtained by covalently integrating electron-rich oligo(phenylenevinylene) amine   (**OPV-amine**) into graphene and its structure, reactivity as well as photo-physical properties.

1.4.3: Experimental section

The graphene derivative soluble in chloroform and DMF was prepared as follows. Graphite oxide (GO), synthesized by employing the literature procedure, was subjected to thermal

exfoliation in a furnace preheated to 1050 °C under argon flow to obtain few-layer graphene (**EG**).[18] Acid functionalized graphene (**EG-Acid**) was prepared by taking conc. nitric acid (2 ml), conc. sulfuric acid (2 ml) and water (16 ml) and adding the mixture to 50 mg of **EG**. The mixture was heated in a microwave oven for 10 min followed by overnight incubation in conventional oven at 100 °C. The product obtained was washed with distilled water and centrifuged repeatedly to remove traces of acid.

Quenching of fluorescence of aromatic molecules: The amide-functionalized graphene (EGA) was obtained by a two step process (i) refluxing with excess $SOCl_2$ for 12 h and the unreacted $SOCl_2$ removed under vacuum and (ii) product was treated with dodecylamine (5 ml) under solvothermal conditions at 100 °C. The obtained product was characterized by IR spectroscopy and other techniques.[3f] EGA was soluble in solvents like DMF and chloroform because of the long hydrocarbon chain attached to the graphene. **PyBS**, **I**, was purchased from Sigma-Aldrich and the **OPV-ester, II** was synthesized according to the literature procedure.[19]
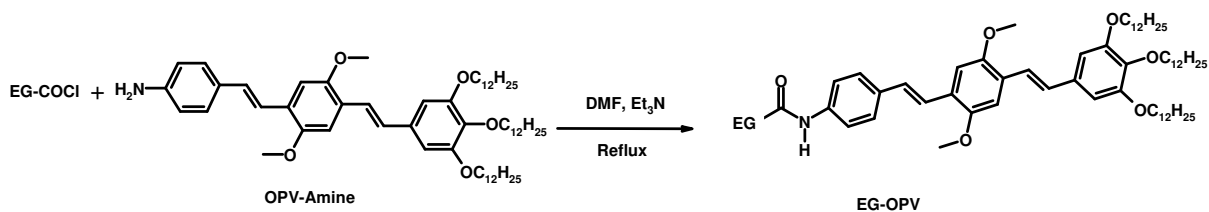

(I)   **(II)**
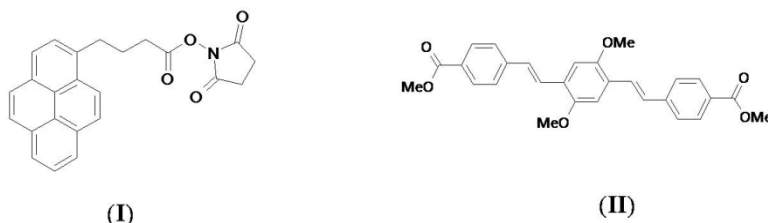
Scheme 1

Covalently Linked Graphene-Oligo(phenylenevinylene) Adduct: OPV-amine was synthesized according to the reported procedure.[20] **EG-OPV** hybrid was prepared by the reaction of **OPV-amine** with **EG-COCl** in dry N,N-dimethylformamide (DMF) and tri ethyl amine under reflux conditions for 24 hours.[21]

Scheme 2: Synthetic route for the **EG-OPV** hybrid.

Characterization

Optical absorption and photoluminescence spectroscopy:

UV-Vis spectra and fluoroscence spectra were recorded with a Perkin-Elmer Lambda 900 spectrometer and a Perkin-Elmer MPF 44B Fluorescence spectrophotometer respectively. UV-Vis spectra were recorded in 1 cm path length quartz cuvette.

Transient absorption spectroscopy:

Fluorescence decay was recorded in a time-correlated single-photon-counting spectrometer of Horiba-Jobin Yvon. Flash photolysis was carried out using a Nd:YAG laser source producing nanosecond pulses (8 ns) of 355 nm light with the energy of the laser pulse being around 200 mJ. Dichroic mirrors were used to separate the third harmonic from the second harmonic and the fundamental output of the Nd-YAG laser. The monitoring source was a 150 W pulsed xenon lamp, which was focused on the sample at 90° to the incident laser beam. The beam emerging through the sample was focused on to a Czerny-Turner monochromator using a pair of lenses. Detection was carried out using a Hamamatsu R-928 photomultiplier tube. Transient signals were captured with an Agilent infinium digital storage oscilloscope and the data was transferred to the computer for further analysis.

Lifetime measurements:

Fluorescence decay was recorded in a time-correlated single-photon-counting spectrometer of Horiba-JobinYvon.

NMR spectroscopy:

^{1}H NMR was recorded on a Bruker AVANCE-400 MHz spectrometer at room temperature.

Infrared and Raman Spectroscopy:

Infrared spectra were recorded using Bruker IFS 66v/S spectrometer. Raman spectra of samples were recorded with a 633 nm Ar laser using JobinYvon Lab Ram HR spectrometer.

Transmission electron microscopy:

Transmission electron microscopy (TEM) images were obtained with a JEOL JEM 3010, operating with an accelerating voltage of 300 kV.

Atomic force microscopy:

AFM measurements were carried on Vecco digital instruments, di Innova.

1.4.4: Results and discussion

Quenching of fluorescence of aromatic molecules by graphene: The graphene sample contains 5 layers on average as determined by transmission electron microscopy (TEM) and atomic force microscopy. In Figure 1(a) we show the typical TEM image of the EG sample
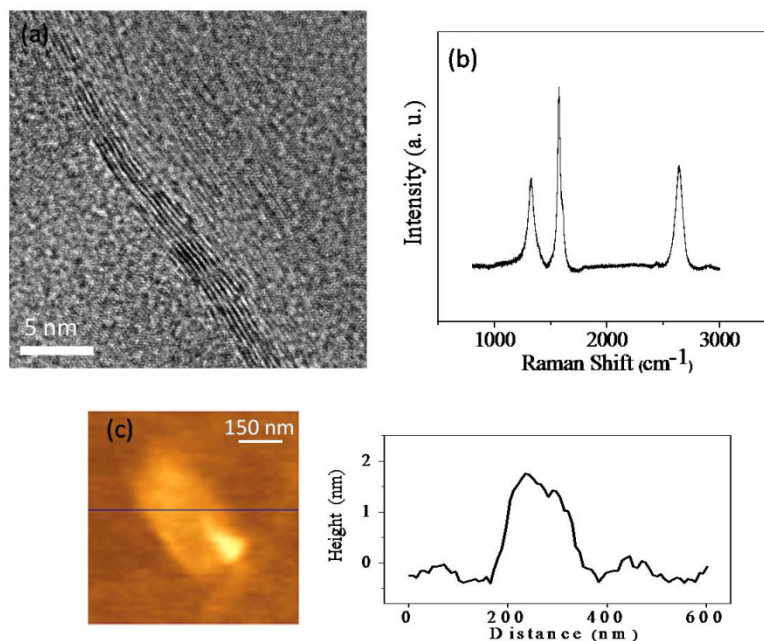
Figure 1: (a) TEM Image (b) Raman spectrum and (c) AFM image along with the height profiles of EG sample.

prepared. In the Figure 1(b) we have the Raman spectrum of EG showing D-, G- and 2D band which are characteristic for the graphene samples. Absorption spectra of **PyBS**, **I,** in DMF solution (10^{-5} M) in the presence of varying concentrations of graphene (EGA) are shown in Figure 2 (a). The spectra show characteristic absorption bands of **I** around 314, 328 and 344 nm, intensities of which show an apparent increase with the EGA concentration.

1.4: Interaction of graphene with electron donor organic molecules

However, on subtracting the pyrene absorption, we obtain a broad band around 270 nm corresponding to the absorption band of graphene. In the Figure 2 (b), we show the
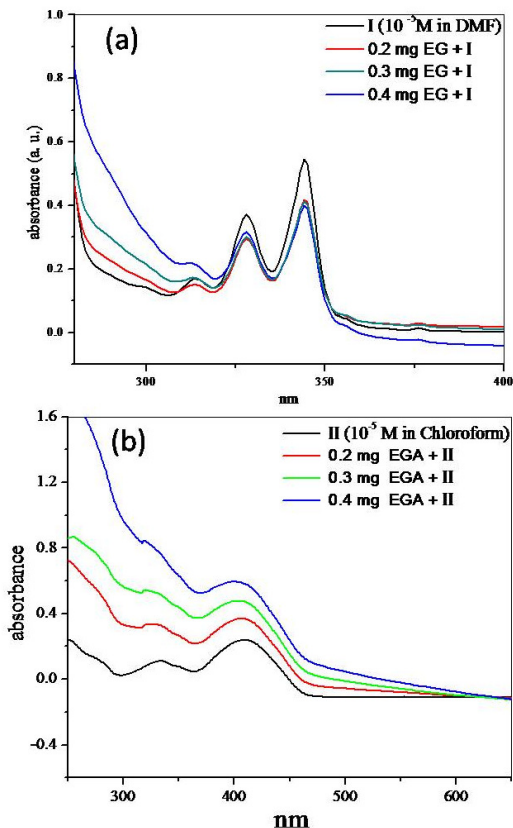
Figure 2: Electronic absorption spectra of (a) **PyBS, I,** $(10^{-5}$ M in DMF) and (b) **OPV ester**, **II**, $(10^{-5}$ M in chloroform) with increasing concentration of graphene (EGA).

electronic absorption spectrum of **OPV ester**, **II** , in chlororform solution $(10^{-5}$ M) as a function of EGA concentration. The **OPV ester** exhibits characteristic absorption bands at 332 nm and 406 nm.[19] The increase in intensities of these bands with the graphene concentration is entirely accounted for the increasing intensity of the graphene absorption band around 270 nm. Thus, electronic absorption spectra of **I** + EGA and **II** + EGA show no evidence of interaction between the two molecules in the ground state and besides this there are no absorption bands attributable to charge-transfer.

Unlike the absorption spectra, fluorescence spectra of **I** and **II** show remarkable changes on the addition of EGA. The intensity of the fluorescence bands decrease markedly

with the increase in EGA concentration as illustrated in the Figure 3. We find similar fluorescence quenching with rhodamine B as well as coronene derivatives. Such strong quenching of fluorescence of aromatics by graphene can only be due to an excited state

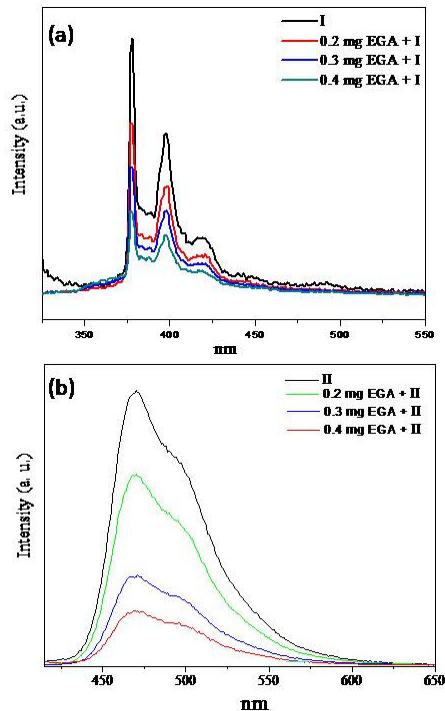
Figure 3: Fluorescence spectra of (a) **PyBS, I,** (10^{-5} M in DMF) and (b) **OPV ester**, **II**, (10^{-5} M in chloroform) with increasing concentration of graphene (EGA).

phenomenon since we do not observe ground state charge-transfer. In the Figure 4 we have shown the Stern–Volmer plots based on the temperature-variation study. There is a decrease in the quenching efficiency with increase in temperature suggesting that mainly a static mechanism is operative[22], possibly with a small dynamic contribution since the plots show an upward curvature.

Fluorescence decay measurements on **I** monitored at 395 nm could be fitted to a three-exponential decay[23] with lifetimes of 1.8, 5.7 and 38.7 ns. Addition of EGA causes a significant decrease in all the three lifetimes (Figure 5) with values 1.2, 4.6 and 29.1 ns respectively for the addition of 0.3 mg of EGA. A similar decrease in lifetime was observed in the case of **II** as well, though the actual decay profile showed slightly different features.

1.4: Interaction of graphene with electron donor organic molecules

Such multiexponential decay has been reported in the case of pyrene and porphyrin derivaties. [23-24]
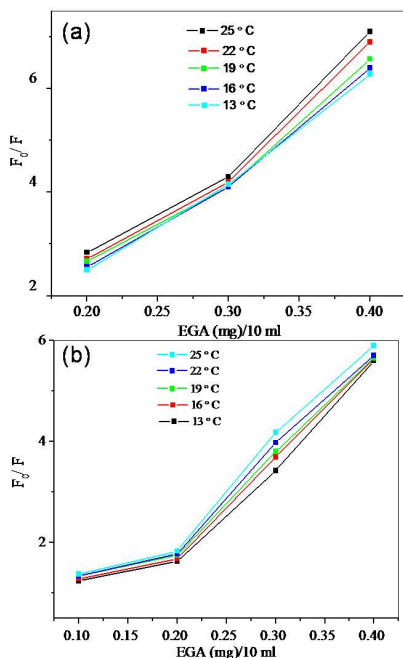
Figure 4: Stern-Volmer plots of (a) **PyBS, I,** $(10^{-5}$ M in DMF) and (b) **OPV ester**, **II**, $(10^{-5}$ M in chloroform) with different concentrations of graphene (EGA).

Considering that the observed fluorescence quenching and life-time changes could be due to an excited state photo-induced energy or electron transfer, we have carried out laser flash photolysis studies to explore the transient species. In Figure 6, we compare the transient absorption spectrum of the pure **I** with that of **I** on addition of 0.3 mg of graphene. The
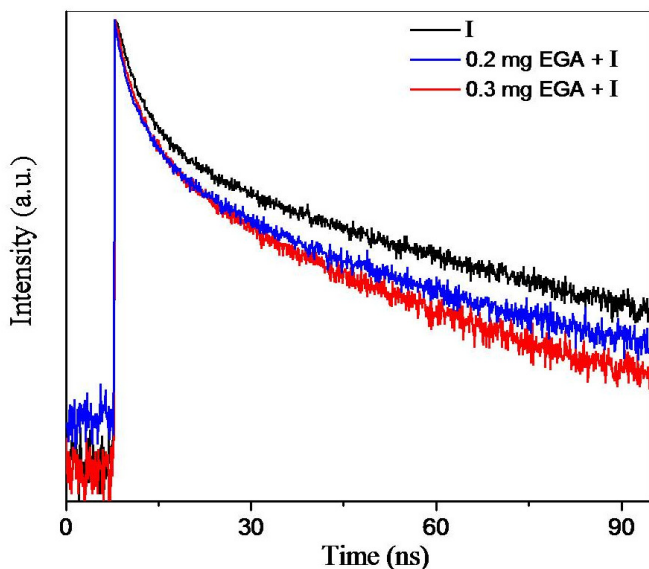
Figure 5: Effect of addition of graphene (EGA) on the fluorescence decay of **PyBS, I,** $(10^{-5}$ M in DMF) at room temperature.

106

spectrum of **PyBS** shows an absorption maximum around 430 nm together with a broad band

in the 450- 530 nm range due to the triplet state.[25] Upon addition of EGA, new bands
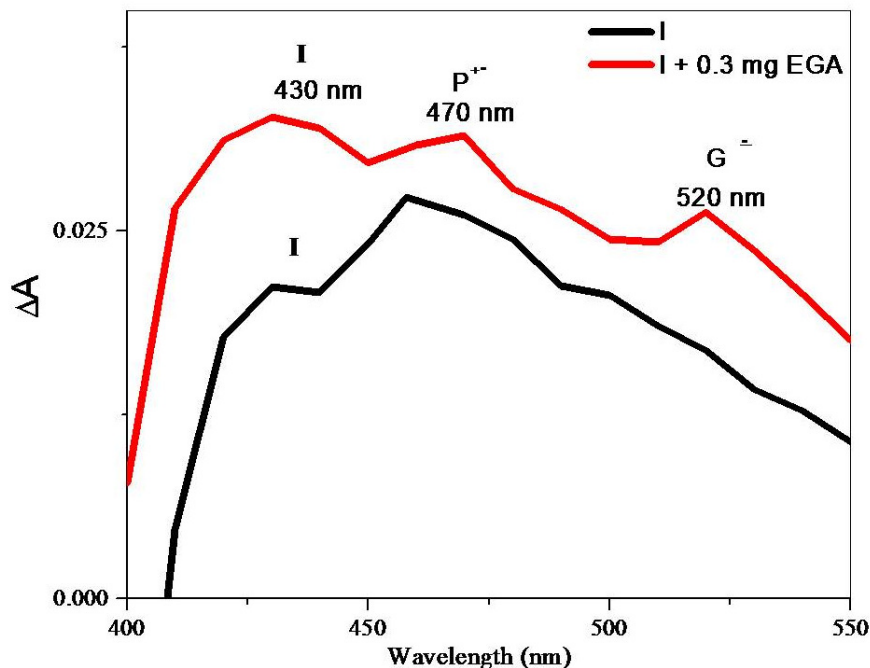
Figure 6: Effect of addition of EGA on the transient absorption spectrum of **PyBS**, **I**, (λ_{exc} = 355 nm) after 500 ns.

emerge around 470 and 520 nm in the transient absorption spectrum at 500 nanoseconds. The

470 nm band can be assigned to the pyrenyl radical cation($P^{+\cdot}$) as reported in the literature,[23]

suggesting the occurrence of photo-induced electron transfer from the **PyBS** to the graphene.
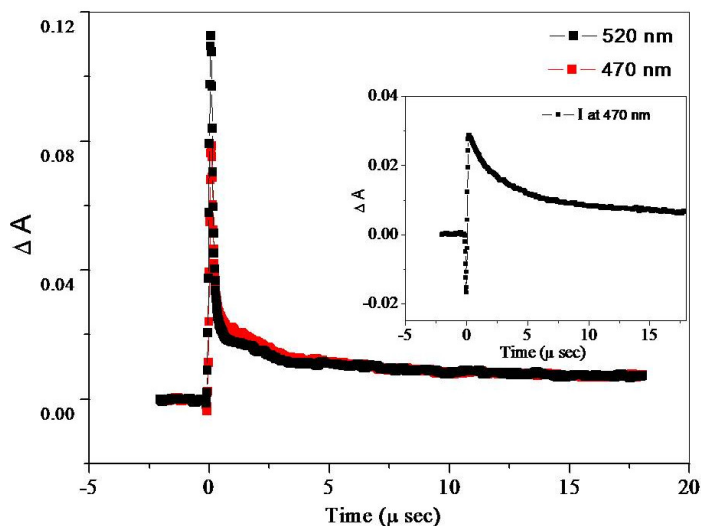
Figure 7: Life time decay of transient species of **PyBS** + EGA recorded at 470 and 520 nm. Inset shows the decay of pure **PyBS** at 470 nm.

1.4: Interaction of graphene with electron donor organic molecules

Accordingly, we observe the transient absorption around 520 nm which we assign to the graphene radical anion (G⁻). The decay of the radical cation formed in the presence of graphene was fast, as evidenced from the appearance of a short-lived component (900 ns) in the decay profile (Figure 7). However, the decay of the transient absorption of pure **PyBS** monitored at 470 nm (see inset of Fig.7) shows a long-lived triplet with a lifetime of 6.17 microseconds. The transient absorption at 520 nm decays simultaneously with that of the pyrene radical cation indicating that it is due to the graphene radical anion. The bi-exponential nature of the decay after the addition of graphene was observed even at longer wavelengths suggesting a broad absorption for the graphene radical anion with maximum at 520 nm, as observed in the transient spectrum.
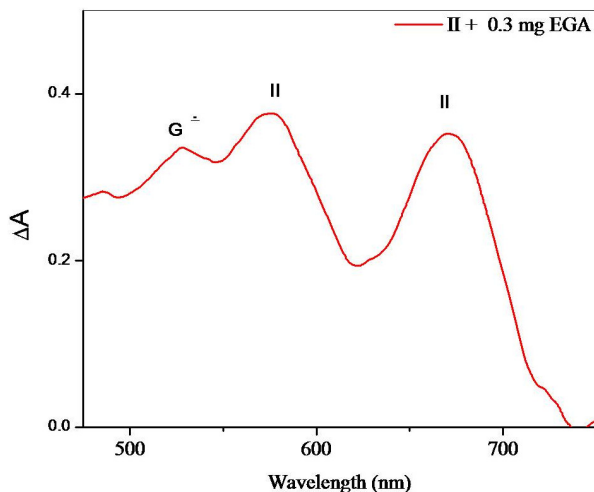
Figure 8: The transient absorption spectrum of **OPV ester** + EGA (λ_{exc} = 355 nm) after 1500 ps.

In order to investigate the intermolecular electron transfer from **II** to EGA, pico-second laser flash photolysis was performed on a mixture of EGA and the OPV ester. In Figure 8, we have shown the transient absorption spectra of **II** with EGA at 1500 ps. Transient absorption spectrum of pure OPV showed a maximum around 600 nm which could be attributed to the triplet state of the OPV following the literature.[26] The transient absorption observed at 690 nm is considered to be due to a singlet-singlet transition. Most

importantly, the transient spectrum at shorter time scales shows a band centered at $\lambda = 520$ nm which we attribute to the graphene radical anion just as in the case of **I**. The absorption band of the OPV radical cation appears in the near-infrared region (1450 nm).[27] Even though the main mechanism is electron-transfer in our systems, there might be chance of having energy transfer[15] as well, where both process are reported in some instances.

Covalently Linked Graphene-Oligo(phenylenevinylene) Adduct: The graphene sample that we used contains 5 layers on average and was prepared by thermal exfoliation of GO. The OPV molecule apart from serving as a useful probe also helps in the exfoliation of graphene layers, rendering the resulting hybrid solution-processable. Interestingly, we find that non-covalent π-π stacking interactions of the phenylenevinylene conjugated backbones results in the unprecedented organization of graphene sheets into bi- or few-layer hybrids sandwiched by OPV molecules.

The three dodecyl chains at the gallic wedge of the **OPV-amine** molecule were excepted to render the resulting material soluble in organic solvents. The OPV-graphene adduct (**EG-OPV**), in which the components are linked by amide bonds, was prepared by the reaction between the **OPV-amine** and acid chloride functionalized EG (**EG-COCl**), in dimethylformamide (Scheme 2).[21] **EG-OPV**, so obtained, was purified by washing several times with chloroform, followed by centrifugation, in order to ensure the complete removal of physically adsorbed OPV ligands, taking advantage of the higher solubility of **OPV-amine** in CHCl$_3$.

Figure 9(a) shows the IR spectra of **EG-acid** and **EG-OPV** which provide evidence for functionalization of graphene through amide bonds. The IR spectrum of **EG-acid** shows a band at 1632 cm^{-1}, due to the C=O stretching frequency of the carboxyl groups, which

shifts to a higher frequency in the corresponding acyl chloride derivative. The spectrum of **EG-OPV,** shows the characteristic amide I and II bands at 1572 and 1639 cm^{-1}, respectively. These observations clearly suggest the formation of the amide bond between **OPV-amine** and graphene. In Figure 9(b), we compare the Raman spectra of **EG-acid**
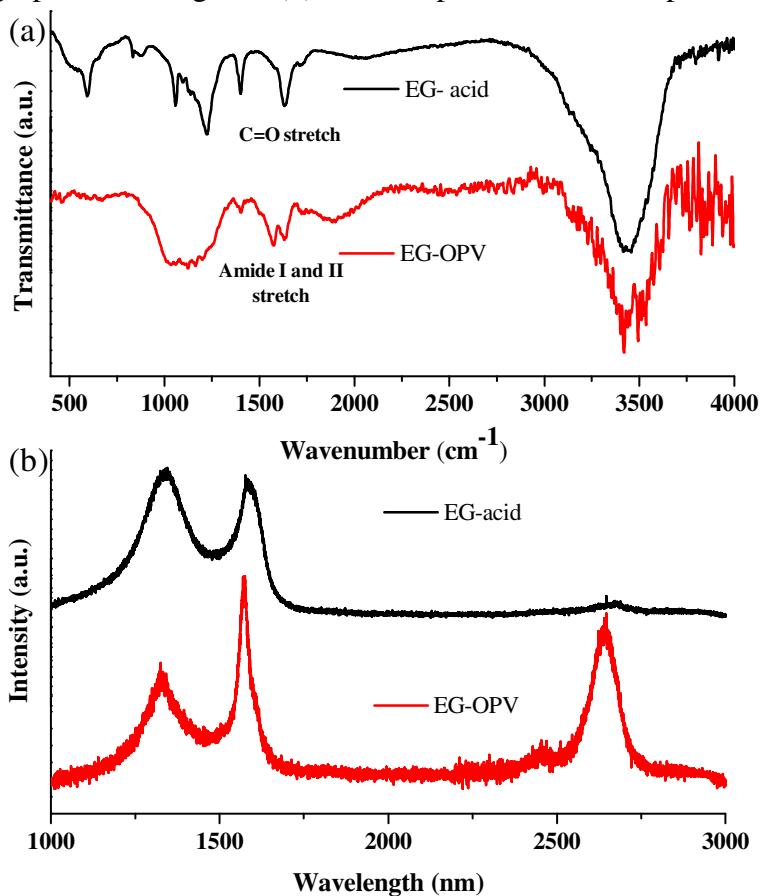
Figure 9: (a) FT-IR and (b) Raman spectra of **EG-acid** and **EG-OPV** hybrid.

and the **EG-OPV** hybrid. The Raman spectrum of **EG-acid** shows three bands namely D-, G- and 2D bands at 1342, 1585 and 2672 cm^{-1} respectively.[1c, 1d] In the case of **EG-OPV,** the G-band shifts to 1572 cm^{-1} while the 2D band appears at 2647 cm^{-1}.[5a] It is well studied and understood from the literature that there will be significant changes in the Raman spectra of graphene when it interacts with either donor or acceptor molecules. Raman G-bands soften on interaction with donor molecules where as it stiffens in the

case of acceptor molecules. From the above results it is clear that there is a softening in the G and 2D bands because the molecule attached is OPV which is a good donor. Softening of the G-band can be explained in terms of electron–phonon coupling in graphene which causes Kohn anomalies in the phonon dispersion which can give rise to phonon softening. Interestingly, the 2D Raman band becomes sharp accompanied by a large increase in the I2D/IG intensity ratio. This is clearly indicative of the decrease in the number of layers due to exfoliation. It is indeed well known that 2D band becomes prominent in single-layer graphene.[1c, 1d] Detailed microscopic studies of **EG-OPV** generated from DMSO solution shows the characteristic morphology of graphene. TEM images reveal the presence of mostly bi-and multi-layered sheets of the hybrids along with the stacked graphene sheets, with an interlayer spacing varying from 2-2.4 nm which is ~ 7 times higher than the usual layer separation in few-layer graphene (Figure 10 (a)).
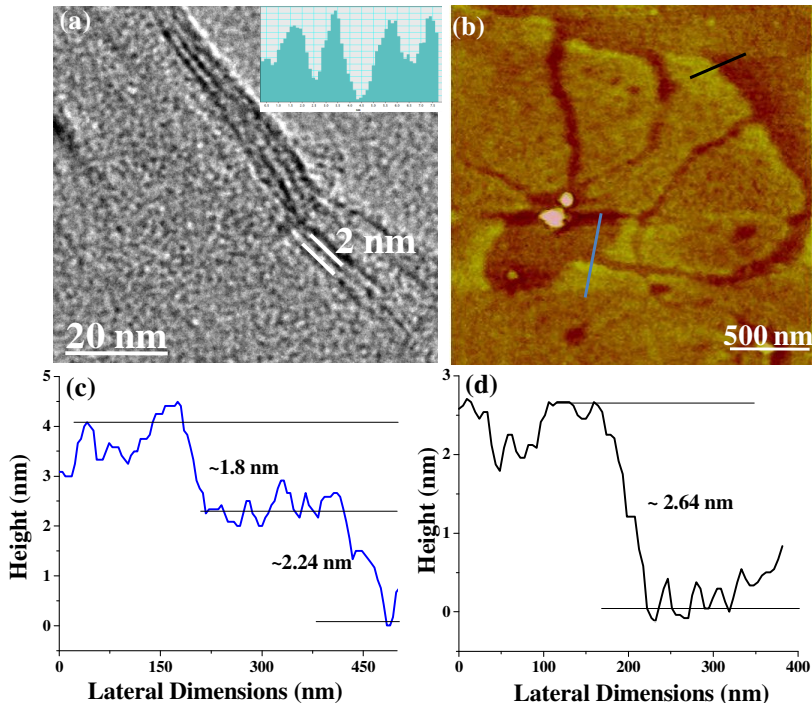
Figure 10: (a) TEM, (b) AFM image of EG-OPV hybrid, height profiles of black and blue lines are shown in (c) and (d) respectively.

AFM studies on the **EG-OPV** hybrid showed the formation of graphene sheets having lateral dimensions extended up to micrometers (Figure 10 (b)). The height profile shown in Figure 10 (c) corresponds to ~ 2.64 nm, which may be due to a single layer of **EG-OPV** hybrid. Further analysis of the **EG-OPV** hybrid at different places also revealed a step wise increase in the height profile as can be seen in Figure 10 (d). It is noteworthy that the step nearly corresponds to the length of the OPV rigid backbone. AFM, TEM and
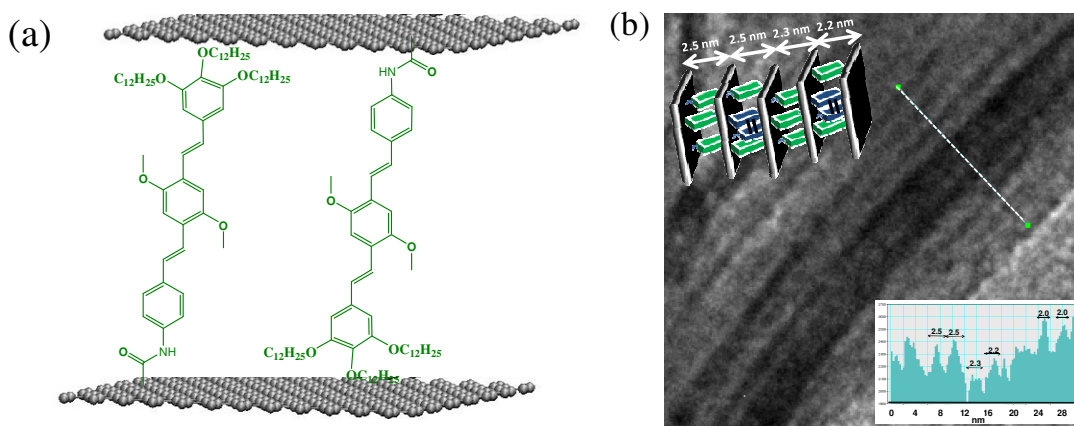
Figure 11: (a) Proposed molecular organization of OPV chromophores in the hybrid and (b) TEM of the layered graphene structures (insets of 'b' shows the interlayer distances across the white line and the graphic representation of the arrangement.)

Raman results suggest intercalation of the organic molecules between the graphene layers, by orienting perpendicular to the plane of the graphene as can be seen in the schematic (inset, Figure 11 (b)). Interestingly, a higher order organization of **EG-OPV** hybrid to multilayered sheets with ~ 2.4 nm spacing could also be visualized in the TEM images (Figure 11(b)). Organization of these hybrids could be driven by the π- π - stacking interactions between the interdigitated OPV-molecules, from neighboring sheets.[28] This argument firmly supports from the observation of topochemical

photodimerization of head-tail oriented OPV ligands of the two adjacent graphene sheets (Figure 11 (a), *vide infra*). In order to probe the interactions between OPV donor molecules and graphene in the hybrid, we have performed steady-state and time resolved photo-luminescence studies of the hybrids. The absorption spectrum of **EG-OPV** shows clear signatures of both EG and OPV absorptions. However, no new band attributable to a ground state charge transfer interaction is seen. Photoluminescence spectrum of the **EG-OPV** hybrid in DMSO shows very weak emission (see inset Figure 12 (a)) with maxima at 460 and 490 nm, when excited at 410 nm (Figure 12 (a)). These emission spectral features are characteristic of isolated OPV molecules, considering that red-shifted emission (~500-550 nm) of these molecules is

found in the presence of intermolecular interactions.[28] This suggests spatially dispersed attachment of OPV chromophores to the graphene, with a perpendicular
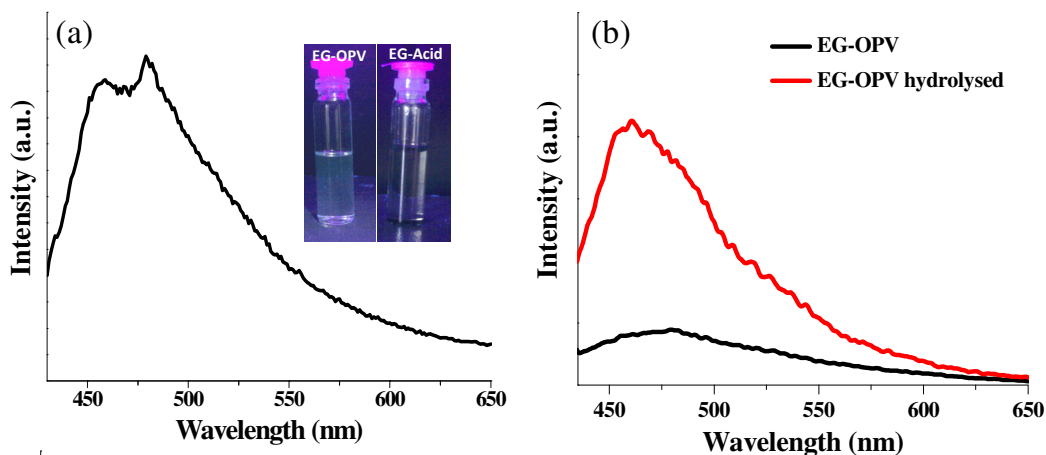
Figure 12: (a) Fluorescence spectrum of **EG-OPV** in DMSO, λ_{exc} = 410 nm (inset depicts the photographs of **EG-acid** and **EG-OPV** under UV illumination) and (b) the quenching quantification experiment of **EG-OPV**.

orientation of its molecular axis (free hanging) rather than a face-on orientation on the graphene plane, which is also supported by the microscopic analysis. The relative intensities of the emission bands are however, different compared to the standard amide

substituted OPV molecules (**OPV-B**) possibly due to the covalent functionalization.[8] The weak photoluminescence of the chromophore-graphene hybrids is attributed to fluorescence quenching of molecules by graphene.[3b, 29] In order to quantify the quenching, we have carried out *in-situ* hydrolysis of the **EG-OPV** hybrid in the cuvette using KOH, resulting in the turn on OPV fluorescence. We have quantified the quenching to be 78 % in the **EG-OPV** hybrid in DMSO (Figure 12(b)). This experiment allowed us to determine the number of OPV molecules attached to the graphene per unit weight. After comparing from a known concentration of **OPV-amine** we elucidated that 0.28 µM
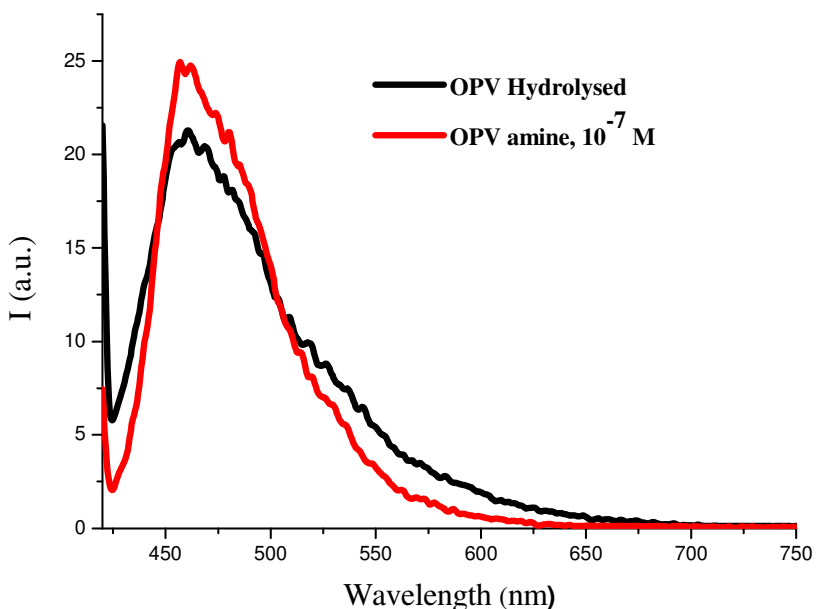
Figure 14: Emission spectra for quantification of functionalization.

of OPV is functionalized per mg of graphene sample (Figure 14). This corresponds to about 5.1×10^{14} molecules of OPV being bonded to 1 mg of graphene (~0.846 nmol of OPV per milligram of graphene).
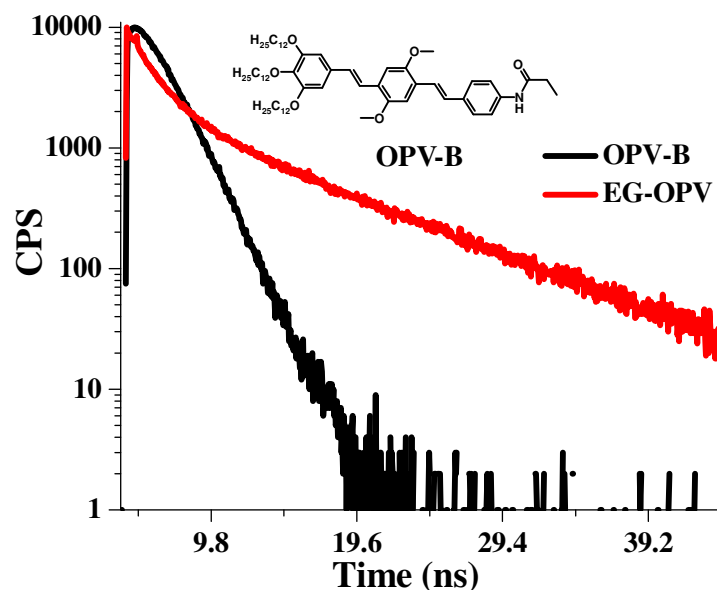
Figure 15: Time-resolved fluorescence decay profiles of the **EG-OPV** hybrid and **OPV-B** excited at 410 nm and emission collected at 500 nm. Inset shows the molecular structure of **OPV-B**

Such efficient quenching of OPV fluorescence indicates that there is a strong interaction between the excited state of OPV and graphene and could only be due to an excited state phenomenon since we do not observe any evidence for ground state charge-transfer from the absorption spectrum. Figure 15 shows the fluorescence decay profiles of the **EG-OPV** hybrid and the control sample **OPV-B** (OPV-amide), in DMSO (λ_{exc} = 410 nm) monitored at 500 nm. It can be clearly seen that **EG-OPV** decays in a multi exponential manner when compared to the mono exponential decay trace of nascent OPV (τ = 1.7 ns). Fluorescence decay measurements on the hybrid could be fitted to a bi-exponential decay with lifetimes of 0.6 and 1.6 ns. The decay of **EG-OPV** hybrid is clearly indicated by a short component and a long component. This multi-exponential decay, apart from being characteristic of hybrid carbon based materials, suggests of
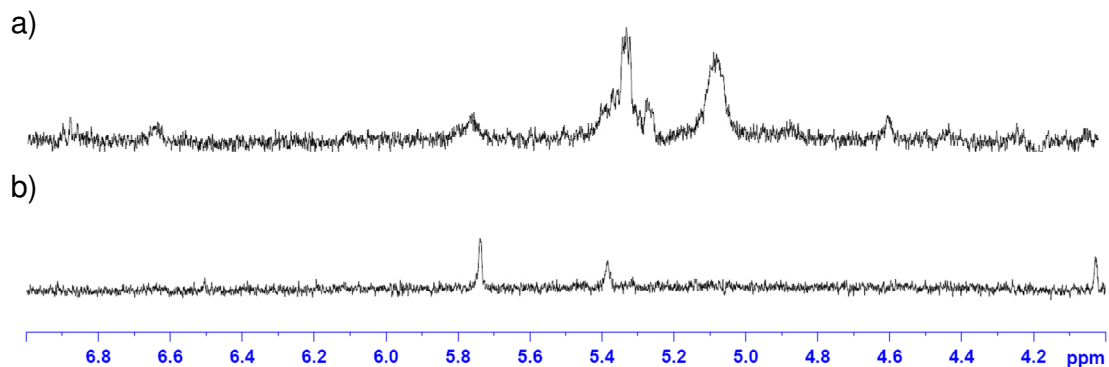
Figure 16: ^{1}H-NMR of a) Hydrolyzed OPV sample and b) EG-Acid clearly showing the cyclobutyl peaks in the former (marked in red).

electronic communication between OPV and graphene. Fluorescence quenching of the excited OPV can arise from photo-induced electron ransfer or energy transfer.[3b, 3e, 15]
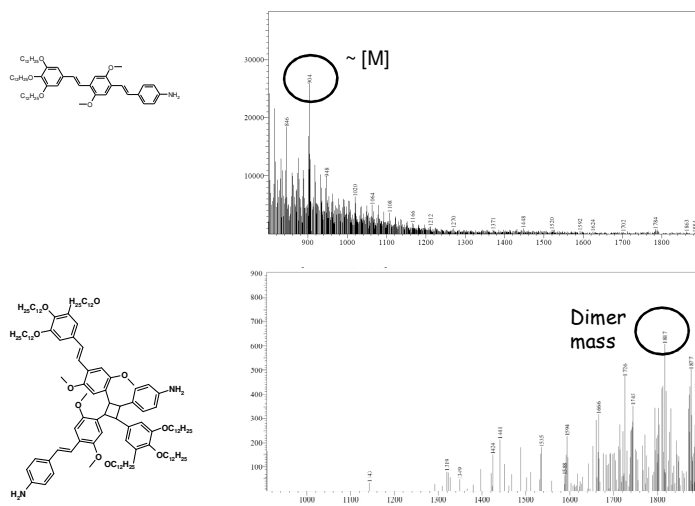
Figure 17: ESI-MS of Hydrolyzed OPV sample.

Similar photoluminescence quenching has been observed in non-covalent hybrids of graphene with OPVs, where an electron transfer mechanism has been shown to occur.[3b]

^{1}H-NMR and mass spectral analysis of the OPV obtained after the hydrolysis of **EG-OPV** showed the presence of dimeric species. Signatures of the cyclobutane methylene could be seen in the ^{1}H-NMR spectrum, indicating the likely occurrence of [2+2] cycloaddition of OPV (Figure:16 and 17).[30] The mass spectrum also showed peaks due to the dimeric species. The cycloaddition process was further evident from the detailed photophysical characterization of the hybrid. Presence of a lesser conjugated species was evident by the blue emission, with maxima around 410 nm and 425 nm, on excitation of the **EG-OPV** solution at 360 nm (Figure 18(a)). This emission is characteristic of less conjugated stilbene derivatives, which would be formed due to cycloaddition reaction.[30]
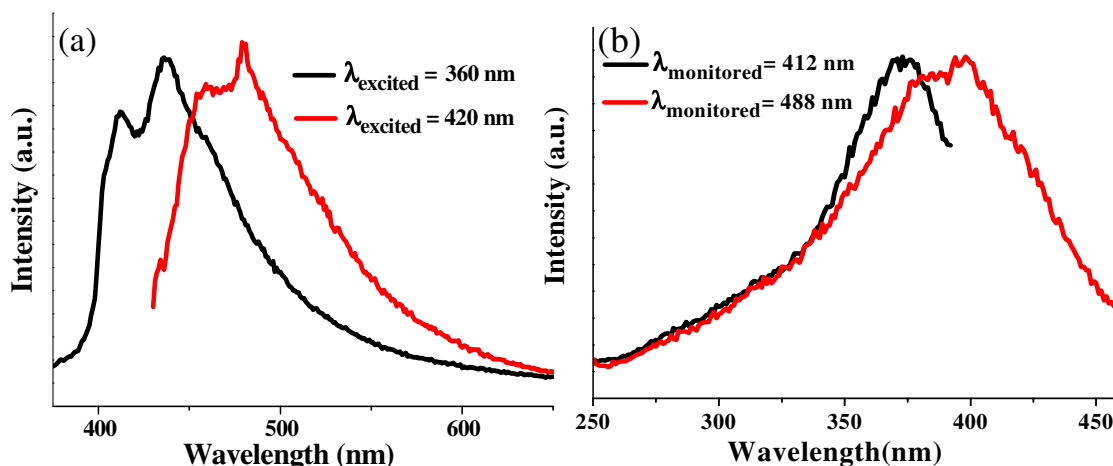
Figure 18: Normalized (a) Emission and (b) excitation spectra of **EG-OPV** hybrids.

Excitation spectra collected at this blue-emission (λ_{mon} = 412 nm) showed a maximum at 360 nm corresponding to the absorption of stilbene derivatives, which further confirmed its origin (Figure 18(b)). The dimerization reaction can result from the head-to-tail organization of the OPV molecules in the hybrid (as shown in Figure 11(a)), which brings the electron-rich and electron-deficient double bonds close to each other.

Additionally, though we do not have a direct proof for a head to tail dimeric species, topological considerations suggest that this is the only possible conformation. The formation of the cyclo-adduct also confirms the π- π interaction between the OPV molecules, which helps the organization of graphene-OPV hybrid sheets into multi-layers. This observation allows us to predict the possibility of using unprecedented aggregation tendency of graphene for bringing photo-labile groups together to procure hybrids with unique properties.

1.4.5: Conclusions

In summary, we observe efficient quenching of fluorescence of aromatic molecules by graphene. Our studies confirm the occurrence of photo-induced electron transfer between the aromatic molecules and graphene. Such electron-transfer has been observed in porphyrin-fullerene/nanohorn and pyrene-carbon nanotube systems. Occurrence of both electron transfer and energy transfer has been invoked by some workers to explain fluorescence quenching and we are not able to entirely preclude the occurrence of energy transfer in the systems studied by us. The charge separated species reported by us in which graphene acts as an acceptor are long-lived. This feature could be of value in the design of photovoltaics.

We have covalently functionalized graphene with oligo (phenylenevinylene). The conjugation results in exfoliation and electronic communication between the two components. In addition the intermolecular interactions and the perpendicular orientation of the OPV chromophores resulted in the self-organization of graphene in periodic intervals. Furthermore, the photochemical dimerization of the OPVs occurs probably due to topological

confinement of these molecules as the graphene conjugates come close, resulting in interdigitation.

1.4.6: References

[1]   a)A. K. Geim, K. S. Novoselov, *Nat. Mater.* **2007**, *6*, 183; b)A. K. Geim, *Science* **2009**, *324*, 1530; c)C. N. R. Rao, A. K. Sood, K. S. Subrahmanyam, A. Govindaraj, *Angew. Chem. Int. Ed.* **2009**, *48*, 7752; d)S. K. Pati, T. Enoki, C. N. R. Rao, World Scientific, Singapore, **2011**.

[2]   a)S. Niyogi, E. Bekyarova, J. Hong, S. Khizroev, C. Berger, W. de Heer, R. C. Haddon, *J. Phys. Chem. Lett.* **2011**, *2*, 2487; b)Z. Z. Sun, D. K. James, J. M. Tour, *J. Phys. Chem. Lett.* **2011**, *2*, 2425.

[3]   a)A. Ghosh, K. V. Rao, S. J. George, C. N. R. Rao, *Chem.- Eur. J.* **2010**, *16*, 2700; b)H. S. S. Ramakrishna Matte, K. S. Subrahmanyam, K. V. Rao, S. J. George, C. N. R. Rao, *Chem. Phys. Lett.* **2011**, *506*, 260; c)A. Ghosh, K. V. Rao, R. Voggu, S. J. George, *Chem. Phys. Lett.* **2010**, *488*, 198; d)N. V. Kozhemyakina, J. M. Englert, G. Yang, E. Spiecker, C. D. Schmidt, F. Hauke, A. Hirsch, *Adv. Mater.* **2010**, *22*, 5483; e)A. Wojcik, P. V. Kamat, *ACS Nano* **2010**, *4*, 6697; f)K. S. Subrahmanyam, A. Ghosh, A. Gomathi, A. Govindaraj, C. N. R. Rao, *Nanosci. Nanotechnol. Lett.* **2009**, *1*, 28; g)S. K. Samanta, K. S. Subrahmanyam, S. Bhattacharya, C. N. R. Rao, *Chem.- Eur. J.* **2012**, *18*, 2890; h)Z. X. Zhang, H. L. Huang, X. M. Yang, L. Zang, *J. Phys. Chem. Lett.* **2011**, *2*, 2897; i)L.-H. Liu, M. Yan, *J. Mater. Chem.* **2011**, *21*, 3273; j)H. Yang, C. Shan, F. Li, D. Han, Q. Zhang, L. Niu, *Chem. Comm.* **2009**, 3880.

[4]   S. Stankovich, R. D. Piner, X. Chen, N. Wu, S. T. Nguyen, R. S. Ruoff, *J. Mater. Chem.* **2006**, *16*, 155.

[5]   a)B. Das, R. Voggu, C. S. Rout, C. N. R. Rao, *Chem. Comm.* **2008**, 5155; b)R. Voggu, B. Das, C. S. Rout, C. N. R. Rao, *J. Phys.: Condensed Mater,* **2008**, *20* 472204; c)K. S. Subrahmanyam, R. Voggu, A. Govindaraj, C. N. R. Rao, *Chem. Phys. Lett.,* **2009** *472*, 96; d)N. Varghese, A. Ghosh, R. Voggu, S. Ghosh, C. N. R. Rao, *J. Phys. Chem. C.,* **2009**, 16855; e)A. K. Manna, S. K. Pati, *Chem. Asian. J.* **2009**, *4* 855.

[6]   S. Niyogi, E. Bekyarova, M. E. Itkis, J. L. McWilliams, M. A. Hamon, R. C. Haddon, *J. Am. Chem. Soc.* **2006**, *128*, 7720.

[7]   K. S. Subrahmanyam, S. R. C. Vivekchand, A. Govindaraj, C. N. R. Rao, *J. Mater. Chem.* **2008**, *18*, 1517.

[8]   J. M. Englert, C. Dotzer, G. Yang, M. Schmid, C. Papp, J. M. Gottfried, H.-P. Steinraick, E. Spiecker, F. Hauke, A. Hirsch, *Nat. Chem.* **2011**, *3*, 279.

[9]   a)Y. F. Xu, Z. B. Liu, X. L. Zhang, Y. Wang, J. G. Tian, Y. Huang, Y. F. Ma, X. Y. Zhang, Y. S. Chen, *Adv. Mater.* **2009**, *21*, 1275; b)Z. B. Liu, Y. F. Xu, X. Y. Zhang, X. L. Zhang, Y. S. Chen, J. G. Tian, *J. Phys. Chem. B* **2009**, *113*, 9681.

[10]   C-H. Lu, H-H. Yang, C-L. Zhu, X. Chen, G.-N. Chen, *Angew. Chem. Int. Ed.* **2009**, *48*, 4785.

[11]   a)E. Treossi, M. Melucci, A. Liscio, M. Gazzano, P. Samorì, V. Palermo, *J. Am. Chem. Soc* **2009**, *131*, 15576; b)P. V. Kamat, *J. Phys. Chem. Lett.* **2009**, *1*, 520; c)L. Xie, X. Ling, Y. Fang, J. Zhang, Z. Liu, *J. Am. Chem. Soc* **2009**, *131*, 9890.

[12]   a)D. M. Guldi, G. M. A. Rahman, V. Sgobba, C. Ehli, *Chem. Soc. Rev.* **2006**, *35*, 471; b)G. Yu, J. Gao, J. C. Hummelen, F. Wudl, A. J. Heeger, *Science* **1995**, *270*, 1789; c)P. A. van Hal, J. Knol, B. M. W. Langeveld-Voss, S. C. J. Meskers, J. C.

Hummelen, R. A. J. Janssen, *J. Phys. Chem. A.* **2000**, *104*, 5974; d)B. Kraabel, D. McBranch, N. S. Sariciftci, D. Moses, A. J. Heeger, *Phys. Rev. B* **1994**, *50*, 18543.

[13]   a)Y.-L. Zhao, J. F. Stoddart, *Acc. Chem. Res.* **2009**, *42*, 1161; b)D. M. Guldi, G. N. A. Rahman, J. Ramey, M. Marcaccio, D. Paolucci, F. Paolucci, S. Qin, W. T. Ford, D. Balbinot, N. Jux, N. Tagmatarchis, M. Prato, *Chem. Comm.,* **2004**, 2034; c)D. M. Guldi, G. M. A. Rahman, F. Zerbetto, M. Prato, *Acc. Chem. Res.* **2005**, *38*, 871.

[14]   a)Y. Xu, Z. Liu, X. Zhang, Y. Wang, J. Tian, Y. Huang, Y. Ma, X. Zhang, Y. Chen, *Adv. Mater.* **2009**, *21*, 1275; b)Y. Xu, L. Zhao, H. Bai, W. Hong, C. Li, G. Shi, *J. Am. Chem. Soc* **2009**, *131*, 13490.

[15]   R. S. Swathi, K. L. Sebastian, *J. Chem. Phys.* **2009**, *130*, 086101.

[16]   a)S. Srinivasan, S. S. Babu, V. K. Praveen, A. Ajayaghosh, *Angew. Chem. Int. Ed.* **2008**, *47*, 5746; b)S. K. Samanta, A. Pal, S. Bhattacharya, C. N. R. Rao, *J. Mater. Chem.* **2010**, *20*, 6881; c)S. Srinivasan, V. K. Praveen, R. Philip, A. Ajayaghosh, *Angew. Chem. Int. Ed.* **2008**, *47*, 5750.

[17]   a)W. R. Collins, W. Lewandowski, E. Schmois, J. Walish, T. M. Swager, *Angew. Chem. Int. Ed.* **2011**, *123*, 9010; b)J. Geng, H.-T. Jung, *J. Phys. Chem. C* **2010**, *114*, 8227; c)C. N. R. Rao, A. Govindaraj, *Nanotubes and Nanowires, Vol. Second Edtion*, The Royal Society of Chemistry, London, **2011**.

[18]   K. S. Subrahmanyam, S. R. C. Vivekchand, A. Govindaraj, C. N. R. Rao, *Journal of Materials Chemistry* **2008**, *18*, 1517.

[19]   A. Ajayaghosh, V. K. Praveen, S. Srinivasan, R. Varghese, *Adv. Mater.* **2007**, *19*, 411.

[20]   a)A. Ajayaghosh, V. K. Praveen, *Acc. Chem. Res.* **2007**, *40*, 644; b)F. J. M. Hoeben, M. Wolffs, J. Zhang, S. De Feyter, P. Leclere, A. Schenning, E. W. Meijer, *J. Am. Chem. Soc.* **2007**, *129*, 9819; c)D. G. Rodriguez, A. P. H. J. Schenning, *Chem. Mater.* **2011**, *23*, 310.

[21]   U. Maitra, A. Jain, S. J. George, C. N. R. Rao, *Nanoscale* **2011**, *3*, 3192.

[22]   Q. Yang, J. Liang, H. Han, *J. Phys. Chem. B.* **2009**, *113*, 10454.

[23]   M. Álvaro, P. Atienzar, J. L. Bourdelande, H. García, *Chem. Phys. Lett.* **2004**, *384*, 119.

[24]   Z.-B. Liu, Y.-F. Xu, X.-Y. Zhang, X.-L. Zhang, Y.-S. Chen, J.-G. Tian, *J. Phys. Chem. B.* **2009**, *113*, 9681.

[25]   V. Y. Shafirovich, P. P. Levin, V. A. Kuzmin, T. E. Thorgeirsson, D. S. Kliger, N. E. Geacintov, *J. Am. Chem. Soc* **1994**, *116*, 63.

[26]   E. Peeters, A. M. Ramos, S. C. J. Meskers, R. A. J. Janssen, *J. Chem. Phys.* **2000**, *112*, 9445.

[27]   A. El-ghayoury, A. P. H. J. Schenning, P. A. van Hal, J. K. J. van Duren, R. A. J. Janssen, E. W. Meijer, *Angew. Chem. Int. Ed.* **2001**, *40*, 3660.

[28]   A. Ajayaghosh, S. J. George, *J. Am. Chem. Soc.* **2001**, *123*, 5148.

[29]   C.-H. Lu, H.-H. Yang, C.-L. Zhu, X. Chen, G.-N. Chen, *Angew. Chem. Int. Ed.* **2009**, *48*, 4785.

[30]   S. J. George, T. F. A. de Greef, R. Bovee, J. L. J. van Dongen, A. P. H. J. Schenning, E. W. Meijer, *Chem. Asian J.* **2009**, *4*, 910.

1.5: Interaction of graphene with FeCl$_3$ and CuCl$_2$

Summary

Graphene is a fascinating two-dimensional nanomaterial wherein its Fermi level can be shifted by doping. Such effects can be monitored by Raman spectroscopy through stiffening or softening of phonons. Effects of interaction of few-layer graphene with electron-acceptors FeCl$_3$ and CuCl$_2$ have been studied. Graphene-FeCl$_3$ and graphene-CuCl$_2$ composites were prepared by sealed tube reactions. Spectroscopic and microscopic studies reveal the occurrence of charge-transfer induced by these metal salts is due to adsorption on the graphene surface rather than intercalation. The Raman G-band of graphene softens on interaction with FeCl$_3$ and CuCl$_2$ and the intensity of the 2D-band decreases markedly accompained by an increase in the full width half maxima of both the bands. Interaction of graphene with CuCl$_2$ provides direct evidence of electron transfer from graphene to CuCl$_2$ through the formation of CuCl.

1.5.1: Introduction

Graphene, exhibiting fascinating properties such as include ballistic electron transport, anomalous integer quantum Hall effect at room temperature and fractional quantum Hall effect at low temperatures and ability to sustain very high current densities.[1] Atomic and electronic structures of graphene have been investigated by employing a variety of microscopic, spectroscopic and other techniques. Direct imaging of individual carbon atoms in single layer graphene by aberration-corrected transmission electron microscopy has shown the formation and annealing of Stone-Wales defects.[2] Studies of graphene are not limited to one-atom thick single-layer graphene alone but also include bi- and few-layer (< 10 layers) graphenes. As a two-dimensional material, graphene has been found to exhibit high crystal quality [3] in which charge carriers can travel thousands of interatomic distances without being scattered.[4]

Graphene is a nearly zero bandgap semiconductor membrane, having tremendous physical strength [5] and high electron mobility at room temperature resulting from extended electron conjugation and delocalization. Charge transfer on interaction with adsorbed species can shift[6] the graphene Fermi level by a large fraction of electron volts. Such adsorption-induced chemical doping relocates the Fermi level without introducing any substitutional impurities, or basal plane reactions, that interrupt the conjugated network. Raman spectra of epitaxial graphene layers grown on SiC show a significant blue shift of the G-band (~20cm^{-1}) and 2D bands (~60cm^{-1}) as compared to exfoliated graphene.[7] This mainly arises due to compressive strain that builds up when sample is cooled down after annealing.

Till date, various methods have been employed for tuning the electronic structure of the graphene. Sensitivity of electronic structure to doping can be seen clearly from the

substrate induced doping in epitaxial graphenes.[8] It has been demonstrated by Das et al. that doping in the graphene can be achieved electrochemically using a top-gated single-layer graphene transistor to reach doping levels up to 5 x10^{13} cm^{-2} by employing in-situ Raman measurements.[9] The G-band of graphene stiffens and sharpens for both electron- and hole-doping, but the 2D-band shows a different response to holes and electrons. The ratio of the intensities of the G- and 2D-bands shows a strong dependence on doping, making it a sensitive parameter to monitor doping.

Charge-transfer interactions of graphene with various electron-donor and acceptor molecules have been studied. Electron donors such as aniline and tetrathiafulvalene (TTF) soften (i.e. shift to lower frequency) the G-band of few-layer graphene progressively with the increasing concentration, while electron-acceptors, such as nitrobenzene and tetracyanoethylene (TCNE), stiffens (i.e. shift to higher frequency) the G-band.[10] The full-width at half maximum (FWHM) of the G-band increases on interaction with these molecules. The intensity of the 2D-band decreases markedly with the concentration of either donor or acceptor molecule. The ratio of intensities of the 2D- and G-bands, I(2D)/I(G), is a sensitive probe to examine doping of graphene by electron-donor and -acceptor molecules. Another important way to shift the Fermi level is by substitutional doping. Boron or nitrogen substitutional doping has been an important strategy widely used in the carbon based materials. Substitutional doping of nitrogen (~ 1 at %) or boron (upto 3 at%) in graphene is accomplished by the arc-discharge method.[11] On doping with boron and nitrogen the Raman G-band stiffens which is similar to what happens with electrochemical doping [12] but differs from the case of molecular charge-transfer.[10a, 13] On doping, the relative intensity of the 2D-

band generally decreases with respect to that of the G-band. B-and N-doped graphenes exhibit higher electrical conductivity than undoped graphene.

Recent literature reports that $FeCl_3$ has been intercalated in graphene by employing the two-zone vapor transport method. The Raman G-band of intercalation compounds were blue shifted and single Lorentzian 2D peaks were observed similar to that of single-layer graphene, indicating the loss of electronic coupling between adjacent graphene layers.[14] In another report, anhydrous ferric chloride was intercalated in 2-4 layer graphene and also doped in graphene monolayers. The G band of heavily doped monolayer graphene upshifts to ~ 1627 cm^{-1} from 1580 cm^{-1}. By performing Raman measurements with different excitation energies, direct evidence of Fermi level downshift up to ~ 0.9 eV was observed.[15]

1.5.2: Scope of the present investigations

In view of the importance of graphene based devices it is worthwhile to explore new and facile methods for altering the electronic structure by tuning the position of Fermi level. Graphene can be chemically doped by both intercalation and adsorption of molecules and its electronic properties will be greatly modified as a result.

We considered it is worthwhile to investigate the effects of interaction of graphene with electron--acceptor molecules on structural and electronic properties. For this purpose, we have prepared graphene samples by the thermal exfoliation of the graphitic oxide. Then, we have studied the interaction of two electron-acceptors, $FeCl_3$ and $CuCl_2$, by employing transmission electron microscopy, Raman spectroscopy and other characterization techniques. Thus far, literature reports intercalation only in graphene obtained from micromechanical cleavage method, but no reports have been there with chemically

synthesized few-layer graphene. It is interesting to examine whether the $FeCl_3$ intercalates and form graphene intercalated compounds or just exhibits charge-transfer interaction. Raman spectroscopy can be successfully employed to differentiate the charge transfer interaction induced by intercalation and surfacial adsorption.

1.5.3: Experimental section

Synthesis of EG+FeCl₃: EG (3mg) and anhydrous $FeCl_3$ (0.1g/0.2g/0.3g) were taken in a quartz tube. The tube was evacuated using a vacuum pump and then, it was sealed. The tube was kept in the furnace at 320 °C for 48 hours. After 48 hours, the tubes were taken out and cooled in liquid nitrogen so as to condense the vapors formed in the sealed tube during the reaction. The tube was then broken. The solid substance present was taken out and washed (centrifuged) with ethanol 5-6 times until the green color of the supernatant vanished. This was done so as to ensure no residual $FeCl_3$ in the sample. The sample was then dried in an oven at 40–50 °C and then characterized.

Synthesis of EG+CuCl₂: EG (3mg) and anhydrous $CuCl_2$ (0.1g/0.2g/0.3g) were taken in a quartz tube. The tube was evacuated using a vacuum pump and then, it was sealed. The tube was kept in the furnace at 550 °C for 48 hours. After 48 hours, the tubes were taken out and cooled in liquid nitrogen so as to condense the vapours formed in sealed tube during the reaction and were then broken. The solid substance present was taken out and washed (centrifuged) with ethanol 5-6 times until the color of the supernatant disappear. This was done to ensure that no residual $CuCl_2$ was present in the sample. The sample was then dried in an oven at 40–50 °C and then characterized.

Characterization Techniques

Field emission scanning electron microscope (FESEM): FESEM images were recorded with a FEI NOVA NANOSEM 600.

Raman spectroscopy : Raman spectra were recorded at different locations of the sample using Jobin Yvon LabRam HR spectrometer with 632 nm (excitation wavelength) Ar laser.

Transmission electron microscopy (TEM): TEM images were obtained with a JEOL JEM 3010 instrument fitted with a Gatan CCD camera operating at an accelerating voltage of 300 kV. The samples were prepared by dispersing the product in ethanol. A drop of the suspension was then put on a holey carbon coated Cu grid and allowed to evaporate.

1.5.4: Results and Discussion

**Graphene+FeCl$_3$:** We have prepared graphene by the thermal exfoliation of graphite oxide by employing the literature procedure[16] (EG) and characterized by Raman spectroscopy, transmission electron microscopy and atomic force microscopy as described in the literature.[17] The number of layers in the graphene samples prepared were found to have five to six. The EG sample (3 mg) was mixed with appropriate amount of anhydrous FeCl$_3$ and sealed in quartz tube after the vacuum reached around 10^{-5} bar in the tube and kept at 350 ^{o}C for 2 days. During the process FeCl$_3$ vapors was expected to diffuse in to the graphene layers. Soon after the reaction was completed we have washed the products with ethanol to remove excess or unreacted FeCl$_3$ present in the product. Later, the product was characterized using various techniques including XRD and electron microscopy.
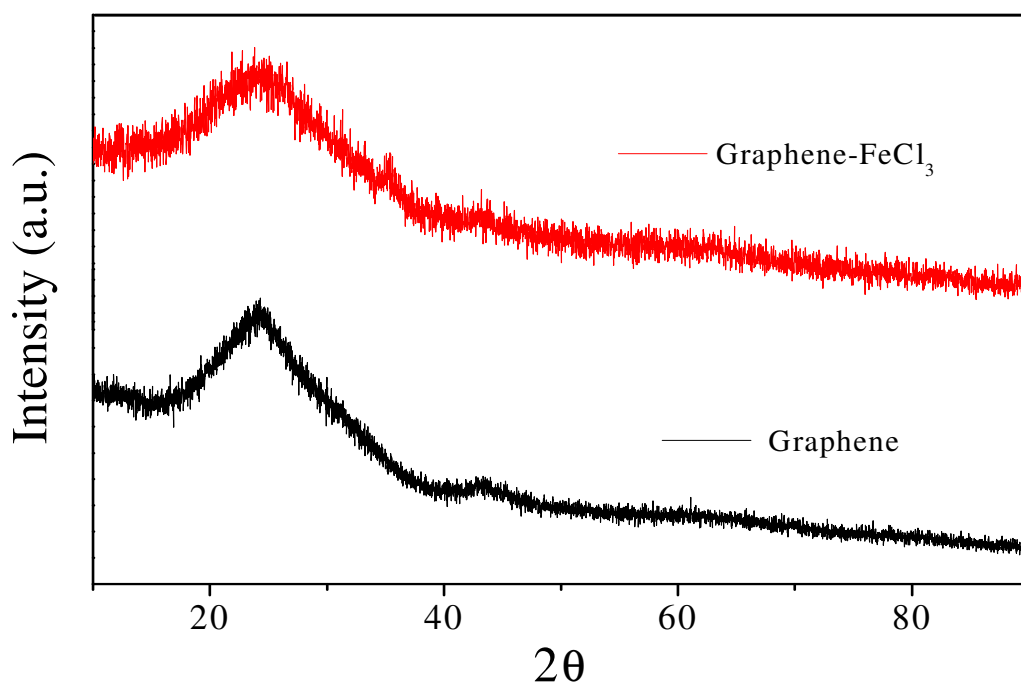
Figure 1: XRD pattern of graphene and graphene-FeCl$_3$.

1.5: Interaction of graphene with FeCl₃ and CuCl₂

In Figure 1, we show the X-ray diffraction pattern of the graphene and graphene-FeCl₃. It can be noticed that there are no changes in the XRD pattern as expected for intercalation compounds or any signatures of FeCl₃ peaks. In Figure 2(a), we have shown FESEM image showing the adsorbed particle like morphology on the surface of sheets. We
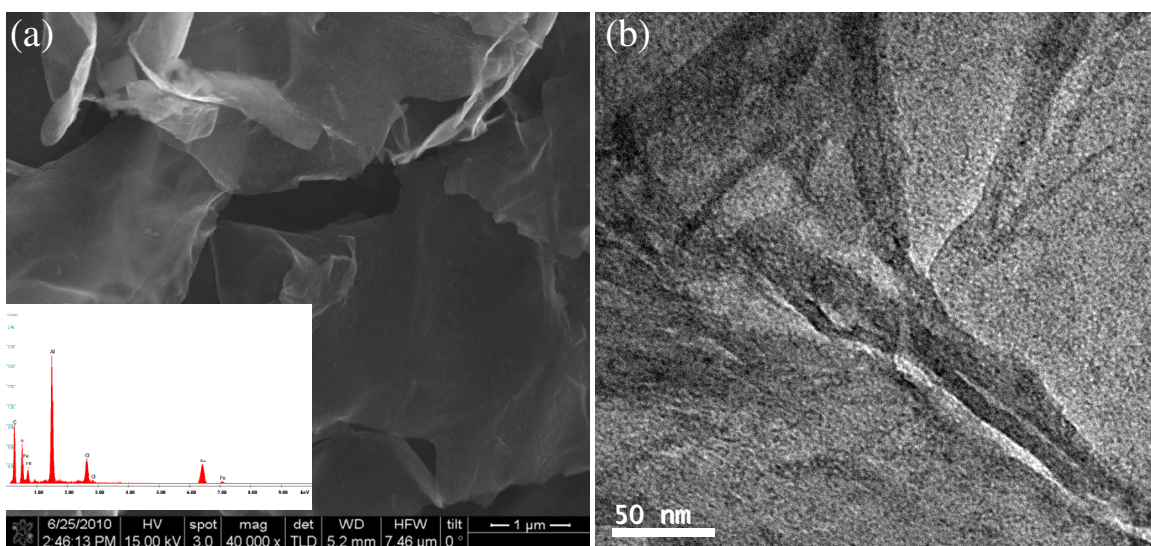
**Figure 2:** (a) FESEM (b) TEM images of graphene-FeCl₃ inset shows EDX analysis.

have carried out EDX analysis to confirm the presence of FeCl₃. EDX has shown the presence of Fe and Cl atoms (inset of Figure 2(a)). Later, we have carried out TEM analysis on the sample, to understand the structure of the composite formed. We have analyzed the sample for many days to observe the increase in interlayer spacing which is an apparent result in the intercalation systems. In the TEM observations we have not observed the increase in the d-spacing. XRD has also not showed any evidence of intercalation mainly because of few-layers in graphene. As can be noticed in Figure 2(b), the TEM image gave the impression that it was decorated by the small particles of FeCl₃. In order to confirm the existence of FeCl₃ coated on graphene surface we have carried out elemental mapping in the aberration corrected (TITAN) microscope. In Figure 3, we have shown the elemental

mapping of Fe, Cl and C. The homogenous distribution of the color further confirms the uniform distribution of $FeCl_3$.

Raman spectroscopy is very important tool to characterize graphene and it is particularly important in the present context to understand the electronic structure of the

Fe Mapping	Cl Mapping	C Mapping
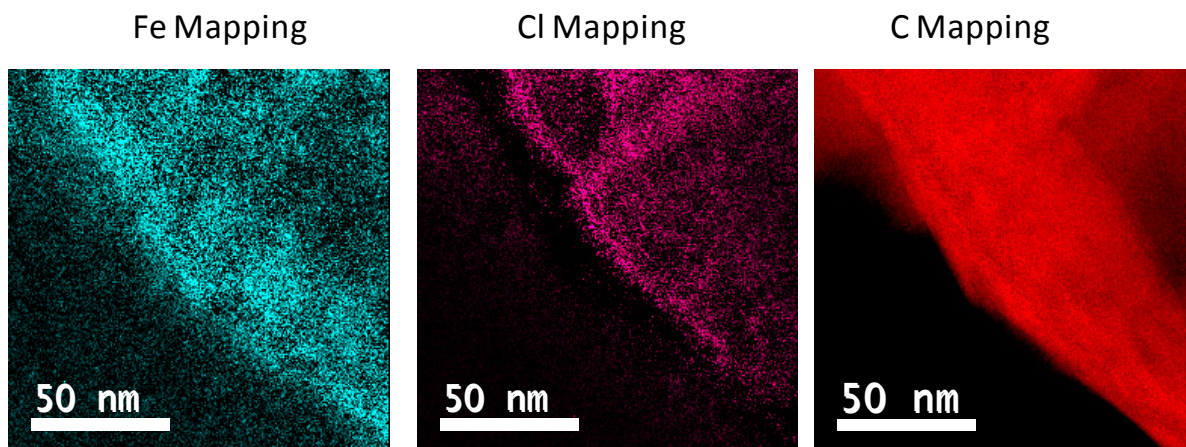
Figure 3: Elemental mapping of Iron, chlorine and carbon from TEM

composite as well as to differentiate the intercalation and the adsorption of $FeCl_3$ with graphene. We have carried out Raman spectroscopic investigation on the composites (Figure 4). It is well known from the literature that $FeCl_3$ acts as electron acceptor. The changes reported in the literature for the charge-transfer interactions due to the adsorption of various donors and acceptor systems with the graphene are as follows. The G-band of the graphene after interaction with electron-donating group softens or a shift to a lower frequency and on interacting with -withdrawing groups stiffens the G-band or an increase in the frequency. The full-width-at-half-maximum (FWHM) of the G-band increases in both the cases. In the case of the 2D-band similar shifts have been observed as of G-band but it is found out that the ratio of the intensities of 2D- and G-bands, $(I_{(2D)}/I_{(G)})$, decreases progressively and it is considered as to be sensitive to charge-transfer interactions. In the case of intercalation of graphene, the G-band softens or stiffens basing on the type of intercalant used which results

from charge transfer-induced effect. Similar trends have been observed with the 2D band as well. The distance between adjacent graphene layers is enlarged from the original 3.4 Å to around 9.4 Å in the intercalated samples. This analysis revealed that adjacent graphene layers can only interact with each other through the intercalant layer, resulting in much weaker coupling between the layers. Raman spectrum of the intercalated sample showed sharp 2D band. These features in the Raman spectrum suggest that the intercalated samples may have properties very similar to single-layer graphene. As a result, the fully intercalated system can be viewed as quasi-individual graphene layers superimposed together with a very weak coupling effect through the intercalated layers. This results in increase in the 2D peak intensity increasing with number of layers. Another important signature in the intercalated graphene is coming from the line width of the 2D peak. For intercalated samples it is much sharper than that of pristine FLG.
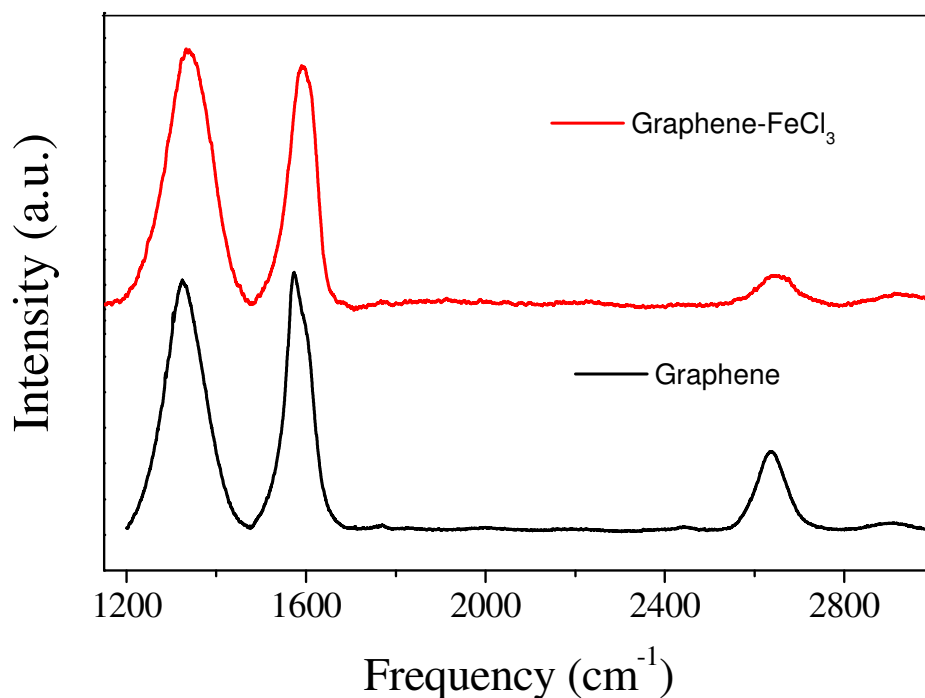
Figure 4: Raman spectra of Graphene and Graphene-$FeCl_3$

1.5: Interaction of graphene with $FeCl_3$ and $CuCl_2$

In the Figure 4, we have compared the Raman spectra of pristine graphene with EG-$FeCl_3$. For, pristine graphene, we found that the G peak can be deconvoluted to two peaks, with positions at 1573 and 1604 cm^{-1} (see Figure 5 (a)) and FWHM having 36 and 41 respectively (Table 1). In the case of $FeCl_3$-EG we observed that the bands have blue shifted to 1586 and 1612 cm^{-1} (see Figure 5 (a)) respectively with increase in FWHM and the values being 71 and 28 cm^{-1} respectively (Table 1).
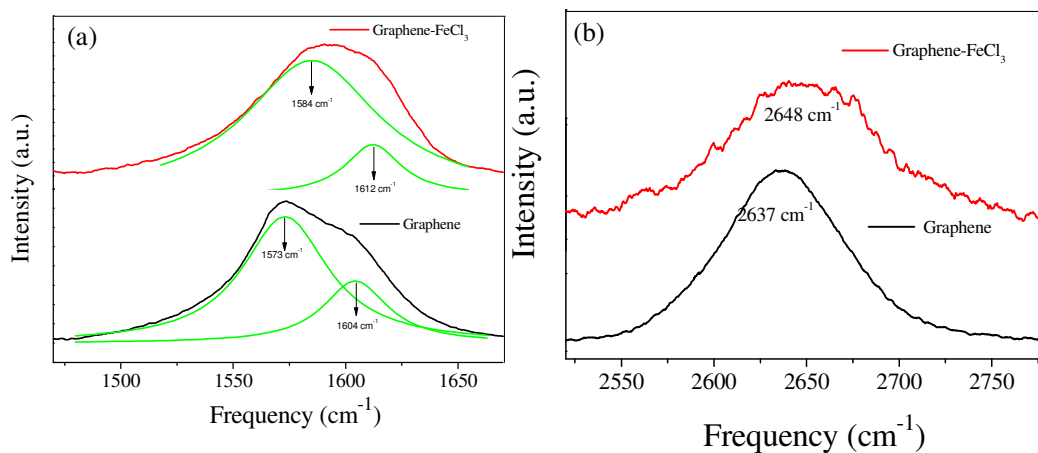

Figure 5: (a) G-band and (b) 2D band of the Raman spectra of Graphene and Graphene-$FeCl_3$

The stiffening of the G-band is attributed to charge-transfer interaction where $FeCl_3$ acts as an acceptor. This is caused by the non-adiabatic removal of the Kohn anomaly at the Γ point. The band broadening suggests the absence of blockage of the decay channels of the phonons into electron-hole pairs in the present situation. In a similar way we have also observed the shifts in the 2D band from 2637 cm^{-1} to 2645 with an increase in the FWHM from 89 to 116 cm^{-1} (see Figure 5(b) and Table 1). The decrease of I_{2D}/I_G value from 0.35 to 0.14 after $FeCl_3$ interaction was observed. From the above discussion it is clear that we have

charge-transfer induced from adsorption rather than from intercalation of $FeCl_3$ corroborating the TEM results.

Graphene+CuCl₂: In Figure 6, we show the XRD pattern of EG with EG-$CuCl_2$. To our surprise we observe peaks correspond to CuCl along with the hump at $2\theta = 25$ degrees corresponds to graphene. It is well known that, graphene can act as
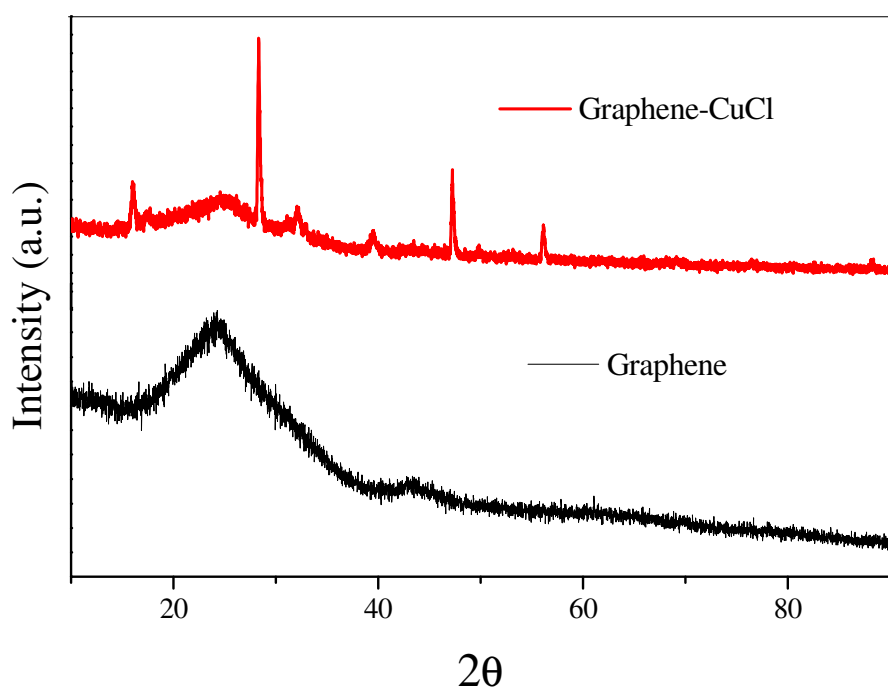
Figure 6: XRD pattern of graphene and CuCl- graphene
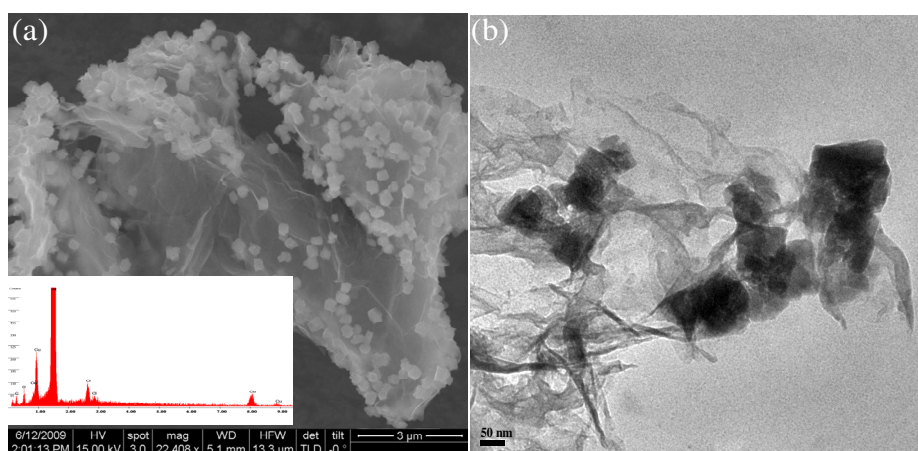
Figure 7: (a) FESEM (b) TEM images of graphene-CuCl inset shows EDX analysis.
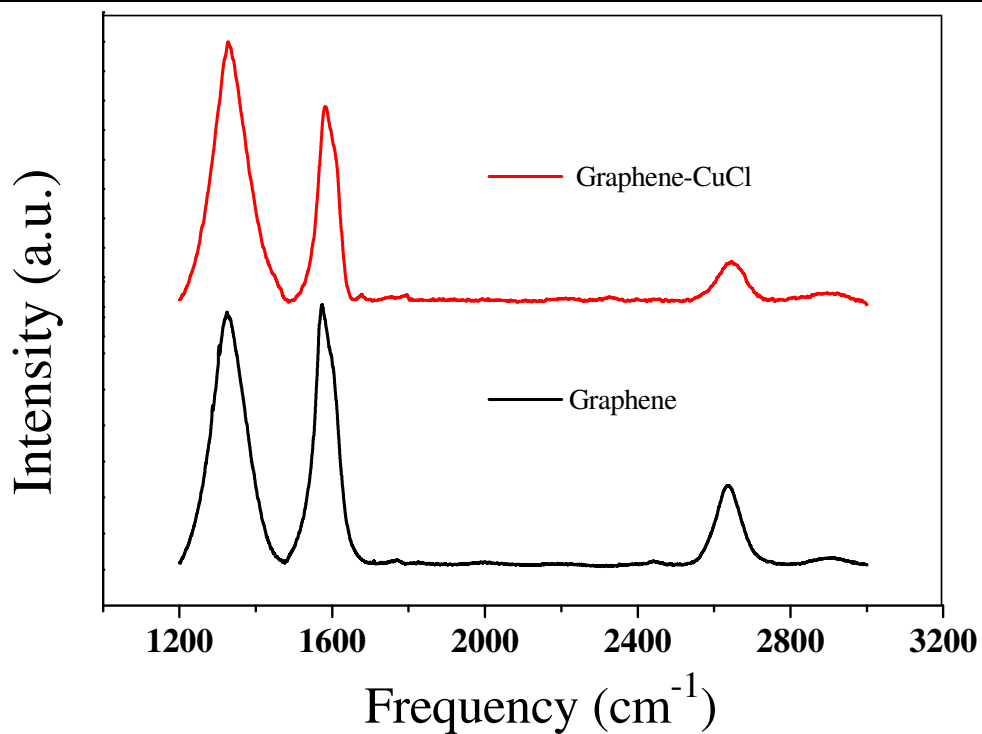
Figure 8: Raman spectra of Graphene and Graphene-CuCl
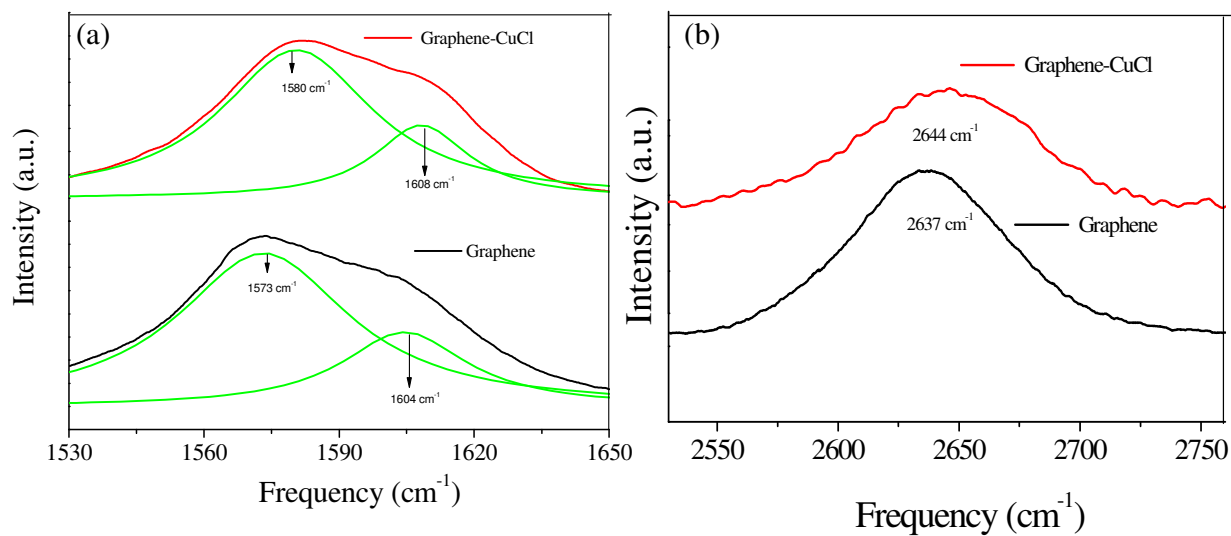
Figure 9: (a) G-band and (b) 2D band of the Raman spectra of Graphene and Graphene-CuCl.

an electron donor as well as an acceptor. Studies have been carried out to reveal the electron transfer between graphene and the donor/acceptor using various spectroscopic techniques.

But in our case, the XRD patterns suggest the formation of graphene-CuCl provide a direct evidence for the electron transfer.

We have carried out the microscopic characterization to understand the CuCl peaks appeared in the XRD pattern. In Figure 7(a), we have shown the FESEM image of graphene-CuCl showing the 50-100 nm clusters on surface and these clusters being rolled with graphene layers. In Figure 7(b) we have shown the TEM image which also shows the existence of CuCl clusters on the graphene surface where as some are wrapped in the graphene.

Sample	G - Band		2D - Band		I_D/I_G	I_{2D}/I_G
	Frequency, cm^{-1}	FWHM	Frequency, cm^{-1}	FWHM		
Graphene	1573	46	2637	89	1.08	0.35
	1604	34				
0.1 g $FeCl_3$ + 3 mg Graphene	1586	71	2645	116	1.08	0.14
	1612	28				
0.1 g $CuCl_2$ + 3 mg Graphene	1580	47	2645	116	1.16	0.16
	1608	29				

Table 1: Raman band positions and intensity ratios of graphene and graphene composites.

In Figure (8), we show the Raman spectra of graphene along with the composites with CuCl. Pristine few-layer graphene shows the G-band at 1580 and 1608 cm^{-1} while graphene-CuCl exhibit stiffening of the G-band. The G-band occurs at 1580 and 1608 cm^{-1}. These results suggest the occurrence of charge-transfer interaction between CuCl and few-layer graphene, similar to that found between graphene and electron acceptor molecules like TCNE and nitrobenzene. These results were also supported by the XRD pattern which show signature peaks of CuCl. Similar to the case of EG-FeCl$_3$, we observe an increase in the FWHM and a decrease in the I_{2D}/I_G value after interacting with CuCl (see Table 1).

1.5.5: Conclusions

We have been able to prepare composites of graphene with FeCl$_3$ and CuCl using sealed tube reactions. Though the conditions employed here were suitable to form intercalation compounds, we have not found evidence of intercalation. The composites show the, occurrence of charge-transfer interaction caused by the adsorption of the metal-salts on graphene layers.

1.5.6: References

[1]   a)A. K. Geim, K. S. Novoselov, *Nat. Mater.* **2007**, *6*, 183; b)C. N. R. Rao, A. K. Sood, K. S. Subrahmanyam, A. Govindaraj, *Angew. Chem. Int. Ed.* **2009**, *48*, 7752; c)C. N. R. Rao, A. K. Sood, R. Voggu, K. S. Subrahmanyam, *J. Phys. Chem. Lett.* **2010**, *1*, 572; d)C. N. R. Rao, K. S. Subrahmanyam, H. S. S. Ramakrishna Matte, B. Abdulhakeem, A. Govindaraj, B. Das, P. Kumar, A. Ghosh, D. J. Late, *Sci. Tech. Adv. Mater.* **2010**, *11*, 054502.

[2]   J. C. Meyer, C. Kisielowski, R. Erni, M. D. Rossell, M. F. Crommie, A. Zettl, *Nano Lett.* **2008**, *8*, 3582.

[3]   a)S. Stankovich, D. A. Dikin, G. H. B. Dommett, K. M. Kohlhaas, E. J. Zimney, E. A. Stach, R. D. Piner, S. T. Nguyen, R. S. Ruoff, *Nature* **2006**, *442*, 282; b)K. S. Novoselov, A. K. Geim, S. V. Morozov, D. Jiang, Y. Zhang, S. V. Dubonos, I. V. Grigorieva, A. A. Firsov, *Science* **2004**, *306*, 666; c)J. C. Meyer, A. K. Geim, M. I. Katsnelson, K. S. Novoselov, T. J. Booth, S. Roth, *Nature* **2007**, *446*, 60.

[4]   a)K. S. Novoselov, A. K. Geim, S. V. Morozov, D. Jiang, M. I. Katsnelson, I. V. Grigorieva, S. V. Dubonos, A. A. Firsov, *Nature* **2005**, *438*, 197; b)Y. Zhang, Y.-W. Tan, H. L. Stormer, P. Kim, *Nature* **2005**, *438*, 201.

[5]   C. Lee, X. Wei, J. W. Kysar, J. Hone, *Science* **2008**, *321*, 385.

[6]   a)K. S. Kim, Y. Zhao, H. Jang, S. Y. Lee, J. M. Kim, K. S. Kim, J.-H. Ahn, P. Kim, J.-Y. Choi, B. H. Hong, *Nature* **2009**, *457*, 706; b)F. Schedin, A. K. Geim, S. V. Morozov, E. W. Hill, P. Blake, M. I. Katsnelson, K. S. Novoselov, *Nat. Mater.* **2007**, *6*, 652.

[7]   a)N. Ferralis, R. Maboudian, C. Carraro, *Phys. Rev. Lett.* **2008**, *101*, 156801; b)Z. H. Ni, W. Chen, X. F. Fan, J. L. Kuo, T. Yu, A. T. S. Wee, Z. X. Shen, *Phys. Rev. B* **2008**, *77*, 115416.

[8]   S. Y. Zhou, G. H. Gweon, A. V. Fedorov, P. N. First, W. A. de Heer, D. H. Lee, F. Guinea, A. H. Castro Neto, A. Lanzara, *Nat. Mater.* **2007**, *6*, 770.

[9]   DasA, PisanaS, ChakrabortyB, PiscanecS, S. K. Saha, U. V. Waghmare, K. S. Novoselov, H. R. Krishnamurthy, A. K. Geim, A. C. Ferrari, A. K. Sood, *Nat. Nanotechnol.* **2008**, *3*, 210.

[10]   a)B. Das, R. Voggu, C. S. Rout, C. N. R. Rao, *Chemical Communications* **2008**, 5155; b)R. Voggu, B. Das, C. S. Rout, C. N. R. Rao, *J. Phys.-Condes. Matter* **2008**, *20*, 5; c)K. S. Subrahmanyam, R. Voggu, A. Govindaraj, C. N. R. Rao, *Chem. Phys. Lett.* **2009**, *472*, 96.

[11]   a)K. S. Subrahmanyam, L. S. Panchakarla, A. Govindaraj, C. N. R. Rao, *The Journal of Physical Chemistry C* **2009**, *113*, 4257; b)L. S. Panchokarla, K. S. Subrahmanyam, S. K. Saha, A. Govindaraj, H. R. Krishnamurthy, U. V. Waghmare, C. N. R. Rao, *Advanced Materials* **2009**, *21*, 4726.

[12]   DasA, PisanaS, ChakrabortyB, PiscanecS, S. K. Saha, U. V. Waghmare, K. S. Novoselov, H. R. Krishnamurthy, A. K. Geim, A. C. Ferrari, A. K. Sood, *Nat Nano* **2008**, *3*, 210.

[13]   R. Voggu, B. Das, C. S. Rout, C. N. R. Rao, *Journal of Physics-Condensed Matter* **2008**, *20*, 5.

[14]   D. Zhan, L. Sun, Z. H. Ni, L. Liu, X. F. Fan, Y. Wang, T. Yu, Y. M. Lam, W. Huang, Z. X. Shen, *Adv. Funct. Mater* **2010**, *20*, 3504.

[15]   W. Zhao, P. H. Tan, J. Liu, A. C. Ferrari, *J. Amer. Chem. Soc.* **2011**, *133*, 5941.

[16]   a)K. S. Subrahmanyam, S. R. C. Vivekchand, A. Govindaraj, C. N. R. Rao, *J. Mater. Chem.* **2008**, *18*, 1517; b)H. C. Schniepp, J.-L. Li, M. J. McAllister, H. Sai, M. Herrera-Alonso, D. H. Adamson, R. K. Prud'homme, R. Car, D. A. Saville, I. A. Aksay, *J. Phys. Chem. B* **2006**, *110*, 8535.

[17]   A. Ghosh, K. S. Subrahmanyam, K. S. Krishna, S. Datta, A. Govindaraj, S. K. Pati, C. N. R. Rao, *J. Phys. Chem. C* **2008**, *112*, 15704.

PART 2

Investigations of inorganic graphene analogues

2.1: Brief overview of inorganic graphene analogues

2.1: Introduction

2.1.1: Inorganic Fullerenes

The discovery of fullerenes by Kroto, Smalley and Curl[1] in 1985 is considered as a major turning point in the exploration of various layered materials with different morphologies. Fullerenes are zero-dimensional (OD) form of carbon possessing layered structure. Similarly, carbon nanotubes (1D) are formed by rolling carbon sheets into seamless cylinders. Intuitively, fullerenes and nanotubes of two-dimensional inorganic layered materials such as MoS_2, WS_2 etc., which are structural analogues to graphite can be formed.[2] The discovery of inorganic nanotubes and fullerene-like structures in 1992, established a new horizon in the field of inorganic nanomaterials having closed cage like structures with polyhedral or nanotubular shapes.[2] In contrast to graphene which is one atomic layer of carbon, molecular sheet of the metal dichalcogenides, has three layers of atoms in which the metal layer is sandwiched between two chalcogen layers with the metal in a trigonal pyramidal or octahedral coordination, these layers are stacked along the c-direction in ABAB fashion[3] (Figure 1). Along the c-axis, the layers show the presence of dangling bonds due to the absence of an X or M atom at the edges. These unsaturated bonds at the

edges are unstable resulting in bending and have a high propensity to form the rolled structure.[4] There are several layered inorganic compounds having similar structure to graphite. These layered materials open up new horizon with attractive properties ranging from semiconducting to superconductivity both at bulk and nanoscale.[5]
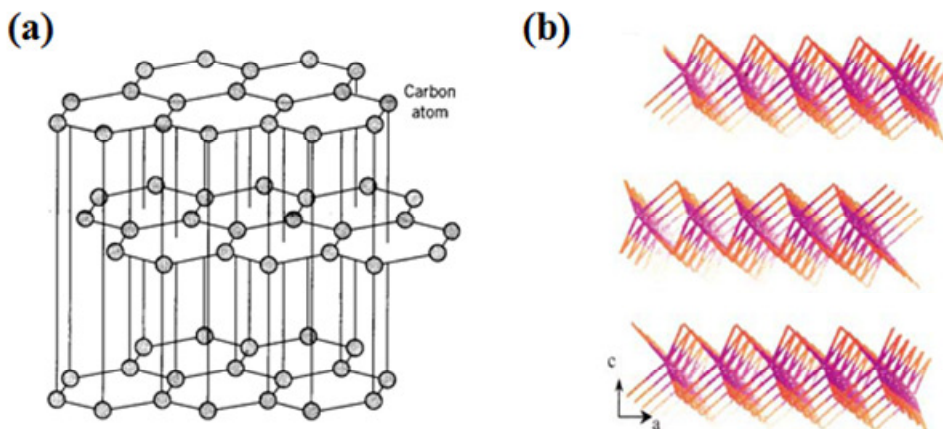
Figure 1: Comparison of the structures of (a) graphite and (b) MoS_2 [from ref 3].

Among, the inorganic layered materials, transition-metal chalcogenides (sulphides, selenides, and tellurides), halides (chlorides, bromides, and iodides), oxides, and numerous other ternary (quaternary) compounds are naturally available.[6] In the last decade, several physical and chemical methods have been developed to prepare inorganic fullerenes (IF) of transition metal sulphides and selenides.[7] Tenne et al. has reported the synthesis of fullerenes of MoS_2 and WS_2 for the first time. In this procedure, IF nanoparticles were prepared by sulfidizing ultra-thin WO_3 (MoO_3) films in a reducing atmosphere at elevated temperatures of 850°C.[2a] Many effective synthetic modifications have been done later in this procedure to increase the yield and to gain greater size control. The mechanism for the

formation of inorganic fullerenes of MoS_2, WS_2 and for their corresponding selenides have been studied when trioxide powders were used as precursors.[8],[9]

Using the metal organic chemical vapor deposition (MOCVD) method inorganic fullerene like particles of Mo, W and Re with S or Se have been prepared.[10] The corresponding metal carbonyls are heated in the presence of elemental sulphur or selenium at high temperatures. The synthesis of IF-MoS_2 and $MoSe_2$ was carried out by using molybdenum hexacarbonyl ($Mo(CO)_6$) and elemental sulphur/selenium as the precursors and carried out in two steps.[10a] The first step involves the reaction between the precursors to give amorphous/quasi crystalline MoS_2 nanoparticles. In the second step, quasi-crystalline nanoparticles were annealed in argon atmosphere and allowed to grow until they were converted to nanosheets which then automatically rolled up into nested fullerene or nanotubular structures. Similarly, IF-WS_2 were prepared by using tungsten hexacarbonyl and elemental sulfur as precursors.[10b] Using the similar procedure, the IF-ReS_2 have been synthesized from dirhenium decacarbonyl and elemental sulphur.[10c]

IF-MoS_2 were also synthesized by using a gas-phase reaction starting from $MoCl_5$ and H_2S. The synthesis was carried out in a two-stage furnace in which the precursor was heated in an auxiliary furnace and passing the vapors of the precursor by flowing N_2 and/or H_2. The reaction occurs in the main reactor where the vapors of the precursor encounter the stream of H_2S gas which is used as the sulphidizing agent. The IF-MoS_2 nanoparticles are spherical, and in some cases faceted, with diameters ranging between 20 and 80 nm (Figure 2). Apart from the fullerene like nanoparticles, nanotubes of MoS_2 (Figure 2) were also obtained in small yields under certain experimental conditions. Similarly, IF-WS_2 were synthesized by a gas phase reaction starting from WCl_n (n = 4,5,6) and H_2S. The effect of the

various metal chloride precursors WCl_n (n = 4, 5, 6) on the formation of the products was investigated. The vapors of the precursor were carried into the main reactor by flowing N_2 and H_2 gases and the obtained IF-WS_2 have the diameter of ~ 50 nm.[11] TiS_2 is another layered structure where the layers of titanium disulphide are stacked together by weak Van-der-Waals forces. IF-TiS_2 was synthesized using $TiCl_4$ and H_2S in a gas-phase reaction, by the both vertical and horizontal reactors. The reported IF's are perfectly spherical with diameters between 60 and 80 nm, consisting of 80–100 concentric layers.[12] IF-NbS_2 were synthesized in the gas phase reaction by reacting $NbCl_5$ with H_2S followed by annealing[13] and it shows superconductivity below 6.23 K. IF-TaS_2 were also produced by the gas-phase reaction between $TaCl_5$ and H_2S. In all these synthetic methods, temperature and concentration have profound effect on the resulting phase, particle size and the crystallinity.[14]
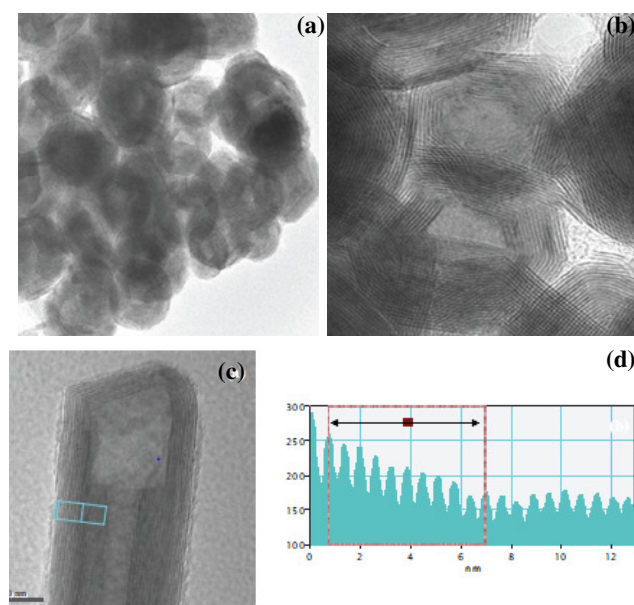
Figure 2: (a) and (b) Low magnification and high magnification TEM images of the IF-MoS_2 nanoparticles (c) HRTEM image of the MoS_2 nanotube, (d) the line profile of the boxed area in the figure (c) gives an interlayer spacing of 6.2 Å [from ref 7(b)].

2.1. Brief overview of inorganic graphene analogues

IF-MoS$_2$ were also obtained by employing electron beam irradiation of MoS$_2$ crystals using an electron accelerator at an energy of 0.5 MeV. The product contained two main structures, one having fullerene-like structure and others having their planes rotated by well-defined angles with respect to each other.[15] IF- MoS$_2$ and IF-WS$_2$ were prepared by reacting Mo(CO)$_6$ or W(CO)$_6$ powders and heated in H$_2$S (1%)/argon atmosphere, under microwave plasma irradiation at 580°C.[16]

2.1.2: Inorganic Nanotubes

Ijima et al. observed some unusual structures of carbon, in which the graphene sheets rolled and folded onto themselves to form hollow structures under transmission electron microscope and termed them as nanotubes of carbon.[17] Following the discovery, intense research has been carried out on carbon nanotubes (CNTs) and found to have single-walled nanotubes (SWNT) double-walled nanotubes (DWNT) and multi- walled (MWNTs).[18] The discovery of inorganic nanotubes of WS$_2$ by Tenne et al. established a new paradigm and has led to the search for other inorganic nanotubes. In this process, several inorganic nanotubes have been prepared and characterized. MoS$_2$, BN, SiO$_2$, TiO$_2$, VO$_x$, NiCl$_2$, NbSe$_2$, Au, CdS, CdSe, ZnS, NbS$_2$, HfS$_2$, ZnO, BaTiO$_3$, ReS$_2$ etc.. being the archetypal examples of inorganic nanotubes.

Inorganic nanotubes can be synthesized using different strategies. Among those, the most studied chemical route is the reaction between needle like tungsten oxide and H$_2$S gas which produces the corresponding sulphide at elevated temperatures (840 °C) with less yields that depends mainly on the various experimental conditions like the total flow rate and

flow rate of hydrogen.[19] Later, vertical fluidized bed reactor was constructed for scaling-up of the process and nanotubes were found as the major product. In a typical reaction, the agglomerated spherical tungsten oxide nanoparticles were reduced and subsequently sulfidized at a much slower rate by diffusion of hydrogen and H_2S leading to the growth of a perfect cylindrical morphology with 5−8 layers thick multi-walled nanotubes[20] (Figure 3).
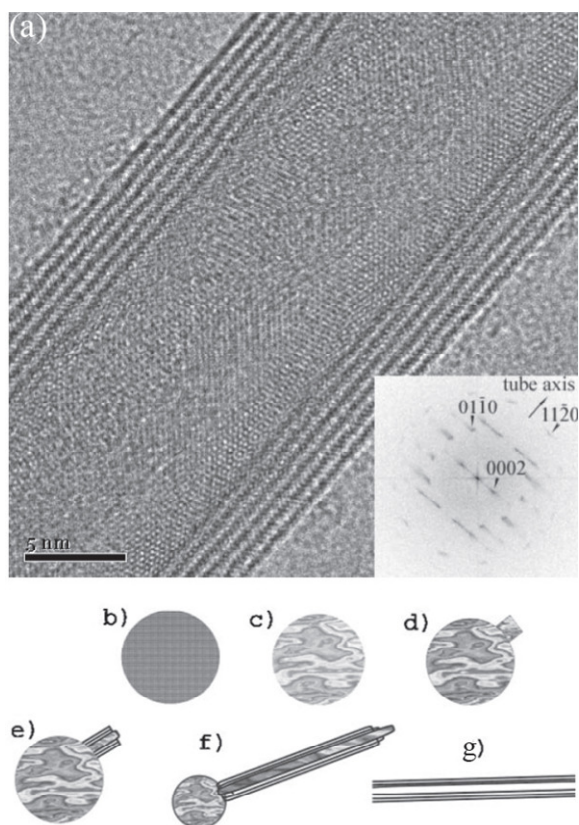

Figure 3: (a) HRTEM micrograph of a WS_2 nanotube consisting of six layers. Fourier transform (FFT) of the nanotube is shown in the insert. (b)–(g) Schematic drawing of the growth mechanism of WS_2 nanotubes, synthesized in the fluidized bed reactor. (b) Starting oxide nanoparticle; (c) The reduced particle with a volatile oxide phase encapsulated; (d) The break-through of the volatile phase through the encapsulating surface; (e) The formation of the root of the nanotube on the top surface of the particle from the emitted oxide; (f) Further growth of the nanotube: the volatile oxide that is emitted from the nanotube's hollow core. Reacting with H_2S it formsWS$_2$ at the tip of the tube; (g) The final obtained nanotubes [from ref 7(a)].

2.1. Brief overview of inorganic graphene analogues

Another important method for the synthesis of WS_2 nanotubes is thermal decomposition of $(NH_4)_2WS_4$ particles prepared by ball milling and heated at a fixed temperature under the flow of H_2 and thiophene. Thiophene acts like a catalyst in the reaction, where 2–5 vol.% has increased the quality of WS_2 nanotubes.[21] WS_2 nanotubes can also be prepared using a direct pyrolysis method in which the inorganic species was WS_4^{2-}, and the surfactant was cetyl trimethyl ammoniumbromide (CTAB). WS_2 nanotubes were formed through removal of the organic surfactants and the simultaneous reduction of WS_4^{2-} when heated to high temperatures where the carbon acts as a reducing agent.[22]
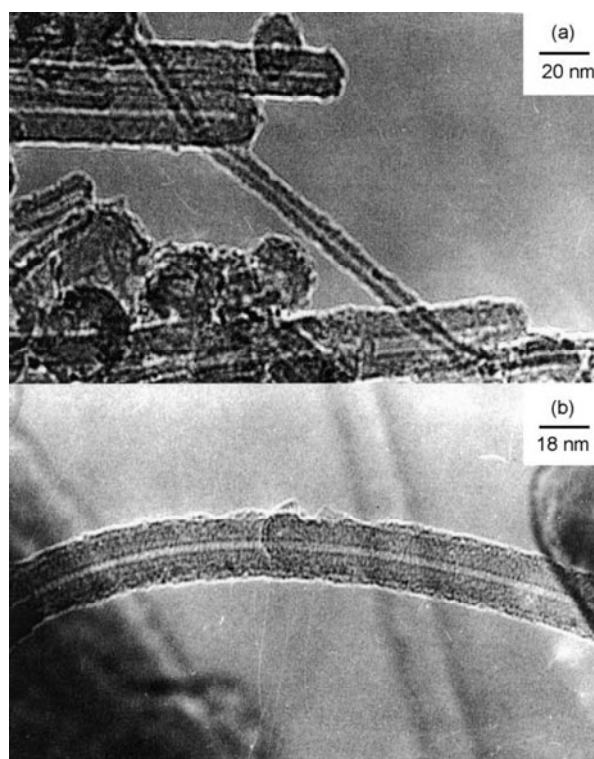
Figure 4: (a) Low-resolution TEM images of MoS_2 nanotubes grown by the decomposition of ammonium thiomolybdate; (b) HREM image of the MoS_2 nanotube [from ref 23].
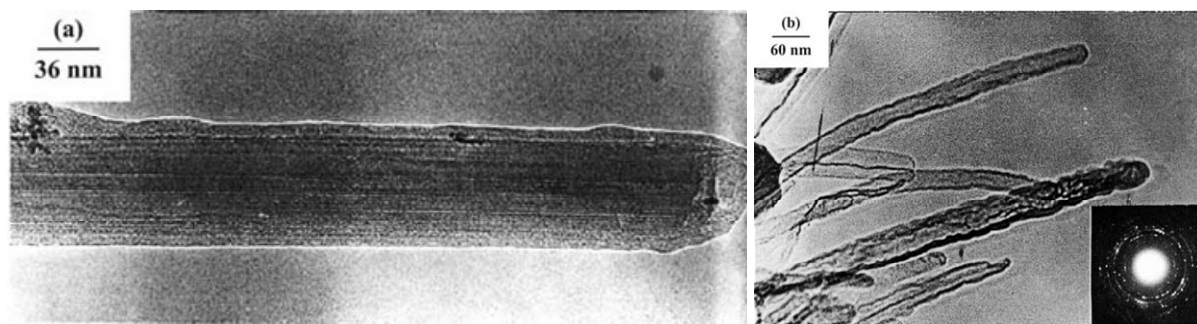
2.1. Brief overview of inorganic graphene analogues

Thermal decomposition of amorphous Mo and W trisulphides has been investigated under a steady gas flow, to explore the formation of the disulphide nanotubes in hydrogen atmosphere.[23] Mo and W trisulphides are prepared by thermal decomposition of the ammonium thiometallates, $(NH_4)_2MS_4$ (M = Mo, W) (Figure 4). Similarly, nanotubes of Mo and W diselenides have been prepared by the decomposition of the triselenide or the ammonium selenometallate at elevated temperatures under the flow of H_2.[24] Confined reactions have been used to control the size of MoS_2 nanotubes by growing in the voids of an anodic alumina membrane, by decomposing $(NH_4)_2MoS_4$ inside the pores of the membranes.[25] MoS_2 nanotubes were obtained by heating MoS_2 powder covered with a Mo foil in the presence of H_2S.[26] Laser ablation of MoS_2 and WS_2 targets produces substantial amounts of inorganic fullerenes and nanotubes.[27] Nanotubes of HfS_2 are obtained by the decomposition of HfS_3 in an atmosphere of H_2 +Ar (1:9), at 1170 K. Bulk HfS_2 is an indirect band gap semiconductor with an energy of ∼2.1 eV. The photoluminescence spectrum of the nanotubes shows a band at 676 nm due to trapped states, and the band is blue shifted with respect to that of bulk HfS_2 powder. The Raman spectrum of the HfS_2 nanotubes shows a band due to the A_{1g} mode, and another due to the E_g. The full-width at half maximum (FWHM) of the A_{1g} band is 11 cm^{-1} in the nanotubes compared to 8 cm^{-1} for the bulk sample.[28] ZrS_2 nanotubes admixed with nanorods have been prepared by the thermal decomposition of ZrS_3 under H_2 and Ar at 1170 K.[28] The nanotubes and nanorods of $NbSe_2$ have been prepared by the decomposition of the corresponding triselenide, at ∼970 K in argon atmosphere.[29] NbS_3 when heated in a stream of H_2 (100 sccm) at 1000 °C for 30–60 min, produces good yield of NbS_2 nanostructures.[30]

2.1. Brief overview of inorganic graphene analogues

For CdSe nanotubes, the metal oxide was reacted with the selenidizing reagent in the presence of a surfactant such as CTAB. The nanotubes of CdSe, though extended in one direction show quantum confinement and the absorption band is blue-shifted to 550 nm from 650 nm of the bulk sample.[31] Layer-rolled structures of nickel sulphide have been obtained by sulphidizing the $Ni(NH_3)_4$ complex by CS_2 in the presence of aqueous ammonia under hydrothermal conditions.[32] Rao et al. have prepared a variety of oxide nanotubes including SiO_2, Al_2O_3, V_2O_5, MoO_3 and RuO_2 employing carbon nanotube as templates (Figure 5). In this synthetic procedure, acid-treated MWNT bundles were coated with a suitable precursor of the metal oxide, and the coated composites heated to high temperatures to remove the carbon template. The nanotube features are essentially retained in the oxide–nanotube composites even after calcination at 500 ^{o}C. The nanotube templates could be removed successfully by heating at 750 ^{o}C for several hours.[33]


Figure 5: (a) TEM image of a ZrO_2 coated CNT. (b) Hollow ZrO_2 nanotubes after removal of the CNT template [from ref 3].

2.1.3: Properties and Applications of Inorganic fullerenes and nanotubes

Electronic properties: MoS_2, $MoSe_2$, WS_2, WSe_2, GaS and GaSe are well known semi-conducting materials and can find suitable applications in the field of electronics. It has been shown experimentally and theoretically that the bandgap of semiconducting nanotubes such as MoS_2 and GaSe, shrinks with decreasing nanotube diameter. This is attributed to two factors: (1) quantum size effect of the closed nanostructures, and (2) the deformation of the chemical bonds in the curved sheet leading to a less than perfect hybridization of the atomic orbitals. It is also shown that armchair nanotubes were often found to have an indirect (Δ–Γ)
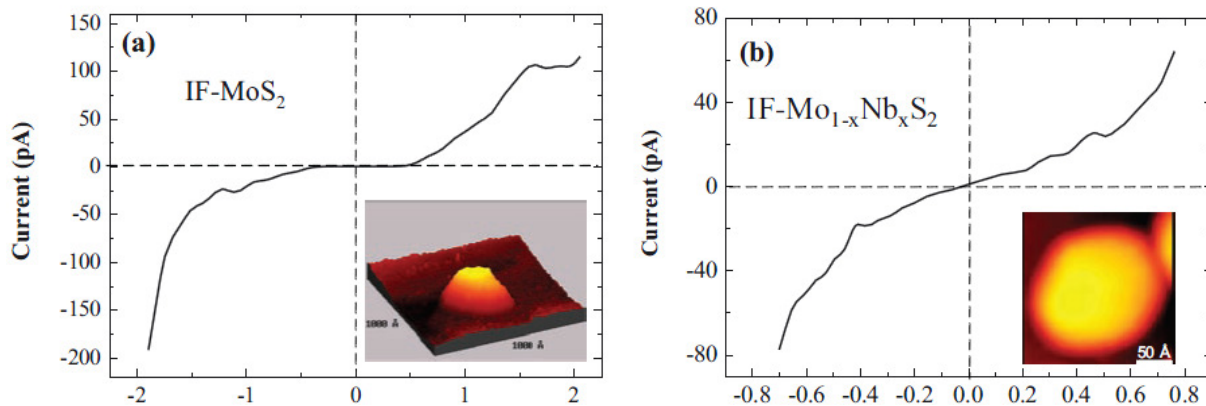
Figure 6: I-V curves at room temperature measured on (a) an IF MoS_2 nanoparticle (~40 nm diameter), (b) an IF-$Mo_{1-x}Nb_xS_2$ nanoparticle (~ 30 nm dia.) The insets show the corresponding topographic images [from ref 34 (b)].

electronic transition, where as zig-zag nanotubes which possess a direct (Γ–Γ) transition may possibly have strong luminescence on optical or electrical excitation.[4] The effect of Nb substitution on the electronic structure of MoS_2 has been investigated theoretically using density functional tight binding method (DFTB) and predicted that mixed $Mo_{1-x}Nb_xS_2$ nanotubes (with varying Nb contents) should exhibit metallic character. IF-$Mo_{1-x}Nb_xS_2$ nanoparticles synthesized by the gas-phase route did exhibit metallic behavior (Figure 6).

2.1. Brief overview of inorganic graphene analogues

This is a remarkable demonstration that doping can significantly alter the electronic properties of semiconducting IF nanoparticles.[34]

Mechanical properties: Mechanical properties of WS_2 nanotubes were studied using atomic force microscopy (AFM) and scanning electron microscopy (SEM). In the first study the force-displacement curve from AFM studies showed a singularity point that was ascribed to the buckling of the WS_2 nanotube and the Young's modulus was estimated at 170GPa using the Euler formula.[35] Later, similar experiments were done in SEM and the Young's modulus was close to 150GPa calculated from the buckled shape according to the Elastic theory.[35b] Fullerene-like WS_2 and MoS_2 nanoparticles were shown to withstand shockwaves of up to 25 and 30 GPa, respectively making these materials probably the strongest cage molecules showing applications for shielding in cars and, also as additives to strengthen the construction materials.[36] Raman spectroscopy of these nanoparticles indicated no degradation under hydrostatic pressures of 20 GPa, indicating again their high pressure resilience[37] compared to carbon nanotubes and fullerenes owing graphite-to-diamond transformation below 1.7 GPa.[38]

Hydrogen storage in inorganic nanotubes: Investigation of hydrogen storage of various nanomaterials is of prime interest because of their high surface areas and large surface to volume ratio, which favors physical or chemical interactions. Chen et al.[39] have studied the electrochemical hydrogen storage in MoS_2 nanotubes with the storage of 0.97% wt. of hydrogen. The interaction of MoS_2 nanotubes and H_2 was found to be in between carbon nanotubes (physisorption) and metal hydride electrodes (chemical process). Hydrogen storage in TiS_2 nanotubes has been explored, since Ti is lighter element than Mo it is

considered as a better candidate for hydrogen storage. It is shown that TiS_2 nanotubes uptakes 2.5 wt.% of hydrogen at 298K and 4MPa.[40]

Catalysis: Layered metal chalcogenides are known to be excellent catalysts for hydrodesulfurization of sulfur containing aromatic hydrocarbons.[41] It is shown that Ni nanoparticles deposited onto a MoS_2 nanotube is found as catalyst for the hydrodesulfurization of thiophene and a few of its derivatives at relatively low temperatures showing the conversion efficiencies up to 96% providing a new way of eliminating sulphur pollution, enabling the efficient and clean utilization of organosulfur compounds.[42] MoS_2 nanotubes obtained by the decomposition of ball-milled ammonium thiomolybdate powder in H_2 and thiophene atmosphere, has been used as a catalyst for the methanation of CO with H_2. Catalyst was found stable even after 50 h of consecutive catalyzing cycles (Figure 8).[43]
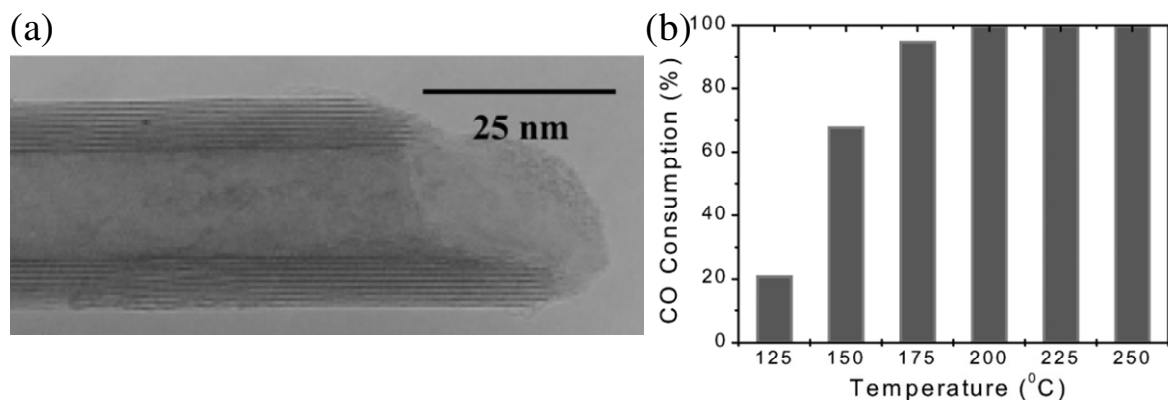

Figure 8: (a) HRTEM image for one open-ended tube tip (b) Catalytic activity of open-ended MoS2 nanotubes for methanation of carbon monoxide and hydrogen [From ref 43].

2.1.4: Inorganic graphene analogues

Synthesis: Graphene, a single-layer of carbon atoms tightly packed in a honeycomb lattice has generated an immense interest in scientific community in the last few-years owing to its outstanding properties and possible potential applications.[44] Synthesizing layered structures which are analogous to graphene is of enormous interest because of the interesting properties and potential applications offered by these atomic layers. Coleman et al.[45] have reported the synthesis of defect free graphene dispersions from bulk graphite by ultrasonication in NMP and other solvents for several hours.[46] Later the same technique has been employed to obtain single- and multi-layers of transition metal dichalcogenides such as MoS_2, WS_2, $MoSe_2$, $MoTe_2$, $TaSe_2$, $NbSe_2$ and $NiTe_2$, along with BN and Bi_2Te_3 in various
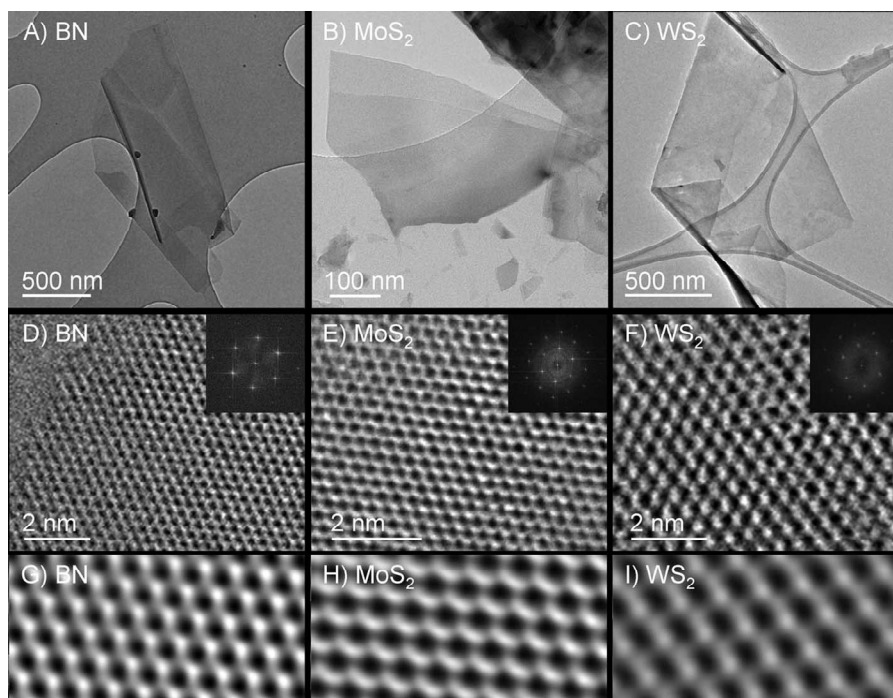
Figure 9: TEM of nanosheets. (A to C) Low resolution TEM images of flakes of BN, MoS_2, and WS_2, respectively. (D to F) High-resolution TEM images of BN, MoS_2, and WS_2 monolayers. (Insets) Fast Fourier transforms of the images. (G to I) Butterworth-filtered images of sections of the images in (D) to (F) [from ref 45].

2.1. Brief overview of inorganic graphene analogues

organic solvents via sonication (Figure 9). The concentrations of the resulting MoS_2 and WS_2 suspensions are 0.30 and 0.15 mg/mL respectively. The important factor for choosing the appropriate solvent for given material is that solvent and the exfoliating material should have the similar surface energy. It is also shown that these material suspensions can blend with other nanomaterials or polymer solutions to prepare composites for various applications.[45] In the detailed study for MoS_2 carried out by the same group reported the importance of the sonication time and centrifuge speed for obtaining the maximum concentration of MoS_2. The dispersed concentration can be increased to ~40 mg/mL by increasing the sonication time to 200 h. However, the lateral size of the flake was found to be ~ 700 nm after 60 h after which it falls off because of sonication induced scission. After centrifuging the dispersion at 5000 rpm the flakes had a mean length and width of $\langle L \rangle \approx 0.3$ μm and $\langle w \rangle \approx 0.15$ μm where as for the 300 rpm the flake dimensions increased by reaching $\langle L \rangle \approx 2$ μm and $\langle w \rangle \approx 1.2$ μm.[47] Zhou et al. reported the mixed-solvent strategy for exfoliating the inorganic layered materials basing on Hansen solubility parameters and found that the ethanol–water at an appropriate ratio gives 0.018 mg/mL for MoS_2 and 0.032 mg/mL for WS_2.[48] Later, Yao et al. reported a procedure using low-energy ball milling combined with sonication procedure for the exfoliation of inorganic layered materials and found that 1.2 mg/mL for BN and 0.8 mg/mL for MoS_2 in 200 mL 0.05 weight% SDS–water.[49]

2.1. Brief overview of inorganic graphene analogues
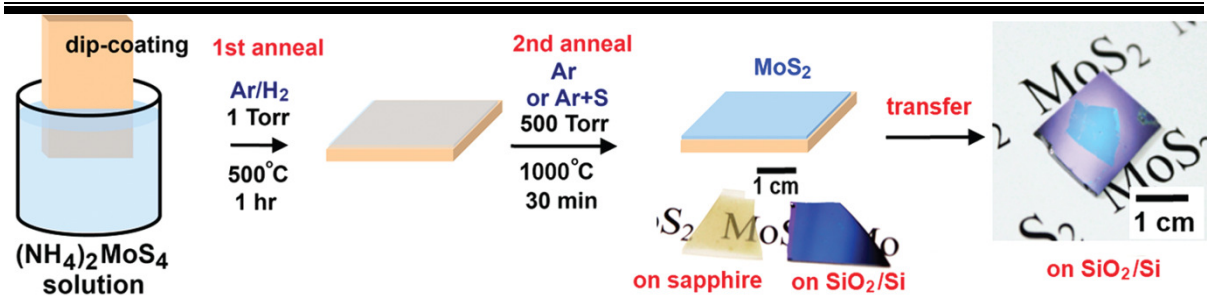
Figure 10: (a) Schematic illustration of the two-step thermolysis process for the synthesis of MoS$_2$ thin layers on insulating substrates. The precursor (NH$_4$)$_2$MoS$_4$ was dip-coated on SiO$_2$/Si or sapphire substrates followed by the two-step annealing process. The as-grown MoS$_2$ film can be transferred onto other arbitrary substrates [from ref 50].

Large-area MoS$_2$ thin layers are prepared by high temperature annealing of a thermally decomposed ammonium thiomolybdate layer in the presence of sulphur (Figure 10). Transistor is fabricated in a bottom gate geometry has shown n-type characteristics with on/off current ratio ~10^5 and electron mobility up to 6 cm^2/(Vs).[50] Large-area MoS$_2$ films were grown on a SiO$_2$ substrate by pre-deposition of Mo film using chemical vapor deposition at temperatures of 500-750 °C. The typical mobilities of few-layer MoS$_2$ obtained by this method ranges from 0.004 to 0.04 cm^2 V^{-1}s^{-1}.[51]

Single layer (SL) MoS$_2$ is obtained on a sulphur-preloaded copper surface where the sulfur source is available only for the first MoS$_2$ monolayer.[52] Free-standing nanosheets of MoS$_2$ and WS$_2$ were synthesized by low-temperature (360 °C) decomposition of single-source precursors (ammonium tetrathiotungstate, ammonium tetrathiomolybdate) containing both metal and sulfur in oleylamine.[53] Laser-thinning of multilayered MoS$_2$ provides a reliable approach to obtain SL-MoS$_2$ with defined shape and size, the semiconducting properties of the laser-fabricated SL-MoS$_2$ are comparable with the pristine SL-MoS$_2$.[54] Synthesis of nanosheets of layered materials such as MoS$_2$, WS$_2$, TiS$_2$, TaS$_2$, ZrS$_2$ and graphite were reported by intercalating lithium electrochemically and subsequent exfoliation

in water.[55] Recently, few-layer MoS_2 has been synthesized on the graphitic surface by heating amorphous MoS_3 and reduced graphite oxide at 1000 °C in high-vacuum conditions to obtain MoS_2 nanoparticles on the graphitic surface.[56] $(NH_4)_2MoS_4$ was used as a precursor for the synthesis of molybdenum sulfide on the graphitic surface followed by annealing at 600 °C and 800 °C.

Characterization of graphene-analogues is inevitable to understand the structure-property relation in these materials. For this purpose, various microscopic and spectroscopic techniques have been employed. Characterization involves determination of the number of layers and purity of sample in terms of absence or presence of defects. X-Ray diffraction is used for determining the purity of the phase formed and calculating the number of layers to some extent. Raman Spectroscopy is employed to understand the behavior of the phonons in few-layer compared to the bulk counterparts. UV-Vis is very useful technique in particular to determine the concentration of the exfoliated samples for liquid phase exfoliation method. Atomic force microscopy provides information about the thickness in turn the average number of layers in the sample prepared. Transmission microscopy is an another important tool to characterize graphene analogues in understanding the structure, stability, edges which help to understand their role in catalysis and the origin of magnetism in these nanostructures.

Transmission electron microscopy studies are carried out on suspended single- and few-layer MoS_2 and found that monolayer MoS_2 display long-range crystalline order, with surface roughness of 1 nm in height which is observed as ripples similar to that of graphene, explaining the stability of two-dimensional materials. Electron diffraction has been effectively utilized to distinguish single-layer from the thick flakes by changing the beam incidence angle, which leads to a stronger variation in the relative spot intensities within the

same lattice plane family {1100}. The observed ripples could also explain the degradation of mobility in MoS_2 due to exfoliation.[57] Recently Komsa et al. reported that during the continuous imaging of a single-layer MoS_2 obtained by mechanical exfoliation at an operating voltage of 80 kV results in increase of the number of vacancy sites (mainly on the S sublattice) accompanied by crack formation along with the lateral shrinkage of the membrane. It has also been shown that it is possible to dope the vacancies created by the electron beam irradiation with impurity atoms.[58] Single-layer MoS_2 obtained by chemical exfoliation has revealed the coexistence of metallic and semiconducting phases in the form of $2H-MoS_2$ and $1T-MoS_2$ within homogeneous two-dimensional MoS_2 nanosheets as shown in Figure 11.[59]
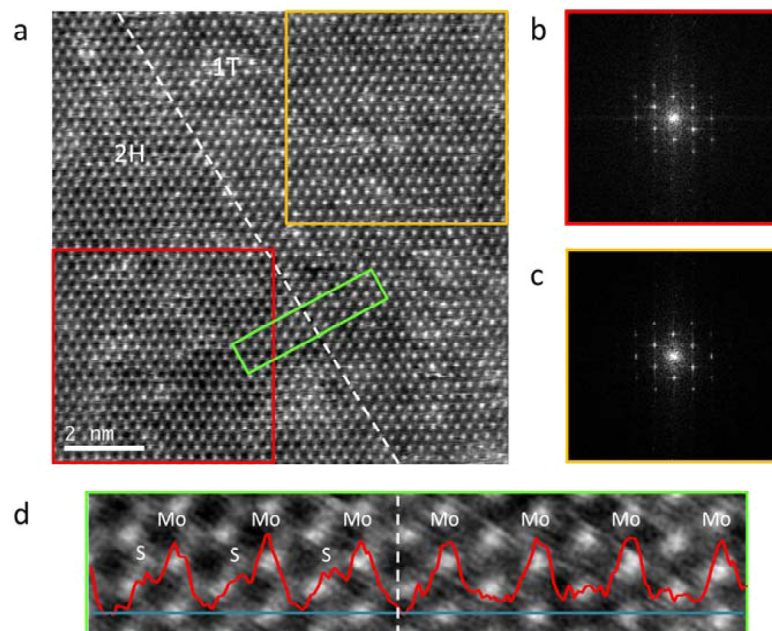
Figure 11: (a) STEM image of a region where a boundary between 2H (left) and 1T (right) phases is observed. The phase boundary is parallel to {-1100} planes and marked by a dashed line. (b, c) Fourier transform image of the (b) lower left and (c) upper right box of the STEM images. (d) Enlarged image of the region indicated by the green rectangle in image a. The intensity profile along the blue line is overlaid on the image. The width of the image corresponds to 3.9 nm [from ref 59].

2.1. Brief overview of inorganic graphene analogues

Properties: Bulk MoS_2 is an indirect band gap semiconductor with an energy gap of ~1.2 eV and has attracted interest as photovoltaic and photocatalytic material.[60] It is of recent interest to investigate the various properties of inorganic layered materials chalcogenides when they exfoliated to single and few-layers. Mak et al. studied the optical properties and electronic structure of ultrathin MoS_2 films as a function of number of layers N= 1; 2; 3; . . ; 6. It is found that with decreasing N, there is a progressive confinement-induced shift in the indirect gap from the bulk value of 1.29 eV to 1.90 eV and transforming it from a indirect band gap semiconductor to direct band gap semiconductor with emerging photoluminescence of greater than 10^4 of its bulk counterpart.[61] Photoluminescence in MoS_2 obtained by mechanical exfoliation was also reported by Splendiani et al. and they observed that there is
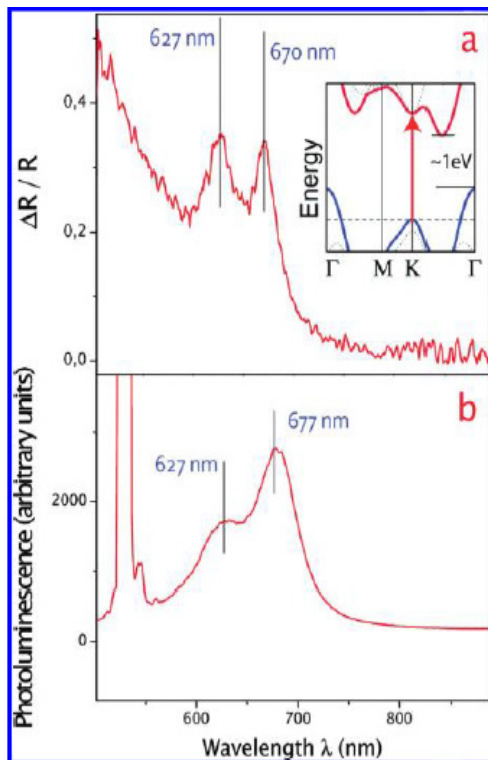
Figure 12: Reflection and photoluminescence spectra of ultrathin MoS_2 layers. (a) Reflection difference due to an ultrathin MoS_2 layer on a quartz substrate, which is proportional to the MoS_2 absorption constant. The observed absorption peaks at 1.85 eV (670 nm) and 1.98 eV (627 nm) correspond to the A_1 and B_1 direct excitonic transitions with the energy split from valence band spin-orbital coupling. The inset shows the bulk MoS_2 band structure neglecting the relatively weak spin-orbital coupling, which has an indirect bandgap around 1 eV and a single higher energy direct excitonic transition at the K point denoted by an arrow. (b) A strong photoluminescence is observed at the direct excitonic transitions energies in a monolayer MoS_2. Such luminescence is absent in the indirect bandgap bulk MoS_2 sample [from ref 62].

an increase in photoluminescence intensity with decreasing layer thickness, and it is maximum for a monolayer (Figure 12).[62] Later, Eda et al. has also observed the emerging photoluminescence from the SL-MoS$_2$ obtained by Li-intercalation of bulk MoS$_2$, indicating that SL-MoS$_2$ retains the structural integrity with low density of critical defects.[63] Gutiérrez et al. reported the synthesis of few-layer WS$_2$ by sulfidation of WO$_3$ sheets at 800 °C and found the room-temperature photoluminescence from few-layer WS$_2$ at 630 nm with high intensity and interestingly it is stronger at edges compared to the center of the sheets by 25 times.[64] Few-layer MoS$_2$ obtained by the liquid phase exfoliation of bulk MoS$_2$ is shown to emit at 440 nm and the fluorescence intensity was further increased by making composites with Ag@SiO$_2$ and explained on the basis of metal-enhanced fluorescence.[65] Cao et al. reported the circularly polarized photoluminescence from SL- MoS$_2$, which shows up to 50% polarization and the first principles calculations also revealed that it is an ideal candidate for studying the valleytronics.[66] SL-MoS$_2$ samples obtained from mechanical exfoliation are studied using spatially and temporally resolved pump-probe measurements. Carriers are injected by direct interband absorption of a 390-nm pump pulse and detected by measuring the differential reflection of a 660-nm probe pulse. It is found that a carrier lifetime of 100 ± 10 ps and a carrier diffusion coefficient of 20 ± 10 cm^2/s, corresponding to a mobility of 800 cm^2/Vs and a diffusion length of 450 nm in SL-MoS$_2$.[67]

Single- and bi-layer MoS$_2$ are mechanically exfoliated from the bulk MoS$_2$ are transferred to a substrate with an array of microfabricated circular holes. Using an atomic force microscope the in-plane stiffness of SL-MoS$_2$ obtained as 180±60 Nm^{-1}, corresponding to an effective Young's modulus of 270±100 GPa, which is comparable to that of steel. The breaking strength or Young's modulus (%) is 11%, corresponds to the upper theoretical limit

2.1. Brief overview of inorganic graphene analogues

which indicates that the material is highly crystalline and defect-free.[68] Castellanos-Gomez et al. obtained an average effective Young's modulus of 330 ± 70 GPa for MoS_2 nanosheets having 5 to 25 layers (Figure 13).[69] Later, theoretical studies have given the insights to the failure of this mechanism, the tensile strength of SL-MoS_2 is governed by out-of-plane soft-mode phonon instability under biaxial tension and uniaxial tension in the armchair direction.[70] MoS_2 nano sheets with the lateral dimensions of 0.7 μm and ~2- 5 μm are obtained by changing the sonicating time and centrifuging speeds of liquid phase exfoliation. The addition of 0.7 μm sized flakes degraded the mechanical properties of PVA with E of 1.6 GPa, where as the larger flakes improved the performance having Young modulus of 3.2 GPa compared with polyvinyl alcohol Young's modulus of 2.8 GPa.[47]
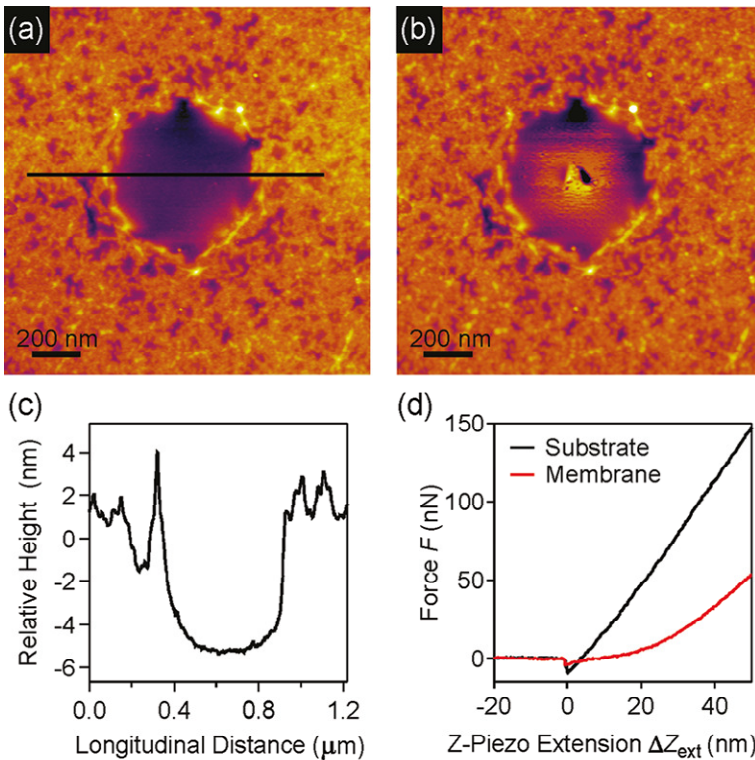
Figure 13: Suspended MoS_2 membranes and their mechanical failure. (a) AFM image of a monolayer MoS_2 flake suspended over a hole before the indentation experiment and (b) after it. A hole can be clearly seen in the center of the membrane at the location where the AFM tip punctured it. (c) Height profile of the section highlighted in (a) shows that the membrane adheres to the sidewalls over a vertical distance on the order of 5 nm, resulting in pretension between 0.02 and 0.1 Nm^{-1}. (d) Acquired force versus z-piezo extension curves for the suspended membrane and the substrate.[from ref 69]

2.1. Brief overview of inorganic graphene analogues

Applications:

Two-dimensional materials have attracted significant attention in the scientific community in the last few years due to their potential transport physics and prospects for technological applications in various fields. In particular, graphene-based transistors have been explored extensively for their potential use in logic and radiofrequency applications. Another application is electrochemical devices.

Transistors: The main advantage of graphene based field-effect transistors (FET) is the associated carrier high mobility of up to 10^6 cm^{2}V^{-1}s^{-1}.[71] However, several problems remain with graphene due to absence of a bandgap, which is essential for transistor applications. Subsequently, considerable efforts have been made to "open" the bandgap of graphene, such as changing the dimensions to form graphene nanoribbons.[72] In this context, there has been an extensive search for other layered materials that are analogous to graphene but with semiconducting characteristics.[73]

Recently Novoselov et al. has fabricated a FET on single-layer of MoS$_2$ obtained by mechanical exfoliation using back gate device fabrication mode and reported that the mobilities are in the range of 0.5–3 cm^{2}V^{2}s^{-1}.[73] Later, Radisavljevic et al. has modified the fabrication procedure by using top gate uisng HfO$_2$ as dielectric and found that at room-temperature single-layer MoS$_2$ has mobilities of at least 200 cm^{2}V^{-1}s^{-1}, with current on/off ratios of 10^8 with ultralow standby power dissipation (Figure 14).[74] Soon after this work there are plenty of reports appeared in the literature by modifying various important parameters.

2.1. Brief overview of inorganic graphene analogues
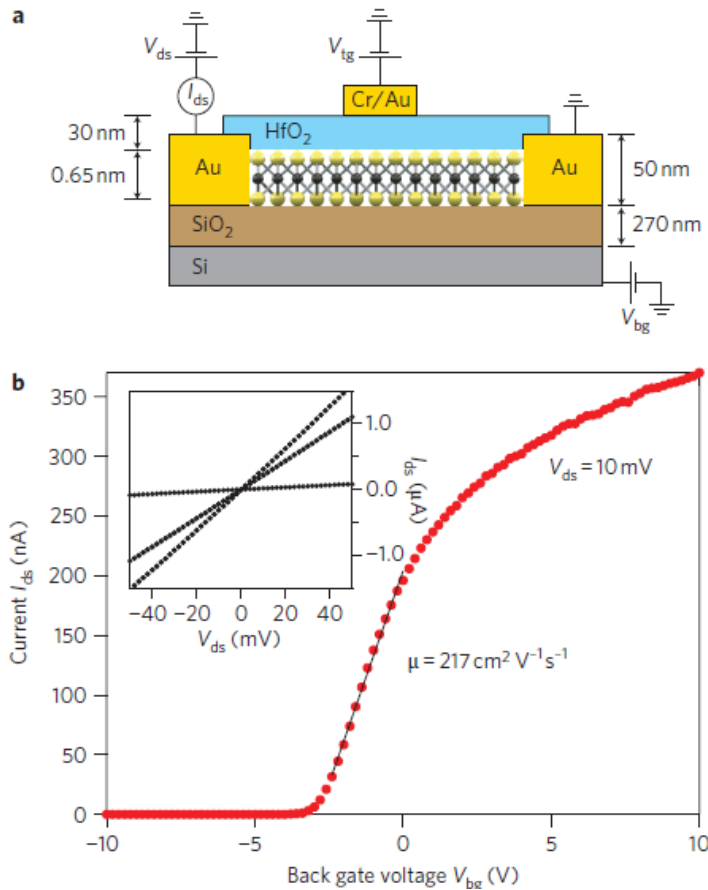
Figure 14: (a) Cross sectional view of the structure of a monolayer MoS_2 FET together with electrical connections used to characterize the device. A single layer of MoS_2 (thickness, 6.5 Å) is deposited on a degenerately doped silicon substrate with 270-nm-thick SiO_2. The substrate acts a back gate. One of the gold electrodes acts as drain and the other source electrode is grounded. The monolayer is separated from the top gate by 30 nm of ALD-grown HfO_2. The top gate width for the device is 4 mm and the top gate length, source–gate and gate–drain spacing are each 500 nm. (b) Room-temperature transfer characteristic for the FET with 10 mV applied bias voltage V_{ds}. Backgate voltage V_{bg} is applied to the substrate and the top gate is disconnected. Inset: I_{ds}–V_{ds} curve acquired for V_{bg} values of 0, 1 and 5 V [From ref 74].

Transistor fabricated on SL-MoS_2 in which Al_2O_3 is used a top-gate dielectric deposited with atomic-layer-deposition technique (ALD). Capacitance-Voltage study has revealed that there is a good interface between SL-MoS_2 and Al_2O_3. It is found that the field-effect mobility of electrons using top-gate is 517 cm^2/Vs with highest current on/off ratios over 10^8.[75] A transistor is fabricated on the 15 nm thick MoS_2 sheet obtained by mechanically exfoliated MoS_2 based on electric double layer transistor (EDLT) technique has demonstrated that it has ambipolar characteristics. It is shown that it has on/off ratios over 200 in thin flake. Hall effect measurements showed that the hole mobility (86 cm^2 $V^{-1}s^{-1}$) is

2.1. Brief overview of inorganic graphene analogues

larger than that of the electrons (44 cm^{2}V^{-1} s^{-1}) suggesting that p-type operation is more favorable for FET devices.[76] MoS$_2$ thin-film transistors were fabricated with ion gel gate
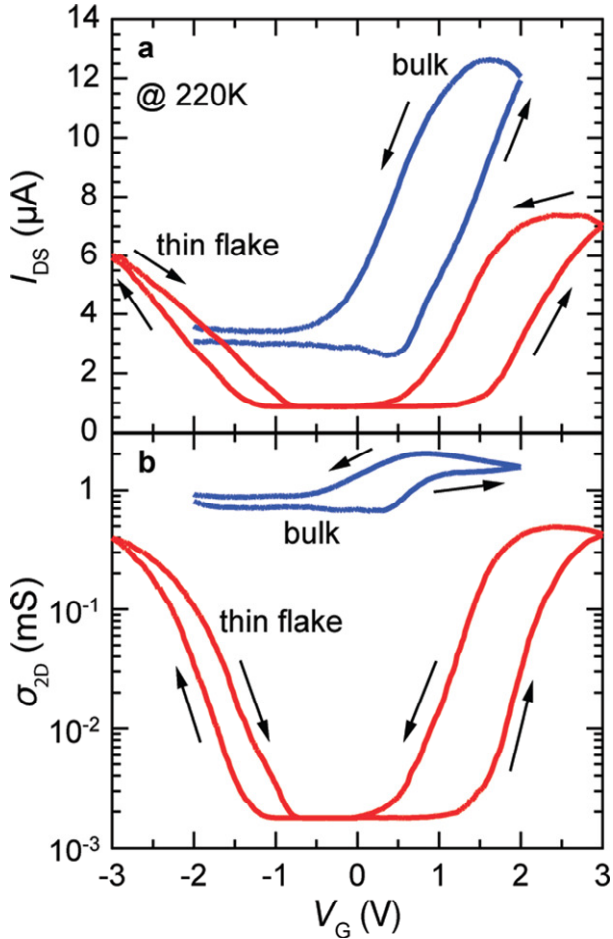
Figure 15: Transfer curve of bulk (1000 μm × 500 μm × 10 μm) and thin flake (20 μm × 20 μm × 15 nm) MoS$_2$ EDLTs. (a) Change in the channel current I$_{DS}$ as a function of gate voltage V$_G$. V$_{DS}$ is 0.2 V for both samples. Ambipolar transistor operation is only observed in thin flake devices, showing an increase in the channel current with an increase in the gate voltage |V$_G$| for both hole and electron conductivities. The I$_{DS}$ (thus on/off ratio) is limited by large contact resistance for both bulk and thin flake devices (b) Change of sheet conductivity σ2D (4-probe) as a function of gate voltage V$_G$. The on/off ratio of the thin flake sample is up to >200 for both electron and hole transport. Transport with high sheet conductivity in the order of ~ mS was observed in the thin flake MoS$_2$ EDLT for both electron and hole carriers. Large conductivity in bulk device is mainly ascribed to the small inside resistance that is parallel to the surface channel [From ref 77].

dielectrics and showed a low threshold voltage (<1 V), high mobility (12.5 cm^2/(Vs)) and a high on/off current ratio (10^5). These transistors exhibited high mechanical flexibility and no degradation in the electrical characteristics even bent after a curvature radius of 0.75 mm(Figure 15).[77] Chakraborthy et al. has reported the in-situ carrier dependent Raman study of a top-gated SL- MoS$_2$ transistor with on-off ratio ~10^5, field-effect mobility of 50 cm^2/Vs has shown that A$_{1g}$ phonon mode softens and broadens with electron doping, whereas E$_{2g}$ mode

2.1. Brief overview of inorganic graphene analogues

remains inert up to electron doping of $\sim 2 \times 10^{13}/cm^2$.[78] Lee et al. has reported the fabrication of two terminal device and FET's on MoS_2 prepared using liquid phase exfoliation. It has n-type FET characteristics with small on/off ratios of 3–4 and mobilities of $0.117\ cm^2V^{-1}s^{-1}$. Possible reasons for low mobilities may be due to adsorption of the solvent remnants or impurities that comes from the exfoliation procedure, and might influence the interface states that result in dipole layers which may screen the external gate field.[79] Low-temperature electrical transport experiments in FET devices with Single-, bi- and tri-layers of MoS_2 have been carried out and found that the electrons in all cases are localized well up to room temperature at most gate voltages and display variable range hopping transport as temperature is lowered. The disorder is likely to arise from Coulomb potential of randomly distributed charges at the MoS_2-SiO_2 interface.[80]

Phototransistor fabricated on SL-MoS_2 has revealed that the photocurrent generation completely depends on the illuminating optical power at a constant drain or gate voltage and has a switching time within 50 ms for photocurrent generation and annihilation.[81] SL-MoS_2 filed-effect transistors have been utilized in fabricating an integrated small-signal analog amplifier by connecting two top-gated MoS_2 transistors connected in series, has a small-signal voltage gain higher than 4 and reaching 10 in the single-transistor configuration, and at higher frequencies up to 2 kHz has a gain higher than 1 and no signal distortion.[82]

After the investigations on FET using MoS_2 as a channel material the other sulphides and selenides of tungsten has also been reported. Hwang et al. has reported the fabrication of FETs with few-layer WS_2 obtained by sonicating the WS_2 crystals in isopropyl alcohol has demonstrated the ambipolar behavior with high ($\sim 10^5$) on/off current ratio and also show clear photo response to visible light because of available band-gap in this material.[83]

2.1. Brief overview of inorganic graphene analogues

Podzorov et al. has fabricated FETs of bulk WSe_2 with ambipolar characteristics having hole mobilities of 500 cm^2/(Vs) and high current on/off ratio as 10^5.[84] FET is fabricated on single-layer of WSe_2 obtained by mechanical exfoliation in the top-gate geometry which has hole mobilities of ~250 cm^2/(Vs), subthreshold swing of ~60 mV/dec, and on/off ratios of 10^6 at room temperature.[85]

Li-ion Batteries: With increase in demand for the energy, lithium-ion batteries have emerged as potential candidates for the energy storage and portability. This has initiated the research community for the intensive search of Li-ion battery based materials with high abundance of elements, power density, high energy, low cost, electrochemical stability, light weight and less environmental concerns. However, rechargeable batteries have not yet replaced primary batteries as the dominant energy storage because of their high cost for a limited cycling life, slow recharging, unsatisfactory energy density and low power capability.

Layered transition metal dichalcogenides MX_2 (M = Mo, Ti, V, and W, X = S or Se) can intercalate and de-intercalate the Li-ions into their structure between the layers along with the fast-ion conductivity. These features, have led them to consider a host materials for application in the field of primary or rechargeable batteries. The first lithium ion battery using MoS_2 as the electrode material gave impressive results which has led to further investigate the different morphologies of MoS_2.[86] MoS_2 with enlarged c-lattice parameter and surface area obtained by exfoliation and restacking of commercially available MoS_2, showed the first charge capacity of 800 mAh/g and maintained a capacity of 750 mAh/g after 20 cycles at current density of 50 mA/g.[87] Bulk MoS_2 electrodes exhibited decrease in the charge capacity from 800 to 226 mh/g after 50 cycles. Feng et al.[88] synthesized MoS_2 nanoflakes by a hydrothermal method and found that the MoS_2 nanoflake electrodes exhibit a

2.1. Brief overview of inorganic graphene analogues

capacity of ~1000 mAh/g. Hierarchical spheres composed of ultrathin MoS_2 nanosheets prepared by polystyrene microsphere-assisted hydrothermal method show lithium storage capacity of 672 mAh /g.[89] MoS_2 nanoflowers synthesized using ionic liquid assisted hydrothermal method showed a reversible capacity of~900 mAh/g.[90] Recently, a simple, one-pot synthesis of graphene-like MoS_2 nanoplates obtained by solvothermal method using molybdenum carbonyl and sulphur showed the first discharge and charge capacities of 1062 and 917 mAh/g, respectively at current density of 1.06 A/g (see Figure 16).[91]

WS_2 has also been studied for the electrochemical applications widely because of having similar structure to MoS_2. The electrochemical study of pristine 3R-WS_2 powder was carried out by Julien et al., demonstrating that 0.6 mols of Li-ions intercalates per mole of WS_2.[92] WS_2 nanotubes shows a reversible capacity of above 500 mA h/g.[93] Co-doped WS_2 nanorods can reversibly store lithium with a capacity of 568 mAh/g at current density of 50 mA/g.[94] Feng et al. proposed a rheological phase reaction for the synthesis of WS_2 nanoflakes, which exhibited higher reversible charging capacity 780 mAh/g with good cycling stability at current density of 47.5 mA/g.[95] Seo et al. obtained the WS_2 nanosheets from $W_{18}O_{49}$ nanorod sulfurization and found that it has the first reversible discharge capacity of 377 mAh/g at current density of 100 mA/g.[96] Ordered mesoporous WS_2 with high surface area has been synthesized using SBA-15 as template which has a storage capacity of 805 mAh/g at a current density of 0.1 A/g.[97] The electrochemical performance of the superacid-treated WS_2 has higher first-cycle reversible capacity of 470 mAh/g at a current density of 25 mA/g.[98]
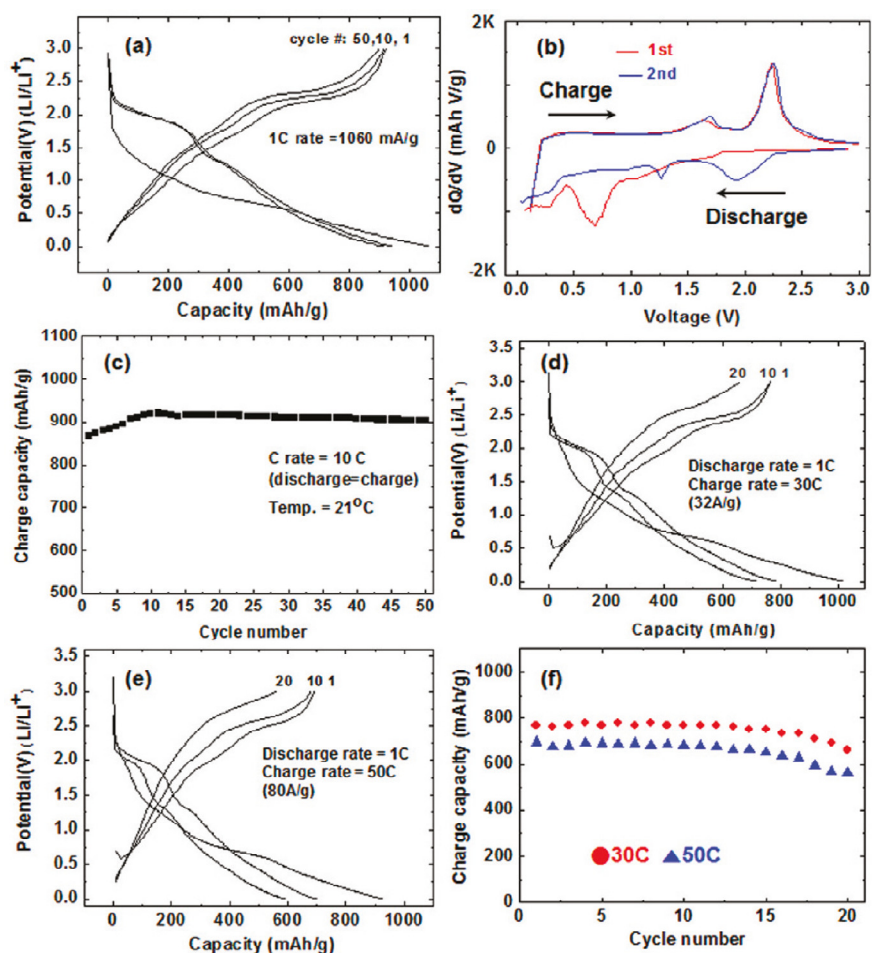
Figure 16: (a) Voltage profiles of MoS$_2$ nanoplates in coin-type lithium half cells between 0 and 3 V at a rate of 1C (=1062 mA/g) (charge and discharge rates were the same) at room temperature. (b) Differential curves of MoS$_2$ nanoplates during the first and second cycles. (c) Plot of charge capacity vs cycle number in coin-type lithium half cells between 0 and 3 V at a rate of 10C rates (charge and discharge rates were the same) at room temperature. (d, e) Voltage profiles of MoS$_2$ nanoplates in coin-type lithium half cells between 0 and 3 V at a rate of 20 and 50C rates (discharge rates to 0 V were 1C) at room temperature. (f) Plot of charge capacity vs cycle number obtained from (d) and (e) [From ref 91].

Commercially available anode material for lithium-ion-batteries is graphite with a relatively small capacity (372 mAh/g).[99] Recently, graphene, a two-dimensional form of graphite, has been studied extensively in electrochemical applications because of large surface area and high chemical tolerance.[44b] Taking this as an advantage, it is used as a

169

matrix for improving the electrochemical performance of various nanomaterials including metal and metal oxides.[100]

Recently, intensive research has been carried out on the composites containing graphene and graphene-like MoS_2 and resulted in significant improvement in both the cyclability and rate capabilities. If the graphene-like MoS_2 is uniformly dispersed in graphene matrix, it inhibits the aggregation and also increases conductivity and leads to enhanced electrochemical properties. In-situ reduction of MoS_2 nanoflakes on graphene nanosheets to form MoS_2/graphene composites has the specific reversible capacity of 1290 mAh/g after 50 cycles at current density of 100mA/g (see Figure 17).[101] Das et al. reported the synthesis of composites of MoS_2 with amorphous carbon via a hydrothermal method with storage capacity of 800 mAh/g at a current of 400 mA/g.[102] Nanocomposites of SL- MoS_2, graphene and amorphous carbon are synthesized using a facile solution-phase method and then annealed in H_2/N_2 atmosphere at 800 °C are used for battery applications and the composites not only has the reversible capacity (900–1100 mAh/g) but also high cyclic stability at 100 mA/g.[103] Graphene-like MoS_2/amorphous-carbon composites prepared by hydrothermal route using sodium molybdate, sulfocarbamide and glucose followed by annealing at 800°C for 2 h in a stream of 10% H_2/N_2 atmosphere has the reversible capacity of 912 mAh/g after 100 cycles.[104] MoS_2/Graphene composites prepared via L-cysteine-

2.1. Brief overview of inorganic graphene analogues
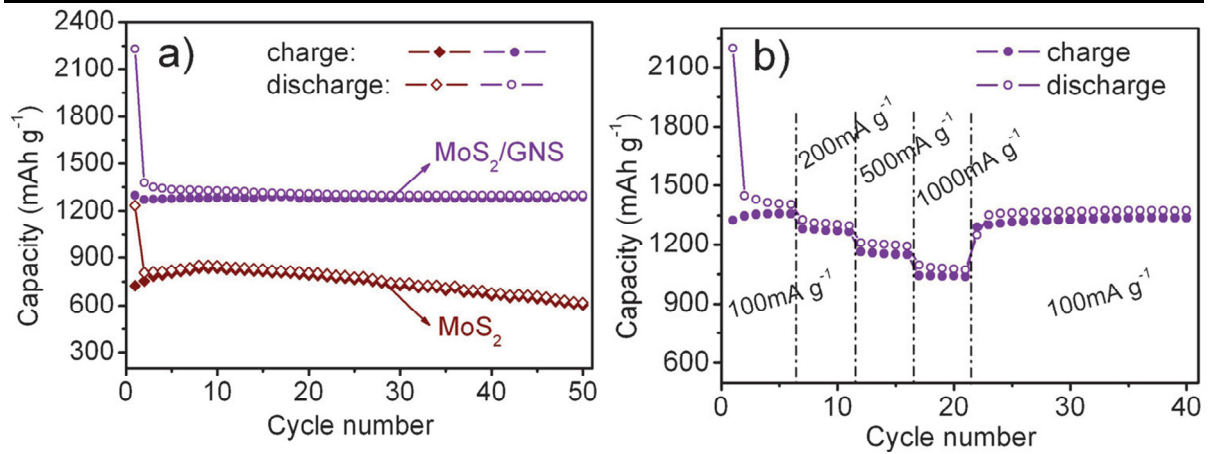
Figure 17: (a) Cycling behaviors of MoS_2 and MoS_2/GNS at a current density of 100 mAg^{-1}. (b) Cycling behavior of MoS_2/GNS at various current densities [From ref 101].

assisted solution phase method followed by annealing in a H_2/N_2 atmosphere at 800 °C for 2 h and has been tested for the Li-ion- batteries and found that the specific capacity of ~1100 mAh/g at a current density of 100 mA/g with no capacity fading even after 100 cycles.[105]

2.1. Brief overview of inorganic graphene analogues

2.1.5: References

[1]   H. W. Kroto, J. R. Heath, S. C. O'Brien, R. F. Curl, R. E. Smalley, *Nature* **1985**, *318*, 162.

[2]   a)R. Tenne, L. Margulis, M. Genut, G. Hodes, *Nature* **1992**, *360*, 444; b)L. Margulis, G. Salitra, R. Tenne, M. Talianker, *Nature* **1993**, *365*, 113; c)Y. Feldman, E. Wasserman, D. J. Srolovitz, R. Tenne, *Science* **1995**, *267*, 222.

[3]   C. N. R. Rao, M. Nath, *Dalton Trans.* **2003**, 1.

[4]   R. Tenne, *Nature Nanotechnol.* **2006**, *1*, 103.

[5]   M. Remškar, *Adv. Mater.* **2004**, *16*, 1497.

[6]   R. Tenne, G. Seifert, *Ann. Rev. Mater. Res.* **2009**, *39*, 387.

[7]   a)M. Bar-Sadan, I. Kaplan-Ashiri, R. Tenne, *Eur. Phys. J. Spec. Top.* **2007**, *149*, 71; b)F. L. Deepak, R. Tenne, *Cent.Eur.J.Chem.* **2008**, *6*, 373; c)M. N. Tahir, A. Yella, J. K. Sahoo, H. Annal-Therese, N. Zink, W. Tremel, *Phys. Status Solidi B* **2010**, *247*, 2338; d)R. Tenne, M. Homyonfer, Y. Feldman, *Chem. Mater.* **1998**, *10*, 3225.

[8]   Y. Feldman, G. L. Frey, M. Homyonfer, V. Lyakhovitskaya, L. Margulis, H. Cohen, G. Hodes, J. L. Hutchison, R. Tenne, *J. Am. Chem. Soc* **1996**, *118*, 5362.

[9]   T. Tsirlina, Y. Feldman, M. Homyonfer, J. Sloan, J. L. Hutchison, R. Tenne, *Fullerene Sci. Tech.* **1998**, *6*, 157

[10]   a)J. Etzkorn, H. A. Therese, F. Rocker, N. Zink, U. Kolb, W. Tremel, *Adv. Mater.* **2005**, *17*, 2372; b)N. Zink, J. Pansiot, J. Kieffer, H. A. Therese, M. Panthöfer, F. Rocker, U. Kolb, W. Tremel, *Chem. Mater.* **2007**, *19*, 6391; c)A. Yella, H. A. Therese, N. Zink, M. Panthöfer, W. Tremel, *Chem. Mater.* **2008**, *20*, 3587.

2.1. Brief overview of inorganic graphene analogues

[11]   A. Margolin, F. L. Deepak, R. Popovitz-Biro, M. Bar-Sadan, Y. Feldman, R. Tenne, *Nanotechnol.* **2008**, *19*, 095601.

[12]   A. Margolin, R. Popovitz-Biro, A. Albu-Yaron, L. Rapoport, R. Tenne, *Chem. Phys. Lett.* **2005**, *411*, 162.

[13]   C. Schuffenhauer, R. Popovitz-Biro, R. Tenne, *J. Mater. Chem.* **2002**, *12*, 1587.

[14]   C. Schuffenhauer, B. A. Parkinson, N. Y. Jin-Phillipp, L. Joly-Pottuz, J.-M. Martin, R. Popovitz-Biro, R. Tenne, *Small* **2005**, *1*, 1100.

[15]   M. Jose-Yacaman, H. Lopez, P. Santiago, D. H. Galvan, I. L. Garzon, A. Reyes, *Appl. Phys. Lett.* **1996**, *69*, 1065.

[16]   D. Vollath, D. V. Szabo, *Mater. Lett.* **1998**, *35*, 236.

[17]   S. Iijima, *Nature* **1991**, *354*, 56.

[18]   C. N. R. Rao, A. Govindaraj, *Acc. Chem. Res.* **2002**, *35*, 998.

[19]   A. Rothschild, J. Sloan, R. Tenne, *J. Am. Chem. Soc* **2000**, *122*, 5169.

[20]   A. Margolin, R. Rosentsveig, A. Albu-Yaron, R. Popovitz-Biro, R. Tenne, *J. Mater. Chem.* **2004**, *14*, 617.

[21]   J. Chen, S.-L. Li, F. Gao, Z.-L. Tao, *Chem. Mater.* **2003**, *15*, 1012.

[22]   Y. D. Li, X. L. Li, R. R. He, J. Zhu, Z. X. Deng, *J. Am. Chem. Soc* **2002**, *124*, 1411.

[23]   M. Nath, A. Govindaraj, C. N. R. Rao, *Adv. Mater.* **2001**, *13*, 283.

[24]   M. Nath, C. N. R. Rao, *Chem. Comm.* **2001**, 2236.

[25]   C. M. Zelenski, P. K. Dorhout, *J. Am. Chem. Soc* **1998**, *120*, 734.

[26]   W. K. Hsu, B. H. Chang, Y. Q. Zhu, W. Q. Han, H. Terrones, M. Terrones, N. Grobert, A. K. Cheetham, H. W. Kroto, D. R. M. Walton, *J. Am. Chem. Soc* **2000**, *122*, 10155.

[27]   R. Sen, A. Govindaraj, K. Suenaga, S. Suzuki, H. Kataura, S. Iijima, Y. Achiba, *Chem. Phys. Lett.* **2001**, *340*, 242.

[28]   M. Nath, C. N. R. Rao, *Angew. Chem. Int. Ed.* **2002**, *41*, 3451.

[29]   M. Nath, S. Kar, A. K. Raychaudhuri, C. N. R. Rao, *Chem. Phys. Lett.* **2003**, *368*, 690.

[30]   M. Nath, C. N. R. Rao, *J. Amer. Chem. Soc.* **2001**, *123*, 4841.

[31]   C. N. R. Rao, A. Govindaraj, F. L. Deepak, N. A. Gunari, M. Nath, *Appl. Phys. Lett.* **2001**, *78*, 1853.

[32]   X. Jiang, Y. Xie, J. Lu, L. Zhu, W. He, Y. Qian, *Adv. Mater.* **2001**, *13*, 1278.

[33]   B. C. Satishkumar, A. Govindaraj, M. Nath, C. N. R. Rao, *J. Mater. Chem.* **2000**, *10*, 2115.

[34]   a)V. V. Ivanovskaya, T. Heine, S. Gemming, G. Seifert, *Phys. Status Solidi B* **2006**, *243*, 1757; b)F. L. Deepak, H. Cohen, S. Cohen, Y. Feldman, R. Popovitz-Biro, D. Azulay, O. Millo, R. Tenne, *J. Am. Chem. Soc* **2007**, *129*, 12549.

[35]   a)I. Kaplan-Ashiri, S.R. Cohen, K. Gartsman, R. Rosentsveig, G. Seifert, R. Tenne, *J. Mater. Res.* **2004**, *19*, 454; b)I. Kaplan-Ashiri, S. R. Cohen, K. Gartsman, V. Ivanovskaya, T. Heine, G. Seifert, I. Wiesel, H. D. Wagner, R. Tenne, *Proc. Natl. Acad. Sci. USA* **2006**, *103*, 523.

[36]   Y. Q. Zhu, T. Sekine, Y. H. Li, M. W. Fay, Y. M. Zhao, C. H. Patrick Poa, W. X. Wang, M. J. Roe, P. D. Brown, N. Fleischer, R. Tenne, *J. Am. Chem. Soc* **2005**, *127*, 16263.

[37]   L. Joly-Pottuz, J. M. Martin, F. Dassenoy, M. Belin, G. Montagnac, B. Reynard, N. Fleischer, *J. Appl. Phys.* **2006**, *99*, 023524.

2.1. Brief overview of inorganic graphene analogues

[38] F. P. Bundy, *J. Geophys. Res.* **1980**, *85*, 6930.

[39] J. Chen, N. Kuriyama, H. Yuan, H. T. Takeshita, T. Sakai, *J. Am. Chem. Soc* **2001**, *123*, 11813.

[40] J. Chen, S.-L. Li, Z.-L. Tao, Y.-T. Shen, C.-X. Cui, *J. Am. Chem. Soc* **2003**, *125*, 5284.

[41] a)R. Prins, in *Adv. Catal., Vol. Volume 46*, Academic Press, **2001**, pp. 399; b)J. V. Lauritsen, M. Nyberg, J. K. Nørskov, B. S. Clausen, H. Topsøe, E. Lægsgaard, F. Besenbacher, *J. Catal.* **2004**, *224*, 94.

[42] F. Y. Cheng, J. Chen, X. L. Gou, *Adv. Mater.* **2006**, *18*, 2561.

[43] J. Chen, S.-L. Li, Q. Xu, K. Tanaka, *Chem. Comm.* **2002**, 1722.

[44] a)C. N. R. Rao, H. S. S. R. Matte, K. S. Subrahmanyam, *Acc. Chem. Res.* **2012**, *doi: 10.1021/ar300033m*; b)C. N. R. Rao, A. K. Sood, K. S. Subrahmanyam, A. Govindaraj, *Angew. Chem. Int. Ed.* **2009**, *48*, 7752.

[45] J. N. Coleman, M. Lotya, A. O'Neill, S. D. Bergin, P. J. King, U. Khan, K. Young, A. Gaucher, S. De, R. J. Smith, I. V. Shvets, S. K. Arora, G. Stanton, H.-Y. Kim, K. Lee, G. T. Kim, G. S. Duesberg, T. Hallam, J. J. Boland, J. J. Wang, J. F. Donegan, J. C. Grunlan, G. Moriarty, A. Shmeliov, R. J. Nicholls, J. M. Perkins, E. M. Grieveson, K. Theuwissen, D. W. McComb, P. D. Nellist, V. Nicolosi, *Science* **2011**, *331*, 568.

[46] Y. Hernandez, V. Nicolosi, M. Lotya, F. M. Blighe, Z. Sun, S. De, I. T. McGovern, B. Holland, M. Byrne, Y. K. Gun'Ko, J. J. Boland, P. Niraj, G. Duesberg, S. Krishnamurthy, R. Goodhue, J. Hutchison, V. Scardaci, A. C. Ferrari, J. N. Coleman, *Nat. Nanotechnol.* **2008**, *3*, 563.

[47] A. O'Neill, U. Khan, J. N. Coleman, *Chem. Mater.* **2012**, *24*, 2414.

[48]   K.-G. Zhou, N.-N. Mao, H.-X. Wang, Y. Peng, H.-L. Zhang, *Angew. Chem. Int. Ed.* **2011**, *50*, 10839.

[49]   Y. Yao, Z. Lin, Z. Li, X. Song, K.-S. Moon, C.-p. Wong, *J. Mater. Chem.* **2012**, *22*, 13494.

[50]   K.-K. Liu, W. Zhang, Y.-H. Lee, Y.-C. Lin, M.-T. Chang, C.-Y. Su, C.-S. Chang, H. Li, Y. Shi, H. Zhang, C.-S. Lai, L.-J. Li, *Nano Lett.* **2012**, *12*, 1538.

[51]   Y. Zhan, Z. Liu, S. Najmaei, P. M. Ajayan, J. Lou, *Small* **2012**, *8*, 966.

[52]   D. Kim, D. Sun, W. Lu, Z. Cheng, Y. Zhu, D. Le, T. S. Rahman, L. Bartels, *Langmuir* **2011**, *27*, 11650.

[53]   C. Altavilla, M. Sarno, P. Ciambelli, *Chem. Mater.* **2011**, *23*, 3879.

[54]   A. Castellanos-Gomez, M. Barkelid, A. M. Goossens, V. E. Calado, H. S. J. van der Zant, G. A. Steele, *Nano Lett.* **2012**, *12*, 3187.

[55]   Z. Zeng, Z. Yin, X. Huang, H. Li, Q. He, G. Lu, F. Boey, H. Zhang, *Angew. Chem. Int. Ed.* **2011**, *50*, 11093.

[56]   V. O. Koroteev, L. G. Bulusheva, A. V. Okotrub, N. F. Yudanov, D. V. Vyalikh, *Phys. Status Solidi B* **2011**, *248*, 2740.

[57]   J. Brivio, D. T. L. Alexander, A. Kis, *Nano Lett.* **2011**, *11*, 5148.

[58]   H.-P. Komsa, J. Kotakoski, S. Kurasch, O. Lehtinen, U. Kaiser, A. V. Krasheninnikov, *Phys. Rev. Lett.* **2012**, *109*, 035503.

[59]   G. Eda, T. Fujita, H. Yamaguchi, D. Voiry, M. Chen, M. Chhowalla, *ACS Nano* **2012**.

[60]   J. A. Wilson, A. D. Yoffe, *Adv. Phys.* **1969**, *18*, 193.

[61]   K. F. Mak, C. Lee, J. Hone, J. Shan, T. F. Heinz, *Phys. Rev. Lett.* **2010**, *105*, 136805.

2.1. Brief overview of inorganic graphene analogues

[62]   A. Splendiani, L. Sun, Y. Zhang, T. Li, J. Kim, C.-Y. Chim, G. Galli, F. Wang, *Nano Lett.* **2010**, *10*, 1271.

[63]   G. Eda, H. Yamaguchi, D. Voiry, T. Fujita, M. Chen, M. Chhowalla, *Nano Lett.* **2011**, *11*, 5111.

[64]   H. R. Gutiérrez, N. Perea-López, A. L. Elías, A. Berkdemir, B. Wang, R. Lv, F. López-Urías, V. H. Crespi, H. Terrones, M. Terrones, *ArXiv* **2012**.

[65]   K. Zhou, Y. Zhu, X. Yang, J. Zhou, C. Li, *Chem Phys Chem* **2012**, *13*, 699.

[66]   T. Cao, G. Wang, W. Han, H. Ye, C. Zhu, J. Shi, Q. Niu, P. Tan, E. Wang, B. Liu, J. Feng, *Nat. Commun.* **2012**, *3*, 887.

[67]   R. Wang, B. A. Ruzicka, N. Kumar, M. Z. Bellus, H.-Y. Chiu, H. Zhao, *Phys. Rev. B* **2012**, *86*, 045406.

[68]   S. Bertolazzi, J. Brivio, A. Kis, *ACS Nano* **2011**, *5*, 9703.

[69]   A. Castellanos-Gomez, M. Poot, G. A. Steele, H. S. J. van der Zant, N. Agraït, G. Rubio-Bollinger, *Adv. Mater.* **2012**, *24*, 772.

[70]   T. Li, *Phys. Rev. B* **2012**, *85*, 235407.

[71]   F. Schwierz, *Nat Nanotechnol.* **2012**, *5* 487.

[72]   X. W. Li, X.; Zhang, L.; Lee, S.; Dai, H., , *Science* **2008**, *319*, 1229.

[73]   K. S. J. Novoselov, D.; Schedin, F.; Booth, T. J.; Khotkevich, V. V.; Morozov, S. V.; Geim, A. K.,, *Proc. Natl. Acad. Sci. USA* **2005** *102,* , 10451.

[74]   Radisavljevic. B, Radenovic. A, Brivio. J, Giacometti. V, Kis. A, *Nat. Nanotecnol.* **2011**, *6*, 147.

[75]   H. Liu, P. D. Ye, *ArXiv* **2011**.

[76]   Y. Zhang, J. Ye, Y. Matsuhashi, Y. Iwasa, *Nano Lett.* **2012**, *12*, 1136.

[77] J. Pu, Y. Yomogida, K.-K. Liu, L.-J. Li, Y. Iwasa, T. Takenobu, *Nano Lett.* **2012**, *12*, 4013.

[78] B. Chakraborty, A. Bera, D. V. S. Muthu, S. Bhowmick, U. V. Waghmare, A. K. Sood, *Phys. Rev. B* **2012**, *85*, 161403.

[79] K. Lee, H.-Y. Kim, M. Lotya, J. N. Coleman, G.-T. Kim, G. S. Duesberg, *Adv. Mater.* **2011**, *23*, 4178.

[80] S. Ghatak, A. N. Pal, A. Ghosh, *ACS Nano* **2011**, *5*, 7707.

[81] Z. Yin, H. Li, H. Li, L. Jiang, Y. Shi, Y. Sun, G. Lu, Q. Zhang, X. Chen, H. Zhang, *ACS Nano* **2011**, *6*, 74.

[82] B. Radisavljevic, M. B. Whitwick, A. Kis, *Appl. Phys. Lett.* **2012**, *101*, 043103.

[83] W. S. Hwang, M. Remskar, R. Yan1, V. Protasenko, K. Tahy, S. D. Chae, P. Zhao, A. Konar, H. G. Xing, A. Seabaugh, D. Jena, *ArXiv* **2012**.

[84] V. Podzorov, M. E. Gershenson, C. Kloc, R. Zeis, E. Bucher, *Appl. Phys. Lett.* **2004**, *84*, 3301.

[85] H. Fang, S. Chuang, T. C. Chang, K. Takei, T. Takahashi, A. Javey, *Nano Lett.* **2012**, *12*, 3788.

[86] R. R. Haering, J. A. R. Stiles, K. Brandt, (Ed.: US Patent 4224390), **1980**.

[87] G. Du, Z. Guo, S. Wang, R. Zeng, Z. Chen, H. Liu, *Chem. Comm.* **2010**, *46*, 1106.

[88] C. Feng, J. Ma, H. Li, R. Zeng, Z. Guo, H. Liu, *Mater. Res. Bull.* **2009**, *44*, 1811.

[89] S. Ding, D. Zhang, J. S. Chen, X. W. Lou, *Nanoscale* **2012**, *4*, 95.

[90] H. Li, W. Li, L. Ma, W. Chen, J. Wang, *J. Alloys Compd.* **2009**, *471*, 442.

[91] H. Hwang, H. Kim, J. Cho, *Nano Lett.* **2011**, *11*, 4826.

2.1. Brief overview of inorganic graphene analogues

[92]   a)C. M. Julien, *Mater. Sci. Eng., R* **2003**, *40*, 47; b)B. Yebka, C. Julien, *Solid State Ionics* **1996**, *90*, 141.

[93]   G. X. Wang, Steve Bewlay, Jane Yao, H. K. Liu, S. X. Dou, *Electrochem. Solid-State Lett.* **2004**, *7*, A321.

[94]   S. Wang, G. Li, G. Du, L. Li, X. Jiang, C. Feng, Z. Guo, S. Kim, *Nanoscale Res. Lett.* **2010,** *5*, 1301–1306.

[95]   C. Feng, L. Huang, Z. Guo, H. Liu, *Electrochem. Commun.* **2007**, *9*, 119.

[96]   J.-w. Seo, Y.-w. Jun, S.-w. Park, H. Nah, T. Moon, B. Park, J.-G. Kim, Y. J. Kim, J. Cheon, *Angew. Chem. Int. Ed.* **2007**, *46*, 8828.

[97]   H. Liu, D. Su, G. Wang, S. Z. Qiao, *J. Mater. Chem.* **2012**.

[98]   R. Bhandavat, L. David, G. Singh, *J. Phys. Chem. Lett.* **2012**, *3*, 1523.

[99]   M. Winter, R. J. Brodd, *Chem. Rev.* **2004**, *104*, 4245.

[100] a)K. Shiva, H. B. Rajendra, K. S. Subrahmanyam, A. J. Bhattacharyya, C. N. R. Rao, *Chem. Eur-J.* **2012**, *18*, 4489; b)H. Wang, H. S. Casalongue, Y. Liang, H. Dai, *J. Am. Chem. Soc* **2010**, *132*, 7472.

[101] K. Chang, W. Chen, *Chem. Comm.* **2011**, *47*, 4252.

[102] S. K. Das, R. Mallavajula, N. Jayaprakash, L. A. Archer, *J. Mater. Chem.* **2012**, *22*, 12988.

[103] K. Chang, W. Chen, *J. Mater. Chem.* **2011**, *21*, 17175.

[104] K. Chang, W. Chen, L. Ma, H. Li, H. Li, F. Huang, Z. Xu, Q. Zhang, J.-Y. Lee, *J. Mater. Chem.* **2011**, *21*, 6251.

[105] K. Chang, W. Chen, *ACS Nano* **2011**, *5*, 4720.

2.2: Synthesis and characterization of graphene analogues based on metal chalcogenides

Summary[*]

Graphene analogues of MoS_2, WS_2, $MoSe_2$ and WSe_2 have been prepared by intercalation of lithium in their bulk counterparts followed by exfoliation in water. Products of these reactions when examined by microscopic techniques show that they contain one- to three-layers. Few-layer MoS_2 and $MoSe_2$ have been prepared under hydrothermal conditions using molybdicacid as the source for Mo and KSCN or selenium metal as the source of sulfur and selenium respectively at low temperatures. We have also prepared few-layer sulfides and selenides of Mo and W using solid state reactions of molybdicacid/tungsticacid with thiourea/selenourea at 500 ^{o}C to yield corresponding graphene analogues. Few-layer graphene-like sheets of MoS_2 and $MoSe_2$ have been prepared by microwave method. In this procedure, ethylene glycol or water is used as a solvent with the same reactants used in the case of hydrothermal method. Irradiation of a dispersion of bulk layered metal dichalcogenides in dimethylformamide by a KrF excimer laser is found to produce inorganic graphenes. Graphene analogues of GaS and GaSe have been obtained by liquid-phase exfoliation and by mechanical exfoliation.

The graphene-like species of all the materials have been characterized by electron microscopy, atomic force microscopy and other techniques. Raman spectra show softening

of the A_{1g} mode in these few-layer materials compared to their bulk counterparts. Discovery of the two-dimensional graphene analogues of transition metal dichalcogenides fills the gap in the spectrum of inorganic nanocarbon analogues which had till now only zero-dimensional fullerenes and one-dimensional nanotubes.

2.2: Graphene analogues based on metal chalcogenides

2.2.1: Introduction

Crystalline MoS_2 occurs as the mineral molybdenite. Laue photographs of good quality of MoS_2 were obtained when a crystal was cleaved from the top surface and cemented on a cover glass. This procedure now popularly called as micromechanical cleavage. A Laue photograph taken with the incident beam normal to the basal plane possessed a hexagonal axis and 6 symmetry planes. This structure, contains 2 MoS_2 in a hexagonal unit cell with d_{0001} = 12.30 Å.[1] In the Mid 1960's Frindt showed that the micromechanical cleavage can be successfully employed for obtaining the thin sheets of 3.5 to 4.0 nm which roughly corresponds to 5-6 layers as determined by shadow masking.[2] Later in the mid 1980's considerable effort has been made to obtain the single-layers of these layered materials particularly by using lithium intercalation. In this regard pioneering work was carried out by Morrison and Frindt in which they gave insights into its structure and electronic properties.

MoS_2 has been exfoliated into mono-layers by lithium-intercalation followed by exfoliation in water. From the X-ray diffraction analysis it was shown that the absence of the {002}, {103}, and {105} peaks results in one-molecule thick sheets.[3] Diffraction studies has revealed that in single-layer MoS_2 contains 'water bilayer' where two monolayers of water are regularly located between each MoS_2 layer, giving support to the integrity of the MoS_2 layers where as in the case of dry restacked MoS_2, the spacing was same as the bulk value.[4]

Later, the exfoliation process has been extended to WS_2 to obtain the single-layer. Li-intercalation was found to be difficult in WS_2 when compared to MoS_2 and it is achieved by sonication for longer times in hexane followed by intercalation with n-butyl

2.2: Graphene analogues based on metal chalcogenides

lithium.[5] Later the same group, has demonstrated that intercalation time does not significantly increase the Li concentration but increases as the intercalation temperature increases and attains saturation when the intercalation temperature reaches 100°C.[6] Frindt et al. has carried out the detailed structural investigation on X-ray diffraction patterns of the single-layer MoS_2 and interestingly found that Mo atoms are octahedrally coordinated in contrast to the trigonal prismatic in the bulk MoS_2. These results were also supported by Raman spectroscopy and energy X-ray absorption fine structure.[7]

Hydrothermal/solvothermal synthesis is a common method to synthesize inorganic nanomaterials. Properties of the reactants, such as their solubility and reactivity changes at elevated temperatures and pressures. In this procedure inorganic nanomaterials are conveniently prepared at temperatures considerably lower than in solid-state reactions. Reaction parameters such as time, temperature, pressure, reactant concentration, pH, reaction cell fill volume can be tuned to obtain the required phase and morphology. There have been considerable efforts to synthesize transition metal dichalcogenides using hydrothermal synthesis. Nanotubes and nanorods of molybdenum disulfide have been successfully synthesized by a hydrothermal method at low temperature using molybdic oxide and potassium thiocyante as respective molybdenum and sulfur source.[8] MoS_2 nanowires with diameters of 4 nm and lengths of 50nm were obtained in hydrothermal conditions using MoO_3 and Na_2S as precursors in 0.4 mol/l HCl solution at 260°C.[9] Single-layer MoS_2 was synthesized using a hydrothermal method at low temperature in the range of 170-200°C using ammonium molybdate [$(NH_4)_6Mo_7O_{24}$.$4H_2O$], elemental sulfur and hydrazine monohydrate (86%) as a reducing agent.[10] Hollow MoS_2 microspheres were synthesized in ionic liquids (1-butyl-3-methylimidazolium chloride,

[BMIM]Cl)/water binary emulsions by the hydrothermal method at 180 °C for 24 h using sodium molybdate and thiourea as the precursors.[11]

Microwave synthesis is commonly employed for the synthesis of various inorganic nanostructures since it is fast, simple and energy-efficient. Microwaves are generally generated using a magnetron. Microwave energy absorbed by the reactants convert into heat thereby causing the rapid decomposition of the precursors and creating highly supersaturated solutions, where nucleation and growth occur to produce the desired nanocrystalline products. This technique has also been employed to obtain the nanostructures of sulphides and selenides of molybdenum and tungsten. Vollath and Szabo have reported the synthesis of nano particles of MoS_2 and WS_2 in a microwave plasma powered from a generator with a frequency of 2.45 GHz by the reaction of H_2S with $Mo(CO)_6$ and $W(CO)_6$ respectively.[12] Microwave-induced plasmas of H_2S and N_2/H_2 have been used to sulfidize and reduce WO_3 to form inorganic fullerenes of WS_2.[13] WS_2 nanowires have been synthesized through a microwave-assisted chemical route using tungstic acid, elemental sulfur and monoethanolamine as starting materials at 750 °C under argon atmosphere for 1.5 h.[14] A microwave-assisted reaction between $Mo(CO)_6$ and Se in ethylene glycol has yielded $MoSe_2$ nanoparticles along with the nanorods of lengths ranging from 45 to 55 nanometers.[15]

Pulsed laser ablation (PLA) is one of the important techniques to obtain the nano structures of various materials. Compared to the other synthetic approaches this method is useful in some aspects like, (i) relative ease and convenience of preparation (ii) purity of the material obtained which is difficult to obtain by chemical reaction and (iii) particularly useful in the case of inorganic analogues of the graphene because dispersions of these

materials in different solvents is difficult to obtain which in turn are advantageous in making composites with other materials.

Tenne et al have reported the synthesis of IF-TaS$_2$ by two different methods using laser ablation in 60–600 Torr argon and in liquid CS$_2$. For the laser ablation in argon, the target was prepared by pressing TaS$_2$ and sulfur, mixed in a molar ratio of 1:100 (TaS$_2$:S), into a pellet, which was held by clamps on a semiautomatic actuator to ensure homogenous ablation of the pellet. For the laser ablation in liquid, a pellet of pure TaS$_2$ was used, which was glued on a metal stub.[16] Later, the same group have reported the formation of inorganic fullerene of molybdenum disulfide by pulsed laser ablation in water using Nd:YAG pulsed laser (532 nm, 5 Hz, pulse duration between 6 and 9 ns and pulse energy of 40-50 mJ) for 20 minutes.[17] Irradiation of MoS$_2$ crystals with electron accelerator which produces a larger irradiation area, and more controlled doses has found the formation of onion like structures. Sen et al. have reported the formation of fullerenes and nanotubes like structures by laser ablating the MoS$_2$ and WS$_2$ at different temperatures.[18] Pulsed laser vaporization has been used to produce nanooctahedra of MoS$_2$ and MoSe$_2$ by pressing MoS$_2$/MoSe$_2$ powder in a 28.8 mm dye at room temperature for 5 min at 10 metric tons. An excimer laser (248 nm) with an energy fluence of 10 J/cm^2 was used for 20 minutes to obtain these nanostructures.[19]

GaS and GaSe are stable layered metal dichalcogenides semiconducting materials with wide bandgaps (E_g = 3.05 eV and 2.10 eV, respectively). The hexagonal structure of GaS and GaSe has a layered (S-Ga-Ga-S and Se-Ga-Ga-Se) repeating unit built by six membered Ga$_3$S$_3$ and Ga$_3$Se$_3$ rings. GaS nanotubes were prepared by heating the bulk GaS precursor in Argon atmosphere at 650 °C for 2 hours.[20] GaS submicrometer tubes

were prepared in a vertical high-frequency induction furnace, with a graphite crucible containing a mixture of Ga_2O_3, ZnS, and activated carbon powders at 1400–1500 °C for 1.5 h, and then rapidly cooled to room temperature in an Ar atmosphere.[21] Allakhverdiev et al. made the first colloidal GaSe samples in 1997 using ultrasonic treatment of bulk GaSe in methanol.[22] Their results show a wide distribution of GaSe particle sizes, based on the absorption spectrum. Stoll et al. have made GaSe nanoparticles of 88 nm in with nanowire like morphology using $Ga_4Se_4R_4$ cubanes by MOCVD.[23] Nanoparticles of GaSe were obtained by the reaction of an organometallic ($GaMe_3$) with trioctyl phosphine selenium in a high temperature solution of trioctyl phosphine (TOP) and trioctyl phosphine oxide (TOPO).[24] Rao et al have reported the synthesis and characterization of GaSe nanotubes and onion-like structures by laser irradiation of GaSe powder in n-octylamine and also by heating the GaSe powder to 900 °C in a sealed tube led to exfoliation, giving rise to nanoflowers and nanotubes.[25]

2.2: Graphene analogues based on metal chalcogenides

2.2.2: Scope of the present investigations

Following the discovery of fullerenes in 1985, it was soon recognized that inorganic layered materials such as MoS_2 and WS_2 can also form fullerene-like structures. After the discovery of carbon nanotubes, inorganic nanotubes analogous to carbon nanotubes were prepared and characterized, nanotubes of MoS_2 and WS_2 being archetypal examples. With the discovery and characterization of graphene, the two dimensional nanocarbon, which has created great sensation in last three to four years it would seem natural to explore the synthesis of graphene analogues of layered inorganic materials. We have attempted to synthesize inorganic graphene analogues of dichalcogenides of tungsten by chemical methods which posses layered structure. From the literature, there were reports on the intercalation and exfoliation of MoS_2 and WS_2. There is an early report on graphene-like MoS_2 prepared by lithium intercalation and exfoliation, but the material was characterized only by X-ray diffraction which is not sufficient to determine the exact nature and number of layers. There have been attempts to prepare single layers of WS_2 by lithium intercalation and exfoliation as well and here again the product was only characterized on the basis of (002) reflection in the X-ray diffraction pattern. Since few-layer inorganic graphenes containing five layers or less do not exhibit the (002) reflection prominently, it is necessary that these materials should be characterized properly different microscopic techniques to understand the nature, morphology and also purity. It is also desirable to explore alternative chemical synthesis of these graphene-like materials.

Synthesizing few-layer MoS_2, WS_2, $MoSe_2$ and WSe_2 by using different chemical approaches is of importance. We have developed a set of synthetic protocols involving hydrothermal synthesis, solid state heating, microwave approach and laser exfoliation.

2.2: Graphene analogues based on metal chalcogenides

Coleman et al has reported the synthesis and characterization of graphene analogues in approximately 30 different solvents. Though this method requires long duration for obtaining stable dispersions in required solvents, solubility of these compounds has caught the interest. It is advantageous to prepare dispersions of inorganic graphene analogues which is suitable for preparing various composites for numerous applications. In this context, we felt it is worthwhile to prepare inorganic graphene analogues in required solvent using laser irradiation in a relatively less time. We have prepared graphene analogues of Mo and W of sulfides and selenides in dimethylformamide.

2.2: Graphene analogues based on metal chalcogenides

2.2.3: Experimental section

Li-intercalation

Lithium intercalation of MoS$_2$/WS$_2$/MoSe$_2$/WSe$_2$: The technique employed to intercalate and exfoliate MoS$_2$/WS$_2$/MoSe$_2$/WSe$_2$ was essentially done in two steps. The first step was to intercalate MoS$_2$/WS$_2$/MoSe$_2$/WSe$_2$ with lithium which was done by soaking 100 mg of MoS$_2$ in 10 ml n-butyl lithium in 5 ml of hexane in a nitrogen atmosphere for 72 hours at 373 K. After this, the intercalated samples were washed with hexane several times to remove any unreacted n-butyllithium. To exfoliate the lithium-intercalated MoS$_2$/WS$_2$/MoSe$_2$/WSe$_2$, the intercalated sample was ultra-sonicated in distilled water in a closed vial during which profuse evolution of gas was observed and an opaque suspension of MoS$_2$/WS$_2$/MoSe$_2$/WSe$_2$ was formed. The suspension was centrifuged and the solid product was collected for further characterization.

Hydrothermal Method

Hydrothermal synthesis of MoS$_2$: MoS$_2$ layers were prepared using hydrothermal method in which molybdic oxide, MoO$_3$, was used as Molybdenum source and KSCN was used as sulphur source as well as reducing agent. In a typical synthesis, 1 mmol of molybdic oxide and 2.5 mmol of KSCN were taken in 10 ml of de-ionised water in 23 ml capacity of Teflon coated autoclave and placed it at 453 K for 24 hours to yield the few-layer MoS$_2$. The product obtained was washed with water and dried at 277 K and characterized further.

Hydrothermal synthesis of MoSe$_2$: MoSe$_2$ layers were prepared using a hydrothermal method wherein 1 mmol of molybdic oxide and 2 mmol of selenium metal and 3 mmol of NaBH$_4$ were taken in 10 ml of de-ionised water in 23 ml capacity of Teflon coated

autoclave and placed it at 453 K for 24 hours to yield the few-layer MoSe$_2$. The product

obtained was washed with ethanol and dried at 278 K and characterized further.

Thiourea/selenourea Method

Synthesis of MoS$_2$ by the thiourea method: In this method MoS$_2$ layers were prepared by

heating molybdic acid with an excess of thiourea at 773 K under nitrogen atmosphere for 3

hours. In a typical synthesis, 0.1 mg of molybdic acid was ground with 1.5 grams of

thiourea and placed in alumina boat and it was then placed inside a quartz tube kept inside

a horizontal tube furnace. Prior to heating, quartz tube was purged with nitrogen for 0.5

hour. The temperature was then raised to 773 K and then held it for 3 hours and it is

cooled to room temperature and characterized further.

Synthesis of WS$_2$ by the thiourea method: In this method WS$_2$ layers were prepared by

heating tungstic acid with an excess of thiourea at 773 K under nitrogen atmosphere for 3

h. For this purpose, tungstic acid was synthesized by dissolving about 0.5 g of

Na$_2$WO$_4$.2H$_2$O was dissolved in 20 ml distilled water. To this conc. HCl was added drop

wise under constant stirring. The yellow tungstic acid thus obtained was washed with

distilled water and dried overnight in hot air oven. In a typical synthesis, 0.1 g of tungstic

acid was ground with 1.2 g of thiourea and placed in an alumina boat which was then

placed inside a quartz tube kept inside a horizontal tube furnace. Prior to heating, the

quartz tube was purged with nitrogen for 0.5 h. The temperature was then raised to 773 k

and then held at the same for 3 h. After 3 h, the sample was cooled down to room

temperature under nitrogen atmosphere. The black product obtained was used as such for

further analysis.

2.2: Graphene analogues based on metal chalcogenides

Synthesis of MoSe$_2$ by the selenourea method: Layered MoSe$_2$ was prepared using selenourea as a selenium source. In a typical synthesis, molybdic acid was ground with excess of selenourea in the ratio 1:48 and heated at 773 K for 3 h under nitrogen atmosphere with heating rate of 20 °C per minute. Then the sample was cooled down to room temperature under nitrogen atmosphere. The black product obtained was used as such for further analysis.

Synthesis of WSe$_2$ by the selenourea method: The procedure to prepare layered WSe$_2$ by employing selenourea is as follows: In a typical synthesis, tungstic acid was ground with excess of selenourea in the 1:48 ratio and heated at 773 K for 3 h under nitrogen atmosphere. After 3 h, the sample was cooled down to room temperature under nitrogen atmosphere. The black product obtained was used as such for further analysis.

Microwave synthesis
Synthesis of few-layer MoS$_2$: MoS$_2$ layers are prepared by reacting 1mM of molybdic acid (H$_2$MoO$_4$) and 2 mM of potassium thiocyanate (KSCN) in 10ml of Ethylene glycol in Teflon-coated autoclave, heated at 450W for 15min in a domestic microwave oven operating at 2.45 GHz. The obtained product was washed with ethanol and dried at 60°C and used for further characterization.

Synthesis of few-layer MoSe$_2$: MoSe$_2$ layers are also prepared by microwave treatment of 1mM of molybdicacid (H$_2$MoO$_4$) with 2 mM of selenium powder (Se) and 3 mM of sodium borohydride (NaBH$_4$) in 10 ml of ethylene glycol taken into a 23ml capacity of Teflon-coated autoclave at 450 W for 20 min. Then the product was washed with ethanol and dried at 60°C and used for further characterization.

2.2: Graphene analogues based on metal chalcogenides

Laser exfoliation: KrF excimer laser (248 nm wavelength, 30 ns pulse width) was employed to exfoliate bulk powders of sulphides and selenides of Mo and W. Irradiation was carried out for 1 hour in a quartz vessel in DMF medium as solvent. The laser fluence and repetition rate used for the purpose were 1.5 J/cm^2 and 5 Hz respectively. During laser treatment the dispersions were stirred using a magnetic stirrer to ensure homogeneity of the dispersion and thereby homogeneous exfoliation. After the laser exfoliation experiment, the resultant solutions were kept for 24 hours and then centrifuged at 2500 rpm for 5 minutes. The supernatant of the centrifuged product was taken for further characterization. After centrifugation, the supernatant was quite stable for 4 months.

Ultrasonication: Probe sonication was employed to exfoliate bulk powders of sulphides and selenides of gallium. Sonication was carried out for 40 min in a quartz vessel in N-methyl pyrrolidone medium as solvent. The probe sonicator used for the purpose operates at 20 Hz with 250 Watt. During sonication, the container is kept in an ice bath avoid unwanted heating during the exfoliation times. After the exfoliation, the resultant solutions were kept for 24 hours and then centrifuged at 2500 rpm for 5 minutes. The materials used for microscopy were collected from the centrifuged solution.

Mechanical Exfoliation: The SiO$_2$/Si substrates were thoroughly cleaned using a standard RCA cleaning method followed by boiling in acetone and isopropyl alcohol for 5 min. Finally, substrates were cleaned using an oxygen plasma for 5 min. Single-layer of GaS, and GaSe were deposited at room temperature in ambient conditions by standard mechanically exfoliating method using bulk materials onto cleaned SiO$_2$/Si substrates (with thicknesses of 50 nm, 300 nm, and 500 nm) in a manner similar to that previously established for single-layer graphene. After deposition of thin samples, the thinnest flakes

were identified by using optical microscopy. The exfoliated thinnest flakes had typical dimensions of tens of micrometers.

Characterization Techniques

X-ray Diffraction:

X-ray diffraction (XRD) patterns of the samples are recorded using Cu Kα radiation on a Bruker D8 Discover diffractometer.

Scanning electron microscopy:

A field-emission scanning electron microscope (FESEM, FEI Nova-Nano SEM-600, Netherlands) was used.

Transmission electron microscopy:

For transmission electron microscopy (TEM), dispersions of the samples were dropped onto the holey carbon-coated Cu grids, and the grids were allowed to dry in the air. The grids were examined using a JEOL (JEM3010) microscope operating with an accelerating voltage of 300 kV. TEM images and atomic arrangement of hexagonal $MoSe_2$ and WSe_2 in Figure 3 (no reconstruction) was obtained from the FEI TITAN (cube) 80-300 kV aberration corrected transmission electron microscope with a negative spherical aberration coefficient (Cs) of ~ -30 µm and a positive defocus about +8 nm, where atomic potentials appear with bright contrast in a dark background.

Optical absorption:

The optical absorption spectroscopy measurements were performed using a Perkin- Elmer Lambda 900 UV/VIS/NIR spectrometer.

Raman Spectroscopy:

Raman spectra were recorded with a LabRAM HR high-resolution Raman spectrometer (Horiba-Jobin Yvon) using a He−Ne laser ($\lambda = 632.8$ nm) and Ar laser (514 nm).

Atomic Force Microscopy:

AFM measurements were carried on Vecco digital instruments, di Innova. Samples for AFM measurements were prepared by spin coating the sample solutions on Si/SiO$_2$ substrate.

Optical Microscopy:

An optical microscope was used to locate the sheets of GaS. The optical microscopy images were acquired with an optical microscope (Nikon Eclipse ME600) imager M1m with white light illumination (100 W halogen lamp, HAL100) using a bright-field imaging mode and $100 \times$ objectives.

2.2: Graphene analogues based on metal chalcogenides

2.2.4: Results and Discussion

Li-intercalation: Intercalation of lithium in bulk MoS_2 (Figure 1(a)) followed by exfoliation at room temperature was not satisfactory. The product contained to exhibit the (002) reflection as can be seen in Figure 1(b). Hence we carried out the reaction at 373 K
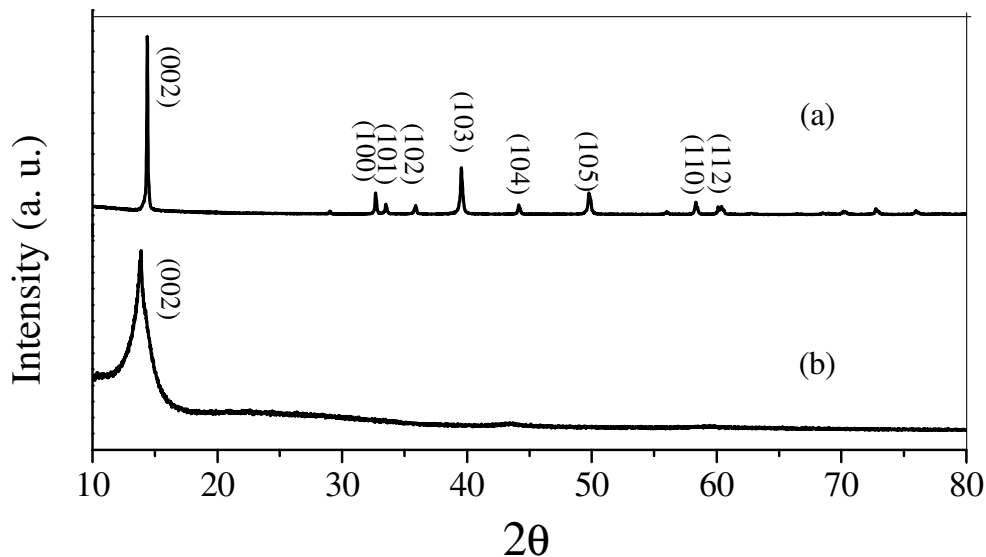
Figure 1: Comparison of XRD patterns of (a) bulk MoS_2 and (b) MoS_2 layers obtained by lithium intercalation.

followed by exfoliation in water. Upon exfoliation, lithium-intercalated MoS_2 gave an opaque suspension in water which was centrifuged at 12000 RPM to obtain a black powder of layered MoS_2. When lithium intercalated chalcogenides are treated with water, it results in the formation of lithium hydroxide and hydrogen gas which account for the separation of the layers or the loss of the periodicity along the *c*-axis. This can be identified from the XRD pattern as shown in Figure 2 where the (002) reflection is absent and confirms that the layers are well separated from each other. We have employed the similar experimental procedure to obtain the few-layer WS_2, $MoSe_2$ and WSe_2.
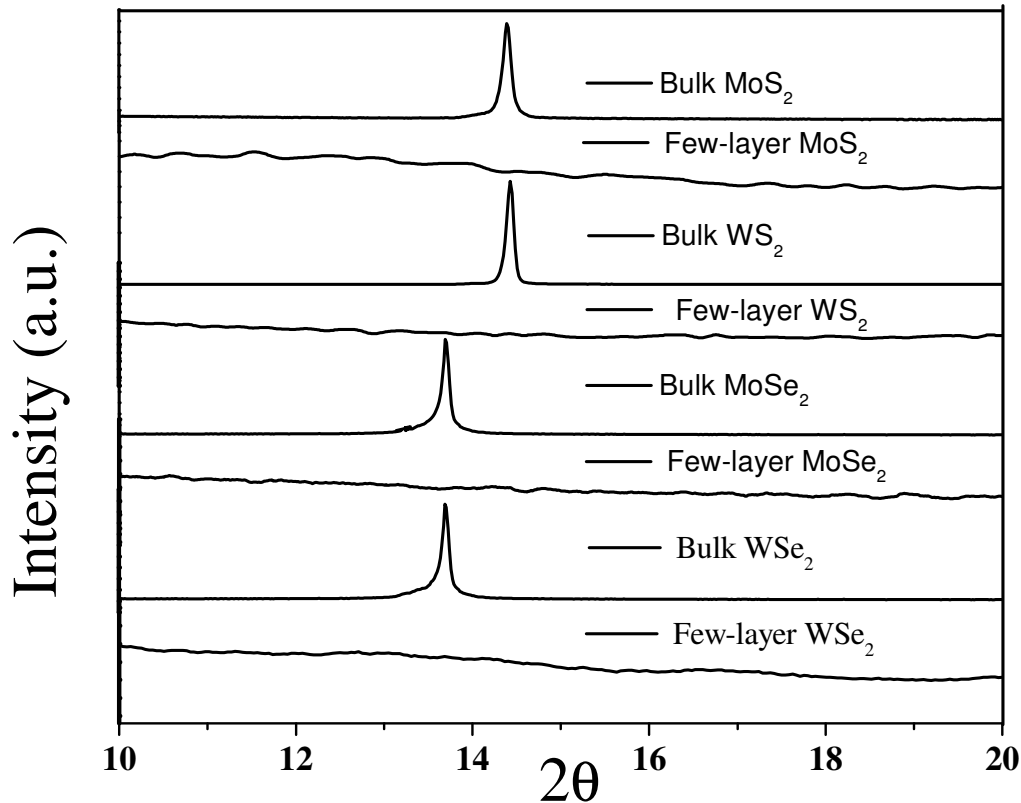
Figure 2: Comparison of XRD patterns of bulk MoS_2, bulk WS_2, bulk $MoSe_2$, bulk WSe_2 and the corresponding few-layers obtained by lithium-intercalation.

All XRD patterns resemble the same without (002) reflection as can be seen from Figure 2. After confirming the formation of few-layer we have carried out the microscopic characterization for unveiling the morphology of the product formed. In Figures 3 (a) and (b) we show the graphene-like MoS_2 layers obtained from lithium intercalation with a layer separation in the range of 0.65 - 0.7 nm. We have also carried out the FESEM studies on few-layer MoS_2 obtained by lithium-intercalation, and it reveals the formation of sheet like morphology. It also provides the evidence for the exfoliation from the bulk MoS_2 as can be seen from Figures 3(c) and (d) where layers are coming out. Evidence provided by FESEM analysis (observe the thick edges) and XRD pattern (the absence of the (002) reflections) has led us to conclude that during the drying process of the single-layer MoS_2 suspensions has restacked in random orientation. TEM image in Figure 3(b)

shows 3-5 layers which are stacked in a regular manner and these units are randomly

oriented with each other further confirming our observations. We have also
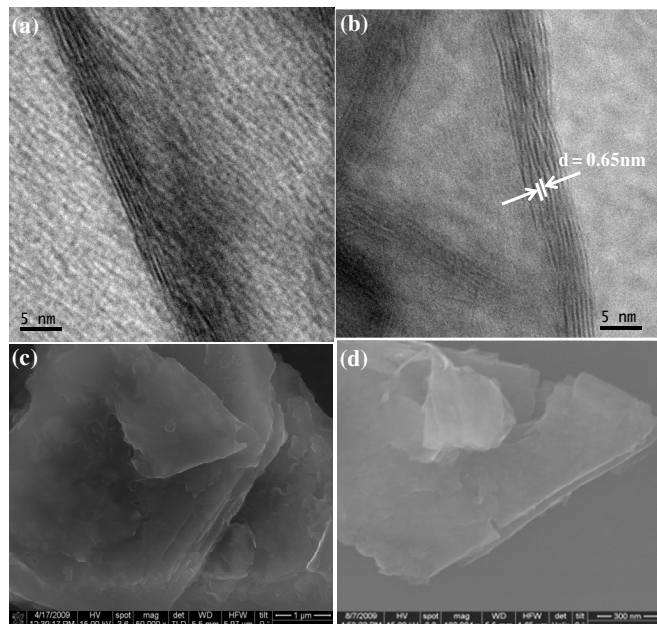
Figure 3: (a) and (b) are the TEM images of MoS_2 layers whereas (c) and (d) are FESEM images of MoS_2 layers obtained by Li-intercalation.

carried out AFM studies on the samples to determine the thickness of the layers. In Figure

4, we show the topographic image of AFM and the corresponding height profile of
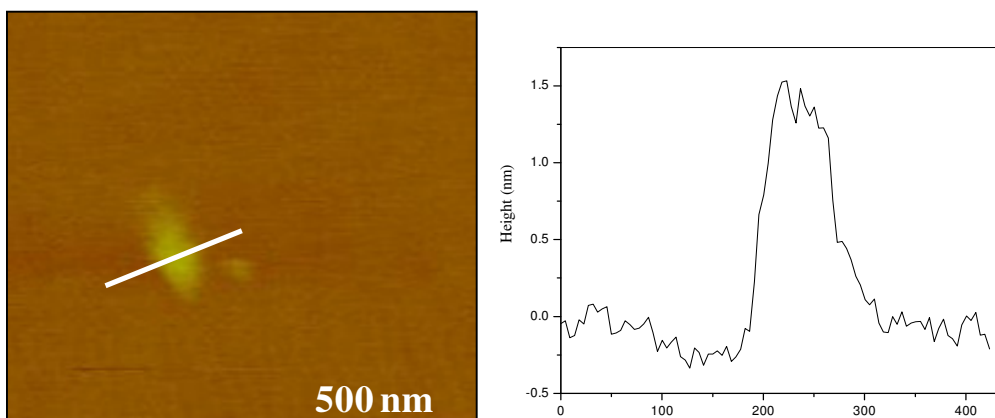
Figure 4: AFM images and the associated height profiles of MoS_2 layers obtained by Li-intercalation.

1.4 nm, with lateral dimensions of ~ 100-150 nm. We have also characterized the product

obtained from lithium intercalated WS_2. TEM images in Figures 5 (a) and (b) reveal
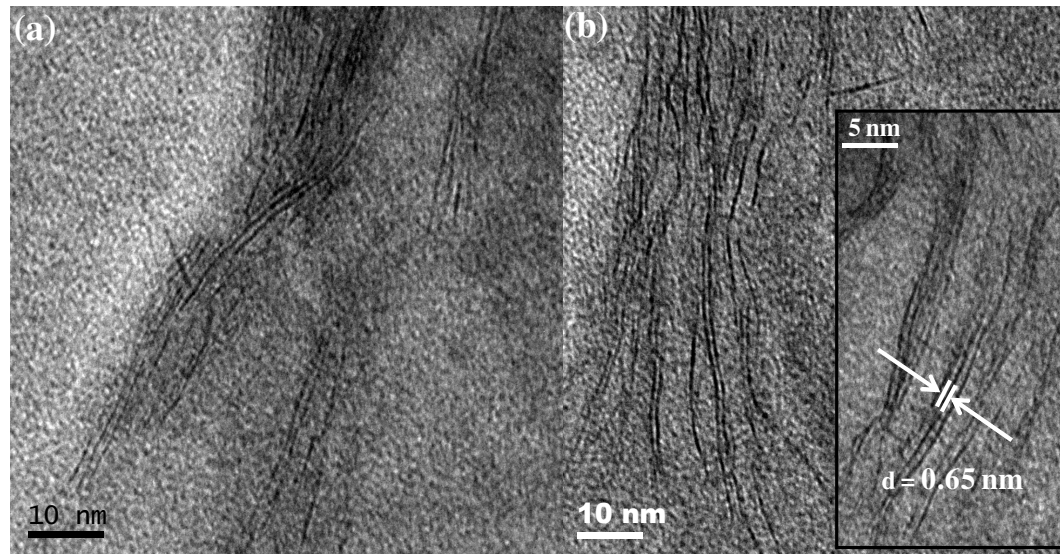
Figure 5: (a) and (b) are the TEM images of WS$_2$ layers obtained by Li-intercalation.
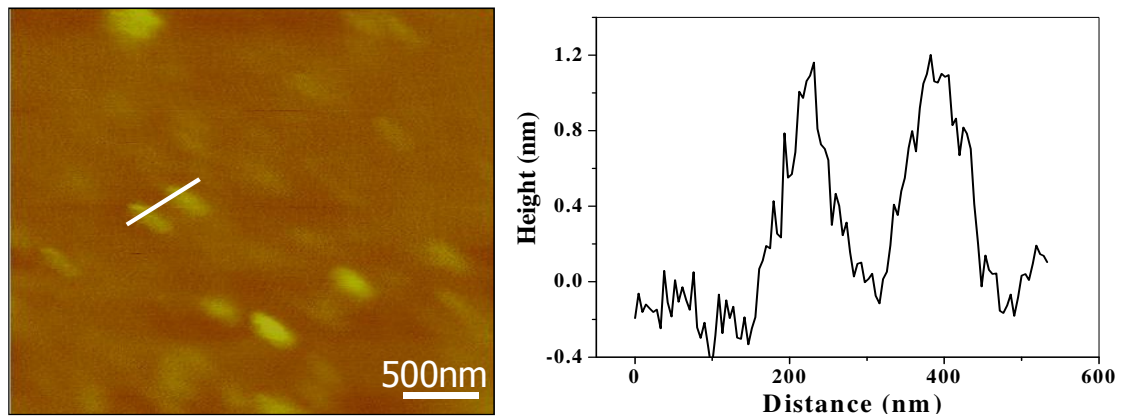
Figure 6: AFM images and the associated height profiles of WS$_2$ layers obtained by Li-intercalation.

that WS$_2$ mostly consists of bi-layers and a reasonable number of single-layers are also observed. From the TEM image it is observed that the exfoliated WS$_2$ layers have an interlayer spacing of 0.65-0.7 nm which is comparable to that of bulk (0.65 nm). The AFM images of WS$_2$ layers synthesized using lithium intercalation is shown in Figure 6. The height profile confirms the existence of 2-3 layers of WS$_2$ with the average thickness of the layers being 1.2-1.3 nm and lateral dimensions are 150-200 nm.
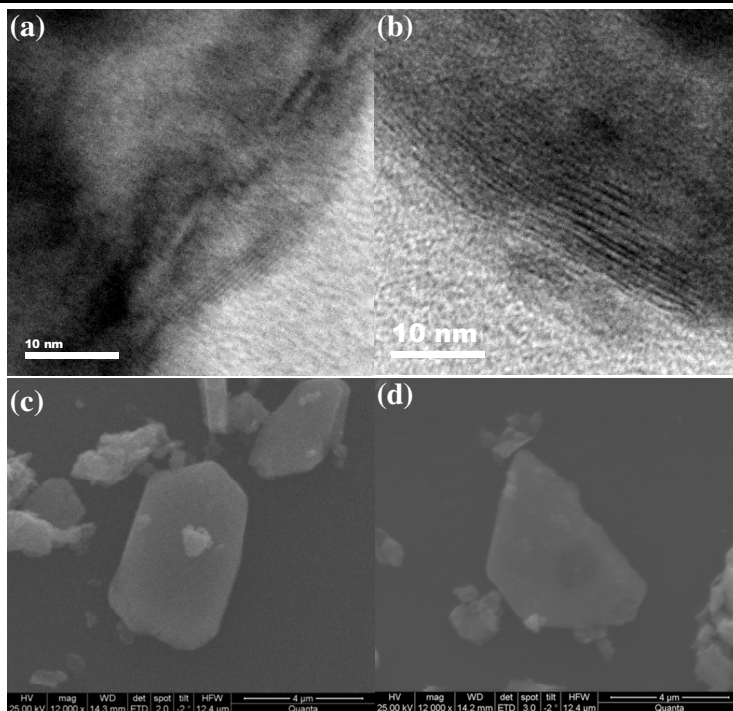
Figure 7: (a) and (b) are the TEM images whereas (c) and (d) are FESEM images of $MoSe_2$ layers obtained by Li-intercalation.
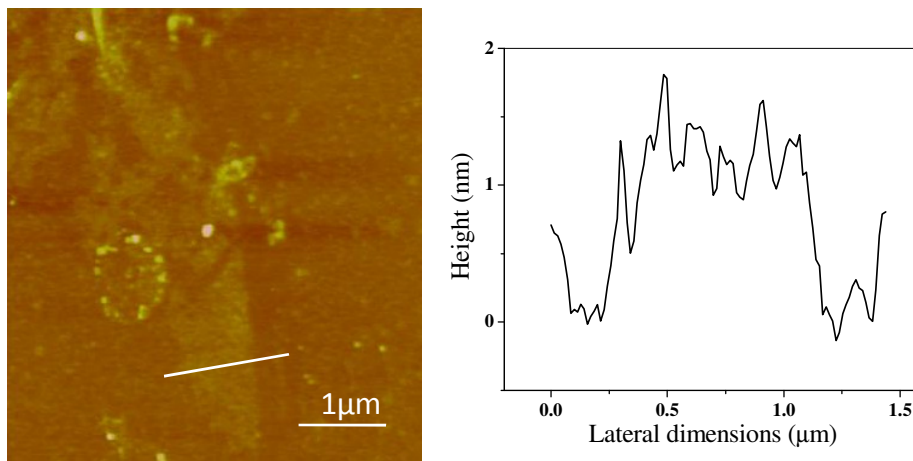
Figure 8: AFM images and the associated height profiles of $MoSe_2$ layers obtained by Li-intercalation.

We have characterized few-layer $MoSe_2$ obtained from lithium intercalation using microscopic techniques. Figures 7 (a) and (b) show the TEM image of $MoSe_2$ layers and the inter-layer separation was around 0.65-0.7 nm. In Figures 7 (c) and (d), we show the

FESEM images with sheet like morphology with several microns of lateral dimensions. Similar argument which is discussed in the case of MoS_2 can also be applied here, with the absence of (002) reflection indicating the complete exfoliation process. AFM characterization of lithium intercalated $MoSe_2$ samples has revealed that the average height is around 1.3 -1.9 nm and the lateral dimensions are in 3-4 μm as shown as in Figure 8. In the similar way, we have characterized the product obtained from the
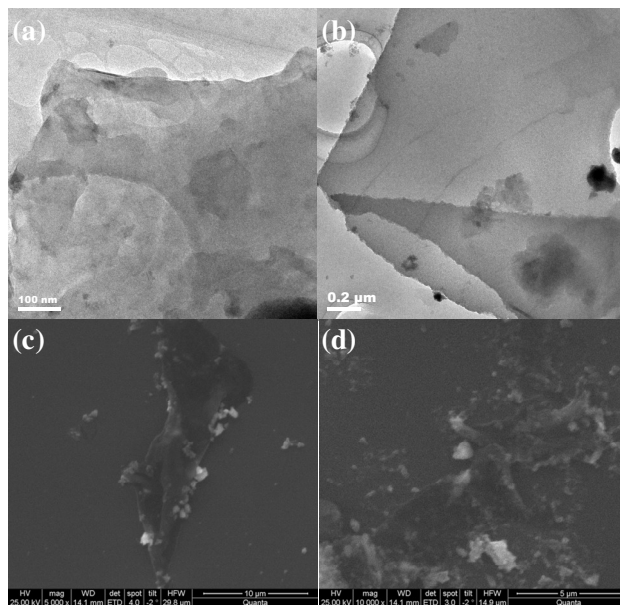
Figure 9: (a) and (b) are the TEM images whereas (c) and (d) are FESEM images of WSe_2 layers obtained by Li-intercalation.

lithium intercalated and exfoliated WSe_2. Figures 9 (a) and (b) show the TEM images of few-layer WSe_2. We can clearly see the sheet like morphology with well defined edges having several microns in lateral dimensions. We show FESEM images in Figures 9(c) and (d) which also confirms the formation of the sheet-like morphology.
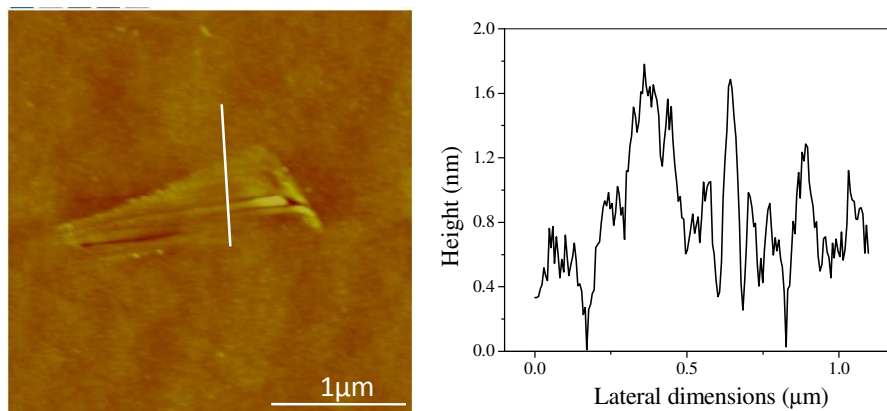
Figure 10: AFM images and the associated height profiles of $MoSe_2$ layers obtained by Li-intercalation.

AFM image in Figure 10 confirms the formation of 2-3 layers with thickness varying between 1.3-1.9 nm and having lateral dimensions of 1-2 μm.

In Figure 11 (a), we compare the Raman spectrum of graphene-like MoS_2 samples prepared by us with the spectrum of bulk MoS_2. The bulk sample gives band at 406.5 cm^{-1} due to the A_{1g} mode with the full-width half maximum (FWHM) of 3.1 cm^{-1}. Interestingly, few-layer MoS_2 prepared by lithium intercalation exhibits the corresponding band at 404.7 cm^{-1}. Furthermore, the FWHM values are larger in the graphene-like samples, the values varying from 10 to 16 cm^{-1} compared to ~ 3 cm^{-1} in the bulk sample. Raman spectrum of WS_2 obtained by lithium intercalation show softening of the bands due to the A_{1g} mode (see Figure 11 (a)). Compared to the narrow bands at 351 (E_{2g}) and 420 cm^{-1} (A_{1g}) of bulk WS_2 with FWHM values around 7.8 and 2.4 cm^{-1} respectively, the spectrum of WS_2 obtained from lithium intercalation shows bands at 350 and 415 cm^{-1} with FWHM values of 13.7 and 8.4 cm^{-1}. The broadening of the Raman bands is considered to be due to the phonon confinement. The broadening also suggests that the lateral dimensions of these

materials are in the nano regime.[19] Analysis of the peak positions will be discussed in the next part of the thesis (see Part 2.5).

R
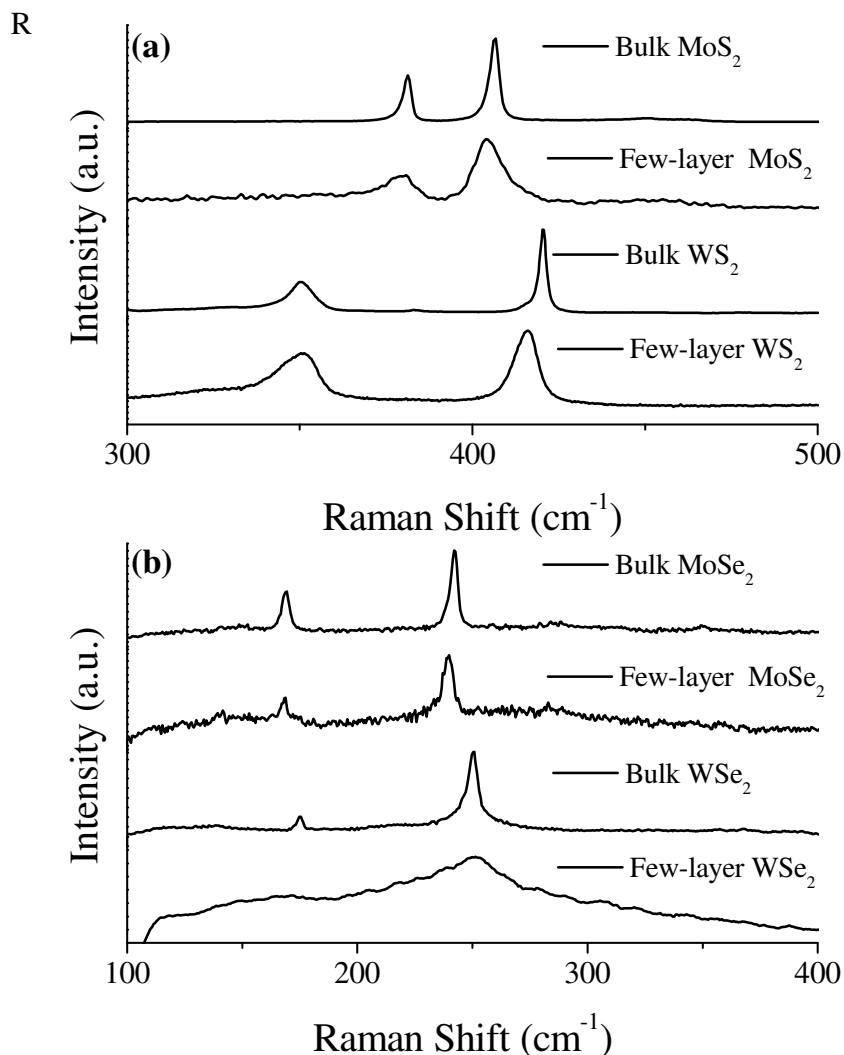
Figure 11: Comparison of Raman spectra of (a) bulk MoS_2 and few-layer MoS_2 layers, bulk WS_2 and few-layer WS_2 layers (b) bulk $MoSe_2$ and few-layer $MoSe_2$ layers, bulk WSe_2 and few-layer WSe_2 layers obtained by Li-intercalation.

Raman spectrum of graphene-like $MoSe_2$ prepared by lithium intercalation were compared with the spectrum of bulk $MoSe_2$. In Figure 11 (b), we have shown the bulk sample gives the Raman bands at 168.8 and 242 cm^{-1} due to the E_{1g} and A_{1g} modes with the full-width half maxima (FWHM) of 4.1 and 3.7 cm^{-1} respectively. Interestingly, few-

layer MoSe$_2$ prepared by us exhibits the corresponding bands at 168.1 and 239.4 cm^{-1}. The FWHM are larger in the graphene-like samples, the values varying from 6-8 cm^{-1} compared to ~ 4 cm^{-1} in bulk MoSe$_2$. Compared to the narrow bands at 255 cm^{-1} (A$_{1g}$) of bulk WSe$_2$ with FWHM value of 5.1 cm^{-1} (Figure 11 (b)) the spectrum of WSe$_2$ obtained from this method shows band at 249.7 cm^{-1} with FWHM value of 43 cm^{-1}.
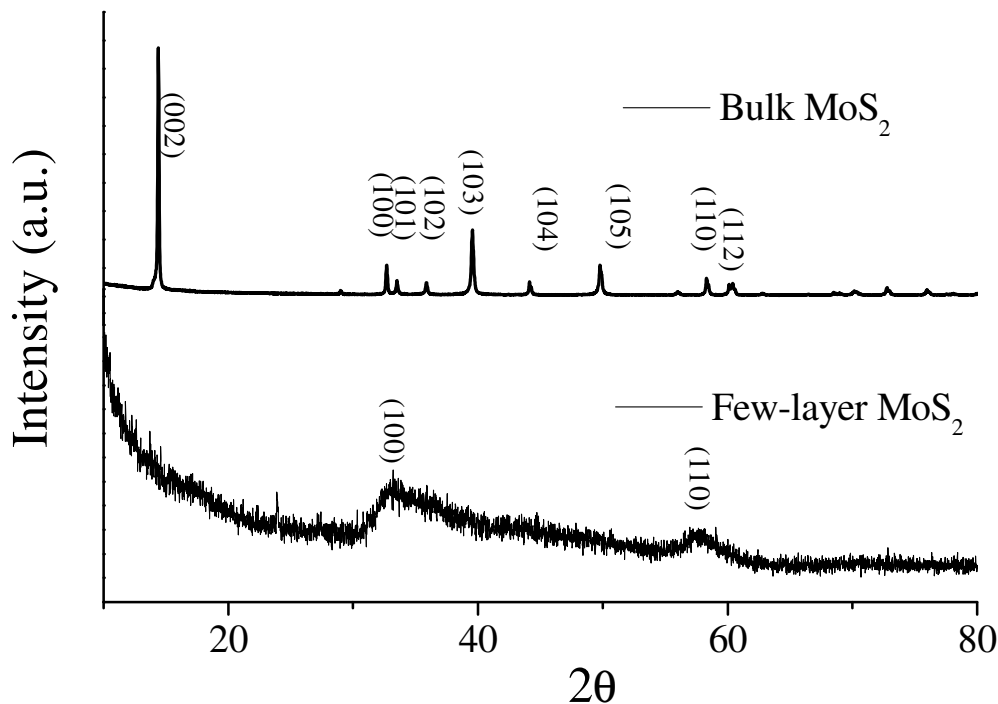
Figure 12: Comparison of XRD patterns of bulk MoS$_2$ with few-layer MoS$_2$ obtained under hydrothermal conditions.

Hydrothermal Method: Using hydrothermal conditions, we have synthesized graphene analogues of sulfides and selenides of the molybdenum. In a typical reaction, molybdic acid was reacted with KSCN/selenium metal under hydrothermal conditions at 180 °C. In this reaction KSCN acts as a reducing reagent as well as a vulcanizer. Some of the of S in SCN$^-$ changes to SO$_4^{2-}$ and reduced Mo $^{(VI)}$ to Mo $^{(IV)}$, and the other part of S forms MoS$_2$ with Mo. In Figure 12, we have compared the XRD pattern of bulk MoS$_2$ with the few-layer MoS$_2$ obtained from hydrothermal conditions. The XRD pattern resembles that of a

single-layer MoS$_2$ with the absence of (002) reflection suggesting the random stacking of

single-layer MoS$_2$. The absence of mixed (hkl) peaks and the asymmetric shape of (hk0)
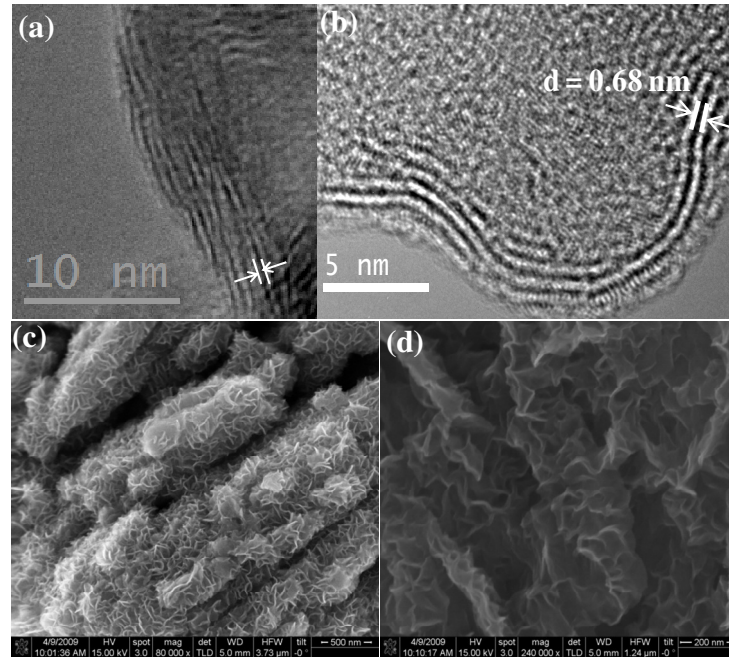
Figure 13: (a) and (b) are the TEM images whereas (c) and (d) are
FESEM images of MoS$_2$ layers obtained from hydrothermal conditions.
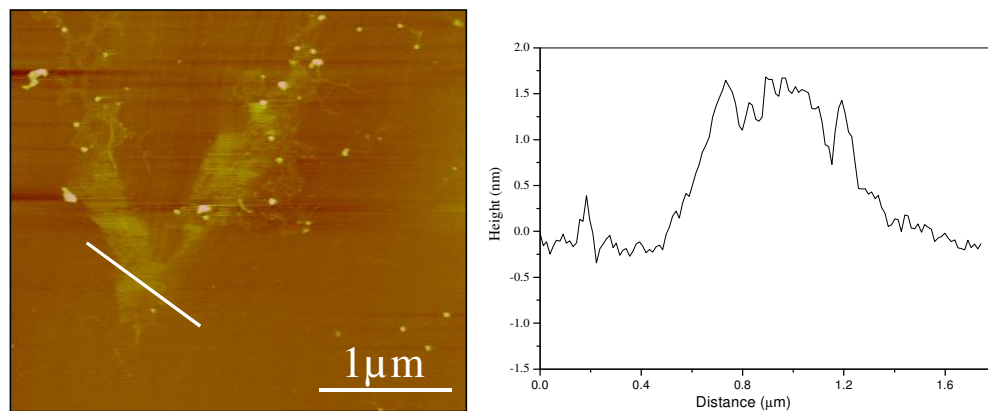
Figure 14: AFM images and the associated height profiles of MoS$_2$ layers obtained under
hydrothermal conditions.

planes further confirms the formation of turbostratic restacked MoS_2. The shape of the (100) peak and the position of the peak indicate a structure in which Mo atoms have trigonal- prism coordination. In Figure 13 we show TEM and FESEM images of MoS_2 obtained from hydrothermal conditions. In Figure 13 (a), we have shown 3-4 layers of MoS_2. In Figure 13 (b), we show the HREM image in which one can observe the slight bending in the layer which is attributed to the defects in the layers. In Figure 13 (c), we have shown the FESEM images showing the curling like structures in which all the layers are mis-oriented to each other further supporting the XRD pattern shown in Figure 11.
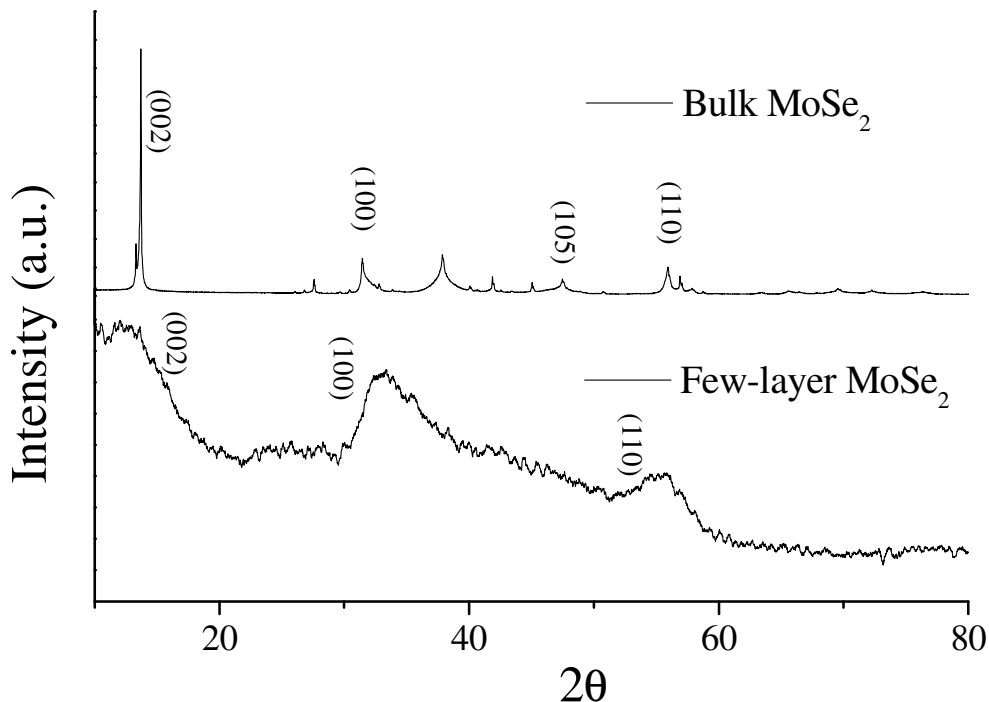
Figure 15: Comparison of XRD patterns of bulk $MoSe_2$ with few-layer $MoSe_2$ obtained under hydrothermal conditions.

AFM analysis showed the formation of bi-layers with the average height profile of 1.4 nm with lateral dimension of few-microns (Figure 14).

We have also synthesized few-layer $MoSe_2$ using hydrothermal conditions in which selenium metal acts as a selenium source and sodium borohydride as a reducing agent at 180 °C for 24 hours. In Figure 15, we have shown the XRD pattern similar to that

of MoS_2 obtained in the hydrothermal procedure confirming the formation of single-layer $MoSe_2$. Figures 16 (a) and (b) show the typical TEM images showing the formation of 2-3 layers. In Figures 16 (c) and (d), we show FESEM images having curls/petals like structures. Further, we have carried out AFM studies (Figure 17) which confirm the formation of the 2-3 layers with the height profile of 1.3 - 2 nm with lateral dimensions lying between 150-300 nm. We have carried out Raman studies on the few-layer MoS_2 and $MoSe_2$ and the results obtained are similar to that of Li-intercalation method (Figure 18).
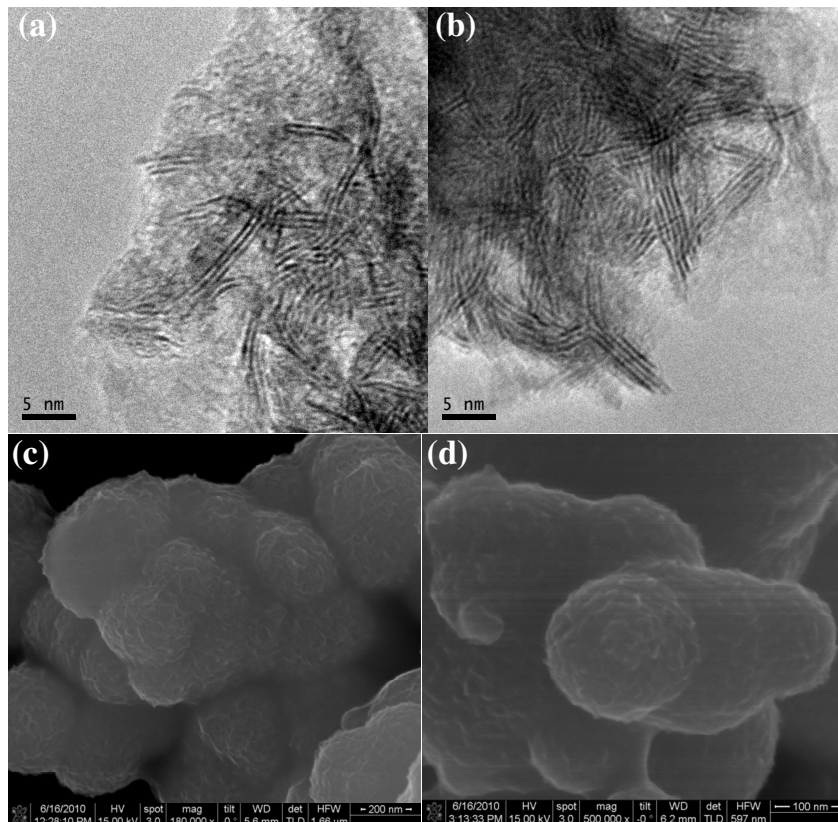
Figure 16: (a) and (b) are the TEM images whereas (c) and (d) are FESEM images of $MoSe_2$ layers obtained under hydrothermal conditions.

2.2: Graphene analogues based on metal chalcogenides

Thio/Seleno urea Method: In the solid state method, we have used of thiourea as a sulfur source, along with either molybdic acid or tungstic acid and heated at 773 K for 3 h under nitrogen atmosphere to obtain the layers of MoS_2 or WS_2 respectively. Using the similar concept, we could prepare the selenides of molybdenum and tungsten taking selenourea as a selenium source under the similar conditions to obtain few-layer $MoSe_2$ and WSe_2
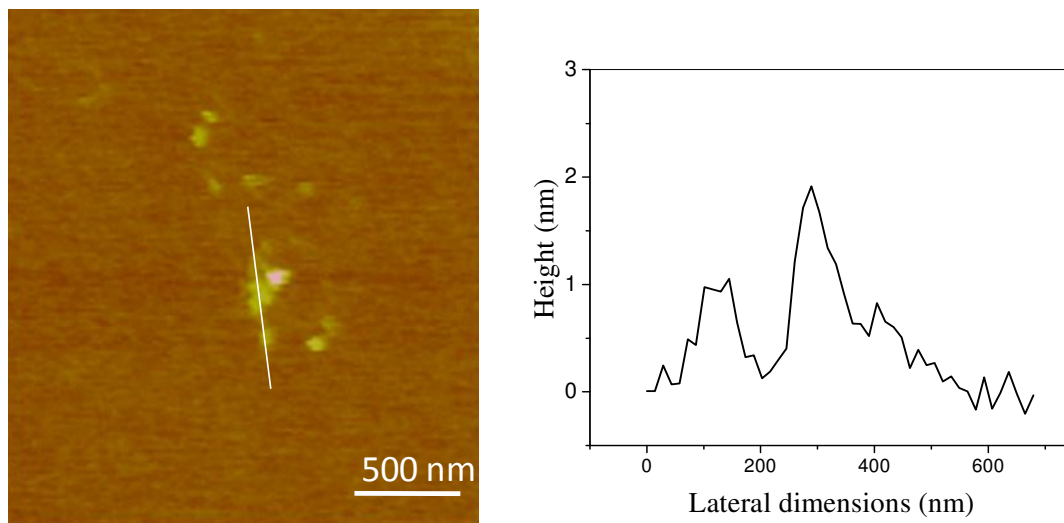

Figure 17: AFM images and the associated height profiles of MoS_2 layers obtained from hydrothermal conditions.
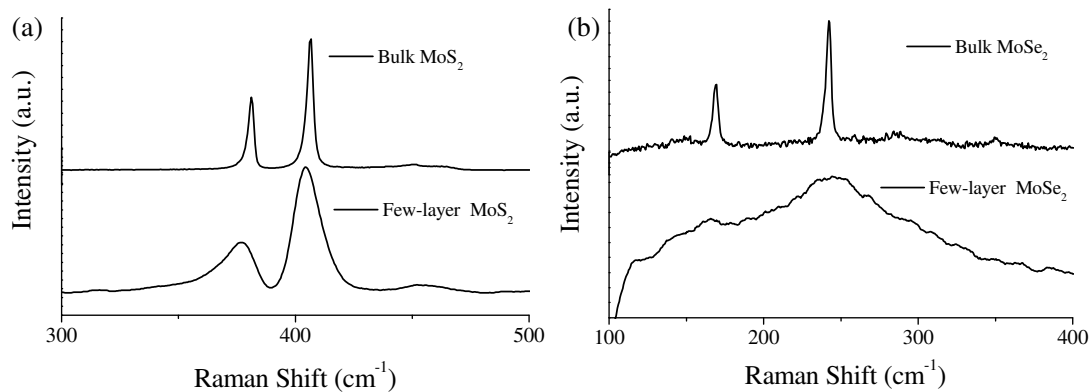
Figure 18: Comparison of Raman spectra of (a) bulk MoS_2 and few-layer MoS_2 layers, (b) bulk $MoSe_2$ and few-layer $MoSe_2$ layers obtained from hydrothermal conditions.

respectively. We have also partly investigated the mechanism for the formation of sheet like morphology of MoS_2. We believe that the same holds with the other sulfides and selenides of the Mo and W. We have carried out the reaction only with the molybdic acid without any sulfur reagent which is essentially a hydride of the molybdenum oxide has formed the sheets of the MoO_3. This has led us to conclude that the MoO_3 sheets acts like a precursor followed by the reduction to sub-oxides of MoO_3 which then converts to the sheets of MoS_2 because of the excess thiourea. In Figure 19, we have shown the the XRD
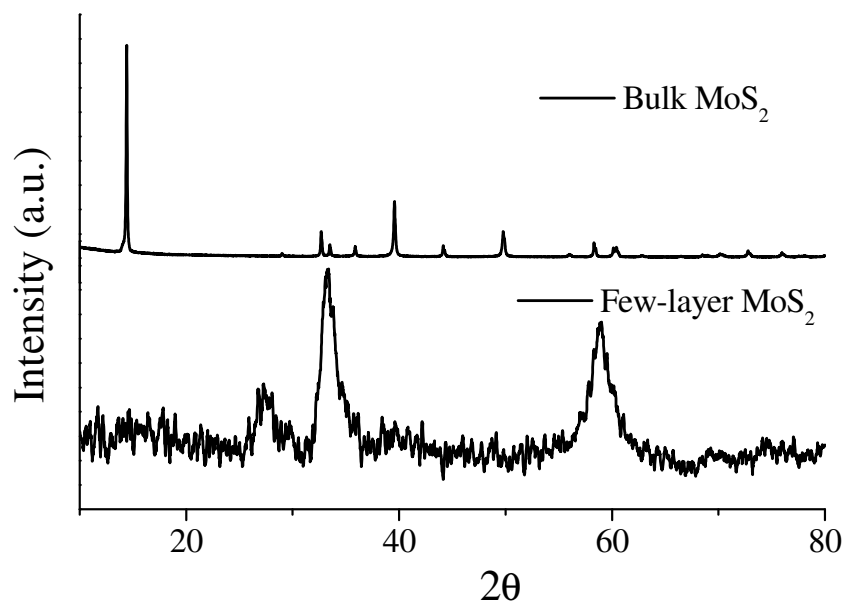

Figure 19: Comparison of XRD patterns of bulk MoS_2 with few-layer MoS_2 obtained from thiourea method.

pattern of the few-layer MoS_2 obtained from the thiourea method in which there is an absence of the (002) reflection and the presences of (110) and (110) plane further confirms the formation of single-layer MoS_2. Figure 20 shows the TEM images obtained for the same confirmed the presence of the 2-3 layers. Figures 20(a) and (c) show the presence of single- and bi-layers of MoS_2 and in Figure 20 (b) shows the d-spacing as 0.65 nm which is similar to that of bulk MoS_2. We have shown the high resolution image in Figure 21 which reveal the hexagonal structure formed by Mo and S atoms. In plane Mo-S distance
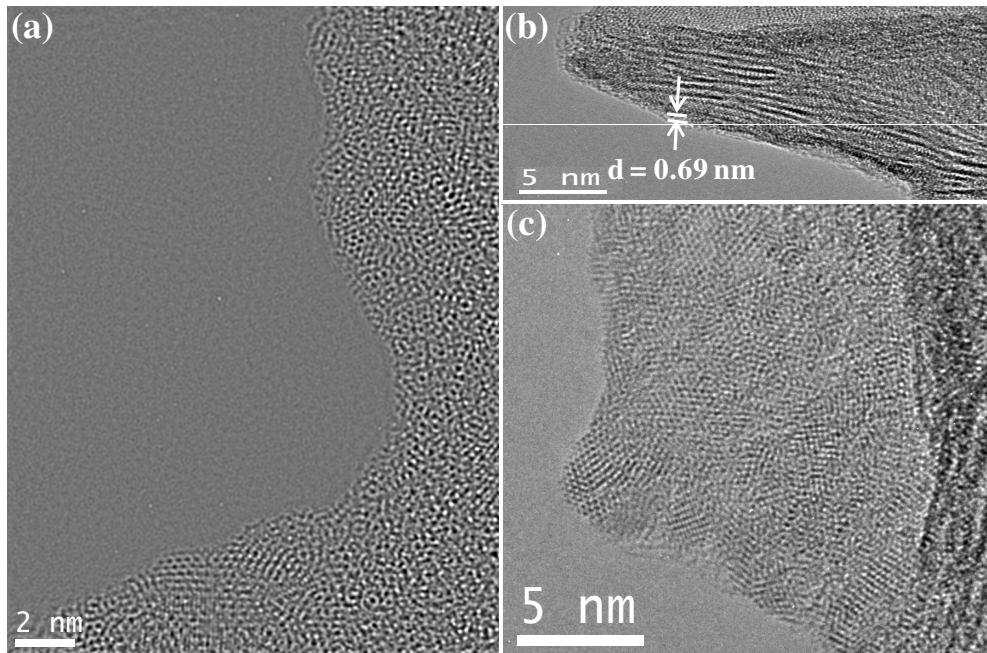
Figure 20: (a), (b) and (c) are the HRTEM images of MoS$_2$ layers obtained from thiuorea method.
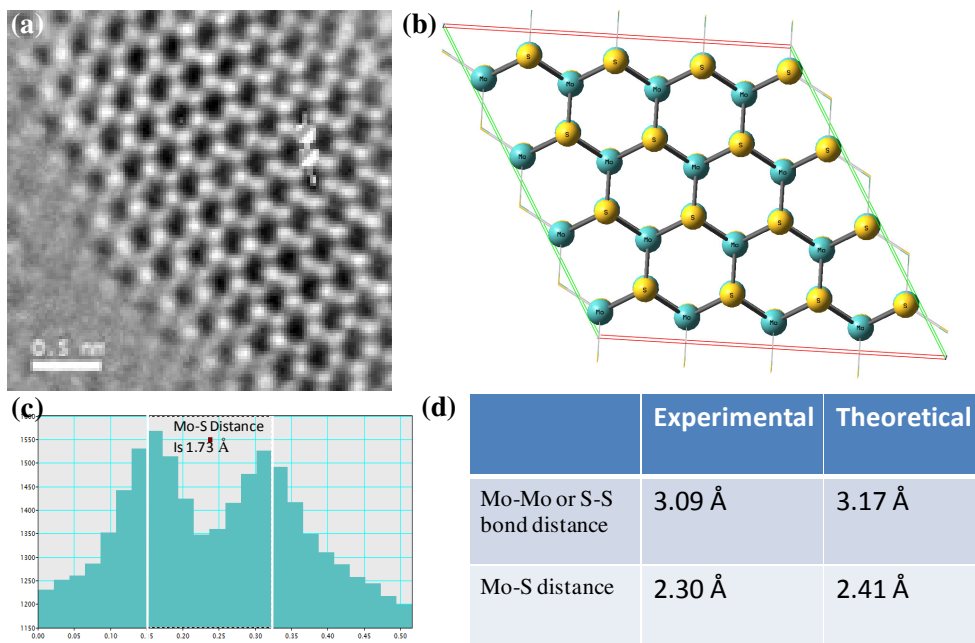
Figure 21: (a) HREM image of Single-layer MoS$_2$ (b) Schematic showing Mo and S atoms in MoS$_2$ (c) showing Mo-S distance (d) bond distances calculated.

is 1.73 Å found experimentally. Taking the angle between S-Mo-S as 82.41° we have calculated the Mo-S bond Distance as 2.31 Å. We have also calculated the Mo-Mo or S-S distance as 3.09 Å where the theoretical value being 3.16 Å. In Figure 22, we show the FESEM images of few-layer MoS_2 further confirming the layer like morphology supporting to the TEM images. From the AFM topographic image shown in Figure 22 (c) and the associated the height profile confirms the formation of few-layer MoS_2. Figure 23 shows the XRD pattern of the as-synthesized WS_2 layers and is similar to that of the MoS_2. From the absence of the (002) reflection in the XRD pattern, it is understood that the sample contains very few-layers of WS_2. Figure 24 shows the TEM images of WS_2 layers obtained by thiourea method and comprise mostly bi-layers. From
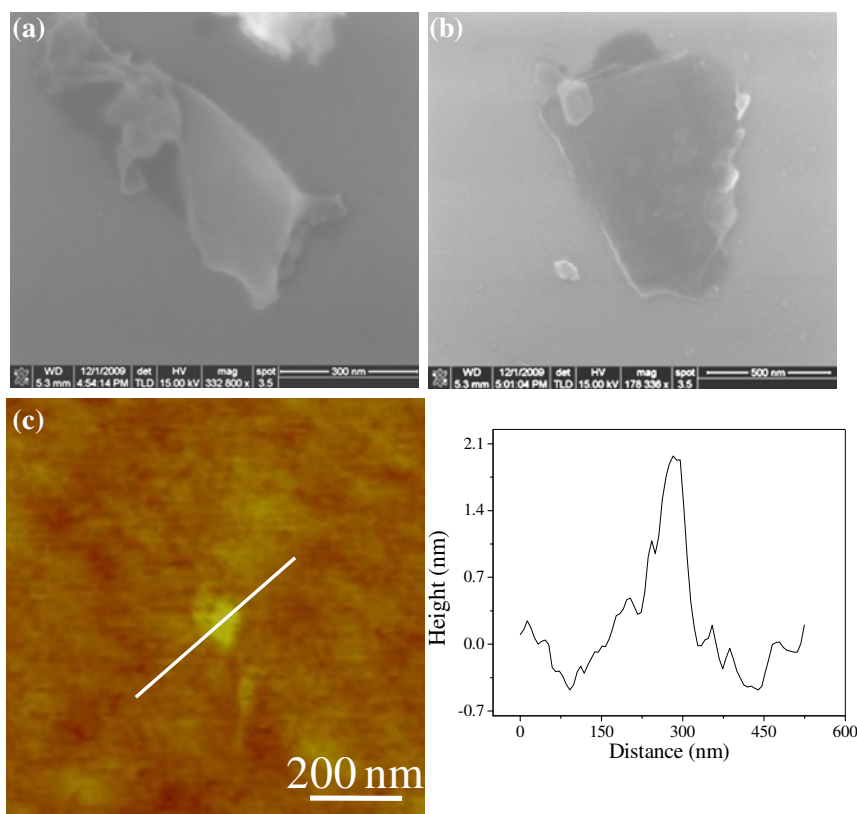
Figure 22: (a) and (b) are FESEM images of MoS_2 layers (c) shows AFM image and the associated height profiles of MoS_2 layers obtained from thiourea method.

the TEM images an interlayer spacing of 0.86-0.95 nm was obtained for WS_2 layers. This interlayer spacing in WS_2 is the separation between either two tungsten or sulphur atoms of adjacent layers. The larger spacing compared to bulk indicates that exfoliation is complete and the formed are monolayers and are decoupled with other layers. Figures 24 (c) and (d) are the TEM images obtained from FEI TITAN microscope. The TEM images showed that the sample mainly consists of bi-layers. Figure 24 (d) shows the high resolution transmission electron microscope (HREM) image of WS_2 showing the
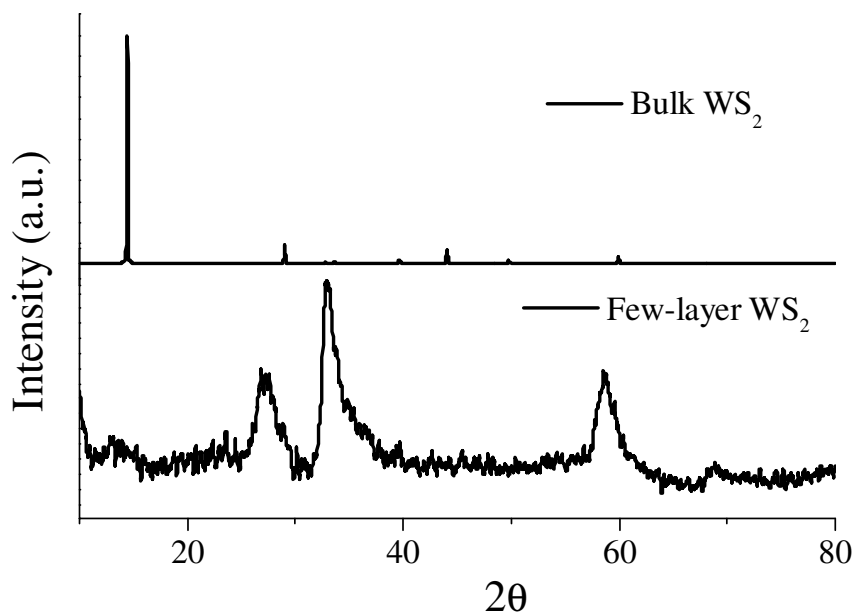
Figure 23: Comparison of XRD patterns of bulk WS_2 with few-layer MoS_2 obtained from thiourea method.

hexagonal arrangement of tungsten and sulphur atoms. The presence of bi-layers was also confirmed by the AFM analysis with the associated height profile of WS_2 layers as shown in Figure 25.
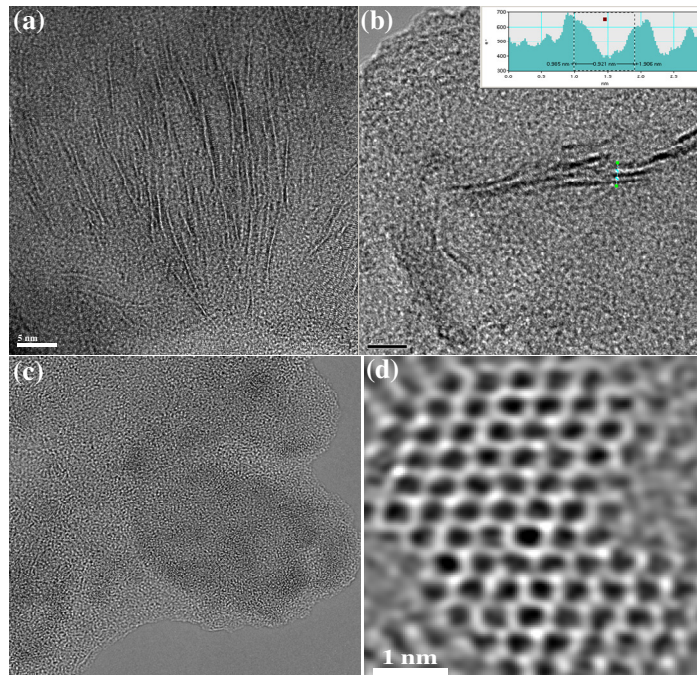
Figure 24: (a), (b) (c) and (d) are the HREM images of WS_2 layers obtained from thiuorea method.

We have synthesized few-layer $MoSe_2$ and WSe_2 using similar methods and characterized the sample with microscopic and spectroscopic techniques. The (002) reflection in the
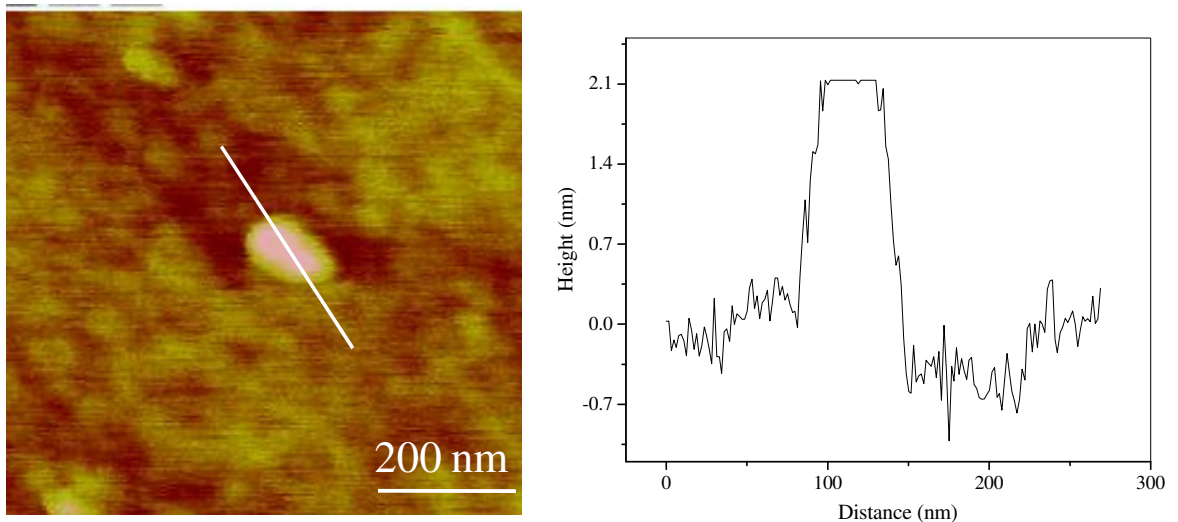

Figure 25: AFM image and the associated height profiles of WS_2 layers obtained from thiourea method.

XRD patterns indicates that the products formed in the reactions contain only few-layers (see Figure 26). Energy dispersive x-ray analysis (EDAX) showed the products to be stoichiometric $MoSe_2$ and WSe_2. In Figure 27, we present TEM of $MoSe_2$ showing the presence of one to three layers with a layer separation of 0.65 - 0.70 nm. In Figure 28, we
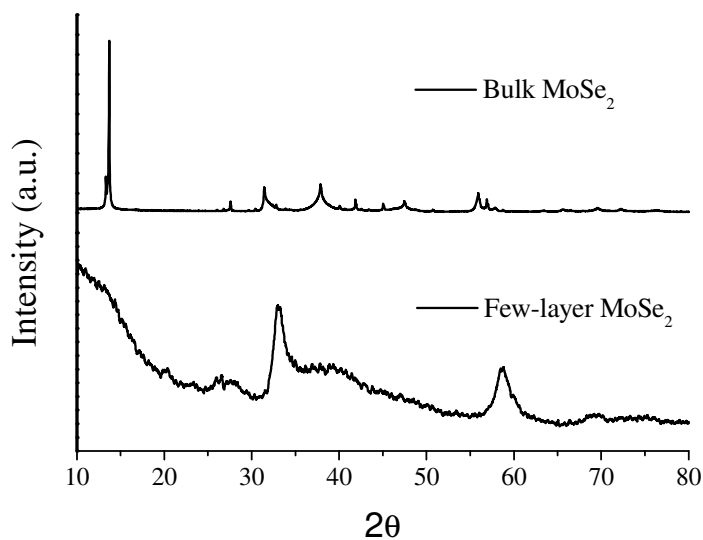
**Figure 26:** Comparison of XRD patterns of bulk $MoSe_2$ with few-layer $MoSe_2$ obtained from selenourea method.
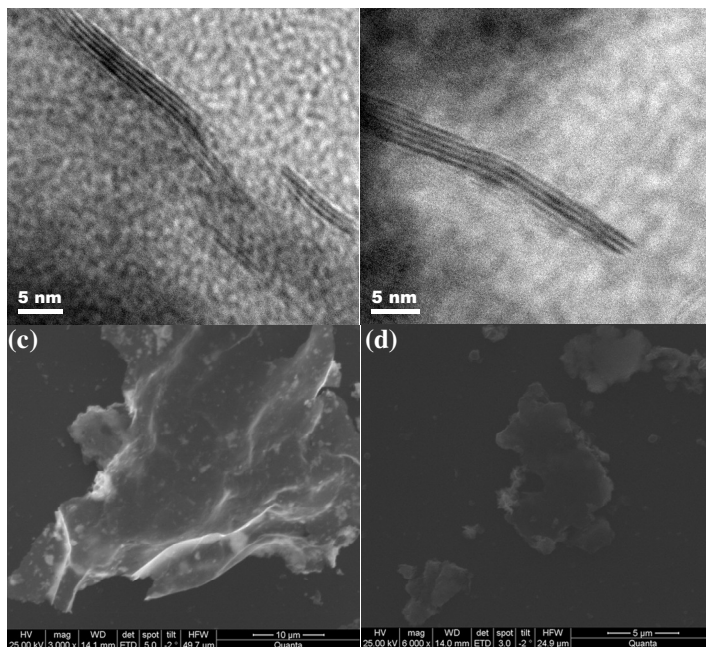
Figure 27: (a) and (b) are the TEM images whereas (c) and (d) are FESEM images of $MoSe_2$ layers obtained from selenourea method.

show HREM images of MoSe$_2$ layers recorded with a FEI TITAN^{3TM} aberration-corrected microscope with a negative C$_s$ ~ 30 µm and a positive defocus Δf ~ 8 nm. Here, the atoms appear bright in a dark background. Figure 28 (a) shows graphene-like MoSe$_2$ with single and bi- layer structures. We have verified the region as single layer using the Fresnel's contrast before performing HREM. Fresnel contrast is formed under defocus condition due to abrupt change in inner potential. Fourier filtered HREM images obtained from the same
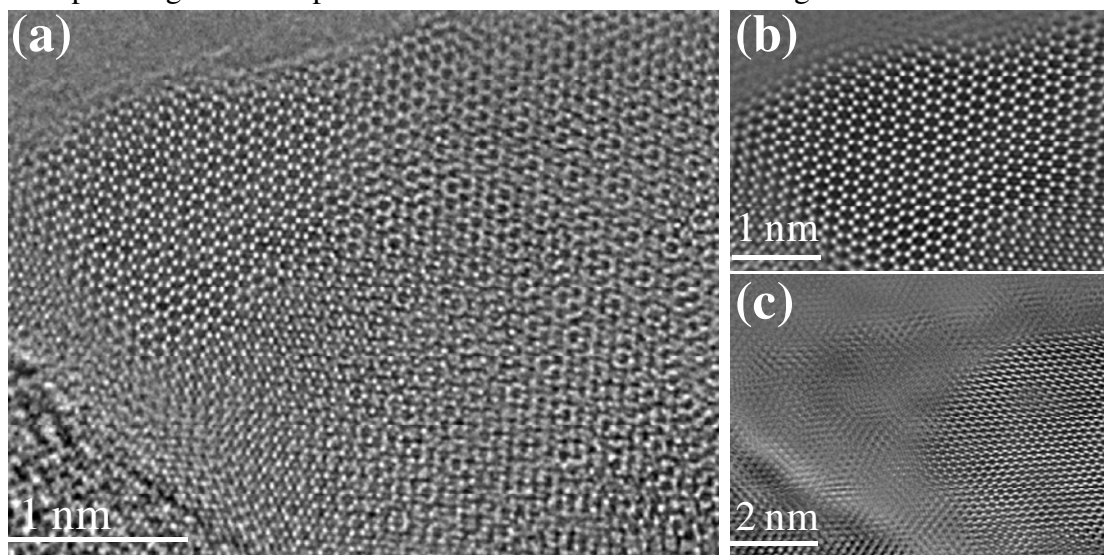
Figure 28: (a) High-resolution TEM image of layered MoSe$_2$ from selenourea method. Fourier transformed images of single and bi-layers are shown in (b) and (c).

area where one can separate out single-layer MoSe$_2$ near the edge and the second layer away from the edge (which is slightly rotated with respect to the first layer) are shown in Figures 28 (b) and (c) respectively. The images and the associated Fourier transforms show hexagonal symmetry. Graphene analogues of molybdenum selenide prepared by selenourea method was characterized by FESEM (see Figures 27(b) and (c)) which also reveals layer like morpholgy. AFM images and the corresponding height profiles of 0.9 nm to 1.9 nm in Figure 29 confirms the presence of one to three layers with the lateral dimensions varying from 300 nm to few micrometers.
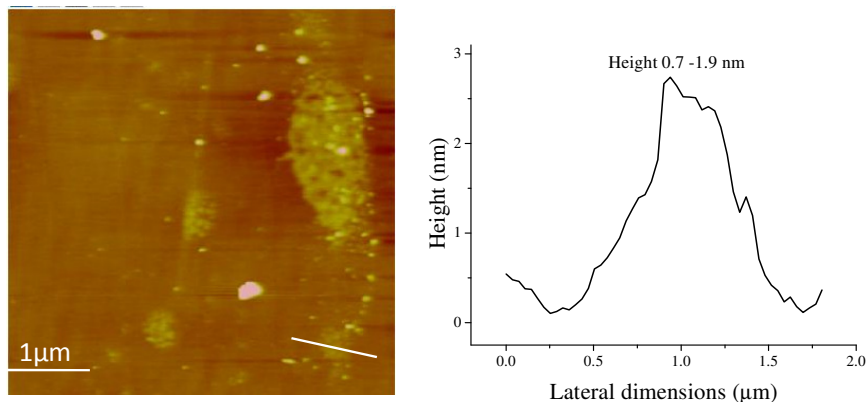
Figure 29: AFM image and the associated height profiles of $MoSe_2$ layers obtained from selenourea method.

Similar XRD patterns also obtained in the case of WSe_2 prepared by selenourea method as shown in Figure 30. A TEM image showing 4-5 layers is shown in Figure 31 (a). Figure 31(b) shows TEM images of WSe_2 prepared by the selenourea method contains predominantly 2 layers. Figures 31 (c) and (d) show the FESEM images
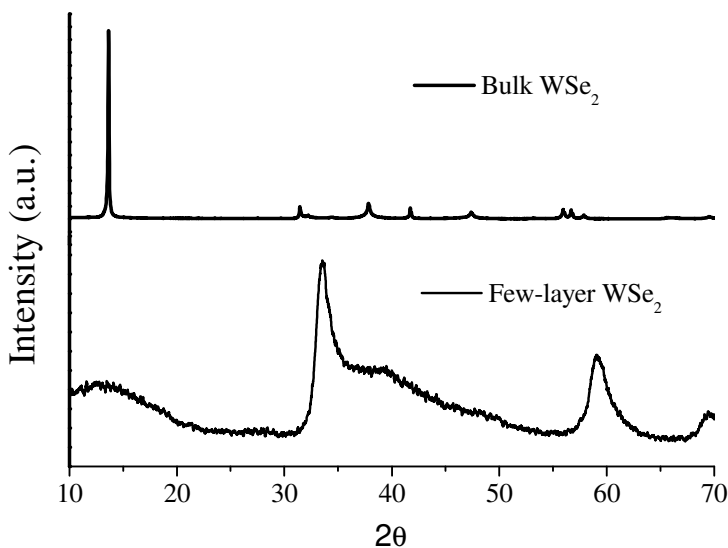

Figure 30: Comparison of XRD patterns of bulk WSe_2 with few-layer WSe_2 obtained from selenourea method.

which corroborates the TEM observation having sheet like morphologies. Figure 32(a) presents a HREM image of single-layer WSe_2. The corresponding Fourier filtered image is

shown in Figure 32 (b), where the bright dots correspond to the heavy W atoms. Figure 33

show AFM height profile of 0.7 - 1.9 nm corresponds to 2-3 layers.
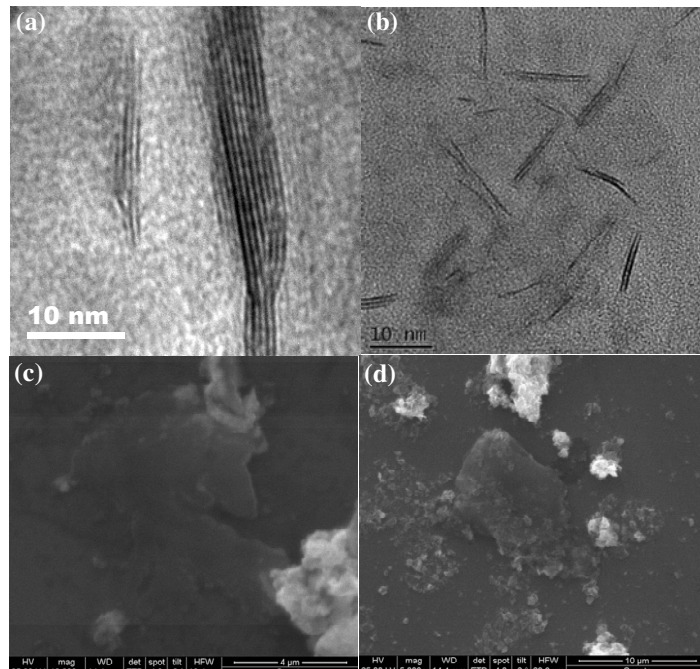
Figure 31: (a) and (b) are the TEM images whereas (c) and (d) are FESEM images of WSe$_2$ layers obtained from selenourea method.
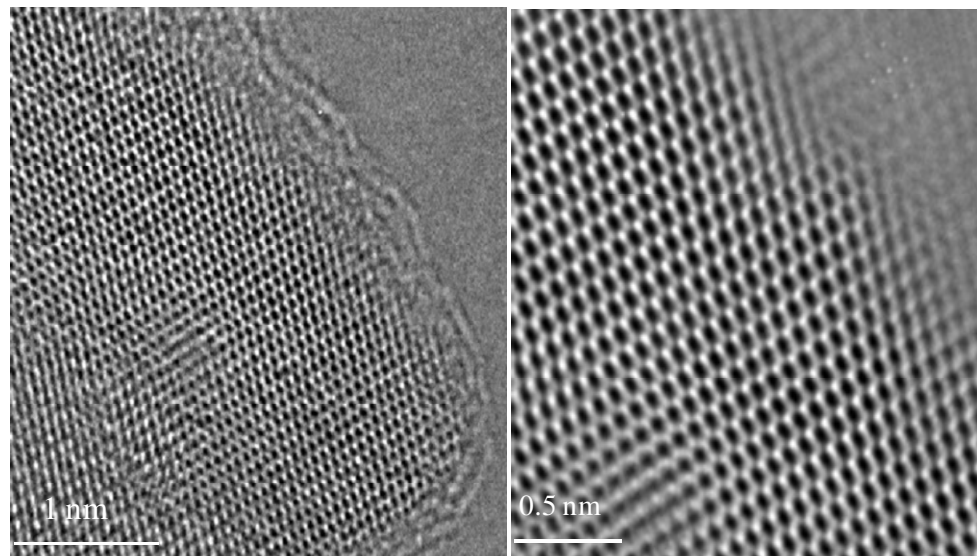
Figure 32: (a) High resolution TEM image ofWSe$_2$ and (b) the Fourier transform image of single layerWSe$_2$

The sample obtained by this method show the Raman bands at 404.7 cm^{-1}. There is an

apparent softening of the A$_{1g}$ mode in the graphene analogues of MoSe$_2$ (see Figure 34

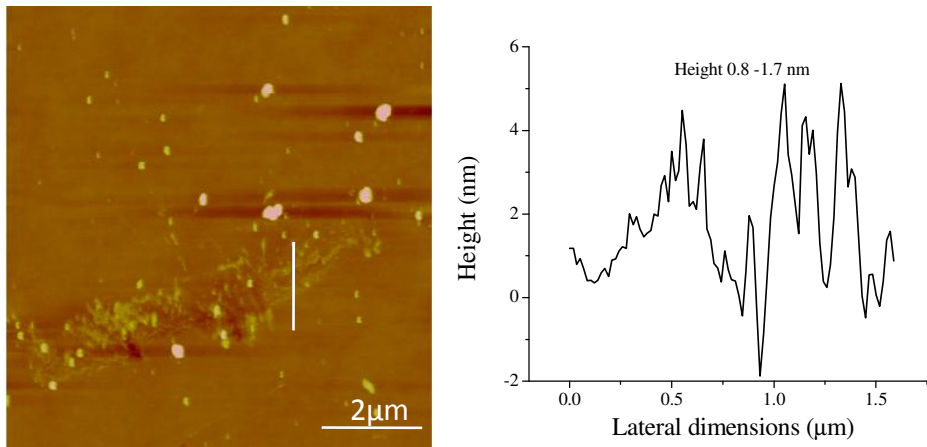(a)). Furthermore, the FWHM values are larger in the graphene-like samples, the values varying from 10 to 16 cm^{-1} compared to ~ 3 cm^{-1} of the bulk sample.

Figure 33: AFM image and the associated height profiles of WSe$_2$ layers obtained from selenourea method.

In Figure 34 (a), we show the Raman spectrum of WS$_2$ layers obtained by thiourea method which shows a similar softening of the A$_{1g}$ mode and an increase in width of the E$_{2g}$ mode. Raman spectrum of graphene-like MoSe$_2$ prepared by this method was compared with the spectrum of bulk MoSe$_2$. The bulk sample gives Raman band at 242 cm^{-1} due to the A$_{1g}$ modes with the full-width half maxima (FWHM) of 4.1 cm^{-1}. Interestingly, few-layer MoSe$_2$ shows this band at 239.9 cm^{-1} (See Figure 34 (b)). There is a clear softening of the A$_{1g}$ mode in the graphene analogues of MoSe$_2$. The softening of modes observed here is
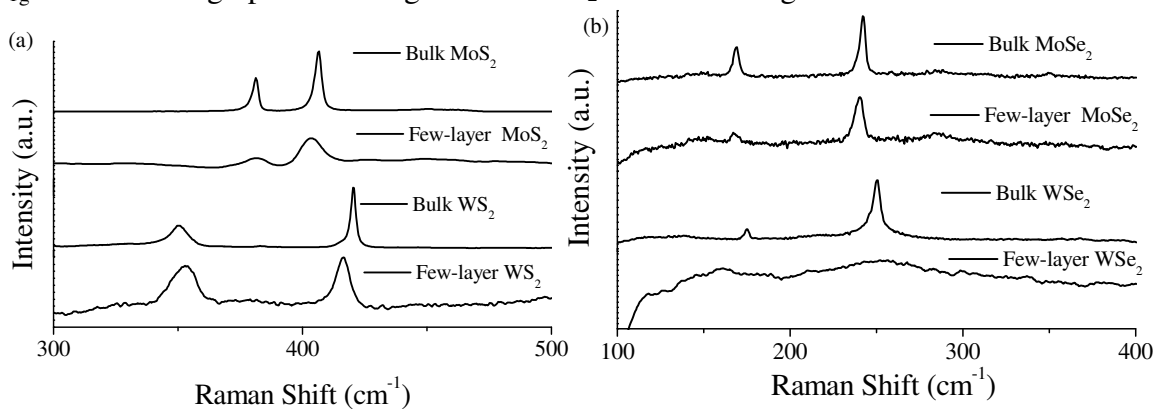
Figure 34: Comparison of Raman spectra of (a) bulk MoS$_2$ and few-layer MoS$_2$ layers, bulk WS$_2$ and few-layer WS$_2$ layers (b) bulk MoSe$_2$ and few-layer MoSe$_2$ layers, bulk WSe$_2$ and few-layer WSe$_2$ layers obtained by thio/seleno urea method.

similar to that reported in the case of graphene analogues of MoS_2. The FWHM values are larger in the graphene-like samples, the values varying from 6-8 cm^{-1} compared to ~ 4 cm^{-1} in bulk $MoSe_2$. Raman spectrum of graphene-like WSe_2 obtained by both the methods show softening of the band due to the A_{1g} mode. Compared to the narrow band at 255 cm^{-1} (A_{1g}) of bulk WSe_2 with FWHM value around 5 cm^{-1} (see Figure 34 (b)). The spectrum of WSe_2 obtained shows band 249.7 cm^{-1} with FWHM of 43 cm^{-1}.
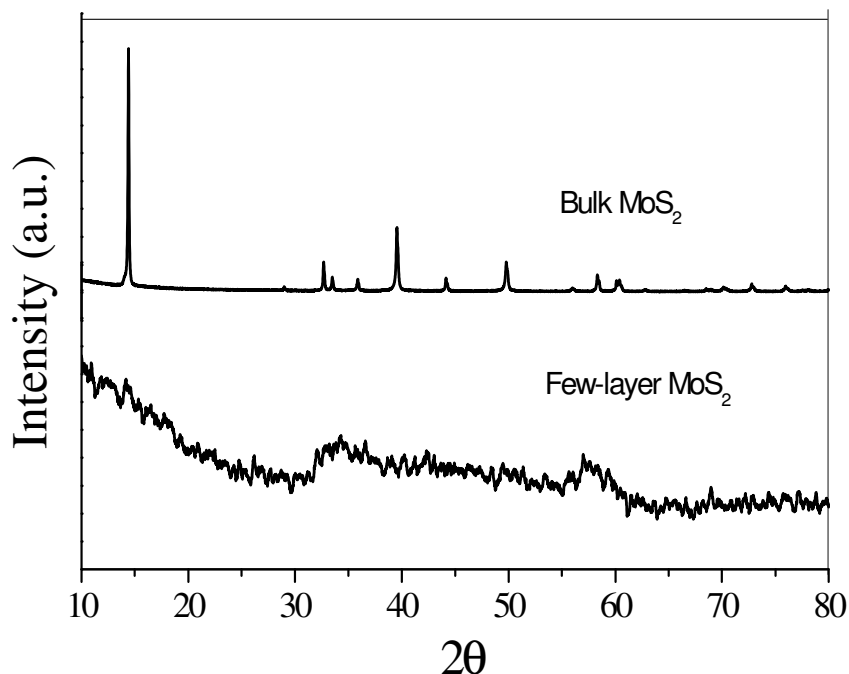
Figure 35: Comparison of XRD patterns of bulk MoS_2 with few-layer MoS_2 obtained under microwave conditions.

Microwave Synthesis: In Figure 35, we have shown the XRD patterns of inorganic graphenes prepared by microwave synthesis using EG as solvent. The absence of (002) reflection in all the XRD patterns indicate the product formed in the reaction contains few layers. We have carried out TEM studies to identify the morphology of the products obtained in the microwave synthesis. In Figure 36 we have shown the TEM images of sulfides of Mo. Figures 36 (a) and (b) show the formation of 3-4 layers of MoS_2

with the inter-layer spacing ranging from 0.6 -0.9 nm. We have also carried out the field

emission scanning electron microscopy images of the inorganic graphenes to examine the
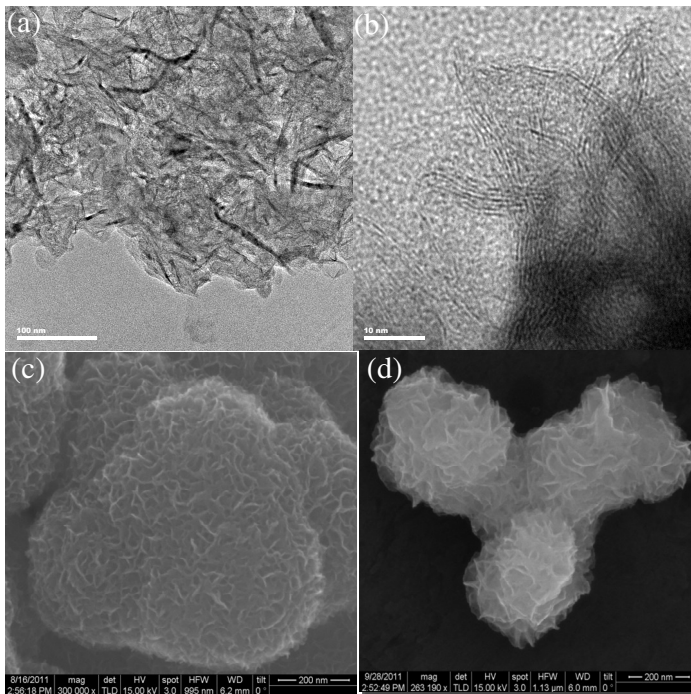
Figure 36: (a) and (b) are the TEM images whereas (c) and (d) are FESEM images of MoS_2 layers obtained under microwave conditions.

overall morphology of the obtained products. Figures 36 (c) and (d) show petals/layers like

morphology of few-layer MoS_2.
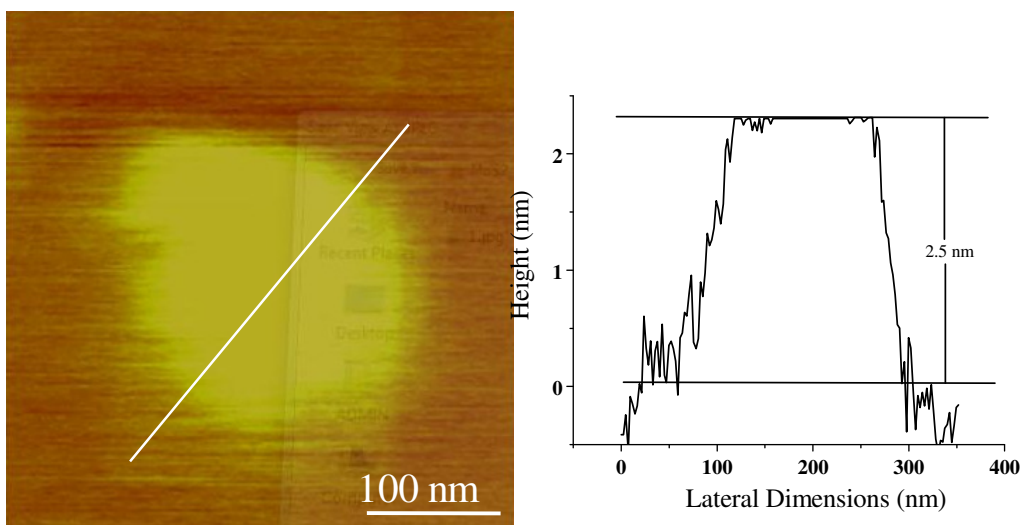
Figure 37: AFM image and the associated height profiles of MoS_2 layers obtained under microwave conditions.
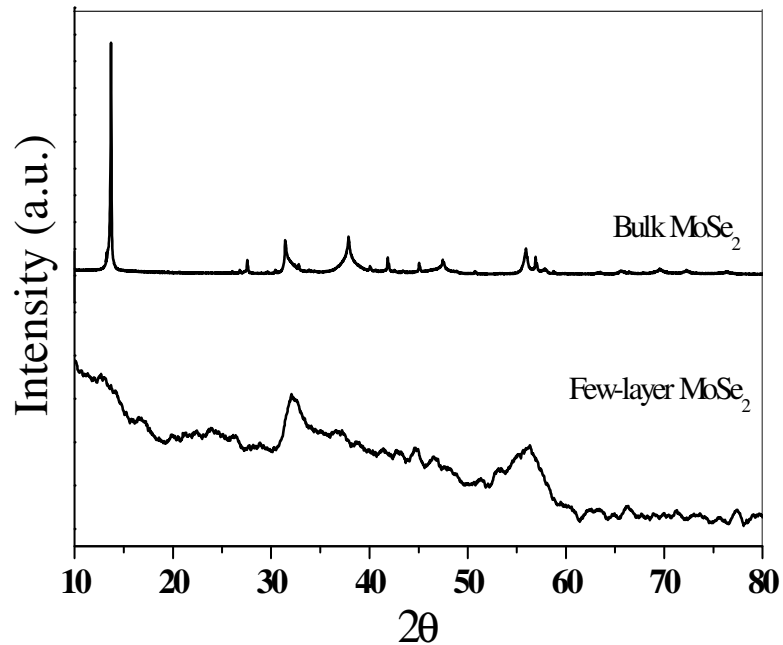
Figure 38: Comparison of XRD patterns of bulk MoSe$_2$ with few-layer MoSe$_2$ obtained from microwave synthetic method.

AFM image and their corresponding height profile in Figure 37 confirm the presence of three to four layers having height profile of 2.5 nm. The lateral dimensions are varying from 300 nm to 500 nm.
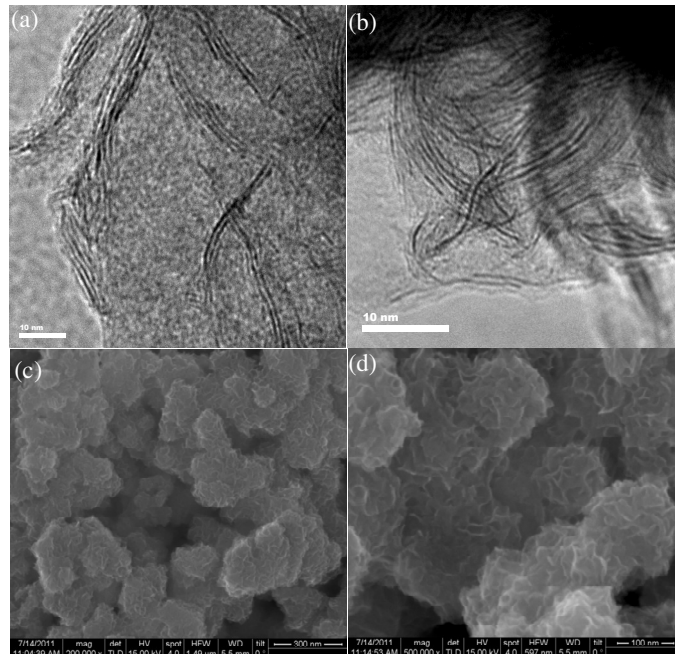
Figure 39: (a) and (b) are the TEM images whereas (c) and (d) are FESEM images of MoSe$_2$ layers obtained under microwave conditions.

221

2.2: Graphene analogues based on metal chalcogenides

Figure 38 shows the XRD of Bulk $MoSe_2$ with few-layer $MoSe_2$ obtained from microwave synthetic procedure. Similar to the earlier XRD patterns we have observed any (002) reflection suggesting the formation of single- or few-layer $MoSe_2$. We have also characterized the $MoSe_2$ sample obtained by microwave method using microscopic techniques. TEM images of $MoSe_2$ having 2-5 layers as can be seen from the Figures 39 (a) and (b). FESEM images shown in Figures 39 (c) and (d) also reveals the formation of $MoSe_2$ layers. To further confirm the number of layers we have measured the height
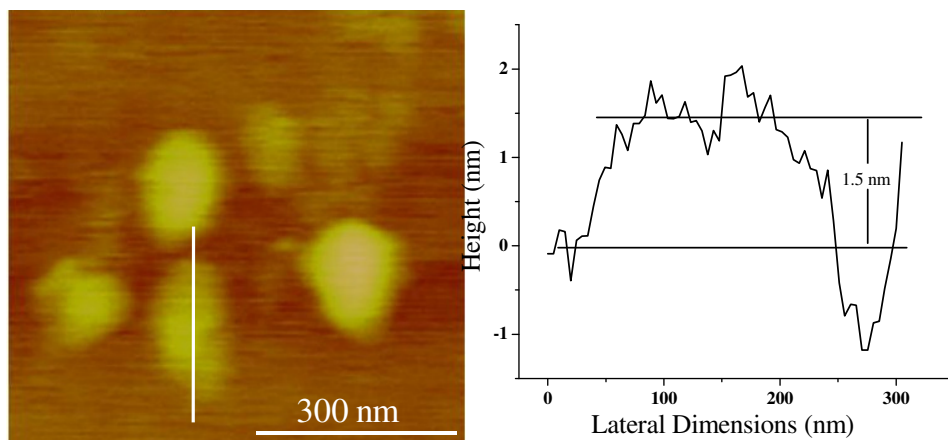
Figure 40: AFM image and the associated height profiles of MoS_2 layers obtained from microwave synthetic method.

profiles of these layers using AFM and found that it contains 2-3 layers with the height of ~ 1.5 nm corroborating the TEM results (Figure 40). We have also carried out the experiment under similar conditions using water as solvent. In this case also we could prepare the pure phase of sulphides and selenides of molybdenum but the yields are relatively less (~ 20 %) when compared to EG as a solvent (~ 60 %). It might be due to the intrinsic nature of EG which can acts as solvent as well as reducing agent. In Figure 41(a), we compare the Raman spectrum of graphene-like MoS_2 samples prepared by us with the spectrum of bulk MoS_2. The bulk sample gives band at 406.5 cm^{-1} due to the A_{1g} mode with full-width half maximum of 3.1 cm^{-1}. Interestingly, few-layered MoS_2 prepared by

microwave method exhibits the corresponding band at 400.7 cm^{-1}. There is a clear softening of the A_{1g} mode in the graphene analogues of MoS_2. Raman spectrum of graphene-like $MoSe_2$ prepared by microwave method was compared with the spectrum of bulk $MoSe_2$. The bulk sample gives Raman band at 242 cm^{-1} due to A_{1g} mode. Whereas in few-layer $MoSe_2$ prepared by microwave method exhibits the corresponding
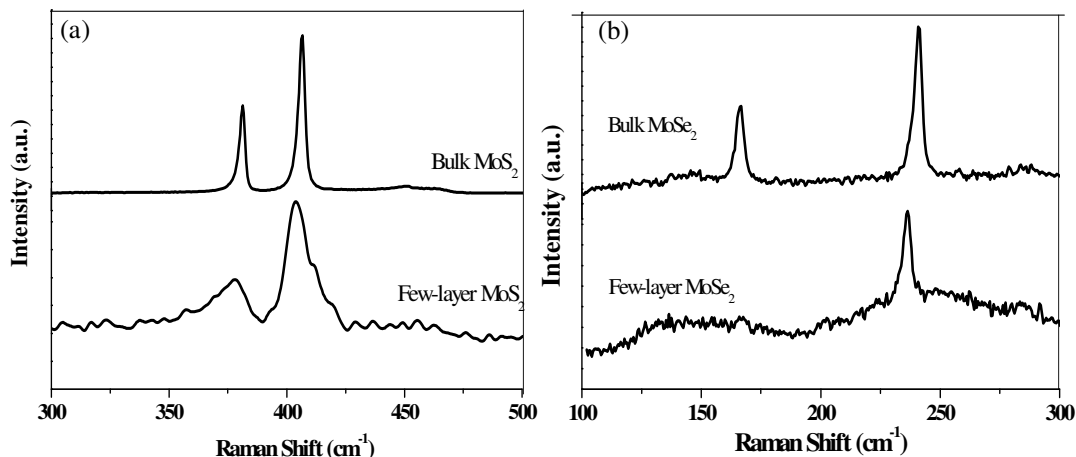
Figure 41: Comparison of Raman spectra of (a) bulk MoS_2 and few-layer MoS_2 layers, (b) bulk $MoSe_2$ and few-layer $MoSe_2$ layers.

band at 236.4 cm^{-1} (see Figure 41 (b)). There is a clear softening of A_{1g} mode in the graphene analogues of $MoSe_2$. The Raman spectrum of MoS_2 and $MoSe_2$ layers synthesized by microwave method shows softening of the Raman band along with the increase in FWHM values.

Laser Exfoliation: We have found that laser irradiation of layered inorganic materials in a polar medium such as dimethylformamide (DMF) readily gives rise to single- as well as few- layer inorganic graphenes. The method of generating graphene-like species by laser irradiation was as follows. A dispersion of MoS_2/WS_2/$MoSe_2$/WSe_2 medium was taken in a quartz vessel and irradiated by a Lambda Physik KrF excimer laser ($\lambda = 248$ nm, $\tau = 30$

ns) at a fluence of 1.5 J/cm^2 and 5Hz repetition rate for 1 hour. The dispersion was continuously stirred with a magnetic stirrer during the irradiation. In a typical preparation, 4 mg of the corresponding layered material was dispersed in 4ml of DMF. After laser irradiation, the resultant product was centrifuged at 3000 RPM for 5minutes. After the centrifugation, the one third of the supernatant was transferred to another container. The supernatant liquids were stable for prolonged duration and contained inorganic-graphene like species. The supernatant liquids were drop cast on to clean silicon substrate and dried to achieve solid films for FESEM analysis. The supernatant liquids were taken on carbon coated copper (TEM) grids and vacuum-dried for the purpose of imaging. TEM images reveal that laser exfoliated graphene-analogues are quite transparent and is therefore only few layers thick (Figures 42(a) and (b)). We show FESEM images of graphene-like species present in the supernatant liquid in Figures 42 (c) and (d). A typical AFM image of
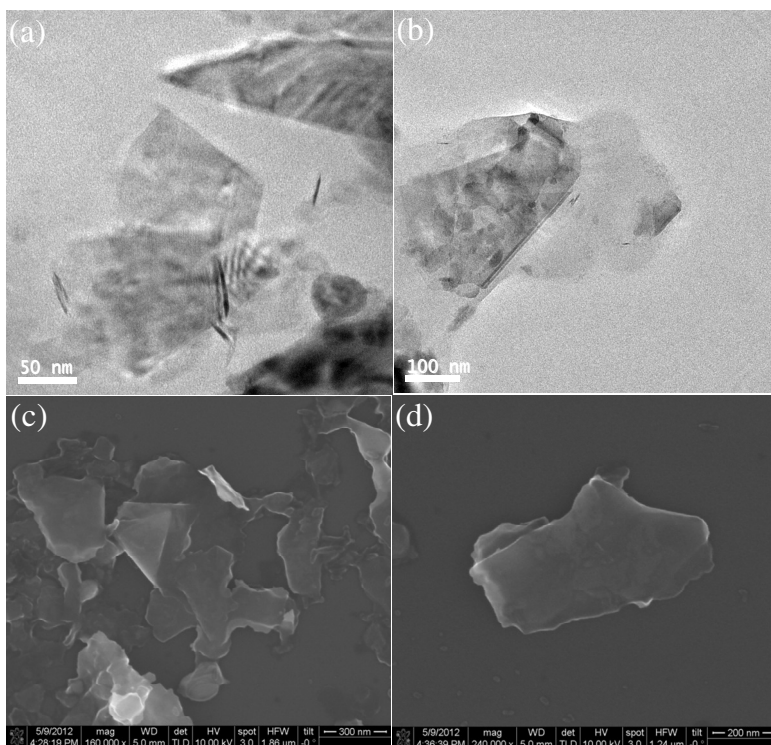
Figure 42: (a) and (b) are the TEM images, (c) and (d) are FESEM images of MoS$_2$ layers obtained by laser exfoliation.

the MoS$_2$ species present in the supernatant liquid after irradiation is shown in Figure 43.

On analyzing the AFM data, it confirms the formation of monolayer with the height of

around 0.9 nm with lateral dimensions varying between 200-400 nm.
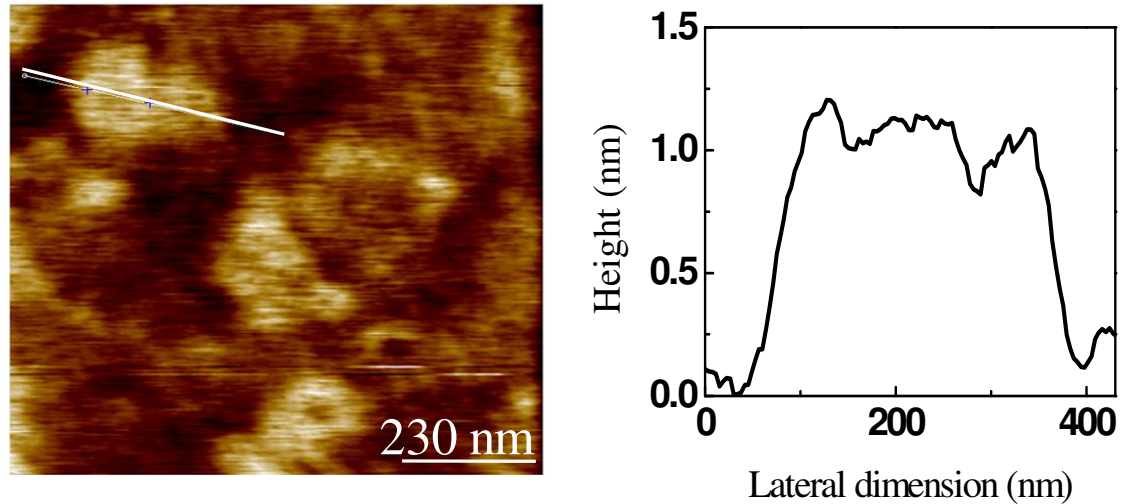
Figure 43: AFM image and the associated height profile of a few-layer MoS$_2$ and the height profile.

The corresponding TEM images of WS$_2$ exfoliated in DMF are shown in Figures

44 (a) and (b) and the corresponding FESEM images are shown in Figures 44 (c) and (d).
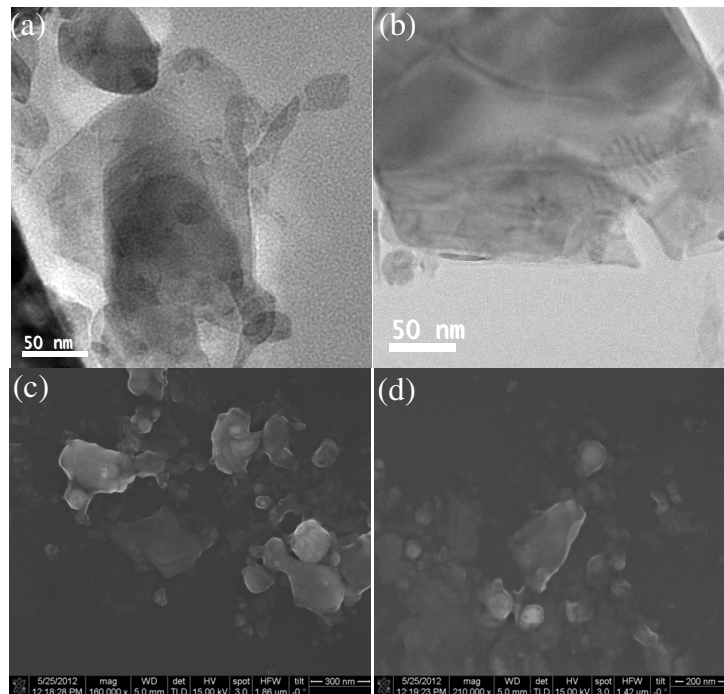
Figure 44: (a) and (b) are the TEM images, (c) and (d) are FESEM images of WS$_2$ layers obtained by laser exfoliation.

225

2.2: Graphene analogues based on metal chalcogenides

AFM image reveals the presence of two-dimensional flakes upto few hundred nanometers in lateral dimension. We show the AFM height profiles of WS$_2$ flakes with a height of ~ 2.5 nm as can be seen in Figure 45, which demonstrates the presence of 3-4 layers.
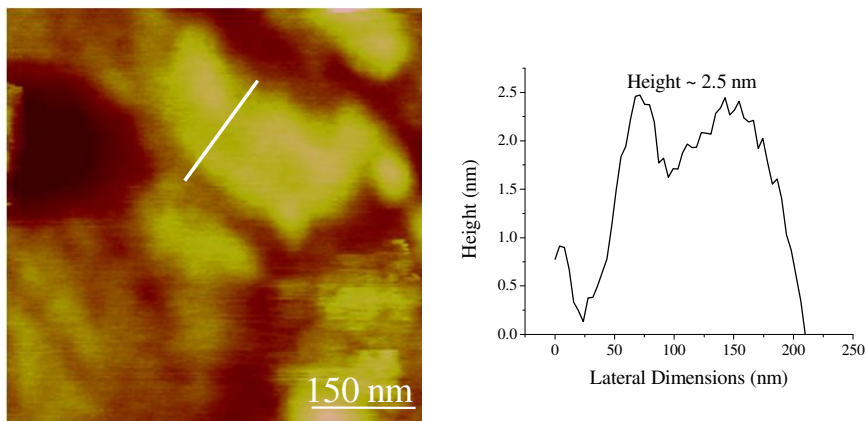
Figure 45: AFM image and the associated height profile of a few-layer WS$_2$ and the corresponding height profile.
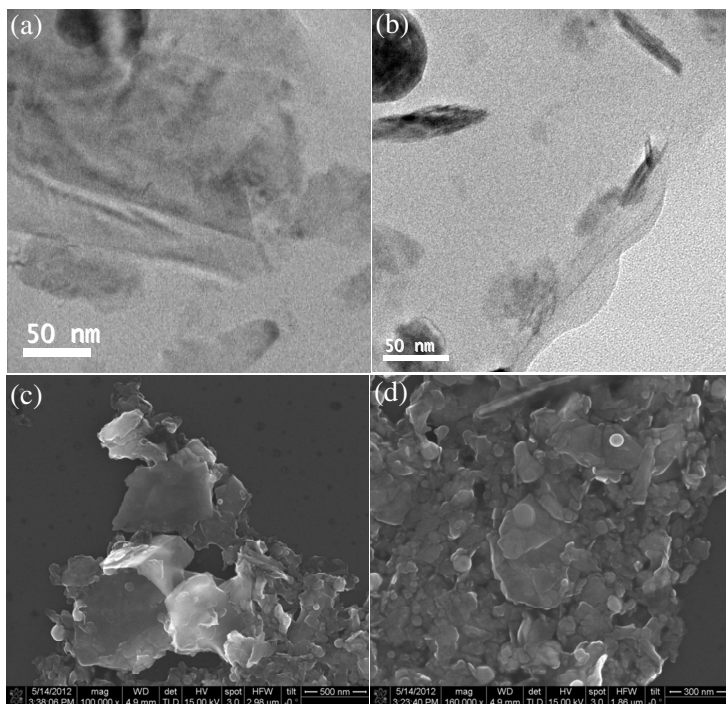


Figure 46: (a) and (b) are the TEM images, (c) and (d) are FESEM images of MoSe$_2$ layers obtained by laser exfoliation.

The supernatant liquid containing two dimensional sheets of MoSe$_2$ has been characterized with FESEM, TEM and AFM. In Figures 46 (a) and (b), we show the TEM images of the MoSe$_2$ sample obtained by this means. Figures 46 (c) and (d) show the corresponding FESEM images further confirming the effectiveness in exfoliation process during the laser treatment. We have carried out AFM studies on these samples in order to
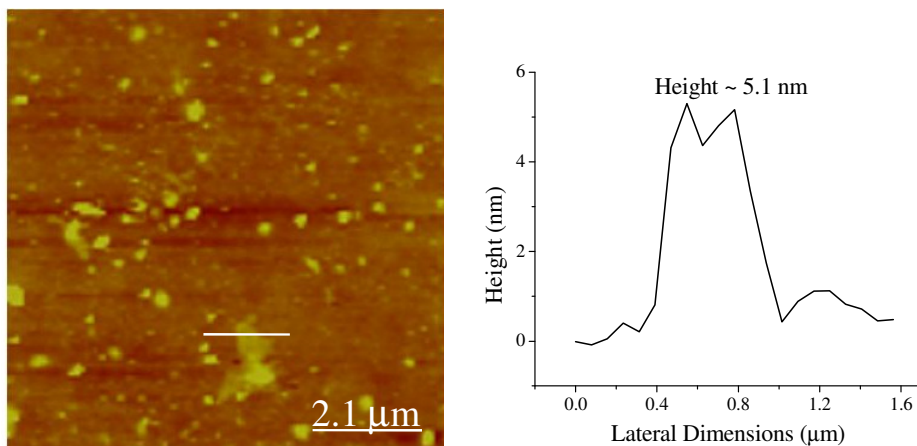
Figure 47: AFM image and the associated height profile of a few-layer WS$_2$ and the corresponding height profile.

estimate the number of layers in the sample. Figure 47 shows AFM image and the lateral dimensions of MoSe$_2$ sheets are in the range 400 nm to 1 μm consisting of 3-6 layers.
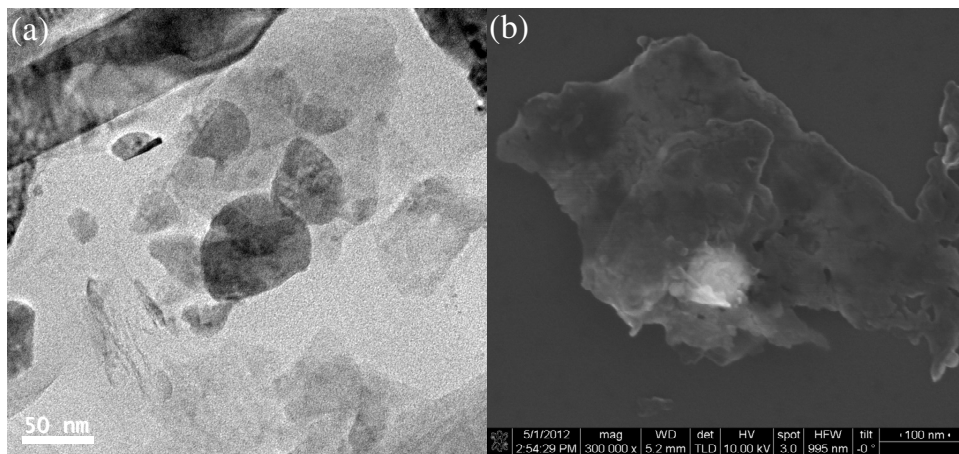
Figure 48: (a) TEM image, (b) FESEM images of WSe$_2$ layers obtained by laser exfoliation.

227

2.2: Graphene analogues based on metal chalcogenides

Nanosheets of WSe$_2$ could also be prepared by laser radiation as can be seen from the TEM and FESEM images in Figures 48 (a) and (b) respectively.

As suggested by Tenne et al. the formation mechanism of inorganic graphenes can be explained as follows. This process involves the interaction between pulsed laser radiation and the material dispersed in the liquid. Stresses produced by laser-induced thermal shock were not relieved and could eventually lead to cracking and flake detachment, i.e., exfoliation.[26] Laser exfoliation causes the delamination of nanosized layer materials. The ejected MoS$_2$ thin flakes and fragments were hit by shock waves produced during subsequent pulses, causing further diminution of particles.[17]

GaS and GaSe: We have used liquid phase exfoliation method for obtaining the few-layer GaS and GaSe from their bulk counter parts in a polar medium such as N-methyl pyrrolidone (NMP). The method of generating graphene-like species by sonication was as follows. A dispersion containing 20 mg of GaS/GaSe in 40 ml of NMP was taken in a beaker and sonicated with probe sonicator operates at 20 Hz with 250 Watt for 20 minutes by giving a gap of 5 minutes for every 2 minutes.
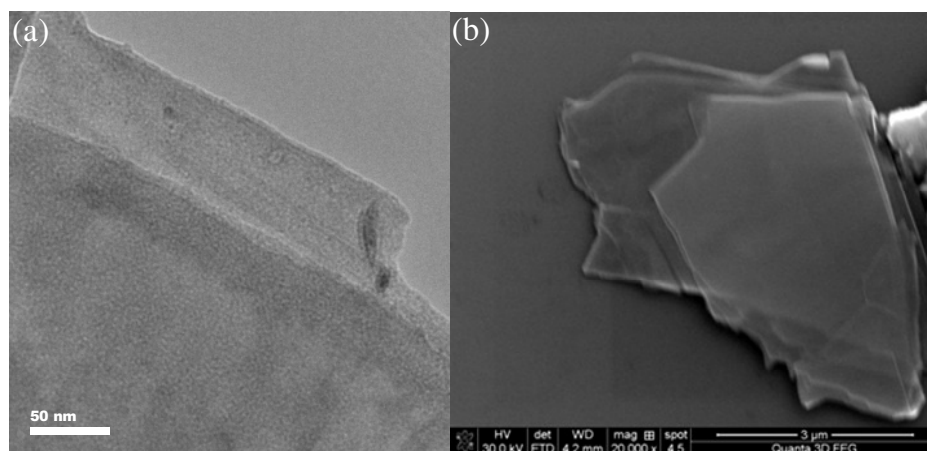
Figure 49: (a) TEM image and (b) FESEM image of GaS sheets obtained by liquid-phase exfoliation.

Figure 49(a) shows the typical TEM image showing the formation of sheet morphology. In Figure 49(b), we show FESEM images having similar features that are
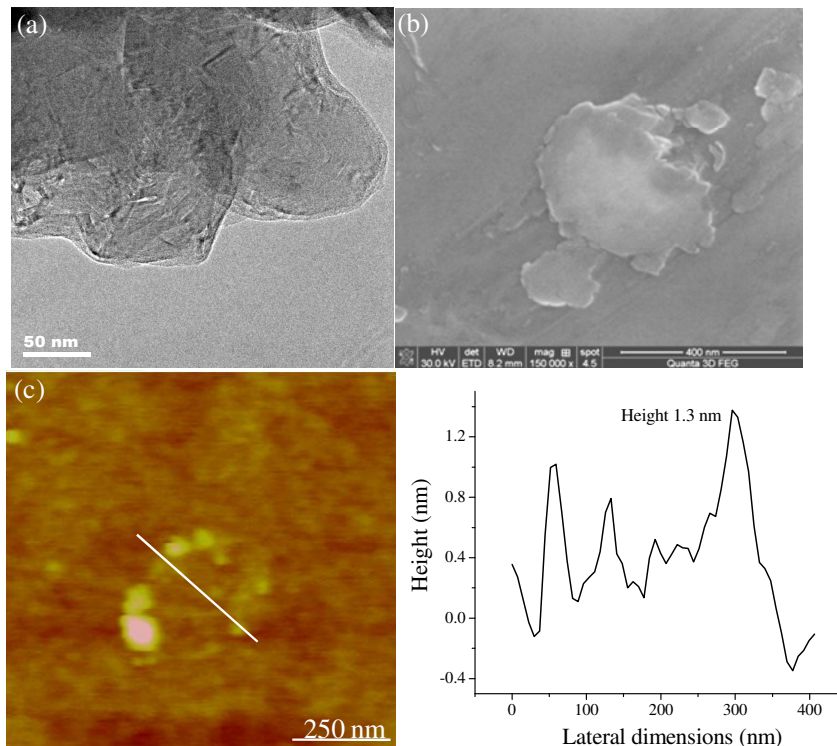
Figure 50: (a) TEM image (b) FESEM image of GaSe sheets obtained by liquid-phase exfoliation and (c) AFM image and the associated height profile of GaSe.

observed in TEM which further confirms the formation of graphene analogues. In Figures 50 (a) and (b), we show the TEM and FESEM images of GaSe sample obtained by this means. The lateral dimensions of the GaSe sheets are in the range 400 nm to 1 μm consisting of 2-4 layers as can be seen from topographic image and from the height profile (Figures 50 (c) and (d)).

Possible mechanism for exfoliation is as follows. During the sonication process the solvent molecules can penetrate between the layers (intercalated compounds), and split the crystal into small crystallites.[27] Most nanosheets were of reduced lateral sizes, which was attributed to the scissoring of parent sheets induced by sonication similar to that of reported in the case of BN. [28]
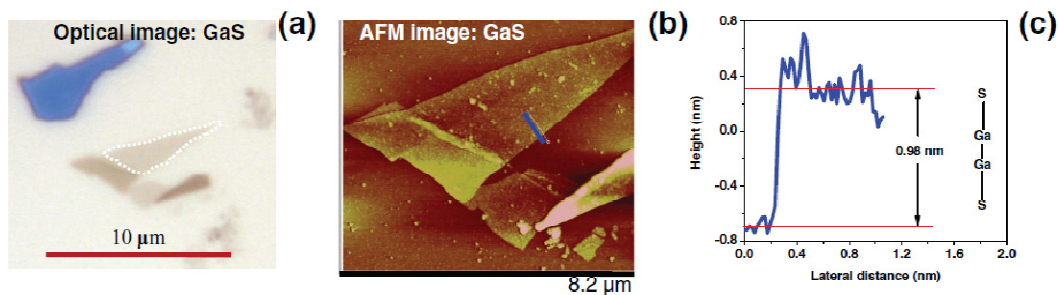
Figure 52: (a) Optical images of ultrathin layer (highlighted by a dashed line) and few layers GaS flakes deposited on 50 nm Si/SiO$_2$ substrate (b) AFM images of ultrathin GaS (c) and the corresponding AFM height profile.

We have also carried out mechanical exfoliation of GaS on Si/SiO$_2$ substrate and has been characterized using optical microscopy, atomic force microscopy and with Raman spectroscopy. Figure 51 (a) shows the optical image of a single-layer GaS on a 50 nm, SiO$_2$/Si substrate. In Figure 51 (b), we show the AFM image corresponds to the marked line in the optical image. Figure 51 (c) shows the height profiles marked in the AFM image of the GaS layer which corresponds to a single-layer of GaS. Raman spectroscopy was also carried out on ultrathin and few layer GaS to find the relationship between the Raman mode shift and the GaS layer thickness.

Figure 52 (a) shows the comparative Raman spectra of bulk and ultrathin layer of GaS. Typically bulk GaS shows Raman modes E^1_{1g} (73.8 cm^{-1}), A^1_{1g} (187.93 cm^{-1}), E^1_{2g} (295.41 cm^{-1}), and A^2_{1g} (359.58 cm^{-1}). Figure 52 (b) depicts the Raman spectra of GaS as function of layer thickness, calculated from AFM height profile. The frequencies shifts of the ultrathin layer GaS Raman modes at room temperature were found be E^1_{1g} (73.12 cm^{-1}), A^1_{1g} (185.53 cm^{-1}), E^1_{2g} (302.5 cm^{-1}), and A^2_{1g} (361.18 cm^{-1}). Figure 52 (c–e) shows the dependence of Raman E^1_{2g}, A^1_{1g}, and A^2_{1g} modes as a function of layer

thickness of GaS. The line width of the layered GaS phonons was studied systematically as a function of layer thickness and is also shown in Figure 52 (c–e) on the right axis. The
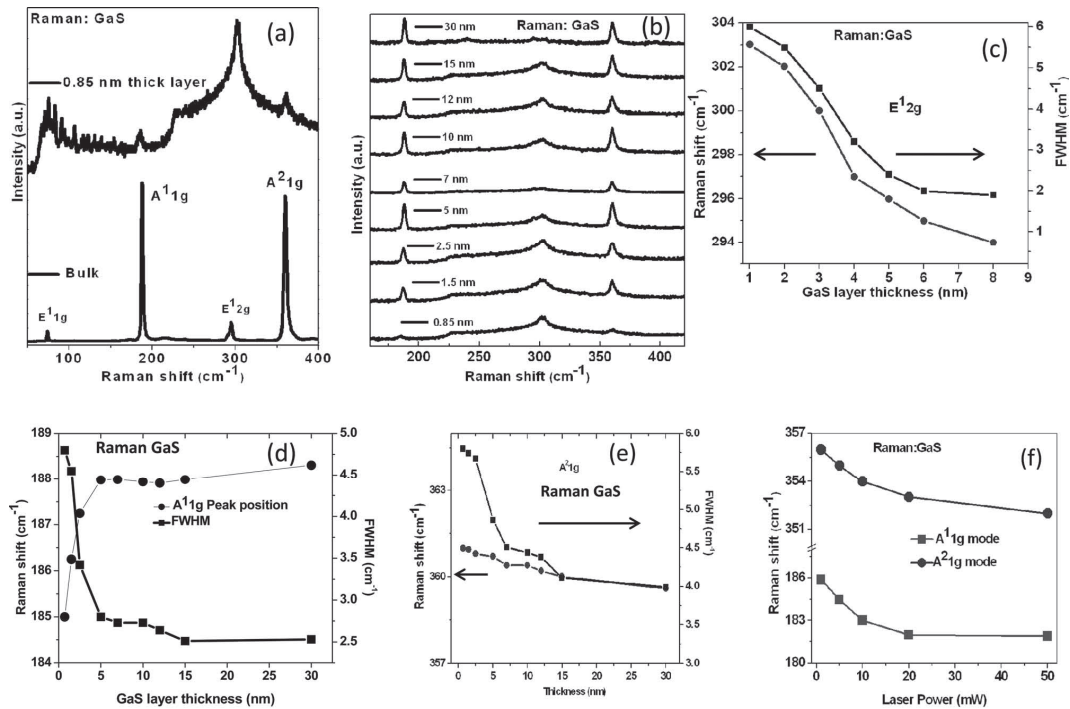
Figure 52: a) Raman spectra of bulk and ultrathin layer GaS and b) Raman spectra of GaS as a function of layer thickness. Effect of GaS layer thickness on c) E^1_{2g}, d) A^1_{1g}, and e) A^2_{1g} modes f) The effect of laser power variation on the GaS A^1_{1g} and A^2_{1g} modes.

line widths of all Raman modes were found to increase as a function of decreasing layer thickness, as previously described for the temperature dependence of GaS layered crystal. We have also studied the effect of laser power variation on GaS layers on A^1_{1g} and A^2_{1g} modes and the data are shown in Figure 52 (f).

2.2.5: Conclusions

It is gratifying that it is possible to prepare graphene analogues of sulphides and selenides of molybdenum and tungsten by different chemical methods and physical methods. Chemical methods employed for the synthesis of graphene analogues includes

2.2: Graphene analogues based on metal chalcogenides

Li-intercalation, hydrothermal synthesis, solid state reaction, microwave synthesis where as physical method involves laser exfoliation and liquid-phase exfoliation. The materials by these methods contain single or two-three layers.

Every method has its own advantages and limitations. Li-intercalation is a general method to obtain single- and few-layers of transition metal chalcogenides but the conditions used are hazardous and need to be taken care during the synthesis. Hydrothermal synthesis uses facile conditions to prepare graphene analogues and we were not able to prepare the graphene-like structures from sulphides and selenides of tungsten and this procedure also needs lot of washing process after the synthesis. The solid state reaction yields all the four compounds of graphene analogues with high quality, and needs high temperature for the synthesis. Microwave synthesis also yields graphene-like structures for MoS_2 and $MoSe_2$ in less time both in water and ethylene glycol. This method also has the same limitations similar to that of the hydrothermal method.

The physical methods which we have employed for the synthesis of graphene analogues involves, laser exfoliation and liquid phase exfoliation by ultrasonication. These methods provide dispersions in different solvents which can be useful for various applications, but the solubility (mg/ml) of these compounds is very less and needs to be improved. We have prepared graphene analogues of GaS and GaSe using liquid phase exfoliation and the products have been characterized with microscopic techniques and found that they have 2-4 layers predominantly. We have also prepared single- and few-layer GaS by micromechanical cleavage and studied the layer dependent Raman spectroscopy.

Raman spectra show softening of the A_{1g} mode in these few-layer materials compared to their bulk counterparts. Thus, we have prepared graphene-like structures of

various layered materials by employing different physical and chemical methods in bulk quantities. The chemical methods employed here can be extended to obtain graphene analogues of other layered materials. We anticipate that our contributions to the synthesis of metal-chalcogenides would enable the scientific community to prepare other layered materials using the similar synthetic protocols and with more control on the number of layers.

These graphene analogues may find applications as solid state lubricants and these may be useful to prepare novel polymer composites. Inorganic analogues of graphene constitute new two-dimensional members of the larger family of inorganic nanocarbon analogues, of which the zero-dimensional fullerenes and one-dimensional nanotubes are already well known.

2.2: Graphene analogues based on metal chalcogenides

2.2.6: References

[1]   R. G. Dickinson, L. Pauling, *J. Am. Chem. Soc.* **1923**, *45*, 1466.

[2]   R. F. Frindt, *J. Appl. Phys.* **1966**, *37*, 1928.

[3]   P. Joensen, R. F. Frindt, S. R. Morrison, *Mat. Res. Bull.* **1986**, *21*, 457.

[4]   P. Joensen, E. D. Crozier, N. Alberding, R. F. Frindt, *J. Phys. C: Solid State Phys.* **1987**, *20*, 4043.

[5]   B. K. Miremadi, S. R. Morrison, *J. Appl. Phys.* **1988**, *63*, 4970.

[6]   D. Yang, R. F. Frindt, *J. Phys. Chem. Solids* **1996**, *57*, 1113.

[7]   D. Yang, S. J. Sandoval, W. M. R. Divigalpitiya, J. C. Irwin, R. F. Frindt, *Phys. Rev. B* **1991**, *43*, 12053.

[8]   Y. Tian, Y. He, Y. Zhu, *Mater. Chem. Phys.* **2004**, *87*, 87.

[9]   W.-J. Li, E.-W. Shi, J.-M. Ko, Z.-z. Chen, H. Ogino, T. Fukuda, *J. Cryst. Growth* **2003**, *250*, 418.

[10]   Y. Peng, Z. Meng, C. Zhong, J. Lu, W. Yu, Z. Yang, Y. Qian, *J. Solid State Chem.* **2001**, *159*, 170.

[11]   H. Luo, C. Xu, D. Zou, L. Wang, T. Ying, *Mater. Lett.* **2008**, *62*, 3558.

[12]   D. Vollath, D. V. Szabo, *Mater. Lett.* **1998**, *35*, 236.

[13]   D. J. Brooks, R. E. Douthwaite, R. Brydson, C. Calvert, M. G. Measures, A. Watson, *Nanotechnol.* **2006**, *17*, 1245.

[14]   P. Pravas Kumar, P. Amita, *Sci.Tech. Adv. Mater.* **2008**, *9*, 045008.

[15]   R. Harpeness, A. Gedanken, A. M. Weiss, M. A. Slifkin, *J. Mat. Chem.* **2003**, *13*, 2603.

[16]   C. Schuffenhauer, B. A. Parkinson, N. Y. Jin-Phillipp, L. Joly-Pottuz, J.-M. Martin, R. Popovitz-Biro, R. Tenne, *Small* **2005**, *1*, 1100.

[17]   H. Wu, R. Yang, B. Song, Q. Han, J. Li, Y. Zhang, Y. Fang, R. Tenne, C. Wang, *ACS Nano* **2011**, *5*, 1276.

[18]   R. Sen, A. Govindaraj, K. Suenaga, S. Suzuki, H. Kataura, S. Iijima, Y. Achiba, *Chem. Phys. Lett.* **2001**, *340*, 242.

[19]   P. A. Parilla, A. C. Dillon, B. A. Parkinson, K. M. Jones, J. Alleman, G. Riker, D. S. Ginley, M. J. Heben, *J. Phys. Chem. B* **2004**, *108*, 6197.

[20]   P. A. Hu, Y. Q. Liu, L. Fu, L. C. Cao, D. B. Zhu, *Appl. Phys. A* **2005**, *80*, 1413.

[21]   J. Q. Hu, Y. Bando, J. H. Zhan, Z. W. Liu, D. Golberg, *Appl. Phys. Lett.* **2005**, *87*, 153112.

[22]   K. Allakhverdiev, J. Hagen, Z. Salaeva, *Phys. Status Solidi* **1997**, *163*, 121.

[23]   S. L. Stoll, E. G. Gillan, A. R. Barron, *Chem. Vap. Deposition* **1996**, *2*, 182.

[24]   V. Chikan, D. F. Kelley, *Nano Lett.* **2001**, *2*, 141.

[25]   U. K. Gautam, S. R. C. Vivekchand, A. Govindaraj, G. U. Kulkarni, N. R. Selvi, C. N. R. Rao, *J. Am. Chem. Soc.* **2005**, *127*, 3658.

[26]   R. Kelly, J. J. Cuomo, P. A. Leary, J. E. Rothenberg, B. E. Braren, C. F. Aliotta, *Phys. Res., Sect. B* **9**, *1985*, 329.

[27]   M. W. Peterson, M. T. Nenadovic, T. Rajh, R. Herak, O. I. Micic, J. P. Goral, A. J. Nozik, *J. Phys. Chem.* **1988**, *92*, 1400.

[28]   Y. Lin, T. V. Williams, T.-B. Xu, W. Cao, H. E. Elsayed-Ali, J. W. Connell, *J. Phys. Chem. C* **2011**, *115*, 2679.

2.3: Synthesis and characterization of nanoscrolls of MoS₂ and other dichalcogenides

Summary

Intercalation of potassium in bulk Mo and W dichalcogenides, followed by exfoliation in water yields nanoscrolls of these materials in contrast to the sheets obtained in the case of Li-intercalation. We have provided the unambiguous proof for the formation of nanoscrolls using various microscopic techniques including atomic force microscopy. We have observed the formation of one-sided, two-sided and all four-side rolled sheets of transition metal chalcogenides. We have proposed a mechanism for the formation of nanoscrolls results in the competition of bending energy and van der Waals interactions.

2.3: Nanoscrolls of metal dichalcogenides

2.3.1: Introduction

Since the discovery of graphene,[1] there has been interest in other nanoforms of carbon. Thus, graphene nanoribbons have gained considerable importance.[2] Nanoscrolls constitute another form of nanocarbons and have been synthesized by potassium (K) intercalation into graphite.[3] Carbon nanoscrolls are expected to possess useful mechanical and electrical properties. [2b], [4] Methods other than K-intercalation into graphite have also been employed to prepare carbon nanoscrolls. Graphene nano-scrolls or as they are more popularly known as carbon nano-scrolls (CNS) were first described by Bacon et al. in as early as 1960.[5] First chemical synthesis to carbon-nanoscrolls was carried out by Viculis et. al.[6] In the process, graphite was first intercalated heavily using potassium metal in pyrex sealed tubes to yield intercalated graphite compound KC_8. On dispersing in ethanol by sonication the graphite undergoes exfoliation and simultaneous rolling up to scrolls. CNS prepared by this method contains average diameter of 40 nm and a very high surface area of 2630 m^2/g. Later, CNS has been prepared from acceptor type graphite intercalation compounds. Graphite nitrate prepared from natural graphite using HNO_3 and ozone was sonicated in ethanol to yield CNS.[7] All the above methods use chemical intercalation and introduce impurities. High quality and pure CNS has been prepared by using isopropanol (IPA) to roll up predefined thin graphene flakes on SiO_2/Si substrates.[8] Zheng et al.[9] used microwave sparks to provide thermal shock to induce exfoliation and rolling up. Graphite flakes immersed in liquid nitrogen while irradiating with microwave sparks. The flakes experienced rapid heating and thus expansion while the surface of each flake was cooled by liquid N_2 and thus underwent contraction. Considering that fullerenes and nanotubes of inorganic layered materials have been prepared,[10] there has been some effort

to prepare and characterize graphene analogues of layered inorganic materials by both physical and chemical methods.[11] Graphene-like structures of layered materials such as MoS_2,[11a] $MoSe_2$,[11b] GaS and GaSe have been reported recently.[11c] These graphene analogues have shown some interesting properties as well.[12]

2.3.2: Scope of the present investigations

Nanoscrolls constitute another form of nanocarbons and have been synthesized by various methods. In view of the recent results on carbon nanoscrolls, we consider it appropriate to investigate the synthesis and characterization of nanoscrolls formed by inorganic layered materials such as MoS_2. MoS_2 is reported to form unusual rag-like structures,[13] but well-defined nanoscrolls of MoS_2 and other dichalcogenides have not been prepared hitherto. We have carried out the intercalation of potassium in bulk dichalcogenides of Mo and W, followed by exfoliation in water to successfully generate nanoscrolls of these materials.

2.3.3: Experimental section

In a typical experiment, MoS_2 (150 mg) and potassium (2 g) were taken in a 13 mm quartz tube, and the tube evacuated for 20 min and sealed. The sealed tube was kept in a furnace at 350 °C for 10 hours and allowed to cool gradually to the room temperature. The sealed tubes were inserted in liquid nitrogen in order to condense the potassium vapour and then broken, followed by the addition of water. During the last step, care should be taken and the process should be carried in a fumehood. The pH at the end of the reaction was 8.5. The product after exfoliation was washed with water (till the pH was ~ 7) followed by ethanol and dried at 40 °C. A similar procedure was employed to prepare nanoscrolls of the other chalcogenides, starting with WS_2 (150 mg) + K (1.5 g), $MoSe_2$ (150 mg) + K (1

g) and WSe_2 (150 mg) + K (1 g). The products of the above reactions were characterized by various techniques.

Characterization

X-ray diffraction (XRD): XRD patterns were recorded (Kα Cu radiation) with a Rich-Siefert XRD-3000-TT diffractometer.

Field emission scanning electron microscopy (FESEM): The morphology was studied by FEI Nova-Nano SEM-600 instrument.

Transmission electron microscopy (TEM): TEM images were recorded with a JEOL JEM 3010 instrument operated with an accelerating voltage of 300 kV.

Raman spectroscopy: Raman spectra were recorded with a LabRAM HR high resolution Raman spectrometer (Horiba-Jobin Yvon) using a He–Ne laser (λ = 514 nm).

Atomic force microscopy: AFM measurements were carried on Vecco digital instruments, di Innova in contact mode.

2.3.4: Results and Discussion

In Figure 1, we show the XRD pattern of bulk MoS_2 and that of nanoscrolls of MoS_2 obtained by K-intercalation followed by exfoliation in water. The nanoscrolls do not exhibit the (002) reflection. In Figure 2, we present the microscopic characterization of MoS_2 nanoscrolls where (a) and (b) show the TEM images of the nanoscrolls formed by the rolling of the 2D sheets. FESEM image in Figure 2(c) show tube like structure of the nanoscrolls and Figure 2 (d) clearly shows the curling of the nanosheets at the edges. We have carried out AFM studies on the nanoscrolls to demonstrate curling of the formed nanoscrolls of MoS_2. Figure 3 shows the deflection image of MoS_2 nanoscrolls.
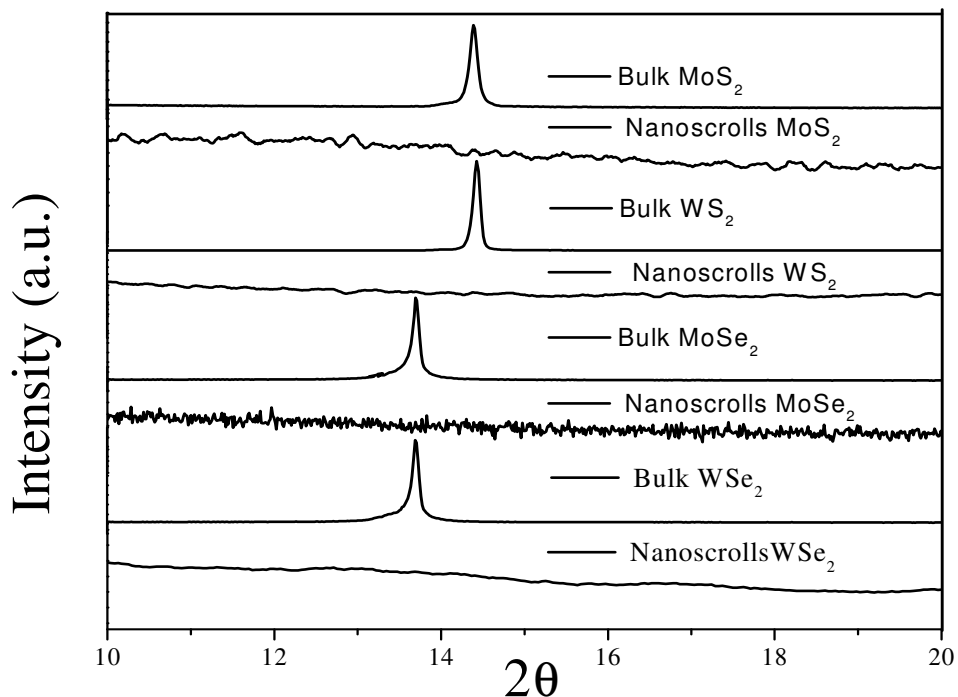
Figure 1: XRD patterns of the bulk samples of MoS_2, WS_2, $MoSe_2$ and WSe_2 and the corresponding nanoscrolls in the (002) region.

Examination of the height profile of AFM image of the scroll, shows a height profile of ~ 0.9 nm corresponding to the thickness of a single-layer of MoS_2 with lateral

dimensions of few microns on one end and the height profile of ~ 4.1 nm indicate a roll

structure with 3-4 curls on the other end suggesting the formation of nanoscrolls.
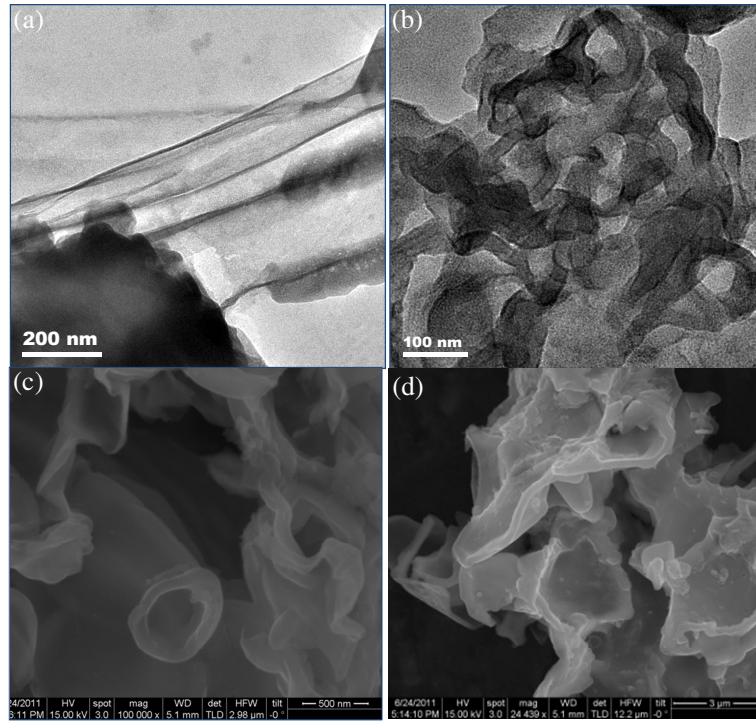
Figure 2: (a) and (b) FESEM images of MoS$_2$ nanoscrolls, (c) and (d) TEM images of MoS$_2$ nanoscrolls.
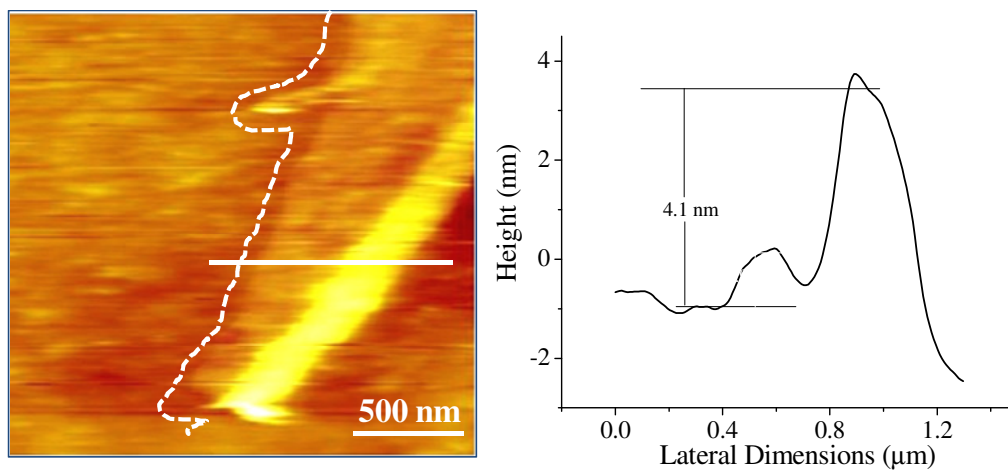
Figure 3: AFM image and the associated height profile of a MoS$_2$ nanoscroll. Dotted line shows the edge of the nanoscroll and full line shows the region corresponding to the height profile

2.3: Nanoscrolls of metal dichalcogenides

Thus AFM studies revealed the formation of nanoscroll by one-side rolling. The, nanoscrolls are formed either by rolling of a single-layer as seen from the AFM studies or from multi-layers as confirmed by the TEM and FESEM studies.

Figure 4: (a) and (b) FESEM images of $MoSe_2$ nanoscrolls, (c) and (d) TEM images of $MoSe_2$ nanoscrolls.
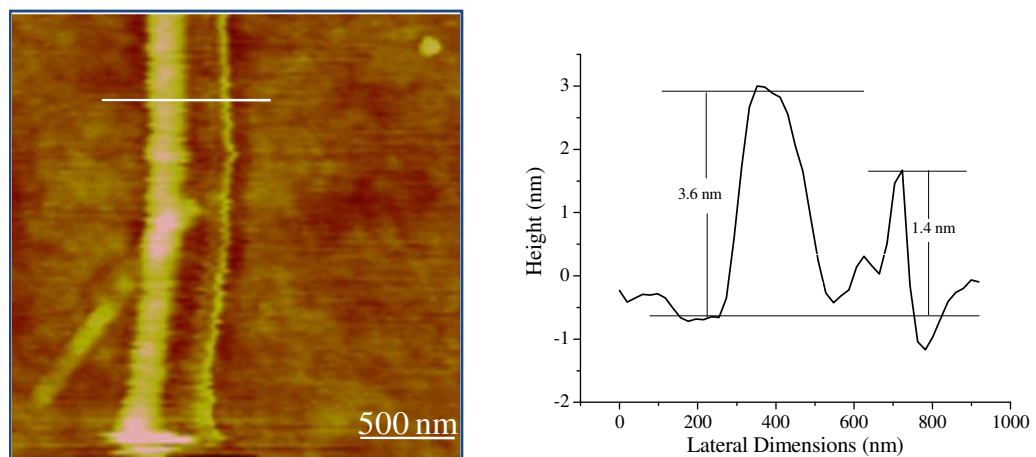
Figure 5: AFM image and the associated height profile of a $MoSe_2$ nanoscroll and full line shows the region corresponds to the height profile.

2.3: Nanoscrolls of metal dichalcogenides

Employing procedure, to that of MoS$_2$ we were able to prepare the nanoscrolls of MoSe$_2$ as well. The XRD pattern shows the absence of the (002) reflection due to the loss of registry along the c-axis of these nanoscrolls. In Figure 4, we show the microscopic characterization of MoSe$_2$ nanoscrolls. Figure 4 (a) show the tube-like structure of nanoscrolls with few-microns in size. Several rolled structures can be seen in Figure 4(b) indicating formation of nanoscrolls. The FESEM images in Figures 4 (c) and (d) show hollow tubular-like structures and the associated curlings there by indicating the formation of nanoscrolls. Results of the AFM studies shown in Figure 5, reveal the formation of two-sided scrolls formed from a single-layer MoSe$_2$. From the height profile of the AFM image, we confirmed that one side of the scrolls has two curls while the other end has 3-4 curls, middle part with a height profile of 0.8 nm evidences the formation of two-sided nanoscrolls from single-layer MoSe$_2$.

Figure 6: (a) and (b) TEM images of WS$_2$ nanoscrolls, (c) and (d) FESEM images of WS$_2$ nanoscrolls.

2.3: Nanoscrolls of metal dichalcogenides

By adapting a similar synthetic procedure, we have prepared WS_2 nanoscrolls. The XRD patterns of WS_2 nanoscrolls show the absence of the (002) reflection (Figure 1). In
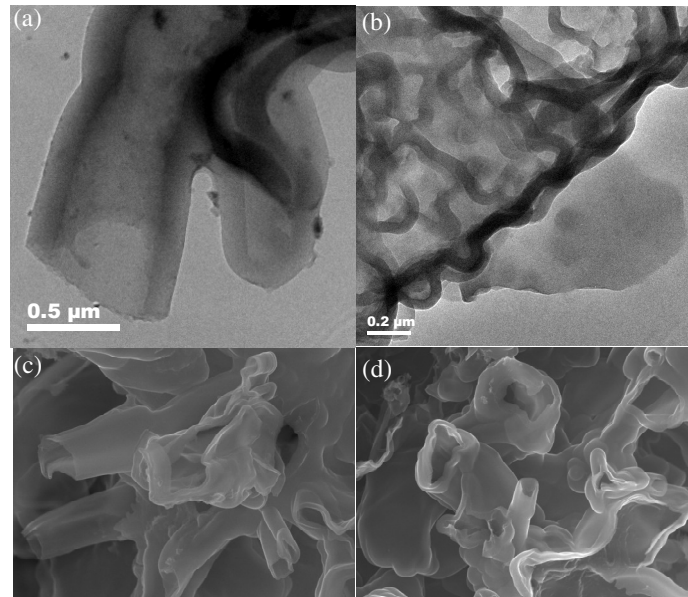

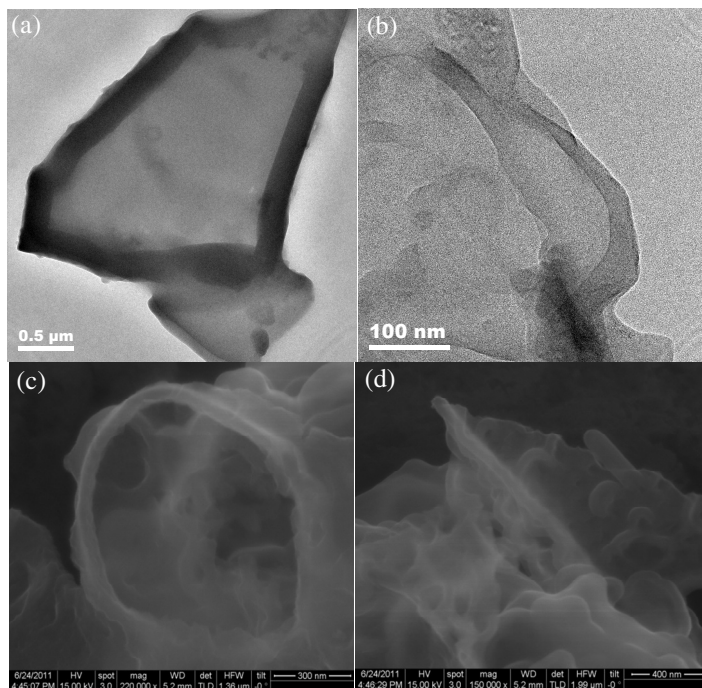**Figure 7:** (a) and (b) TEM images of WSe_2 nanoscrolls, (c) and (d) FESEM images of WSe_2 nanoscrolls.
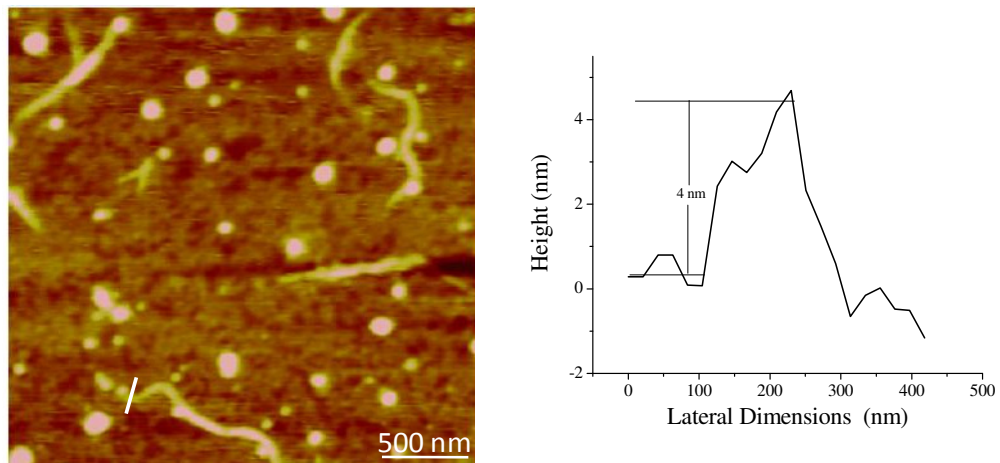
Figure 8: AFM image and the associated height profile of a WSe_2 nanoscroll and full line shows the region corresponds to the height profile.
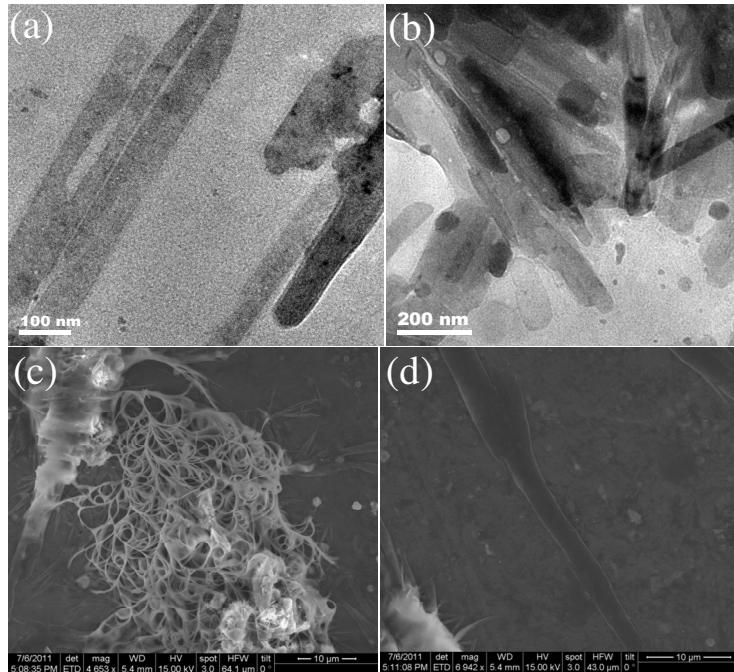
2.3: Nanoscrolls of metal dichalcogenides

Figure 6 (a), we have shown the curlings of the edges of the sheet, where as in Figure 6 (b) shows rolling from only one side. Figures 6(c) and (d) show the FESEM images of the
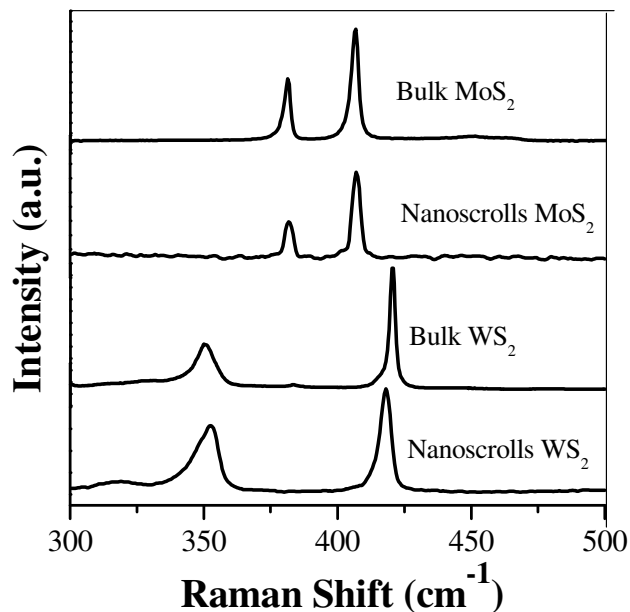
Figure 9: Raman spectra of the bulk samples and nanoscrolls of MoS_2 and WS_2.

nanoscrolls of WS_2 which also reveals the same information supporting the TEM observations. Results with WSe_2 nanoscrolls prepared by K-intercalation are similar those of the molybdenum chalcogenides. The XRD pattern of the WSe_2 nanoscrolls in Figure 1 shows the absence of the (002) reflection. In Figures 7 (a) and (b), we show the nanoscrolls obtained from WSe_2 which are not hollow and cannot be distinguished by the inner cavity as observed in TEM (Figures 7 (a) and (b)). Figures7 (c) and (d) show the FESEM images of WSe_2 nanoscrolls. AFM studies show that scrolls are formed by the curlings of the 3-4 layers with the height profile of ~ 4 nm (see Figure 8).

Raman studies on the MoS_2 nanoscrolls show bands at 404.7 (A_{1g}) and 383.7 (E_{2g}) cm^{-1} compared to 406.5 and 381.2 cm^{-1} of the bulk sample. There is a clear softening of the

2.3: Nanoscrolls of metal dichalcogenides

A_{1g} mode and stiffening of the E_{2g} modes in the nanoscrolls of MoS_2 just as in the case of graphene-like sheets.[14] Furthermore, the FWHM values are larger in the graphene-like samples, the values varying from 5 to 10 cm^{-1} compared to ~3 cm^{-1} in the bulk sample. Raman spectra of the nanoscrolls of $MoSe_2$ show softening of the modes compared to their bulk counterparts. The Raman spectrum of WS_2 nanoscrolls exhibit softening of the A_{1g} bands and stiffening of E_{2g} mode (Figure 9). Compared to the narrow Raman bands at 351 (E_{2g}) and 420 cm^{-1} (A_{1g}) of bulk WS_2 with FWHM values around 7.8 and 2.4 cm^{-1} respectively, the spectrum of the nanoscrolls of WS_2 shows bands at 349 and 417 cm^{-1} with FWHM values of ~ 10-12 cm^{-1}.

Possible mechanism for the formation of inorganic nanoscrolls is governed by two major energetic contributions, the elastic energy increase caused by bending the graphite sheet (decreasing stability) and the free energy decrease generated by the van der Waals interaction energy of overlapping regions of the sheet (increasing stability). This implies that the transition from layered materials to obtain nanoscroll like structures must be energy assisted. In this case, exfoliation carried out by adding water to the K-intercalated bulk sulfides and selenides of Mo and W releases enormous amount of energy, which is sufficient enough to scroll the sheets. Though, we have carried out Li-intercalation previously, we observed only the formation of sheets. But the energy released in K-intercalation is larger than that of lithium interacting with water, thus enabling us to produce nanoscrolls of inorganic layered materials. There is a critical value of layer overlap above which the rolling process evolves spontaneously as a result of Van der Waals interlayer forces. One-sided nanoscrolls, two-sided or four-sided nanoscrolls formations depend on the initial sheet dimensions and the amount of K-intercalated.

2.3.5: Conclusions

We have developed a general procedure for the synthesis of nanoscrolls of layered chalcogenides of Mo and W by K-intercalation in the bulk samples followed by exfoliation in water. The method predominantly yields nanoscrolls with a small portion of sheets. Thus our results suggest the need to search of other synthetic protocols for the high quality nanoscrolls. These may find potential applications in fabricating devices, anode materials for battery applications and polymer composites.

2.3.6: References

[1]   a)K. S. Novoselov, A. K. Geim, S. V. Morozov, D. Jiang, Y. Zhang, S. V. Dubonos, I. V. Grigorieva, A. A. Firsov, *Science* **2004**, *306*, 666; b)A. K. Geim, K. S. Novoselov, *Nature Mater.* **2007**, *6*, 183; c)A. K. Geim, *Science* **2009**, *324*, 1530; d)C. N. R. Rao, A. K. Sood, K. S. Subrahmanyam, A. Govindaraj, *Angew. Chem. Int. Ed.* **2009**, *48*, 7752; e)J. N. Coleman, *Acc. Chem. Res.* **2012**, *DOI: 10.1021/ar300009f*; f)C.N.R.Rao, H. S. S. R. Matte, K. S. Subrahamanyam, *Acc. Chem. Res.* **2012**, DOI:*.org/10.1021/ar300033m*.

[2]   a)X. Li, X. Wang, L. Zhang, S. Lee, H. Dai, *Science* **2008**, *319*, 1229; b)S. Dutta, S. K. Pati, *J. Mater. Chem.* **2010**, *20*, 8207.

[3]   L. M. Viculis, J. J. Mack, R. B. Kaner, *Science* **2003**, *299*, 1361.

[4]   S. F. Braga, V. R. Coluci, S. B. Legoas, R. Giro, D. S. Galvazo, R. H. Baughman, *Nano Lett.* **2004**, *4*, 881.

[5]   R. Bacon, *J. Appl. Phys.* **1960**, *31*, 283.

[6]   L. M. Viculis, J. J. Mack, R. B. Kaner, *Science* **2003**, *299*, 1361.

[7]   M. V. Savoskin, V. N. Mochalin, A. P. Yaroshenko, N. I. Lazareva, T. E. Konstantinova, I. V. Barsukov, I. G. Prokofiev, *Carbon* **2007**, *45*, 2797.

[8]   X. Xie, L. Ju, X. Feng, Y. Sun, R. Zhou, K. Liu, S. Fan, Q. Li, K. Jiang, *Nano Lett.* **2009**, *9*, 2565.

[9]   J. Zheng, H. Liu, B. Wu, Y. Guo, T. Wu, G. Yu, Y. Liu, D. Zhu, *Adv. Mater.* **2011**, *23*, 2460.

[10] a)L. Margulis, G. Salitra, R. Tenne, M. Talianker, *Nature* **1993**, *365*, 113; b)R. Tenne, C. N. R. Rao, *Phil. Trans. R. Soc. Lond. A.* **2004**, *362*, 2099; c)R. Tenne,

Nat. Nanotechnol. **2006**, *1*, 103; d)C. N. R. Rao, A. Govindaraj, *Adv. Mater.* **2009**, *21*, 4208.

[11]   a)H. S. S. R. Matte, A. Gomathi, A. K. Manna, D. J. Late, R. Datta, S. K. Pati, C. N. R. Rao, *Angew. Chem. Int. Ed.* **2010**, *49*, 4059; b)H. S. S. R. Matte, B. Plowman, R. Datta, C. N. R. Rao, *Dalton Trans.* **2011**, *40*, 10322; c)D. J. Late, B. Liu, H. S. S. R. Matte, C. N. R. Rao, V. P. Dravid, *Adv. Funct. Mater.* **2012**, *22*, 1894; d)J. N. Coleman et al., *Science* **2011**, *331*, 568.

[12]   a)J. A. Wilson, A. D. Yoffe, *Adv. Phys.* **1969**, *18*, 193; b)B. Radisavljevic, A. Radenovic., J. Brivio, Giacometti. V, A. Kis, *Nat Nanotechnol.* **2012**, *6*, 147; c)K. Lee, H.-Y. Kim, M. Lotya, J. N. Coleman, G.-T. Kim, G. S. Duesberg, *Adv. Mater.* **2011**, *23*, 4178; d)D. J. Late, B. Liu, H. S. S. R. Matte, V. P. Dravid, C. N. R. Rao, *ACS Nano* **2012**,*6*, 5635; e)D. J. Late, B. Liu, J. Luo, A. Yan, H. S. S. R. Matte, M. Grayson, C N R Rao, V. P. Dravid, *Adv. Mater.* **2012**, *24*,3549.

[13]   R. R. Chianelli, E. B. Prestridge, T. A. Pecoraro, J. P. Deneufville, *Science* **1979**, *203*, 1105.

[14]   C. Lee, H. Yan, L. E. Brus, T. F. Heinz, J. Hone, S. Ryu, *ACS Nano* **2010**, *4*, 2695.

2.4: Magnetic properties of metal chalcogenide-based graphene analogues

Summary∗

We report the ferromagnetism of few-layer MoS_2 and other transition metal dichalcogenides at room temperature. These inorganic graphene analogues show exchange bias effect at room temperature. High resolution microscopic images reveal the presence of zig-zag edges and the defects in the samples. A disorder mode corresponding to a zone-edge phonon has been observed in the Raman spectrum of MoS_2. We attribute the existence of ferromagnetism at room temperature partly to the presence of defects and zigzag edges and the latter being an essential feature of these materials. The magnetic properties of graphene mimics may have potential applications.

2.4: Magnetic properties of graphene analogues

2.4.1: Introduction

Magnetism in bulk materials arises from the collective interaction of magnetic moments of the atoms or ions constituting the material, and the typical examples are iron, Fe_3O_4 and CrO_2. From the arrangement of these magnetic atoms or ions their moments interact through a molecular exchange field which gives the long-range magnetic ordering.[1] In 1961, Néel has predicted that nanoparticles of antiferromagnetic materials will have a small net magnetic moment because of the finite size.[2] Later, Ferromagnetism in otherwise nonmagnetic materials has emerged as an important area of research. Otherwise nonmagnetic materials are compounds in which the magnetism arises without involvement of unpaired d or f electrons.[1] Venkatesan et al has reported the observation of ferromagnetism in HfO_2 thin films.[3] Recent studies on inorganic nanoparticles like ZnO, Al_2O_3, MgO, GaN, and CdS have shown room-temperature ferromagnetism, where as their bulk counterparts are known to be diamagnetic.[4] Magnetic semiconductors are the materials which exhibit ferromagnetism along with the semiconductor properties. In traditional semiconductor devices, the charge carriers are either n- or p-type whereas in the case of magnetic semiconductors it would allow to control the quantum spin state in either spin up or spin down. Spin polarization is an important property for spintronics applications.[5]

Molybdenum disulfide (MoS_2) which is a structural analogue of graphene has received tremendous attention because of its interesting physical and chemical properties.[6] Various methods have been reported for the large-scale synthesis of MoS_2.[7] It has already been shown that MoS_2 upon cleavage to single-layer turns out to be a direct band gap semiconductor from the indirect band gap in its bulk form.[8] It is shown that

these single-layer MoS_2 flakes are mechanically stable[9] and also been investigated in diverse fields like transistors,[10] sensors,[11] Li-ion batteries [12] and hydrogen evolution reactions.[13]

Panich et al reported the electron paramagnetic resonance (EPR) investigations of inorganic fullerene-like MoS_2 nanoparticles and found that they show a larger density of dangling bonds carrying unpaired electrons, indicating a more defective structure compared to the bulk sample.[14] Later, MoS_2 and WS_2 clusters (Mo_6S_{12} and W_6S_{12}) have shown to be magnetic, the magnetism arising from the unsaturated metal center due to partially filled d orbitals.[15] Zhang et al.[16] have prepared MoS_2 with high density of prismatic edges and showed them to be ferromagnetic at room temperature, the magnetism arising from non-stoichiometry of the unsaturated Mo and S atoms at the edges. Commercially available bulk MoS_2 was lithiated by soaking in butyllithium in argon atmosphere and the obtained Li-MoS_2 showed room temperature ferromagnetism.[17] Magnetic properties of single crystal MoS_2 in the bulk limit are measured, and have observed that it is comprised of both diamagnetic and the ferromagnetic terms and the ferromagnetism persists from 10 K up to room temperature. The existence of ferromagnetism is attributed partly due to the presence of zigzag edges in the magnetic ground state.[18] MoS_2 exhibited room temperature magnetic ordering when exposed to a 2 MeV proton beam. The temperature dependence of magnetization showed a ferrimagnetic behavior with a Curie temperature of 895 K. Possible sources for observing room temperature ferromagnetism are isolated vacancies, vacancy clusters, formation of edge states, and reconstructions of the lattice.[19] Density functional calculations on inorganic analogue of graphite, MoS_2 reveal that edge states are magnetic.[20] It appears that

magnetism originates at the sulfur terminated edges due to the splitting of metallic edge states at the Fermi level.

2.4.2: Scope of the present investigations

Bulk MoS_2 is a diamagnetic and indirect band gap semiconductor. Exfoliation of bulk MoS_2 to single-layer renders a direct band gap n-type semiconductor. It is of great interest to prepare magnetic semiconductors which will have obvious advantages in various applications. The awareness gained from graphene that it exhibits room temperature ferromagnetism, has led us to investigate the magnetism in these transition metal dichalcogenides which have essentially same structural features as number of layers and lateral dimensions. Previous observations have also revealed the fact that ferromagnetic and antiferromagnetic domains coexist in graphene. This has given curiosity to explore the exchange bias effect in these materials, which is an obvious phenomena to be appeared if such domains exist.

2.4.3: Experimental section

Synthesis of MoS_2 /WS_2 using thiourea method

In this method MoS_2/WS_2 layers were prepared by heating molybdicacid/tungsticacid with an excess of thiourea at 773 K under nitrogen atmosphere for 3 hours. In a typical synthesis, 1 mmol of molybdicacid/ tungsticacid was ground with 1.5 grams of thiourea and placed in alumina boat and then placed inside a quartz tube kept inside a horizontal tube furnace. Prior to heating, the quartz tube was purged with nitrogen for 0.5 hour. The temperature was then raised to 773 K and then held it for 3 hours and it is cooled to room temperature and characterized further.

2.4: Magnetic properties of graphene analogues

Synthesis of MoSe₂/WSe₂ using selenourea method

Layered $MoSe_2$/WSe_2 were prepared using selenourea as a selenium source. In a typical synthesis, molybdic acid/ tungsticacid was ground with excess of selenourea in the ratio 1:48 and heated at 773 K for 3 h under nitrogen atmosphere with heating rate of 20 °C per minute. Then the sample was cooled down to room temperature under nitrogen atmosphere. The black product obtained was used as such for further analysis.

Characterization
Transmission electron microscopy

For transmission electron microscopy (TEM), dispersions of the samples were dropped onto the holey carbon-coated Cu grids, and the grids were allowed to dry in the air. TEM images and atomic arrangement of hexagonal MoS_2 and $MoSe_2$ was obtained from the FEI TITAN (cube) 80-300 kV aberration corrected transmission electron microscope.

Raman Spectroscopy

Raman spectra were recorded with a LabRAM HR high-resolution Raman spectrometer (Horiba-Jobin Yvon) using a He−Ne laser ($\lambda = 632.8$ nm) and Ar laser (514 nm).

Physical Property Measuring System

Magnetic measurements were carried out with vibrating sample magnetometer in Physical Properties Measurement System (PPMS, Quantum Design, USA). Rectangular pellets of dimension 6 mm x 3 mm were hydraulically pressed. The pellet was mounted in quartz sample holder and wrapped with brown tape both provided by Quantum Design. For background correction magnetic measurement of sample holder and brown tape only were carried out.

2.4.4: Results and Discussion

We have carried out the investigations on magnetic properties of sulfides and selenides Mo and W. Temperature-dependent magnetization data of the 3-6 layered MoS_2 sample at 500 Oe is shown in Figure 1(a). We see divergence between the field-cooled (FC) and zero-field-cooled (ZFC) data starting around 300 K, a behavior common to all the layered samples prepared by us. The divergence nearly disappears on application of higher fields (see inset of Figure 1(a)). This type of behavior is generally observed in magnetically frustrated systems such as spin glasses where usually ferromagnetic and antiferromagnetic bonds are randomly distributed. A similar behavior has been observed in
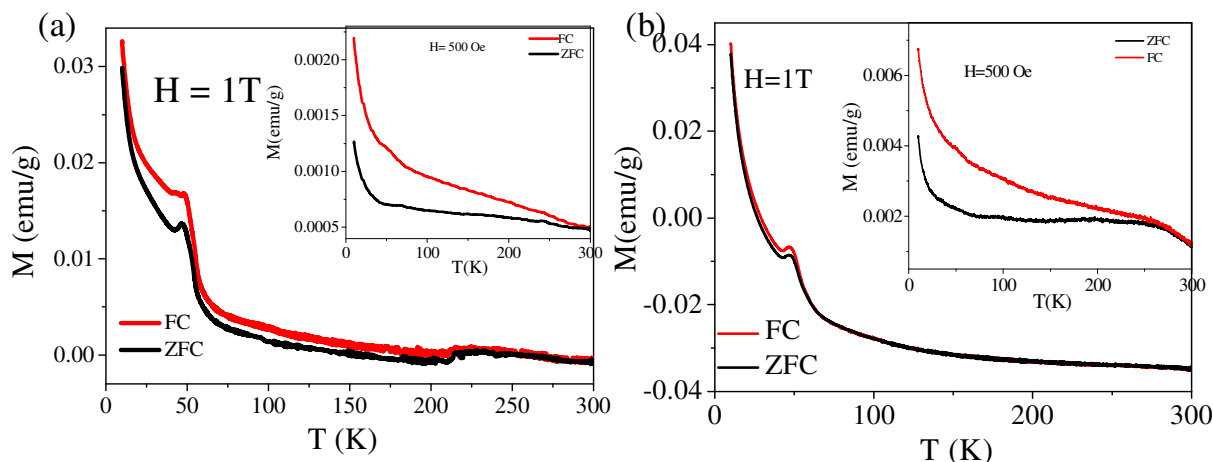
Figure 1: Temperature dependent magnetization (ZFC and FC) of under 1T field. Inset shows the temperature dependence of magnetization under 500 Oe field (a) few-layer MoS_2 (b) few-layer WS_2

few-layer graphene as well.[21] We also observe a low temperature upturn in the magnetization showing a Curie-like tail. Such a Curie like tail is known to arise at low temperatures where the paramagnetic component takes over ferromagnetic or antiferromagnetic interactions. This behavior is found in several graphitic materials.[22] We observe a hump around 220K in the temperature-dependent magnetization data at 1T. Figure 1(b) shows the temperature dependent magnetization data of few-layer WS_2 at 1 T. Interestingly, In the case of WS_2 a stronger hump is noticed around 270 K at a much lower

field of 500 Oe (see inset figure 1(b)) Such magnetic anomalies are often found in graphene samples.[21]

Figures 2 (a) and (b) we show the magnetic hysteresis of few-layer MoS_2 at room temperature and at 10 K which are the characteristic of ferromagnetic materials. The saturation magnetization (M_S), remnant magnetization (M_R) and coercive field (H_C) are
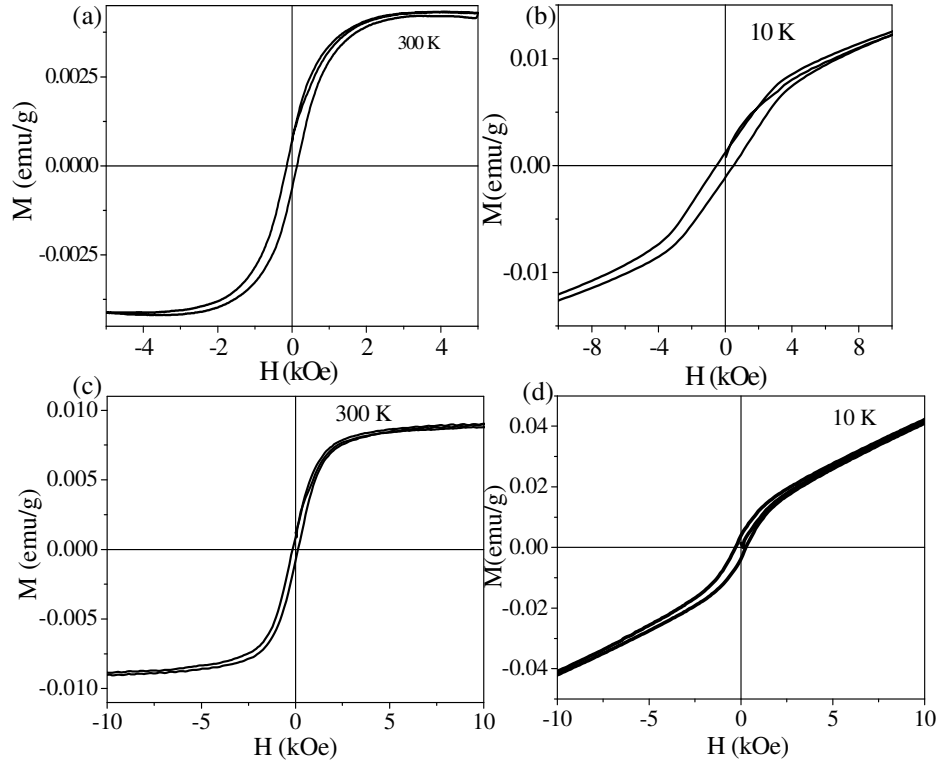
Figure 2: Hysteresis of few-layer MoS_2 (a) 300 K (b) 10 K and hysteresis of few-layer $MoSe_2$ (c) 300 K and (d) 10 K.

listed in Table 1. Similarly we have shown the magnetic hysteresis of few-layer WS_2 at 300K and 10 K in Figures 2(c) and (d). All the other layered metal sulfides and selenides show a similar ferromagnetic behavior at room temperature. We have also carried out the temperature dependent magnetization for few-layer $MoSe_2$ and few-layer WSe_2 at 500 Oe (see Figures 3(a) and (c)). In these cases also we have observed the anomalies at temperature around 50-80 K which are similar to that graphene, confirming the presence of ferromagnetic and antiferromagnetic domains. Room temperature hysteresis of few-

layer MoSe$_2$ and few-layer WSe$_2$ is shown in Figures 3(b) and 3 (d). Among all these few-layered materials WS$_2$ exhibits the maximum saturation magnetization value while WSe$_2$ exhibits the maximum coercive field. The saturation magnetization increases by almost an order of magnitude at 10 K as compared to that at 300 K (see Table 1). It may be noted that ferromagnetism is a general feature of all inorganic nanomaterials.[23]
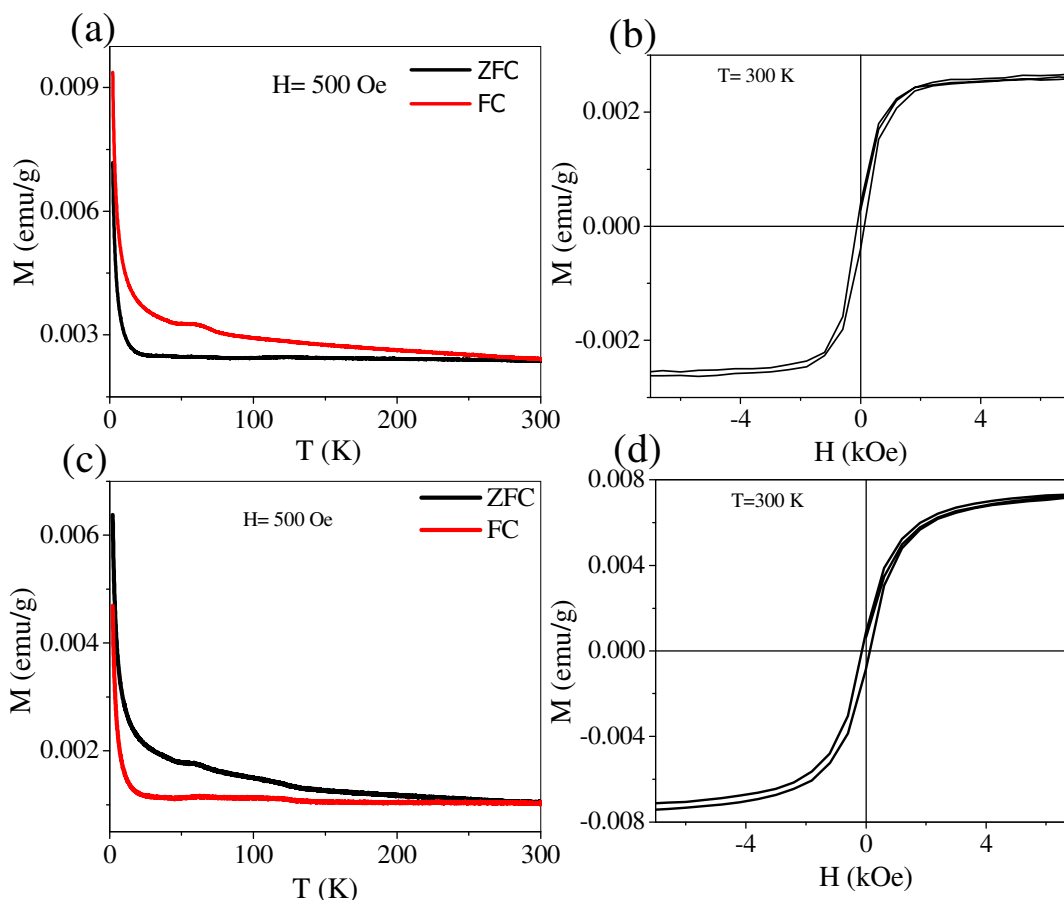
Figure 3: (a) Temperature dependent magnetization (ZFC and FC) of few-layer MoSe$_2$ under 500 Oe field. (b) Hysteresis of few-layer MoSe$_2$ at 300 K. (c) Temperature dependent magnetization (ZFC and FC) of few-layer WSe$_2$ under 500 Oe field. (d) Hysteresis of few-layer MoSe$_2$ at 300 K.

The temperature dependent magnetization together with room temperature hysteresis of few-layer MoS$_2$ and other dichalcogenides suggest the presence of both ferromagnetic and antiferromagnetic domains. In order to verify this, we carried out isothermal magnetization measurements at different temperatures by cooling the sample

Table 1: Magnetic properties of few-layer metal disulfides and diselenides

Samples	No. of layers	M_S (x10^{-2} emu/g)		M_R (x10^{-2} emu/g)		H_C (Oe)	
		10 K	300 K	10 K	300 K	10 K	300 K
MoS_2	3-5	1.9	0.43	0.14	0.06	517	146
WS_2	3-5	9.8	0.90	0.4	0.09	295	130
$MoSe_2$	3-6	1.3	0.26	0.09	0.04	435	40
WSe_2	3-5	7.8	0.73	0.1	0.09	578	200

under an applied field to observe the exchange bias behavior. Exchange bias is a phenomenon known to occur in magnetic materials where ferromagnetic and antiferromagnetic layers or domains are strongly coupled to each other. In such strongly coupled systems, the ferromagnetic spins get pinned by the more anisotropic antiferromagnetic spins. Reversal of the ferromagnetic moment will therefore have an
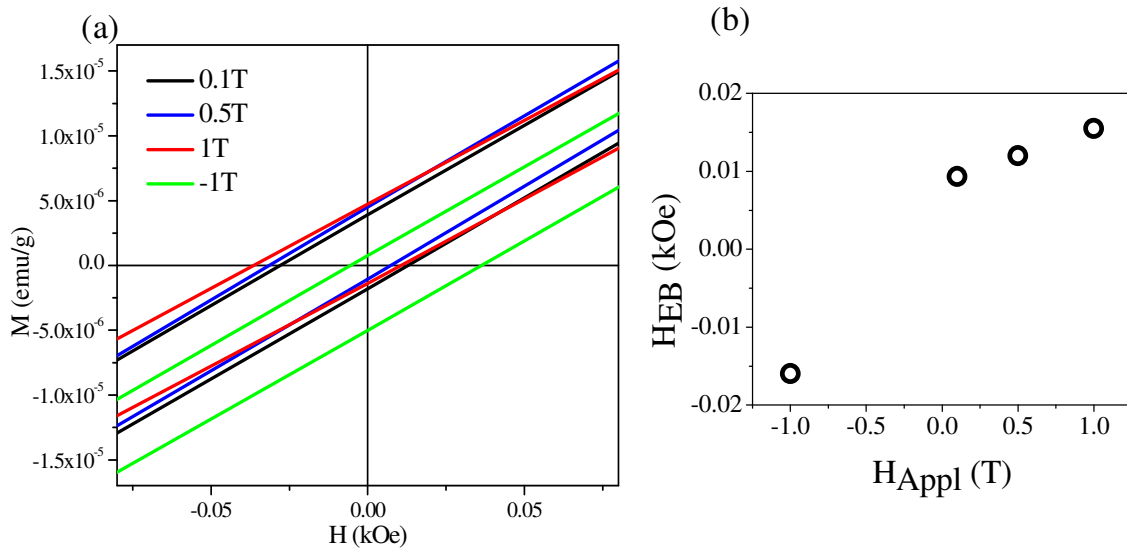
Figure 4: (a) Plot of magnetzation vs field of few-layer MoS_2 at 2K cooled under different applied fields, (b) Dependence of exchange bias on the applied field.

energy cost corresponding to the amount of energy required to reverse the pinned moments. This manifests as a shift in the hysteresis. Such phenomenon has been observed in nanoribbons of graphene and is considered to be due to the presence of ferromagnetic clusters along with antiferromagnetic regions. [24] Figure 4(a) shows the exchange bias behavior in 3-6 layered MoS_2 samples under different fields. A negative exchange bias of 15.5 Oe is observed with an applied field of 1T. The exchange bias decreases with the decrease in the applied field and reverses by applying bias field of -1T to -15.5 Oe as shown in Figure 4(b). Metal selenides also show similar behavior with an exchange bias field of 19 Oe on application of 1T.
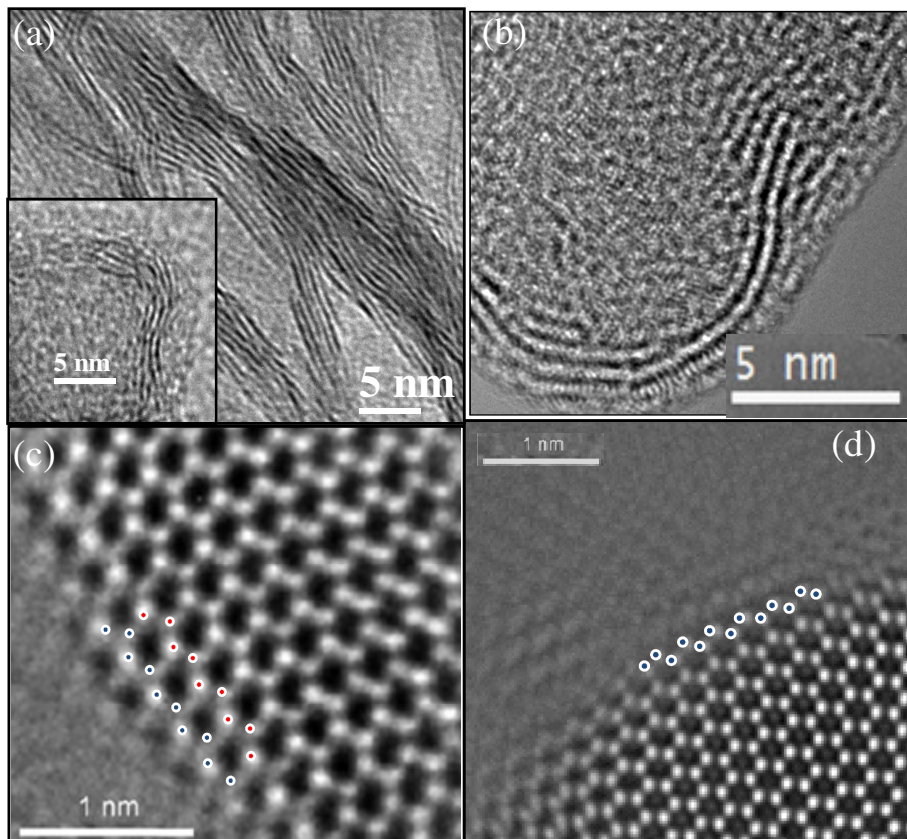
Figure 5: TEM images of few-layer (a) and (b) MoS_2, (Fourier transform high resolution TEM images of (c) MoS_2 and (d) $MoSe_2$. Bends in the edges can be seen in the inset of (a).

2.4: Magnetic properties of graphene analogues

Layered materials like graphene, graphene nanoribbons [25] and MoS_2 are known to exhibit edge states [26]. In the case of graphene nanoribbons some of these edge states are magnetic.[27] Graphene prepared by different methods is predominantly ferromagnetic at room temperature along with some antiferromagnetic interactions. Enoki *et al.*[28] have shown that edge states as well as adsorbed species affect the magnetic properties of graphene.
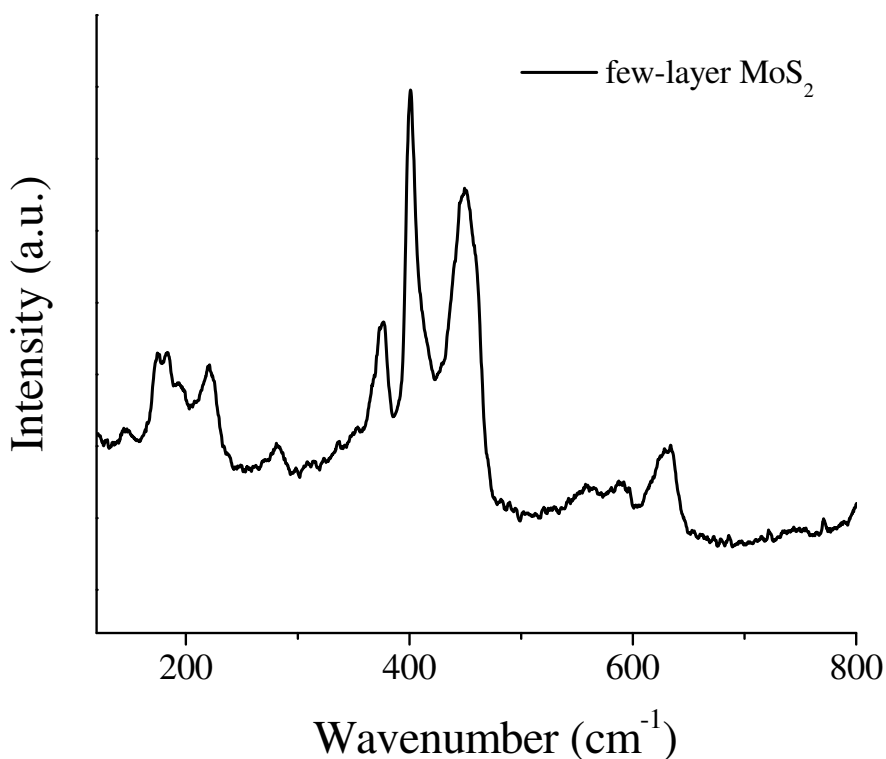
Figure 6: Raman spectrum of few-layer MoS_2.

In order to understand the origin of magnetism in few-layer MoS_2 and $MoSe_2$, we have carried out high-resolution electron microscopic studies. These samples which were 3-5 layers show the presence of defects as can be seen from the images in Figures 5(a) and (b). The bends in the layers shown in the inset of Figure 5(a) and Figure 5(b) may arise when the atoms are removed from the lattice. Figures 5(c) and (d) show the atomically

resolved HREM images hexagonal arrangement of atoms show the presence of the zig-zag edges.

The atoms at the edges are marked with the colored circles to guide the eye for the observation of the zig-zag edges. Such defect centers and edges would be associated with the metal atoms which are undercoordinated, resulting in partially filled d orbitals. This would render the spin-polarized state lower in energy compared to the spin-unpolarized state. A high concentration of such edges and defects in our samples could be one of the possible reasons for the observation of ferromagnetism. First principles calculations on arm-chair and zig-zag MoS_2 nanoribbons show that zig-zag nanoribbons have the spin-polarized state as the ground state while for the arm-chair ribbons the ground state is spin-unpolarized. It is argued that zig-zag MoS_2 nanoribbons with a ribbon width in the nanoscale will be magnetic.[29] Raman spectroscopy is an effective tool to characterize the defect related bands in the case of graphene.[30] In the case of MoS_2 as reported in the literature resonance Raman scattering gives the information about the defects in the system. The E^1_{2g} mode at 375 cm^{-1} and A_{1g} mode at 402 cm^{-1} is clearly seen in Figure 6 which are characteristics bands of MoS_2. The appearances of a mode at 450 cm^{-1} is due to the second order of LA(M) phonons, which indicate the presence of lattice defects as reported in the case of MoS_2 fullerenes.[31]

2.4.5: Conclusions

In conclusion, ferromagnetism at high temperatures exhibited by the few-layer chalcogenides is a unique feature. While defects can be of importance, the role of edges in these materials seems to be vital. Since the edges of zig-zag type are generally present in

graphenes analogues, one would surmise that the magnetism is an intrinsic feature of these samples. Raman spectroscopy and transmission electron microscopy results indicate the presence of defects in the samples. It is noteworthy that defect-related magnetism is observed in nanoparticles of inorganic nanomaterials such as ZnO and Al_2O_3 which are otherwise nonmagnetic. The observation of magnetism in MoS_2 and other dichalcogenides may be useful for future applications of these materials.

2.4.6: References

[1]   a)A. Sundaresan, C. N. R. Rao, *Nano Today* **2009**, *4*, 96; b)A. Sundaresan, C. N. R. Rao, *Solid State Comm.* **2009**, *149*, 1197.

[2]   L. Néel, in *University of Grenoble, Gordon and Beach* (Ed.: C. D.-M. C. Dewitt, B. Dreyfus, P.D. de Gennes (Eds.),), Low Temperature Physics: Lectures Delivered at Les Houches During the 1961 Session of the Summer School of Theoretical Physics, New York, **1962**, p. 433.

[3]   M. Venkatesan, C. B. Fitzgerald, J. M. D. Coey, *Nature* **2004**, *430*, 630.

[4]   A. Sundaresan, R. Bhargavi, N. Rangarajan, U. Siddesh, C. N. R. Rao, *Phys. Rev. B* **2006**, *74*, 161306.

[5]   http://en.wikipedia.org/wiki/Magnetic_semiconductor.

[6]   J. N. Coleman, M. Lotya, A. O'Neill, S. D. Bergin, P. J. King, U. Khan, K. Young, A. Gaucher, S. De, R. J. Smith, I. V. Shvets, S. K. Arora, G. Stanton, H.-Y. Kim, K. Lee, G. T. Kim, G. S. Duesberg, T. Hallam, J. J. Boland, J. J. Wang, J. F. Donegan, J. C. Grunlan, G. Moriarty, A. Shmeliov, R. J. Nicholls, J. M. Perkins, E. M. Grieveson, K. Theuwissen, D. W. McComb, P. D. Nellist, V. Nicolosi, *Science* **2011**, *331*, 568.

[7]   Y. Zhan, Z. Liu, S. Najmaei, P. M. Ajayan, J. Lou, *Small* **2012**, *8*, 966.

[8]   K. F. Mak, C. Lee, J. Hone, J. Shan, T. F. Heinz, *Phys. Rev. Lett.* **2010**, *105*, 136805.

[9]   A. Castellanos-Gomez, M. Poot, G. A. Steele, H. S. J. van der Zant, N. Agraït, G. Rubio-Bollinger, *Adv. Mater.* **2012**, *24*, 772.

[10]   Radisavljevic. B, Radenovic. A, Brivio. J, Giacometti. V, Kis. A, *Nat. Nanotecnol.*
         2011, *6*, 147.

[11]   Z. Zeng, Z. Yin, X. Huang, H. Li, Q. He, G. Lu, F. Boey, H. Zhang, *Angew. Chem.
         Int. Ed.* **2011**, *50*, 11093.

[12]   H. Hwang, H. Kim, J. Cho, *Nano Lett.* **2011**, *11*, 4826.

[13]   T. F. Jaramillo, K. P. Jørgensen, J. Bonde, J. H. Nielsen, S. Horch, I. Chorkendorff,
         Science **2007**, *317*, 100.

[14]   A. M. Panich, A. I. Shames, R. Rosentsveig, R. Tenne, *J. Phys.: Condens. Matter*
         2009, *21*, 395301.

[15]   P. Murugan, V. Kumar, Y. Kawazoe, N. Ota, *Phys. Rev. A* **2005**, *71*, 063203.

[16]   J. Zhang, J. M. Soon, K. P. Loh, J. Yin, J. Ding, M. B. Sullivian, P. Wu, *Nano Lett.*
         2007, *7*, 2370.

[17]   Dan Li, Chaofeng Zhang, G. D, R. Zeng, S. Wang, Z. Guo, Z. Chenc, H. Liua, *J.
         Chin. Chem. Soc.* **2012**, *59*, 1196.

[18]   S. Tongay, S. S. Varnoosfaderani, B. R. Appleton, J. Wu, A. F. Hebard, *Appl.
         Phys. Lett.* **2012**, *101*, 123105.

[19]   S. Mathew, K. Gopinadhan, T. K. Chan, X. J. Yu, D. Zhan, L. Cao, A. Rusydi, M.
         B. H. Breese, S. Dhar, Z. X. Shen, T. Venkatesan, J. T. L. Thong, *Appl. Phys. Lett.*
         2012, *101*, 102103.

[20]   A. Vojvodic, B. Hinnemann, J. K. Nørskov, *Phys. Rev. B* **2009**, *80*, 125416.

[21]   a)H. S. S. R. Matte, K. S. Subrahmanyam, C. N. R. Rao, *The Journal of Physical
         Chemistry C* **2009**, *113*, 9982; b)C. N. R. Rao, H. S. S. R. Matte, K. S.
         Subrahmanyam, U. Maitra, *Chemical Science* **2012**, *3*, 45.

[22]   T. L. Makarova, K. H. Han, P. Esquinazi, R. R. da Silva, Y. Kopelevich, I. B. Zakharova, B. Sundqvist, *Carbon* **2003**, *41*, 1575.

[23]   A. Sundaresan, C. N. R. Rao, *Nano Today* **2009**, *4*, 96.

[24]   S. S. Rao, S. N. Jammalamadaka, A. Stesmans, V. V. Moshchalkov, J. v. Tol, D. V. Kosynkin, A. Higginbotham-Duque, J. M. Tour, *Nano Lett.* **2012**, *12*, 1210.

[25]   a)M. Fujita, K. Wakabayashi, K. Nakada, K. Kusakabe, *J. Phys. Soc. Jpn.* **1996**, *65*, 1920; b)K. Nakada, M. Fujita, G. Dresselhaus, M. S. Dresselhaus, *Physical Review B* **1996**, *54*, 17954; c)P. L. Giunta, S. P. Kelty, *J. Chem. Phys.* **2001**, *114*, 1807.

[26]   a)M. V. Bollinger, J. V. Lauritsen, K. W. Jacobsen, J. K. Nørskov, S. Helveg, F. Besenbacher, *Physical Review Letters* **2001**, *87*, 196803; b)S. Helveg, J. V. Lauritsen, E. Lægsgaard, I. Stensgaard, J. K. Nørskov, B. S. Clausen, H. Topsøe, F. Besenbacher, *Phys. Rev. Lett.* **2000**, *84*, 951; c)M. V. Bollinger, K. W. Jacobsen, J. K. Nørskov, *Physical Review B* **2003**, *67*, 085410.

[27]   a)K. Wakabayashi, M. Fujita, H. Ajiki, M. Sigrist, *Physical Review B* **1999**, *59*, 8271; b)T. Enoki, N. Kawatsu, Y. Shibayama, H. Sato, R. Kobori, S. Maruyama, K. Kaneko, *Polyhedron* **2001**, *20*, 1311.

[28]   a)T. Enoki, Y. Kobayashi, *Journal of Materials Chemistry* **2005**, *15*, 3999; b)T. Enoki, K. Takai, *Dalton Transactions* **2008**, 3773.

[29]   Y. Li, Z. Zhou, S. Zhang, Z. Chen, *J. Am. Chem. Soc.* **2008**, *130*, 16739.

[30]   C. N. R. Rao, A. K. Sood, K. S. Subrahmanyam, A. Govindaraj, *Angew. Chem. Int. Ed.* **2009**, *48*, 7752.

[31]   G. L. Frey, R. Tenne, M. J. Matthews, M. S. Dresselhaus, G. Dresselhaus, *Phys. Rev. B* **1999**, *60*, 2883.

Appendix*
Field-effect transistors based on graphene analogues of MoS₂ and GaS(Se)

Hysteresis in Single-Layer MoS₂ Field-Effect Transistors: We have examined origin of the hysteretic and transient behaviors and suggest that hysteresis of MoS₂ field effect transistors is largely due to absorption of moisture on the surface and intensified by high photosensitivity of MoS₂. Uniform encapsulation of MoS₂ transistor structures with silicon nitride grown by plasma-enhanced chemical vapor deposition is effective in minimizing the hysteresis, while the device mobility is improved by over 1 order of magnitude.
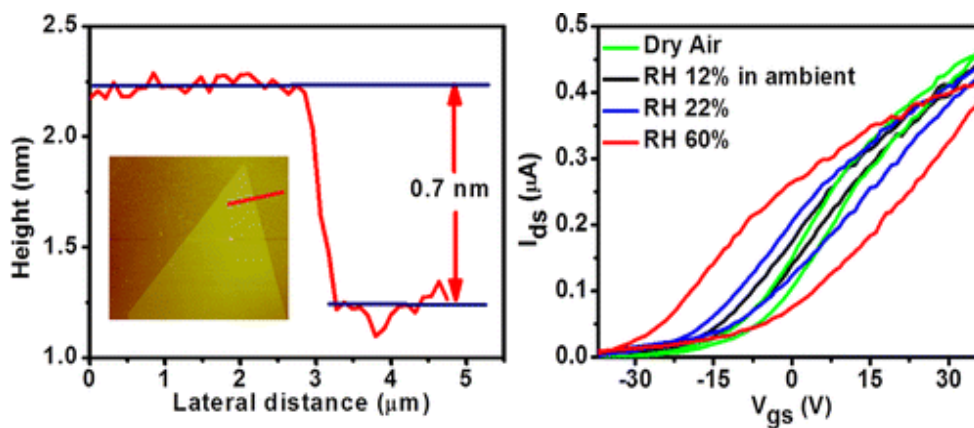
Figure 1: (a) AFM height profile of monolayer MoS₂; inset is the corresponding AFM image (b) Hysteresis evolution of same device under different humidity

GaS and GaSe Ultrathin Layer Transistors: We have measured room-temperature bottom-gate geometry transistor characteristics based on single-sheets of GaS and GaSe, which show typical n-type and p-type conductance, respectively. Single-sheet of GaS and GaSe exhibit field-effect respective differential mobilities of $\approx$0.1 cm^2 V^{-1} s^{-1} and 0.6 cm^2 V^{-1} s^{-1} along with good ON/OFF current ratios in the range of $\approx$10^4–10^5
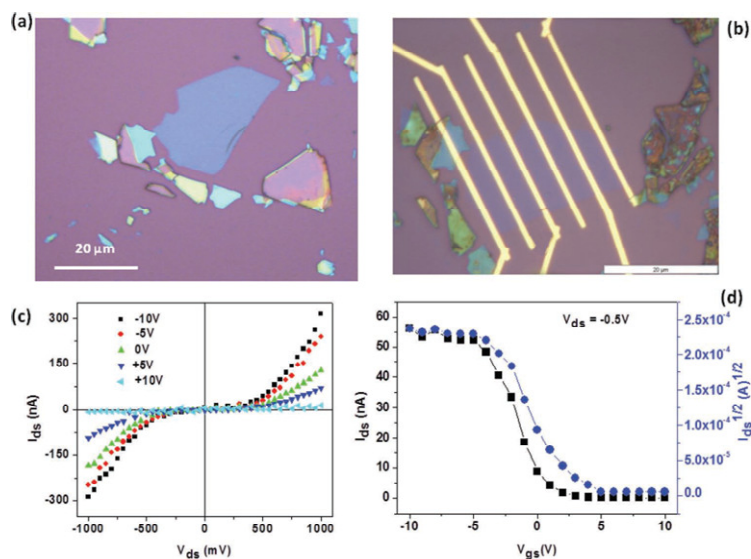
Figure 2: Single-sheet GaSe: a) Typical optical image before patterning electrode and b) optical image after patterning electrode. c) Room-temperature FET output characteristics of single-sheet of GaSe in dark at constant humidity (22%) and d) transfer characteristics of a GaSe single sheet FET.

2.5: Layer-dependent resonant Raman scattering of molybdenum sulphide

Summary[*]

We report resonant Raman scattering of MoS_2 layers comprising of single-, bi-, four- and seven layers, showing a strong dependence on the layer thickness. Indirect band gap MoS_2 in bulk becomes a direct band gap semiconductor in the monolayer form. New Raman modes are seen in the spectra of single- and few-layer MoS_2 samples which are absent in the bulk. The Raman mode at ~230 cm^{-1} appears for two, four and seven layers. This mode has been attributed to the longitudinal acoustic phonon branch at the M point (LA(M)) of the Brillouin zone. The mode at ~ 179 cm^{-1} shows asymmetric character for a few-layer sample. The asymmetry is explained by the dispersion of the LA(M) branch along the Γ-M direction. The most intense spectral region near 455 cm^{-1} shows a layer-dependent variation of peak positions and relative intensities. The high energy region between 510 and 645 cm^{-1} is marked by the appearance of prominent new Raman bands, varying in intensity with layer numbers. Resonant Raman spectroscopy thus serves as a promising non invasive technique to accurately estimate the thickness of MoS_2 layers down to a few atoms thick.

2.5: Layer-dependent Raman scattering of MoS_2

2.5.1: Introduction

The advent of mechanical exfoliation technique to create two dimensional structures from their three dimensional counterparts has made it possible to explore the physics of single- and few-layer semiconducting systems other than graphene.[1] Graphene, a two-dimensional form of carbon, is the most recently discovered allotrope in 2004[1a], following discoveries of zero-dimensional fullerenes and one-dimensional nanotubes in the past decades. This two-dimensional material has unique physical properties as compared to the three-dimensional allotropic forms of carbons, namely, diamond and graphite, as well as the above-mentioned lower dimensional forms.[2,3]

Recently, a few quintuples of Bi_2Te_3, a topological insulator, has been obtained from mechanical exfoliation.[4] Another system of recent interest is $2H\text{-}MoS_2$, a layered compound in which a single hexagonal sheet of Mo atoms is sandwiched between two layers of sulphur atoms, and successive layers of this covalently bonded S–Mo–S sheets are weakly coupled by van der Waals forces, thereby forming a three-dimensional layered structure. In its bulk form, MoS_2 is a semiconductor with indirect band gap of 1.2 eV and a direct gap of 1.9 eV at room temperature.[5] There are two sharp peaks in the absorption spectrum of the bulk MoS_2, revealing two excitonic transitions, namely the A and B excitons at 1.88 eV and 2.06 eV, respectively.[6] It has been recently shown from photoluminescence studies[7] that this indirect band gap semiconductor becomes a direct gap semiconductor in its monolayer form. The indirect band gap in a few-layer system is sensitive to the number of layers. Thus, a red shift of the indirect band gap is found, as the thickness is increased from two to four layers.[7b] Graphene-like layers of MoS_2 and WS_2 were synthesized by Matte et al. by various chemical methods.[8] Mechanical exfoliation

2.5: Layer-dependent Raman scattering of MoS$_2$

used in making graphene layers has been demonstrated to yield one to six layers thick films of MoS$_2$.[7, 9] Recently, monolayer MoS$_2$ field effect transistor has been demonstrated[10] to have an on-off ratio around 10^8, and in-situ Raman experiments have been done to study phonon renormalization. Large area growth of MoS$_2$ atomic layers have been made possible by Zhan et al.[11] using chemical vapour deposition technique. Raman spectroscopy is a powerful probe to determine the number of layers in graphene samples.[12] The stacking of layers, in particular, can have strong influence on the electron–phonon coupling of different phonon modes as is evident from the doping dependent Raman studies of single and bilayer graphene.[13] Resonance Raman scattering, in particular, is a sensitive probe for materials with different electronic band structures depending on the number of layers. Group theoretical analysis at the zone centre Γ point in the hexagonal Brillouin zone of single crystal 2H-MoS$_2$ predicts four first-order Raman active modes: E^2_{2g}, E_{1g}, E^1_{2g} and A_{1g} with wavenumbers approximately at 32 cm^{-1}, 286cm^{-1}, 383cm^{-1} and 408 cm^{-1}, respectively.[14] Modes other than the E^2_{2g} mode involve the intralayer (S–Mo–S) atomic vibrations. The E^2_{2g} mode is an interlayer mode caused by the vibrations of two rigid layers against each other. The E_{1g} mode is forbidden in back scattering geometry on the surface perpendicular to the c axis. Here, we review some of the recent results on the Raman studies on the graphene analogues of MoS$_2$. Lee et al. [9] have shown the effect of layer thickness on the first-order E^1_{2g} and A_{1g} modes using 514.5 nm laser irradiation, which is an off-resonance condition. With decreasing number of layers (n), these two modes shift in opposite direction, the E^1_{2g} mode shows a blue shift of ~2 cm^{-1}, while the A_{1g} is red shifted by ~ 4 cm^{-1}. Further, the integrated intensities of both the E^1_{2g} and A_{1g} modes show a maximum for MoS$_2$ sample of n=4 layers. The linewidth of the A_{1g} mode shows a maximum at n=2, whereas the linewidth of the E^1_{2g} mode does not

depend on n. Raman spectroscopy has been used to study the interlayer shear mode in few-layer MoS$_2$ and found that a large frequency shift of the shear mode to higher wave numbers with increasing number of layers.[15] Ultrathin MoS$_2$ flakes have been investigated systematically using Raman and resonance Raman spectroscopy. Resonance Raman spectra show that the coupling between electronic transition at K point and A$_{1g}$ phonon is weakened in ultrathin MoS$_2$ in comparison with that in bulk MoS$_2$, which is explained on the basis of increased transition energy at K point due to the perpendicular quantum confinement or elongated intralayer atomic bonds. It is confirmed that the asymmetric Raman band centered at 454 cm^{-1} in bulk MoS$_2$ is found as a combinational band involving LA(M) and A$_{2u}$ modes. The consistent E$^1_{2g}$ and A$_{1g}$ peak frequencies of monolayer MoS$_2$ using various laser lines show that Raman spectroscopy is a reliable tool to identify the thickness of the few-layer MoS$_2$.[16] Raman spectra of chalcogenides flakes on dielectric substrates showed clear high-order enhancement peaks in atomically flat samples and reveal the role played by optical interference in the spectra of stacked systems. Even freely suspended few-layer flakes show a stronger response than bulks due to inner optical interference.[17] Najmaei et al have studied the thermal effects on the Raman spectra of few-layer MoS$_2$ and found that with increasing the laser energy, there is an red shift in the peak position and has thrown light on the anharmonic terms in the lattice potential energy.[18] Later, some theoretical calculations have been carried out to understand the anomalous phonon behavior in the few-layer MoS$_2$. Coming from single-layer MoS$_2$, to bulk we expect the increase in the frequency of the A$_{1g}$ mode because of increase in the force constant of the extra layer. Though E$_{2g}$ mode should also behave in the same way, or the effect should be less, due to the absence of interlayer interaction. But, the stiffening of E$_{2g}$ mode has been explained basing on the possibility that the lattice

constant of 1H-MoS$_2$ a can get smaller than the lateral lattice constant of 3D MoS$_2$ a = 3.16 Å, and repeated the calculations for 1H-MoS$_2$ using a = 3.14 Å and found that the frequency of E$_{2g}$ increases from 381.2 to 385 cm^{-1} confirming the anomalous effect.[19] Later Wirtz et al. explained the dependence of E$^1_{2g}$ mode wavenumber on n has recently been understood as follows: the long range Coulombic interaction between the Mo atoms decreases with increasing layer number due to the increase in the dielectric tensor.[20]

2.5.2: Scope of the present investigations

The off-resonance[14] and resonance[21] Raman spectra for bulk 2H-MoS$_2$ have been well studied. We present a resonant Raman scattering study of the dependence of the first- and second-order Raman modes of MoS$_2$ on the number of layers n. The resonance condition is achieved by exciting the sample with 1.96 eV laser photon energy. Several new modes appear in the resonant spectra of few-layer thick samples. It is seen that the linewidth of the A$_{1g}$ mode is broadened in the resonance spectrum, and the most intense band near 460 cm^{-1} becomes asymmetric as the sample thickness is increased from a monolayer to seven layers. Distinct modes, not seen in the bulk MoS$_2$, appear between 510 and 645 cm^{-1} with intensity varying with the layer thickness.

2.5.3: Experimental section

Mechanical Exfoliation : Single-, bi- and a few-layer MoS$_2$ films were prepared by mechanical exfoliation of a 2H-MoS$_2$ single crystal (procured from M/s SPI Supplies, USA[22]) and were subsequently deposited on 300 nm SiO$_2$/Si substrate. In this procedure, similar to that used for preparing graphene devices, the SiO$_2$/Si substrate was subjected to RCA cleaning.[23] Then, a piece of scotch tape was pressed against the MoS$_2$ crystal surface, peeled off gently and pressed against the cleaned SiO$_2$/Si substrate.

Characterization

Raman Spectroscopy

Raman spectra were recorded with a LabRAM HR high-resolution Raman spectrometer (Horiba-Jobin Yvon) using a He–Ne laser ($\lambda = 632.8$ nm) and Ar laser (514 nm).

Atomic force Microscopy

AFM measurements were carried on Vecco digital instruments, di Innova.

2.5: Layer-dependent Raman scattering of MoS$_2$

2.5.4: Results and Discussion

Figure 1(a) and (b) shows the optical and AFM images of the MoS$_2$ films, respectively. The AFM height profile for the single, bi, four and seven layers is shown in Figure 1 (c–f). Single layer height as deduced from the AFM scan was ~0.8 nm. The height of other layers was deduced similarly by scanning different portions of the sample and measuring the height from the AFM line scan. The measured height (H) using AFM was fitted to H = nd + d$_0$ where n is the assigned layer number, d is the ideal thickness of MoS$_2$ single layer and d$_0$ is the instrumental offset arising from difference in interaction between the tip and
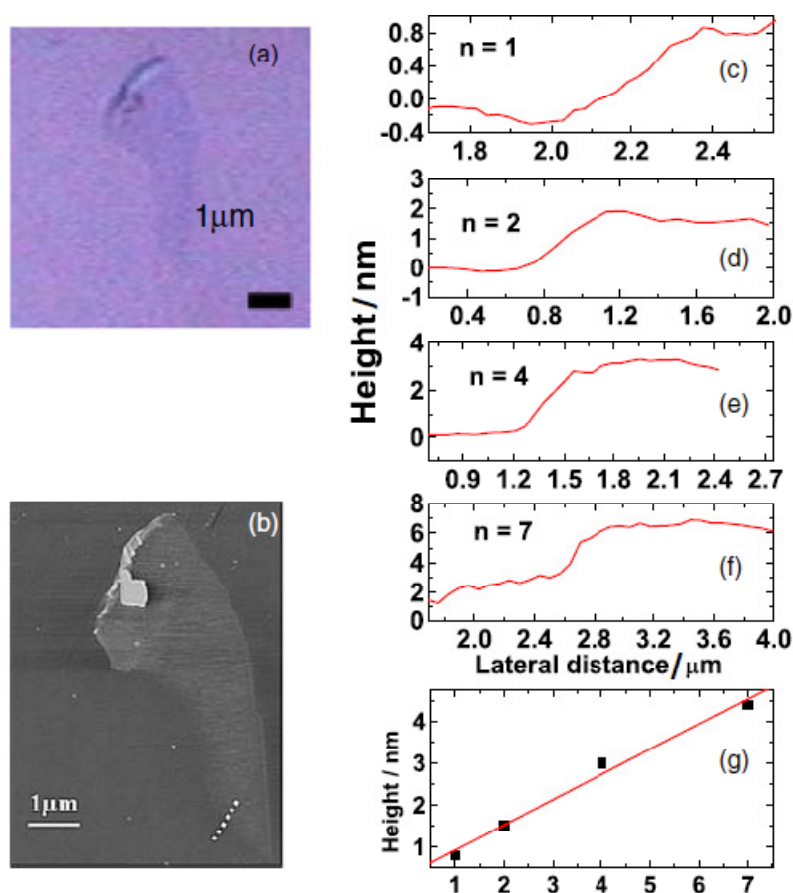
Figure 1: (Color online) (a) Optical image and (b) AFM image of the monolayer. AFM line scan was done along the white dashed line. (c)–(f) AFM height profile for n=1, n=2, n = 4 and n = 7. (g) Measured height (H) as a function of n. Squares are experimental data, and the line is the linear fit.

2.5: Layer-dependent Raman scattering of MoS_2

MoS_2 and vis-a-vis the tip and SiO_2. The values obtained from the fit are d=0.60nm and d_0=0.32nm (see Figure 1(g)). Room temperature confocal Raman spectra were recorded in LabRam spectrometer (M/s Horiba) using 100 objective. The laser spot size is ~0.9 μm which is smaller than the MoS_2 flake size. The spectral resolution is ~1 cm^{-1}. For off resonance Raman measurement, 514.5 nm (2.41 eV) laser line from an argon ion laser was used. Resonance Raman spectra were measured using 633 nm (1.96 eV) laser line from a He–Ne laser. Laser powers for both the experiments were kept below 1mW to avoid heating of the samples.

Figure 2a shows the Raman spectra of different layers of MoS_2 recorded using 514.5 nm laser line. The main Raman bands in the off-resonance spectra (Figure 2(a)) correspond to the zone centre first-order E^1_{2g} mode at ~383 cm^{-1} and the A_{1g} mode at ~ 408 cm^{-1}. The wavenumbers of the modes show opposite trend as a function of layer number n: the wavenumber of the A_{1g} mode decreases whereas that of E^1_{2g} mode increases as the layer number is reduced. One way to understand this could be in terms of phonon confinement within the framework of spatial correlation model.[24] This would require that the dispersion relation of the A_{1g} mode should have wavenumber decreasing with wavevector q, and for the E^1_{2g} mode, wavenumber should increase with q. This is not the case for MoS_2 and hence spatial correlation model cannot explain the behaviour of A_{1g} and E^1_{2g} modes. The dependence of E^1_{2g} mode wavenumber on n has recently been understood as follows: the long range Coulombic interaction between the Mo atoms decreases with increasing layer number due to the increase in the dielectric tensor.[20] This results in softening of the E^1_{2g} mode with increasing n as this mode involves in-plane vibrations of the Mo atoms. On the other hand, the A_{1g} mode involves only the out-of-plane
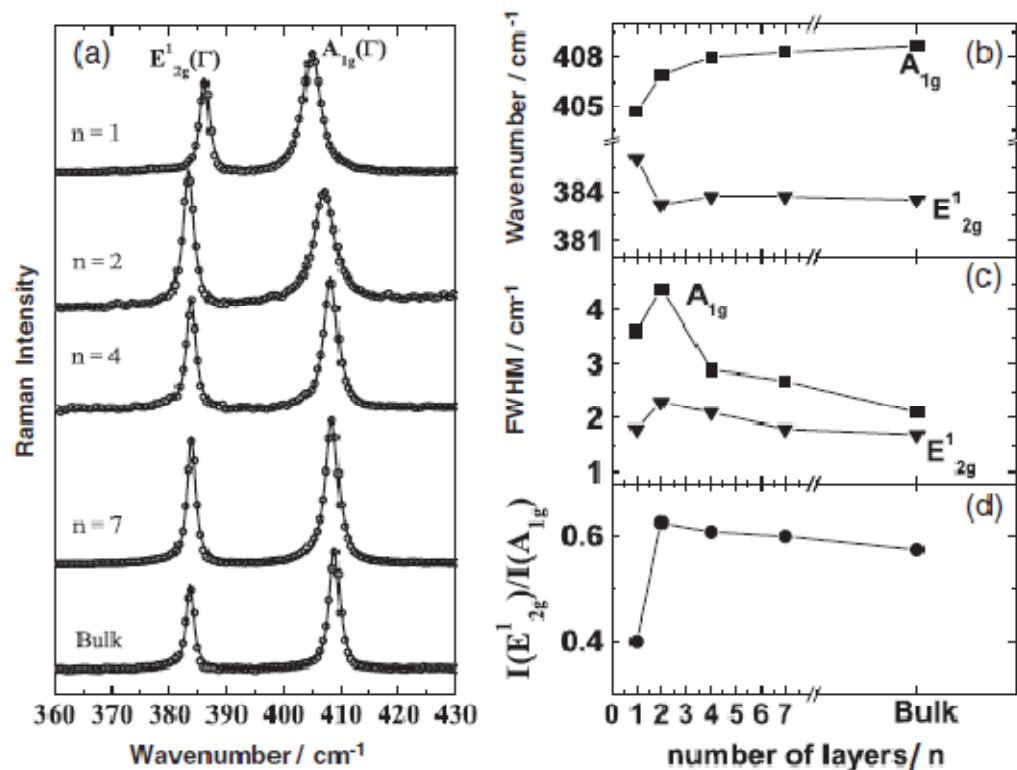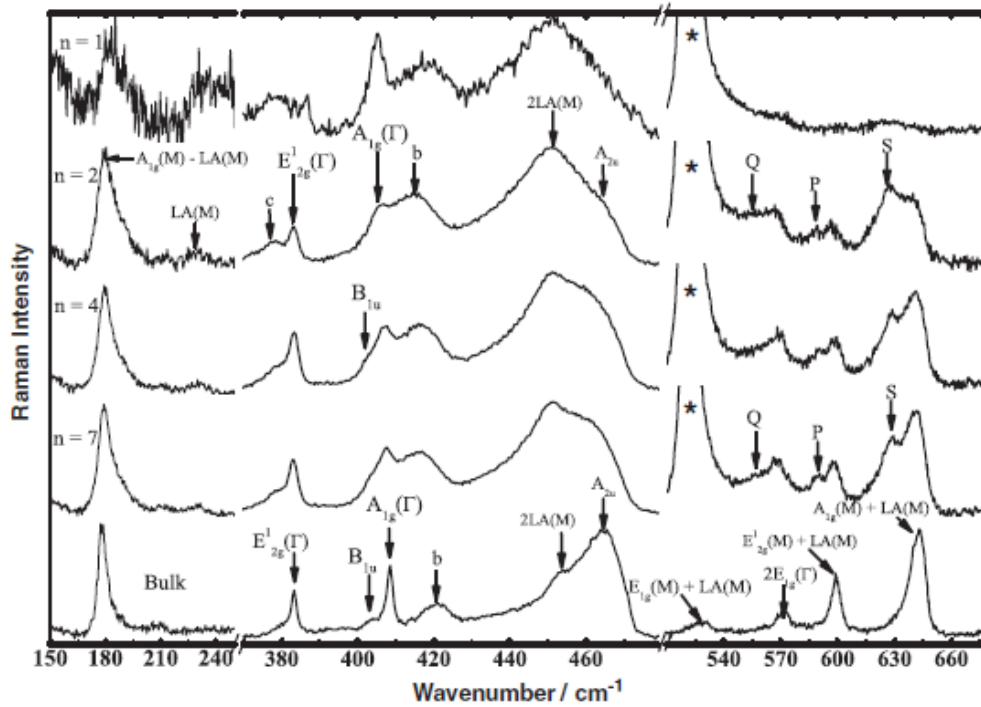
Figure 2: Raman spectra for different layers with (a) 514.5nm laser line showing two most prominent features namely the E$^1_{2g}$ and A$_{1g}$ modes. Circles are experimental points and solid lines are Lorentzian fit. The layer number is marked for each spectrum. (b) Wavenumber and (c) FWHM of E$^1_{2g}$ (triangle) and A$_{1g}$ (squares) modes as a function of layer number. (d) Integrated intensity ratio of E$^1_{2g}$ and A$_{1g}$ mode as a function of layer number. The intensity represents the area under the curve.

displacements of the S atoms and hence is not influenced by the screening. The increase in the A$_{1g}$ mode wavenumber is attributed to the enhanced restoring forces on the S atoms due to interlayer interactions. The FWHM for the A$_{1g}$ mode increases from ~2 cm^{-1} to ~5 cm^{-1} as n decreases from bulk to two layers. The linewidth reduces as n is further reduced to a monolayer. The FWHM for E$^1_{2g}$ mode, on the other hand, remains constant for all n. All the results agree with Ref. [9]. Figure 3 shows resonant Raman spectra of the samples with n = 1, 2, 4, 7 along with the bulk MoS$_2$. The wavenumbers and FWHM values of the E$^1_{2g}$ and A$_{1g}$ modes, shown, respectively, in Fig. 4a and b, follow the same trend as in the off-resonant case with the difference that the linewidth of the A$_{1g}$ mode is higher in

resonant condition. The relative integrated intensity of the E$^1_{2g}$ mode with respect to the A$_{1g}$ mode (Figure 4(c) black circles) also has a similar trend to that in the off-resonant condition. A noticeable feature in the resonant spectra is the appearance of new modes and their evolution with the number of layers. In the wavenumber range of 360–430 cm^{-1}, four new modes are seen which are absent in the off-resonant spectrum.

Figure 3: Resonant Raman spectra of different layers of MoS$_2$ using 633nm laser line. The layer numbers (n) are marked. Different modes are marked with arrow. The strong Raman mode marked * comes from the SiO$_2$/Si substrate and is completely absent in thick multilayer (labeled as bulk) MoS$_2$ spectrum. The symmetry assignments are also shown for different modes. The noticeable feature is the appearance of completely new modes and their evolution with layer thickness.

A mode denoted as 'c' at ~377 cm^{-1} can be clearly resolved from the E$^1_{2g}$ mode. In a single-layer spectrum, this band is broad but becomes sharp in n=2, 4 and 7. This mode belongs to the transverse optical (TO) branch (Δ_6 branch along c axis [21a, 21c, 25]) with a finite wave vector near the Γ point and has been assigned to the E$^2_{1u}$ symmetry.[21a, 21c] Unlike in Ref.[21a] we do not refer to this mode as E$^2_{1u}$ mode since from the IR

measurements, the position of the E^2_{1u} mode has been found to be on the higher side of the E^1_{2g} mode.[14a] The wavenumber of this mode does not depend on n. However, its relative integrated intensity with respect to E^1_{2g} [$(I_{(c)})/(E^1_{2g})$] mode decreases with increasing n (Figure 4(e)) feature in the resonance Raman spectra appears at ~ 409 cm^{-1}, evolving with layer thickness. This band is assigned to B_{1u} symmetry in bulk MoS_2. [21a, 21c] This Raman inactive mode is observed under resonant conditions and is the Davydov couple of the A_{1g} mode.[26] The relative intensity of this mode to the A_{1g} mode, shown in Figure 4(f) (in solid squares), increases with n. Another prominent feature, completely absent in the off-resonant spectrum is at ~ 420 cm^{-1}, marked 'b' in Figure 3. This mode in bulk MoS_2 [21a, 21c] appears when the exciting laser energy is just above the 1 s level of the A exciton and shows a strong dispersion with incident laser photon energies. It is assigned to a two-phonon Raman process involving the successive emission of a dispersive quasi-acoustic (QA) phonon and a dispersionless TO phonon (of E^2_{1u} symmetry), both along the c axis.[21a, 21c] This mode is a sum combination process ($\omega_b = \omega_{QA} + \omega_{TO}$), and the QA phonon belongs to the Δ_2 branch[25] ending in the B^2_{2g} silent mode at the Γ point. The TO phonon in the combination appears as 'c' band in Figure 3.[21a, 21c, 25] In the low wavenumber spectral region (160–250 cm^{-1}) shown in Figure 3, Raman band at 179 cm^{-1} in bulk MoS_2 is assigned to the two phonon difference combination mode ($A_{1g}(M) - LA(M)$).[14b, 21b, 27] This feature does not show any dependence on n. The lineshape asymmetry increases for n=2, 4 and 7. The asymmetric character is a consequence of the phonon dispersion curves near the M point of the hexagonal Brillouin zone. The A_{1g}, E_g and E^1_{2g} branches are almost dispersionless along the Γ-M direction, while the longitudinal acoustic branch (LA) is concave down at M.[25, 27] The difference combination modes would thus show asymmetric

lineshape in the high wavenumber side. An additional band near 230 cm^{-1} is seen for n = 2, 4 and 7 layers. From lattice dynamic calculations,[28] this mode can be identified as the first-order LA(M) mode. The appearance of this mode had been reported by Frey et al.[21b] for MoS_2 nanoparticles and has been attributed to disorder-induced scattering from the zone edge M point. The rigid-layer E^2_{2g} mode wavenumber increases along the Γ-M direction to reach the LA at M point (LA(M)). This has been experimentally demonstrated in inelastic neutron scattering [25] where the phonon density of states had been shown to have a peak near 230 cm^{-1}. A prominent appearance of this mode in a few atomic layers
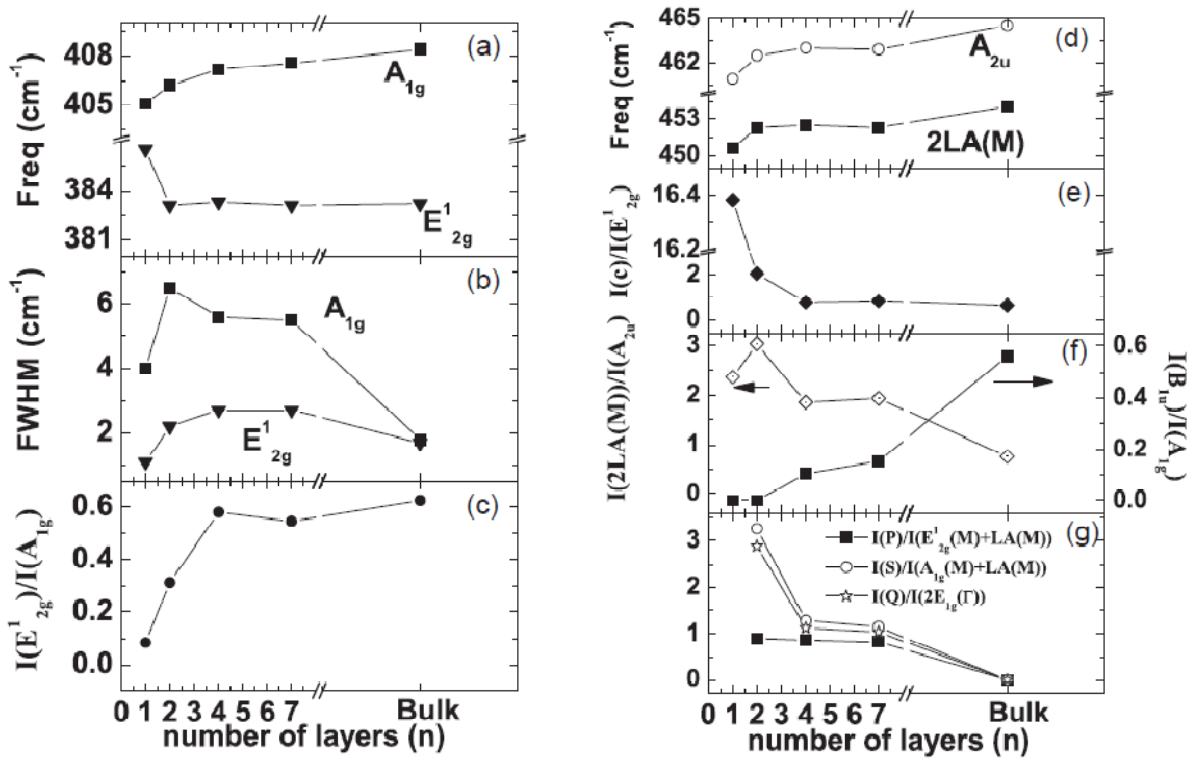
Figure 4: (a) Wavenumber and (b) FWHM of E^1_{2g} (triangle) and A_{1g} (squares) modes in the resonant spectra as a function of layer number. (c) Integrated intensity ratio between E^1_{2g} and A_{1g} as a function of layer number n. (d) Wavenumber of the two modes marked 2LA(M) (squares) and A_{2u} (open circles)as a function layer number. (e), (f) and (g) show the integrated intensity ratios of different modes from different regions of the resonant spectra. All the parameters are extracted by fitting the resonant spectra, for each layer, with Lorentzian profiles.

predicts that structural defect-induced scattering, like in nanoparticles, becomes important. The spectral region between 430 and 490 cm^{-1} assigned to the second-order Raman spectra [25]shows layer dependence and has high intensity bands. The mode near the 450 cm^{-1} (in bulk) is associated with 2LA(M) mode[21a, 21b, 27], while the one near 466 cm^{-1} (in bulk) is assigned to the A_{2u} mode.[21b, 25] The peak wavenumbers of 2LA(M) and A_{2u} bands (Figure 4(d)) increase with n. The relative intensity of the 2LA(M) with respect to the A_{2u} band shown in Figure 4(f) (open diamonds) decreases with n. This is similar to the intensity ratio dependence on the size of the MoS_2 nanoparticles.[25] In the high wavenumber region between 510 and 630 cm^{-1}, bulk MoS_2 has modes at 526 cm^{-1} (E_{1g}(M) + LA (M)), 571 cm^{-1} ($2E_{1g}(\Gamma)$), 599 cm^{-1} (E^1_{2g} (M) + LA(M)) and 642 cm^{-1} (A_{1g}(M) + LA(M)), where the mode assignments are taken from Ref.[25] It is to be noted that although back scattering experimental geometry forbids the appearance of E_{1g} (Γ) mode, the second order of this mode is seen in all the samples. As mentioned earlier, due to the LA(M) phonon branch being concave down and nearly flat dispersion for A_{1g}, E_{1g} and E^1_{2g} branches along Γ-M direction, the sum bands will have an asymmetric tail towards low wavenumber side.[27] The new bands (not seen in Bulk as well as MoS_2 nanoparticles [25]) clearly seen in samples with n = 2, 4 and 7 with respect to the bulk MoS_2 are: ~ 554 cm^{-1} (labelled as Q), 588 cm^{-1} (P) and 628 cm^{-1} (S). The wavenumbers of these modes do not vary with n. The relative intensities of these modes with respect to the neighboring bands are shown in Figure 4(g), clearly showing layer thickness dependence. A quantitative understanding of these new features would require theoretical calculations of phonon dispersion and two phonon density of states as a function of number of layers. We hope that our data will motivate such calculations in future.

2.5.5: Conclusions

In summary, resonance Raman spectra of one-, two-, four- and seven-layer MoS$_2$ are reported. Apart from the zone centre E$^1_{2g}$ and A$_{1g}$ modes, several prominent new Raman bands appear in resonant condition. Thus, examination of the resonance Raman spectra in different wavenumber regions can be used to estimate the thickness of graphene-like MoS$_2$ samples.

2.5: Layer-dependent Raman scattering of MoS$_2$

2.5.6: References

[1]   a)K. S. Novoselov, A. K. Geim, S. V. Morozov, D. Jiang, Y. Zhang, S. V. Dubonos, I. V. Grigorieva, A. A. Firsov, *Science* **2004**, *306*, 666; b)A. K. Geim, *Science* **2009**, *324*, 1530; c)A. K. Geim, K. S. Novoselov, *Nat. Mater.* **2007**, *6*, 183; d)C. N. R. Rao, A. K. Sood, K. S. Subrahmanyam, A. Govindaraj, *Angew. Chem. Int. Ed.* **2009**, *48*, 7752.

[2]   a)A. H. Castro Neto, F. Guinea, N. M. R. Peres, K. S. Novoselov, A. K. Geim, *Rev. Mod. Phys.,* **2009**, *81*, 109; b)N. M. R. Peres, *Rev. Mod. Phys.,* **2010**, *82*, 2673.

[3]   a)L. M. Malard, M. A. Pimenta, G. Dresselhaus, M. S. Dresselhaus, *Phys. Rep.,* **2009**, *473*, 51; b)M. S. Dresselhaus, A. Jorio, R. Saito, *Annu. Rev. Condens. Matter Phys.,* **2010**, *1*, 89.

[4]   D. Teweldebrhan, V. Goyal, A. A. Balandin, *Nano Lett.* **2010,** *10*, 1209.

[5]   G. L. Frey, S. Elani, M. Homyonfer, Y. Feldman, R. Tenne, *Phys. Rev. B* **1998**, *57*, 6666.

[6]   a)J. V. Acrivos, W. Y. Liang, J. A. Wilson, A. D. Yoffe, *J. Phys. C.* **1971**, *4* L 18; b)R. Coehoorn, C. Haas, J. Dijkstra, C. J. F. Flipse, R. A. de Groot, A. Wold, *Phys. Rev. B* **1987**, *35*, 6195.

[7]   a)A. Splendiani, L. Sun, Y. Zhang, T. Li, J. Kim, C.-Y. Chim, G. Galli, F. Wang, *Nano Lett.* **2010**, *10*, 1271; b)K. F. Mak, C. Lee, J. Hone, J. Shan, T. F. Heinz, *Phys. Rev. Lett.* **2010**, *105*, 136805.

[8]   H. S. S. R. Matte, A. Gomathi, A. K. Manna, D. J. Late, R. Datta, S. K. Pati, C. N. R. Rao, *Angew. Chem. Int. Ed.* **2010**, *49*, 4059.

[9]   C. Lee, H. Yan, L. E. Brus, T. F. Heinz, J. Hone, S. Ryu, *ACS Nano* **2010**, *4*, 2695.

[10]   B. Radisavljevic, A. Radenovic., J. Brivio, Giacometti. V, A. Kis, *Nat Nanotechnol.* **2012**, *6*, 147.

[11]   Y. Zhan, Z. Liu, S. Najmaei, P. M. Ajayan, J. Lou, *Small* **2012**, *8*, 966.

[12]   a)A. C. Ferrari, J. C. Meyer, V. Scardaci, C. Casiraghi, M. Lazzeri, F. Mauri, S. Piscanec, D. Jiang, K. S. Novoselov, S. Roth, A. K. Geim, *Phys. Rev. Lett* **2006**, *97*, 187401; b)S. K. Pati, T. Enoki, C. N. R. Rao, World Scientific, Singapore, 2011.

[13]   a)DasA, PisanaS, ChakrabortyB, PiscanecS, S. K. Saha, U. V. Waghmare, K. S. Novoselov, H. R. Krishnamurthy, A. K. Geim, A. C. Ferrari, A. K. Sood, *Nat. Nanotechnol.* **2008**, *3*, 210; b)J. Yan, T. Villarson, E. A. Henriksen, P. Kim, A. Pinczuk, *Phys. Rev. B* **2009**, *80*, 241417.

[14]   a)T. J. Wieting, J. L. Verble, *Phys. Rev. B* 1971, *3*, 4286; b)J. M. Chen, C. S. Wang, *Solid State Commun.* **1974**, *14*, 857.

[15]   G. Plechinger, S. Heydrich, J. Eroms, D. Weiss, C. Schuller, T. Korn, *Appl. Phys. Lett.* **2012**, *101*, 101906.

[16]   H. Li, Q. Zhang, C. C. R. Yap, B. K. Tay, T. H. T. Edwin, A. Olivier, D. Baillargeat, *Adv. Func. Mater.* **2012**, *22*, 1385.

[17]   S.-L. Li, H. Miyazaki, H. Song, H. Kuramochi, S. Nakaharai, K. Tsukagoshi, *ACS Nano* **2012**, *6*, 7381.

[18]   S. Najmaei, Z. Liu, P. M. Ajayan, J. Lou, *Appl. Phys. Lett.* **2012**, *100*, 013106.

[19]   C. Ataca, M. Topsakal, E. Aktürk, S. Ciraci, *J. Phys. Chem. C* **2011**, *115*, 16354.

[20]   A. Molina-Sánchez, L. Wirtz, *Phys. Rev. B* **2011**, *84*, 155413.

[21]   a)Tomoyuki Sekine, Kunimitsu Uchinokura, Tsuneo Nakashizu, Etsuyuki Matsuura, R. Yoshizaki1, *J. Phys. Soc. Jpn.* **1984,** *53* 811; b)G. L. Frey, R. Tenne, M. J. Matthews, M. S. Dresselhaus, G. Dresselhaus, *Phys. Rev. B* **1999**, *60*, 2883; c)T. Livneh, E. Sterer, *Phys. Rev. B* **2010**, *81*, 195209.

[22]   http://www.2spi.com/.

[23]   X. Liang, B. A. Sperling, I. Calizo, G. Cheng, C. A. Hacker, Q. Zhang, Y. Obeng, K. Yan, H. Peng, Q. Li, X. Zhu, H. Yuan, A. R. Hight Walker, Z. Liu, L.-m. Peng, C. A. Richter, *ACS Nano* **2011**, *5*, 9144.

[24]   H. Richter, Z. P. Wang, L. Ley, *Solid State Commun.* **1981**, *39*, 625.

[25]   N. Wakabayashi, H. G. Smith, R. M. Nicklow, *Phys. Rev. B* **1975**, *12*, 659.

[26]   J. L. Verble, T. J. Wieting, *Phys. Rev. Lett.* **1970**, *25*, 362.

[27]   A. M. Stacy, D. T. Hodul, *J. Phys. Chem. Solids* **1985**, *46*, 405.

[28]   F. C. C. Sourisseau, M. Fouassier, *Chem. Phys.* **1991**, *150*, 281.

2.6: Superior infrared detection properties of few-layer molybdenum selenide

Summary

Considering the favorable electronic properties of $MoSe_2$, graphene-like few-layered samples prepared by a solution-based chemical procedure have been investigated for their infrared detection properties. The study has revealed that few-layer $MoSe_2$ exhibits attractive features in terms of responsivity and external quantum efficiency, the values being 50 mA/W and 6 % respectively. First-principles calculations show how graphene-like $MoSe_2$ has desirable features for infrared detection.

2.6: Superior infrared detection properties of few-layer MoSe₂

2.6.1: Introduction

Graphene exhibits ambipolar electric field effect, ballistic conduction of charge carriers and quantum Hall effect at room temperature. The optoelectronic properties of graphene are of particular interest because of their significant importance in academic as well as in various industries. The rise of graphene in photonics and optoelectronics is shown by recent results, ranging from solar cells, light-emitting devices, touch screens, and photodetectors to ultrafast lasers. Here, we review some of the recent results in the optoelectronic properties of graphene. The photoconductivity of graphene films has been observed up on the illumination of laser source with wavelength of 1064 nm. The photoconductivity of graphene film increased with increasing light intensity and external electric field under the same photon energy.[1] Ghosh et al. reported that RGO films can be used as Infrared (IR) detectors and sensitivity depends on the position of the laser illumination.[2] The maximum photoresponse of 193% was obtained at the metal electrode/RGO film interface. Graphene nanoribbons (GNRs) with substantial gaps have been used as phototransistors,[3] specially for far-infrared detection.[4] It has been possible to prepare highly selective, sensitive and high-speed nanoscale photodetectors and photoelectronic switches by drop casting RGO and GNR on two terminal 15 μm gap Cr(5nm)/ Au (300 nm) electrodes.[5] Electrical conductivities of RGO and GNRs increase with IR laser radiation. A RGO detector can sense the IR radiation emitted from a human body. The detector current responsivity (R_λ), and the external quantum efficiency (EQE), for RGO photoconductors are 4 mA/W and 0.3% respectively while for GNR these values are higher, being 1 A/W and 80 % respectively for an incident wavelength of 1550 nm at 2 V for RGO and GNRs. On absorbing light from IR source, electron-hole pairs are

generated[6] due to a Schottky-like barrier at the metal/ graphene contact. The electron–hole pairs generated in graphene would normally recombine on a timescale of tens of picoseconds, depending on the quality and carrier concentration of the graphene.[6-7] On application of an external field, the pairs get separated and a photocurrent is generated. A similar phenomenon can occur in the presence of an internal field formed by photoexcitation.[8] Graphene is also a very good UV absorber.[9]It has been possible to prepare UV-detectors using RGO. The photodetecting responsivity is found to be 0.12 A/W with an external quantum efficiency of 40 %.[10]

The extraordinary electronic[11] and photonic properties[2, 5, 12] of graphene have catalyzed research on other two-dimensional systems formed by layered inorganic materials with comparable properties. In this context, layered transition metal dichalcogenides with the formula MX_2 (M=Mo, W etc and X =Se, S etc) are promising candidates for exploration. The most stable crystal structure of this class of compounds is hexagonal with each unit cell consisting of two chalcogenide-metal-chalcogenide sandwich layers bound by van der Waals forces. Because of the weak interlayer and strong intralayer interactions, these metal chalcogenides easily form 2D layered materials analogous to graphene.[13] Since the zero bandgap in graphene could be a limitation in some of the applications, several ways have been devised to engineer the band gap.[14] A band gap of ~ 400 meV has been attained by converting graphene into graphene-nanoribbons at the cost of mobility.[15] Layered transition metal chalcogenides, besides possessing useful electronic, optical, catalytic and lubricating properties,[16] enable the study of mesoscopic transport in two dimensions. Thus, monolayer MoS_2 has been used to fabricate field effect transistors.[17],[18] Electrical properties of few-layer MoS_2 have been

characterized[19] and are found to be useful as gas sensors.[20] Fabrication of single-layer MoS$_2$ devices are relatively tough compared to the few-layer MoS$_2$ and the physics of few-layer MoS$_2$, is more attractive than single layer MoS$_2$ for FET applications in a thin-film transistor configuration.[21] The density of states in multilayer MoS$_2$ is three times higher than in single-layer MoS$_2$, which can produce considerably high drive currents in the ballistic limit.[22] Multilayer MoS$_2$ offers a wider spectral response compared to single layer MoS$_2$–from ultraviolet (UV) to near infrared (NIR) wavelengths – due to its narrower bandgap, which can be advantageous in a variety of photodetector applications.[23] Recently, MoS$_2$ with different thickness of 1 nm, 4nm and 40 nm have been used for the detection of UV-radiation to near IR radiation successfully.[24]

2.6.2: Scope of the present investigations

Molybdenum diselenide, MoSe$_2$, is an indirect bandgap semiconductor in bulk, with a band gap of 1.1 eV.[16d, 25] Being structurally analogous to graphene, but with a non-zero band gap, MoSe$_2$ is clearly a potential candidate for application in opto-electronics. Optical absorption,[26],[27] reflectivity[28] and photoconductivity measurements of MoSe$_2$ have been reported.[29] In the light of recent reports on good responsivity of graphene as an IR photodetector, we considered it important to investigate the IR-detection properties of graphene-like MoS$_2$ and MoSe$_2$. We have employed a simple hydrothermal method to prepare few-layer MoS$_2$ and MoSe$_2$ for our investigations.[13] We have carried out first-principles density functional calculations on monolayer MoSe$_2$ and MoS$_2$ to understand the experimental results.

2.6.3: Experimental section

Preparation of few-layer MoSe₂: Few-layer MoSe$_2$ was prepared by using a hydrothermal method wherein 1 mM of molybdic acid, 2 mM of selenium metal and 30 mM of NaBH$_4$ were taken in 10 ml of deionized water in a 23 ml capacity of Teflon-coated autoclave and heated at 453 K for 24 hours to yield few-layer MoSe$_2$. The product was washed with ethanol and dried at 278 K.

Preparation of few-layer MoS₂: Few-layer MoS$_2$ was prepared by using a hydrothermal method wherein 1 mM of molybdic acid, 3 mM of KSCN were taken in 10 ml of deionized water in a 23 ml capacity of Teflon-coated autoclave and heated at 453 K for 24 hours to yield few-layer MoS$_2$. The product was washed with ethanol and dried at 278 K.

Device fabrication: Few-layered MoSe$_2$ and MoS$_2$ devices were fabricated by drop casting the MoSe$_2$ dispersions in ethanol over preformed Cr (5 nm)/Au (200 nm) electrodes (using e-beam evaporation) on 300 nm SiO$_2$ on Si substrate. The distance between the two electrodes is 115 µm and the width of electrodes is 2 mm. The residual solvent was removed by drying the devices overnight in vacuum.

Method of Calculation We use ABINIT[30] implementation of density functional theory (DFT) with a local density approximation to exchange correlation energy and Hartwigsen- Goedecker-Hutter (HGH) relativistic pseudopotentials[31] to represent interaction of nuclei and core electrons with valence electrons (we include semicore states of Mo in the valence). Kohn-Sham wave functions are represented with plane wave basis cutoff at the energy of 80 Ry. We use a 3-dimensional periodic cell to simulate 2-dimensional monolayers with a vacuum of 12 Å thickness separating their periodic

images. Integrations over Brillouin zone are sampled with a uniform mesh with 15x15x1 k-points to ensure good convergence. Phonons, Born effective charges and electronic dielectric constant are determined using density functional theory linear response.

Characterization Techniques

X-ray Diffraction:

X-ray diffraction (XRD) patterns of the samples were recorded using Cu Kα radiation on a Bruker D8 Discover diffractometer.

Scanning electron microscopy

A field-emission scanning electron microscope (FESEM, FEI Nova-Nano SEM-600, Netherlands) was used.

Transmission electron microscopy

For transmission electron microscopy (TEM), dispersions of the samples were dropped onto the holey carbon-coated Cu grids, and the grids were allowed to dry in the air. The grids were examined using a JEOL (JEM3010) microscope operating with an accelerating voltage of 300 kV.

Optical absorption

The optical absorption spectroscopy measurements were performed using a Perkin- Elmer Lambda 900 UV/VIS/NIR spectrometer..

Raman Spectroscopy

Raman spectra were recorded with a LabRAM HR high-resolution Raman spectrometer (Horiba-Jobin Yvon) using a He−Ne laser ($\lambda = 632.8$ nm) and Ar laser (514 nm).

Atomic force Microscopy

AFM measurements were carried on Vecco digital instruments, di Innova. Samples for AFM measurements were prepared by spin coating the sample solutions on Si/SiO$_2$ substrate.

Electrical characterization

Electrical characterization of the devices was performed using a Keithley 6430 meter under ambient conditions. A semiconductor laser diode with peak wavelength of 1064 nm was used as the IR source to measure the photoconductivity of the devices.

2.6.4: Results and Discussion
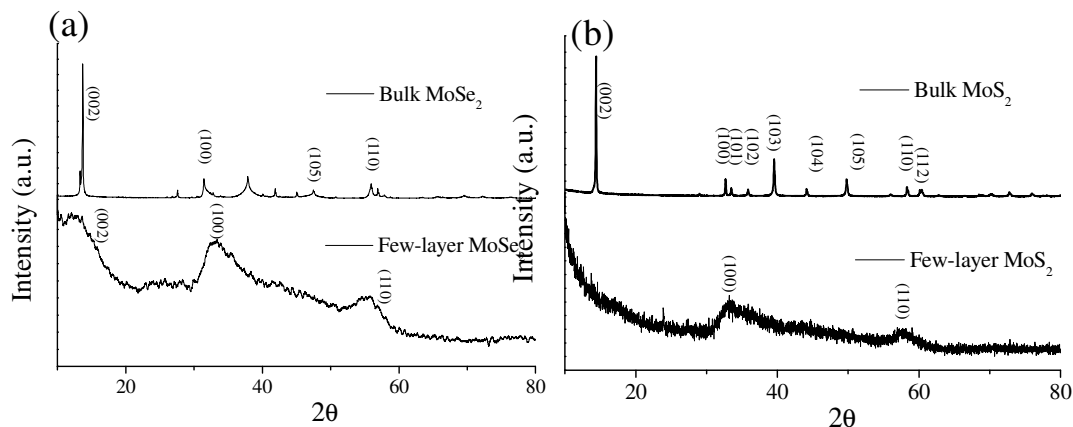
Figure 1: XRD patterns of (a) bulk and few-layer MoSe$_2$ (b) bulk and few-layer MoS$_2$

Few-layered MoSe$_2$, prepared by the reaction of selenium metal with molybdic acid under hydrothermal conditions, does not show the (002) reflection in the XRD pattern as can be seen from Figure 1 (a), suggesting the presence of only a few-layers and the XRD pattern of few-layer MoS$_2$ was shown in Figure 1(b). In Figure 2 (a) we compare Raman spectra of few-layer MoSe$_2$ along with that of the bulk sample. Few-layer MoSe$_2$
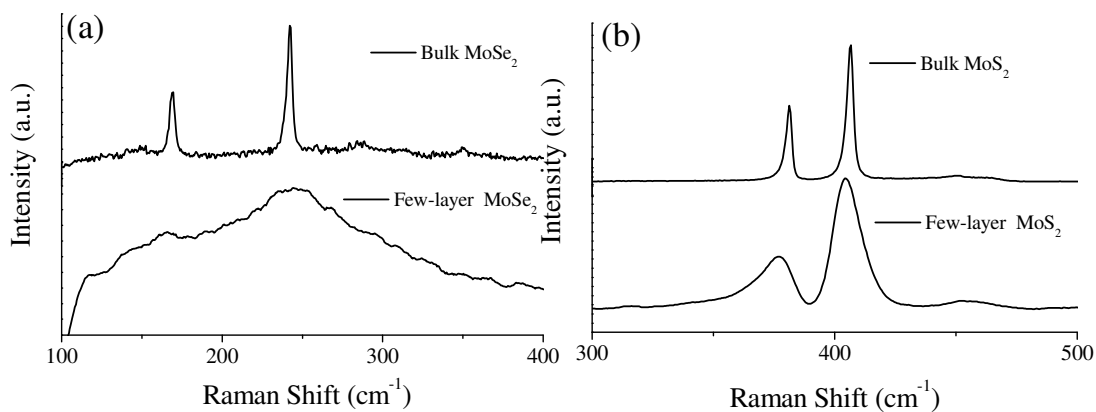

Figure 2: Raman spectra of (a) bulk and few-layer MoSe$_2$ (b) bulk and few-layer MoS$_2$
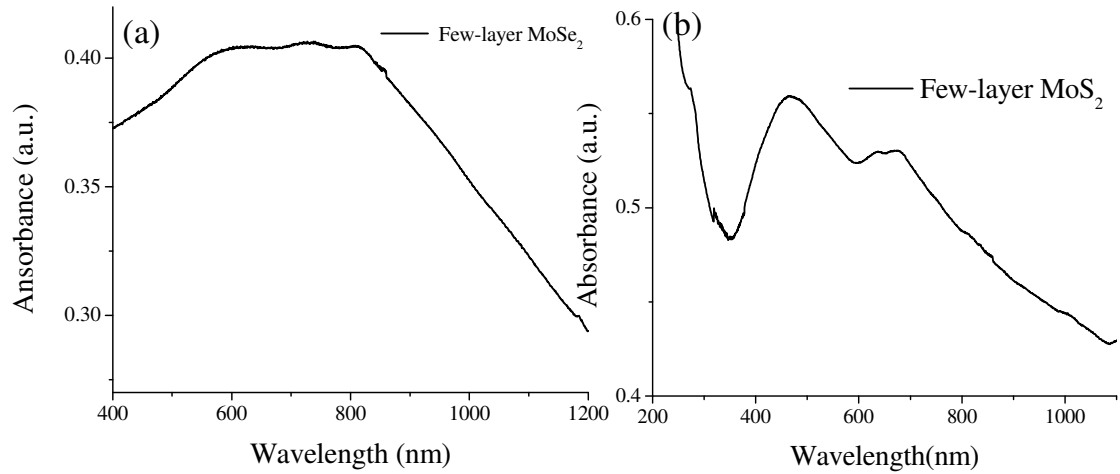
Figure 3: Absorption spectrum of (a) few-layer MoSe$_2$ (b) few-layer MoS$_2$

shows softening and broadening of the Raman bands at 168 and 239 cm^{-1} relative to the bulk sample. Figure 2 (b) shows the Raman spectra of Bulk and few-layer MoS$_2$ with softening of the modes and increase in the full width half maxima compared to its bulk counterpart. We have recorded the UV-Vis absorption spectrum few-layer MoSe$_2$ the characteristic bands corresponding with a broad band from 500 to 630 nm, 738 nm and 813 nm and few-layer MoS$_2$ has around 406 nm,447 nm, 637 nm and 674 nm similar to
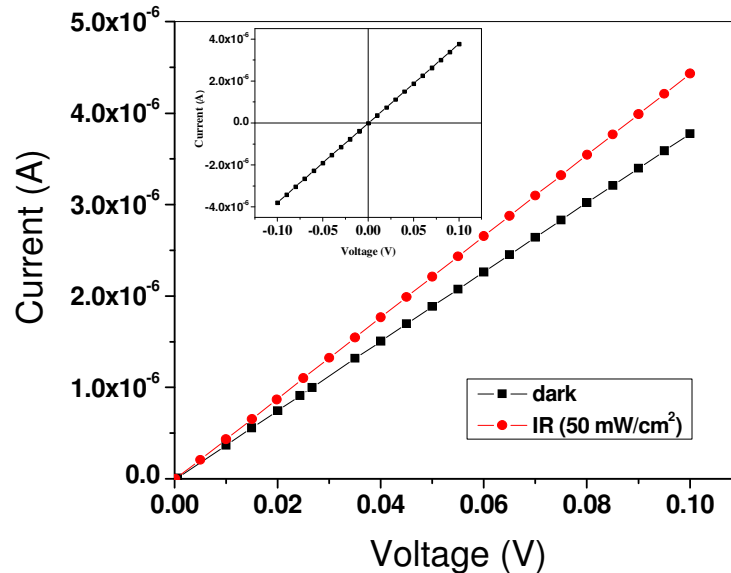

Figure 4: I-V characteristics of few-layer MoSe$_2$ in the dark (black) and under IR illumination (red) at 1064 nm with the inset showing confirmation of ohmic contacts in MoSe$_2$ device.

reported in the literature (Figure 3).[32]

I-V characteristics of few-layer MoSe$_2$ measured in the dark and under 1064 nm illumination with an incident optical intensity 50 mW/cm^2 are shown in Figure 4. The presence of ohmic contacts to the nanostructured MoSe$_2$ is demonistarted by the I-V curve given in the inset of Figure 4 (data in dark). There is a marked increase in the conductivity of few-layered MoSe$_2$ on irradiation. We observe a rise of 17 % at a V$_{bias}$ of 0.1 V. The electrical conductivity of few-layer MoSe$_2$ increases with increase in IR laser radiation intensity (Figure 4). The photo-response of the MoSe$_2$ device is presented in Figure 5 shows the photocurrent variation as a function of time with different IR intensities at a bias voltage of 0.1 V. The variation of responsivity with the incident optical intensity is shown as an inset in Figure 5.
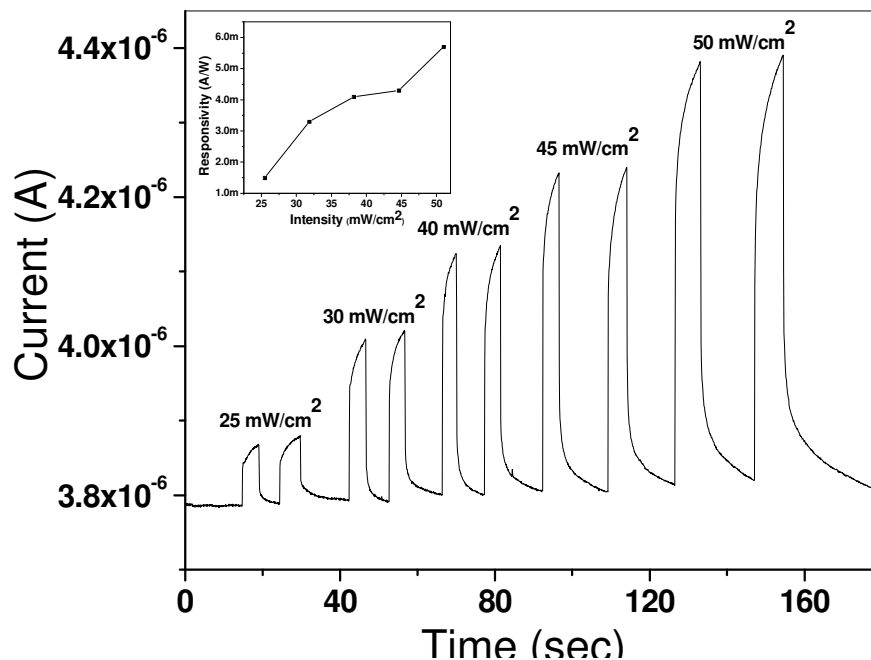
Figure 5: Photocurrent as a function of time with different IR intensities at 0.1 V for few-layer MoSe$_2$ and the inset shows variation of responsivity with the incident optical intensity.

The optoelectronic behavior of few-layer MoSe$_2$ can be attributed to photogeneration under light irradiation due to its wide absorption range (400-1200 nm).[33] On absorption of light, electron-hole pairs are generated causing an increase in charge

carrier density and hence in photocurrent.[5] When the intensity of the laser radiation is increased, more excitons are generated, resulting in a larger photocurrent as shown in Figure 5. We have calculated the responsivity (R_λ) and external quantum efficiency (EQE) which determine the performance of a detector is as follows:[5]

$$R_\lambda = I_\lambda /(P_\lambda .S), \quad EQE = hcR_\lambda/(e.\lambda)$$

Here, I_λ is the photocurrent (I $_{illumination}$ − I $_{dark}$), P_λ the light intensity, S the effective illuminated area, h is the Planck's constant, c the velocity of light, e the electronic charge, and λ the excitation wavelength. In our study, values of R_λ and EQE values are found to be 50 mA/W and 6 % respectively. We, therefore, conclude that few-layer MoSe$_2$ may find
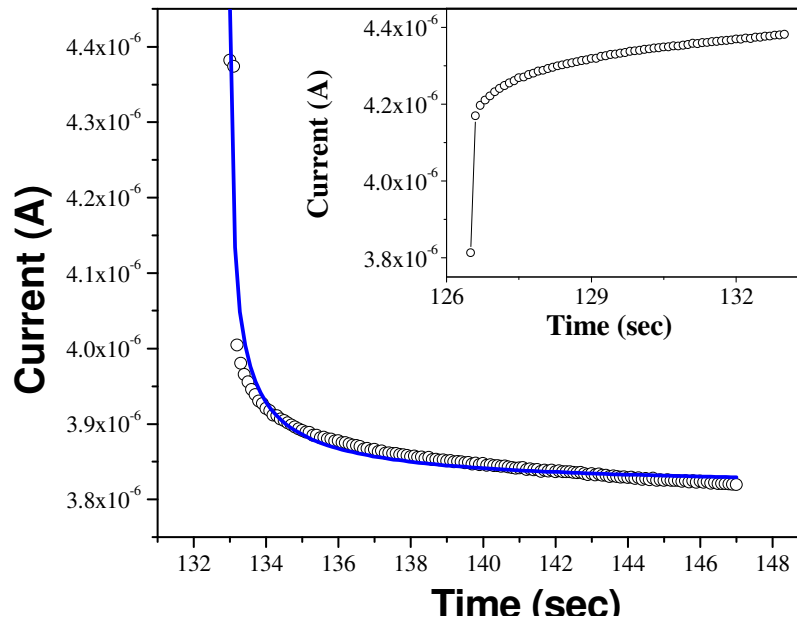
Figure 6: Time response of photocurrent decay of few-layer MoSe$_2$ and the inset shows growth.

applications in nanoscale photodetectors and photoelectronic switches with high selectivity and sensitivity.

Figure 6 shows the rise and decay of the photocurrent of few-layer MoSe$_2$ in response to the turn-off of the IR illumination. The photocurrent decay curves is given by the following relaxation law.[34]

$I_{(t)} = I_d + I_{(0)}\exp[-((t-t_0)/\tau)^\beta]$, $0<\beta<1$ Here, $I_{(t)}$ is the current at decay time t, $I_{(0)}$ is the current obtained after immediate switching off the light source, I_d is the initial dark current, t_0 is the time when light source is switched off, τ is the photocurrent decay
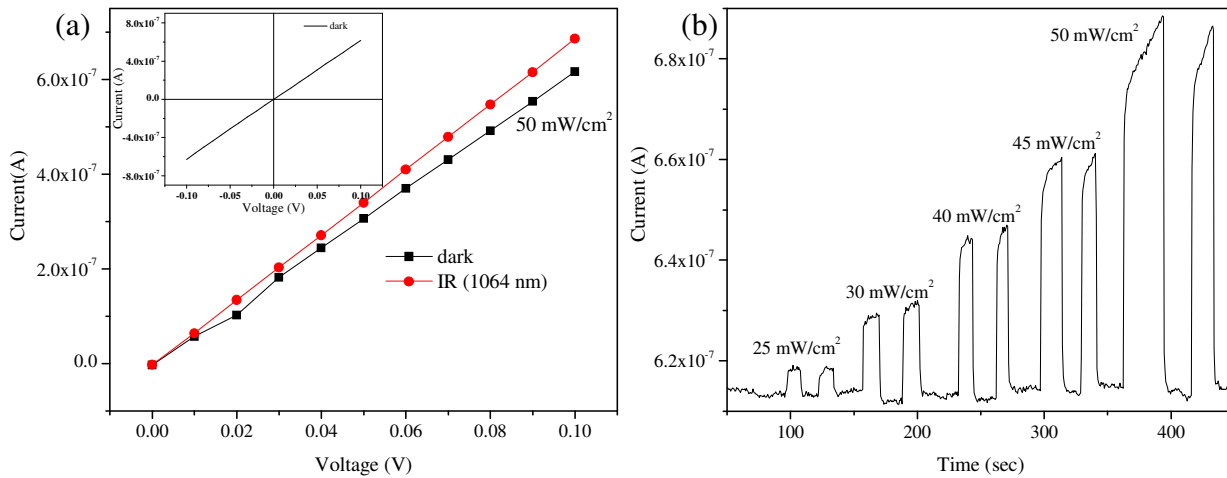
Figure 7: (a) I-V characteristics of MoS₂ in the dark (black) and under IR illumination (red) at 1064 nm, with the inset showing confirmation of ohmic contacts in MoS₂ device. (b) Photocurrent as a function of time with different IR intensities at 2V for few-layer MoS₂.

constant and β is defined as the decay exponent. The decay time constant for MoSe₂ is found to be 16 msec. We have not observed any persistent photoconductivity (PPC) after terminating the illumination, in the present study in agreement with previous report.[34] The photocurrent shows exponential growth initially followed by a slower increase as can be seen in the inset in Figure 5. The performance of MoSe₂ devices shows no degradation under ambient conditions.

We have also carried out photoconductivity measurements on 2-4 layers MoS₂. The presence of ohmic contacts to the nanostructure MoS₂ is verified by the inset of Figure 7(a) (data in dark). The electrical conductivity of few-layer MoS₂ increases with increase in IR laser radiation intensity (Figure 7(a)). The photo-response of the MoS₂ device, presented in Figure 7(b), shows that the photocurrent varies as a function of time with

different IR intensities at a bias voltage of 0.1 V. The R_λ and EQE values of the few-layer MoS$_2$ device are found to be 3 mA/W and 0.4 % respectively. These values are considerably smaller than those exhibited by few-layer MoSe$_2$. The decay time for few-layer MoS$_2$ is 31 msec, far higher than that of few-layer MoSe$_2$ (for similar β values).

We shall now examine the results of our calculations on mono-layers of MoS$_2$ and MoSe$_2$. While MoS$_2$ and MoSe$_2$ in bulk crystalline form are indirect band gap semiconductors[25], MoS$_2$ is known to become a direct band gap semiconductor in its monolayer form.[35] The electronic structures of mono-layers of MoS$_2$ and MoSe$_2$ determined from our calculations at the experimental lattice constant a clearly reveal that they are direct band gap semiconductors, with energy gaps of 1.80 and 1.29 eV respectively (Figure 8) at K-point in the Brillouin zone. While electronic band gaps are generally underestimated in Kohn-Sham DFT calculations, our estimates appear quite close to the experimental values.[35] Close inspection through projected density of electronic states shows that the top of the valence band consists of a single band constituted primarily of 4d states of Mo. It is isolated from the rest in case of MoS$_2$, while it has a weak overlap with p-states of selenium in MoSe$_2$ due to its greater covalency. This covalency also results in a smaller band gap of MoSe$_2$ than of MoS$_2$. Conduction bands in both these materials arise from the unoccupied d-states of Mo.

Bandgaps of MoS$_2$ and MoSe$_2$ are larger than the energy of IR radiation (~ 1.16 eV) used in experiments reported here. Secondly, the electronic states in the valence and conduction bands near K-point have d_{xy} and d_{z2} character respectively, indicating a relatively weak coupling with electromagnetic field. On the other hand, electron-phonon coupling in MoS$_2$ was shown to be quite strong. Thus, we expect the interaction of IR radiation with MoSe$_2$ to be strongly influenced by (a) edge states which appear in the gap,

and (b) IR-active phonons which are polar in nature and can absorb IR radiation and formation of a polariton.

We now present a comparative theoretical analysis of phonons and related properties of MoS_2 and $MoSe_2$. To have an idea of size of the LDA errors, we report
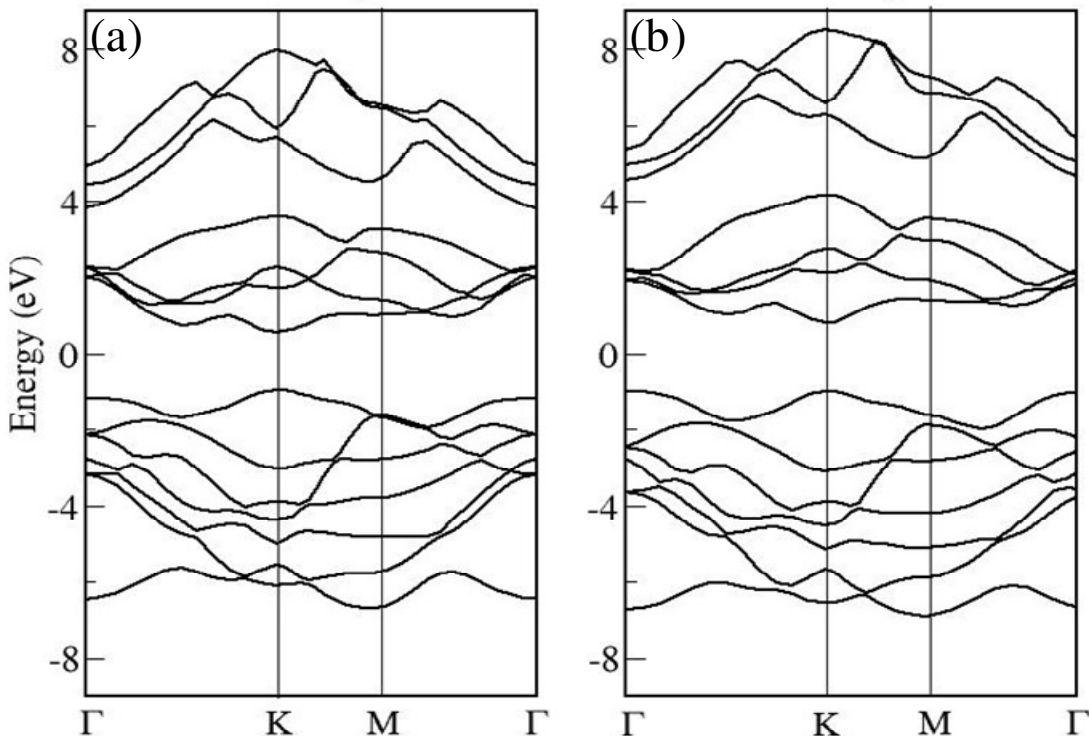
Figure 8: Electronic structure of $MoSe_2$ and MoS_2 along high symmetry lines in the Brillouin zone with direct band gaps of 1.29 and 1.80 eV respectively at K-point. E=0 eV is in the middle of the band gap.

results at both experimental and LDA lattice constants (which are about 2 % smaller than experimental ones). Due to symmetry, properties such as dielectric constant and phonon frequencies are doubly degenerate in the ab-plane and relatively weak along the c-axis as expected for two-dimensional materials. There is one doubly degenerate IR-active mode (polarizaiton in ab plane) and one non-degenerate mode (with c-polarization) in MoX_2. Owing to stronger covalency, Born effective charges of $MoSe_2$ (measure of coupling of the lattice to IR radiation) are significantly larger and more anomalous than those of MoS_2,

and the corresponding oscillator strength of $MoSe_2$ is more than three times larger than that of MoS_2. Smaller electronic band-gap of $MoSe_2$ is also reflected in its electronic dielectric response that is 10 % larger than that of MoS_2. Secondly, due to heavier mass of Se and softer bonds, IR-active modes of $MoSe_2$ are almost 25 % softer than those of MoS_2. Thus, absorption of IR radiation (with resonance around 36 meV) is expected to be much stronger in $MoSe_2$ than in MoS_2. As the electronic band gap of $MoSe_2$ is closer to the energy of IR radiation, and we expect absorption of IR radiation by the lattice is stronger in the case of $MoSe_2$ than MoS_2, $MoSe_2$ is expected to be much better for IR-detection, as found in our experiments.

2.6.5: Conclusions

In conclusion, we have the studied the infrared radiation detecting properties of few-layer $MoSe_2$ in comparison with those of few-layer MoS_2. The responsivity and external quantum efficiency of the $MoSe_2$ device are significantly higher than those of the MoS_2 device, the values being 50 mA/W and 6 % respectively at an incident wavelength of 1064 nm. It, therefore, appears that few-layer $MoSe_2$ can be used effectively for infrared detection. Our theoretical calculations also show graphene-like $MoSe_2$ to be more effective for IR detection than MoS_2.

2.6.6: References

[1]   X. Lv, Y. Huang, Z. Liu, J. Tian, Y. Wang, Y. Ma, J. Liang, S. Fu, X. Wan, Y. Chen, *Small* **2009**, *5*, 1682.

[2]   S. Ghosh, B. K. Sarker, A. Chunder, L. Zhai, S. I. Khondaker, *Appl. Phys. Lett.* **2010**, *96*, 163109.

[3]   V. Ryzhii, M. Ryzhii, T. Otsuji, *Appl. Phys. Exp.* **2008**, *1*, 013001.

[4]   V. Ryzhii, M. Ryzhii, N. Ryabova, V. Mitin, T. Otsuji, *Jpn. J. Appl. Phys.* **2009**, *48*, 04C144.

[5]   B. Chitara, L. S. Panchakarla, S. B. Krupanidhi, C. N. R. Rao, *Adv. Mater.* **2011**, *23* 5419.

[6]   F. Rana, P. A. George, J. H. Strait, J. Dawlaty, S. Shivaraman, M. Chandrashekhar, M. G. Spencer, *Phys. Rev. B* **2009**, *79*, 115447.

[7]   a)P. A. George, J. Strait, J. Dawlaty, S. Shivaraman, M. Chandrashekhar, F. Rana, M. G. Spencer, *Nano Letters* **2008**, *8*, 4248; b)F. T. Vasko, V. Ryzhii, *Phys. Rev. B* **2007**, *76*, 233404.

[8]   a)J. H. LeeEduardo, K. Balasubramanian, R. T. Weitz, M. Burghard, K. Kern, *Nat. Nanotechnol.* **2008**, *3*, 486; b)F. Xia, T. Mueller, R. Golizadeh-Mojarad, M. Freitag, Y.-m. Lin, J. Tsang, V. Perebeinos, P. Avouris, *Nano Lett.* **2009**, *9*, 1039; c)T. Mueller, F. Xia, M. Freitag, J. Tsang, P. Avouris, *Phys. Rev. B* **2009**, *79*, 245430.

[9]   C. Lee, J. Y. Kim, S. Bae, K. S. Kim, B. H. Hong, E. J. Choi, *Appl. Phys. Lett.* **2011**, *98*, 071905.

[10]   B. Chitara, S. B. Krupanidhi, C. N. R. Rao, *Appl. Phys. Lett.* **2011**, *99*, 113114.

[11] a)K. S. Novoselov, A. K. Geim, S. V. Morozov, D. Jiang, Y. Zhang, S. V. Dubonos, I. V. Grigorieva, A. A. Firsov, *Science* **2004**, *306*, 666; b)K. S. Novoselov, A. K. Geim, S. V. Morozov, D. Jiang, M. I. Katsnelson, I. V. Grigorieva, S. V. Dubonos, A. A. Firsov, *Nature* **2005**, *438*, 197; c)Y. Zhang, Y.-W. Tan, H. L. Stormer, P. Kim, *Nature* **2005**, *438*, 201; d)C. N. R. Rao, A. K. Sood, K. S. Subrahmanyam, A. Govindaraj, *Angew. Chem. Int. Ed.* **2009**, *48*, 7752; e)C. N. R. Rao, K. S. Subrahmanyam, H. S. S. R. Matte, B. Abdulhakeem, A. Govindaraj, D. Barun, K. Prashant, G. Anupama, J. L. Dattatray, *Sci. Technol. Adv. Mater.* **2010**, *11*, 054502.

[12] a)P. Avouris, Z. Chen, V. Perebeinos, *Nature Nanotechnol.* **2007**, *2*, 605; b)F. Xia, T. Mueller, Y.-m. Lin, A. Valdes-Garcia, P. Avouris, *Nature Nanotechnol.* **2009**, *4*, 839; c)T. Mueller, F. Xia, P. Avouris, *Nature Photon.* **2010**, *4*, 297; d)R. R. Nair, P. Blake, A. N. Grigorenko, K. S. Novoselov, T. J. Booth, T. Stauber, N. M. R. Peres, A. K. Geim, *Science* **2008**, *320*, 1308.

[13] a)H. S. S. Ramakrishna Matte, A. Gomathi, A. K. Manna, D. J. Late, R. Datta, S. K. Pati, C. N. R. Rao, *Angew. Chem. Int. Ed.* **2010**, *49*, 4059; b)H. S. S. R. Matte, B. Plowman, R. Datta, C. N. R. Rao, *Dalt. Trans.* **2011**, *40*, 10322.

[14] Z. Zhang, H. Huang, X. Yang, L. Zang, *J. Phys. Chem. Lett.* **2011**, *2*, 2897.

[15] X. Li, X. Wang, L. Zhang, S. Lee, H. Dai, *Science* **2008**, *319*, 1229.

[16] a)R. V. Kasowski, *Phys. Rev. Lett.* **1973**, *30*, 1175; b)L. F. Mattheiss, *Phys. Rev. Lett.* **1973**, *30*, 784; c)L. F. Mattheiss, *Phys. Rev. B* **1973**, *8*, 3719; d)R. Coehoorn, C. Haas, J. Dijkstra, C. J. F. Flipse, R. A. de Groot, A. Wold, *Phys. Rev. B* **1987**, *35*, 6195; e)R. Coehoorn, C. Haas, R. A. de Groot, *Phys. Rev. B* **1987**, *35*, 6203; f)X. Zong, H. Yan, G. Wu, G. Ma, F. Wen, L. Wang, C. Li, *J. Am. Chem. Soc.*

2008, *130*, 7176; g)Y. Li, H. Wang, L. Xie, Y. Liang, G. Hong, H. Dai, *J. Am. Chem. Soc.* **2011**, *133*, 7296; h)L. Rapoport, Y. Bilik, Y. Feldman, M. Homyonfer, S. R. a. Cohen, R. Tenne, *Nature* **1997**, *387*, 791.

[17]   Radisavljevic. B, Radenovic. A, Brivio. J, Giacometti. V, Kis. A, *Nature Nanotechnol.* **2010**, *6*, 147.

[18]   Z. Yin, H. Li, H. Li, L. Jiang, Y. Shi, Y. Sun, G. Lu, Q. Zhang, X. Chen, H. Zhang, *ACS Nano* **2011**, *10.1021/nn2024557*.

[19]   K. Lee, H.-Y. Kim, M. Lotya, J. N. Coleman, G.-T. Kim, G. S. Duesberg, *Adv. Mater.* **2011**, *23*, 4178.

[20]   H. Li, Z. Yin, Q. He, H. Li, X. Huang, G. Lu, D. W. H. Fam, A. I. Y. Tok, Q. Zhang, H. Zhang, *Small* **2012**, *8*, 63.

[21]   S. Kim, A. Konar, W.-S. Hwang, J. H. Lee, J. Lee, J. Yang, C. Jung, H. Kim, J.-B. Yoo, J.-Y. Choi, Y. W. Jin, S. Y. Lee, D. Jena, W. Choi, K. Kim, *Nat Commun* **2012**, *3*, 1011.

[22]   K. Natori, *J. Appl. Phys.* **1994**, *76*, 4879.

[23]   X. Gong, M. Tong, Y. Xia, W. Cai, J. S. Moon, Y. Cao, G. Yu, C.-L. Shieh, B. Nilsson, A. J. Heeger, *Science* **2009**, *325*, 1665.

[24]   W. Choi, M. Y. Cho, A. Konar, J. H. Lee, G.-B. Cha, S. C. Hong, S. Kim, J. Kim, D. Jena, J. Joo, S. Kim, *Adv. Mater.* **2012**, *DOI: 10.1002/adma.201201909*.

[25]   T. Boker, R. Severin, A. Muller, C. Janowitz, R. Manzke, D. Vob, P. Kruger, A. Mazur, J. Pollmann, *Phys. Rev. B* **2001**, *64*, 235305.

[26]   A. R. Beal, J. C. Knights, W. Y. Liang, *J. Phys. C* **1972**, *5*, 3540.

[27]   A. M. Goldberg, A. R. Beal, F. A. Levy, E. A. Davis, *Phil. Mag.* **1975**, *32*, 367.

[28]   H. P. Hughes, W. Y. Liang, *J. Phys. C* **1974**, *7*, 1023.

[29]   W. Kautek, *J. Phys. C* **1982**, *15*, L519.

[30]   X. Gonze, J. M. Beuken, R. Caracas, F. Detraux, M. Fuchs, G. M. Rignanese, L. Sindic, M. Verstraete, G. Zerah, F. Jollet, M. Torrent, A. Roy, M. Mikami, P. Ghosez, J. Y. Raty, D. C. Allan, *Comput. Mat. Science* **2002**, *25*, 478.

[31]   C. Hartwigsen, S. Goedecker, J. Hutter, *Phys. Rev. B* **1998**, *58*, 3641.

[32]   J. N. Coleman, M. Lotya, A. ONeill, S. D. Bergin, P. J. King, U. Khan, K. Young, A. Gaucher, S. De, R. J. Smith, I. V. Shvets, S. K. Arora, G. Stanton, H.-Y. Kim, K. Lee, G. T. Kim, G. S. Duesberg, T. Hallam, J. J. Boland, J. J. Wang, J. F. Donegan, J. C. Grunlan, G. Moriarty, A. Shmeliov, R. J. Nicholls, J. M. Perkins, E. M. Grieveson, K. Theuwissen, D. W. McComb, P. D. Nellist, V. Nicolosi, *Science*, *331*, 568.

[33]   J. N. Coleman, M. Lotya, A. O'Neill, S. D. Bergin, P. J. King, U. Khan, K. Young, A. Gaucher, S. De, R. J. Smith, I. V. Shvets, S. K. Arora, G. Stanton, H.-Y. Kim, K. Lee, G. T. Kim, G. S. Duesberg, T. Hallam, J. J. Boland, J. J. Wang, J. F. Donegan, J. C. Grunlan, G. Moriarty, A. Shmeliov, R. J. Nicholls, J. M. Perkins, E. M. Grieveson, K. Theuwissen, D. W. McComb, P. D. Nellist, V. Nicolosi, *Science* **2011**, *331*, 568.

[34]   Y. C. Lee, J. L. Shen, K. W. Chen, W. Z. Lee, S. Y. Hu, K. K. Tiong, Y. S. Huang, *J. Appl. Phys.* **2006**, *99*, 063706.

[35]   K. F. Mak, C. Lee, J. Hone, J. Shan, T. F. Heinz, *Phys. Rev. Lett.* **2010**, *105*, 136805.

2.7: Superconductivity of few-layer NbSe$_2$

Summary

We have synthesized graphene analogues of NbSe$_2$ in a sealed tube reaction at 1000 ^{o}C. Thus obtained few-layer NbSe$_2$ was characterized using microscopic and spectroscopic techniques. TEM and AFM analysis have revealed that the sample mainly consists of 2-4 layers. We have also measured the superconducting properties of the bulk and few-layer NbSe$_2$ and found that the superconducting transition temperature was lower than its bulk counterpart.

2.7: Superconductivity of few-layer NbSe$_2$

2.7.1: Introduction

The NbSe$_2$ crystal is made up of stacks of NbSe$_2$ layers, each layer consisting of a sheet of Nb atoms between two sheets of Se atoms. The separation of the sheets is 6.3 Å. One-dimensional NbSe$_2$ nanostructures have been prepared by the intense electron irradiation of bulk NbSe$_2$.[1] Thermal decomposition of NbSe$_3$ in a flow of argon at 700 °C is used for synthesizing nanotubes.[2] Chemical vapor transport with elemental Nb and Se in an evacuated silica ampule at 800 °C have been employed for the synthesis of nanotubes and nanofibres.[3] The layered compounds 2H-NbSe$_2$ have been intercalated with organic molecules and the resulting superconducting transition temperature is reduced in the NbSe$_2$ complex down to 0.36 K.[4] The superconducting resistive transition temperature (T$_c$) decreased as the crystal thickness is reduced below six NbSe$_2$ layers, and a T$_c$ of 3.6 K is predicted for a single layer. Odem et al. have reported a soft chemical method for the synthesis of one- (1D) and two-dimensional (2D) NbSe$_2$ structures but they have not reported the superconducting properties.[5]

2.7.2: Scope of the present investigations

Recently, there is considerable interest in the possibility of "two-dimensional" superconductivity occurring in layer compounds. It has been documented in the early 70's by Frindt about the change in the transition temperature with varying e thickness of NbSe$_2$ slabs.[6] Later, there were some efforts in synthesizing various structures of NbSe$_2$ but there is no report yet on the superconducting properties of these materials which are synthesized by chemical methods. Having this in mind we were interested in preparing sheets of niobium diselenide, NbSe$_2$, one of the objectives being to explore the possible superconducting properties.

2.7.3: Experimental section

Synthesis of NbSe$_2$

For the synthesis of few-layer NbSe$_2$, 1 mM of Niobium powder was grounded with 2 mM of selenium granules uniformly for 20 minutes and then placed in a 9 mm dia quartz tube. The tube was flame-sealed under vacuum of 10^{-5} torr, to prevent oxidation during heating. was then placed in a vertically aligned tube furnace and heated to 1000 $^{\circ}$C over the period of 8 h. Furnace is maintained at that temperature for 2 h and allowed for proper homogenization, followed by cooling to 800 $^{\circ}$C in 2 h and kept there isothermally for 4 days. Finally, the system was allowed to cool to room temperature (30 $^{\circ}$C) in 10 h.

Characterization

Transmission electron microscopy: For transmission electron microscopy (TEM), dispersions of the samples were dropped onto the holey carbon-coated Cu grids, and the grids were allowed to dry in the air. The grids were examined using a JEOL (JEM3010) microscope operating with an accelerating voltage of 300 kV. TEM images and atomic arrangement of hexagonal NbSe$_2$ in Figure 3 (no reconstruction) was obtained from the FEI TITAN (cube) 80-300 kV aberration corrected transmission electron microscope with a negative spherical aberration coefficient (Cs) of ~ -30 µm and a positive defocus about +8 nm, where atomic potentials appear with bright contrast in a dark background.

X-ray diffraction (XRD): XRD patterns were recorded (Kα Cu radiation) with a Rich-Siefert XRD-3000-TT diffractometer.

Atomic force microscopy: AFM measurements were carried on Vecco digital instruments, di Innova in contact mode.

2.7: Superconductivity of few-layer NbSe$_2$

2.7.4: Results and Discussion

We have prepared few-layer NbSe$_2$ by solid state mixing of the precursors in the right proportion and sealed the mixture in the vacuum of about 10^{-6} bar. The sealed tube was kept in a vertical furnace at 1000 ^{o}C and cooled to room temperature followed the heating rate and ramp rate as mentioned in the experimental section. Prior to breaking the tube, it was kept in liquid nitrogen for few-minutes to condense any gases present in the tube. The sample was collected after breaking the tube and was characterized by various techniques including XRD and TEM.
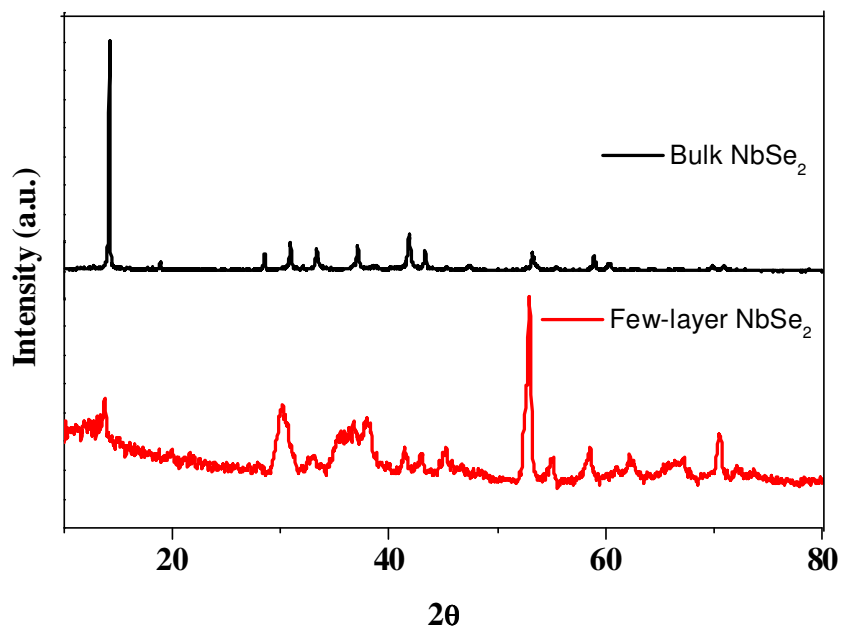

Figure 1: XRD patterns of the bulk samples of NbSe$_2$ and few-layer NbSe$_2$.

In Figure 1 we have shown the XRD pattern of few-layer NbSe$_2$ in comparison with bulk NbSe$_2$. As can be seen from the XRD pattern all the peaks are matching with the bulk counterpart other than the (002) reflection with very less intensity suggesting the formation of few-layer NbSe$_2$ and confirms that there was no registry along the c-axis. Figures 2 (a) and (b) show the TEM images showing the formation of 2-4 layers as

indicated by the XRD pattern. Further we have carried out AFM studies (Figure 2 (c)) which confirm the formation of the 2-3 layers having height of 1.6 nm with typical lateral dimensions in the range of 200-500 nm. In Figure 3 we have shown the HREM images obtained using FEI TITAN microscope. TEM images showed that the sample mainly consists of bi-layers. Figure 3 (a) shows the high resolution transmission electron microscope (HREM) image of NbSe$_2$ showing the hexagonal arrangement of niobium and selenium atoms. The lattice spacing of 3.0 Å shown in the HREM image (Figure 3 (b)) is
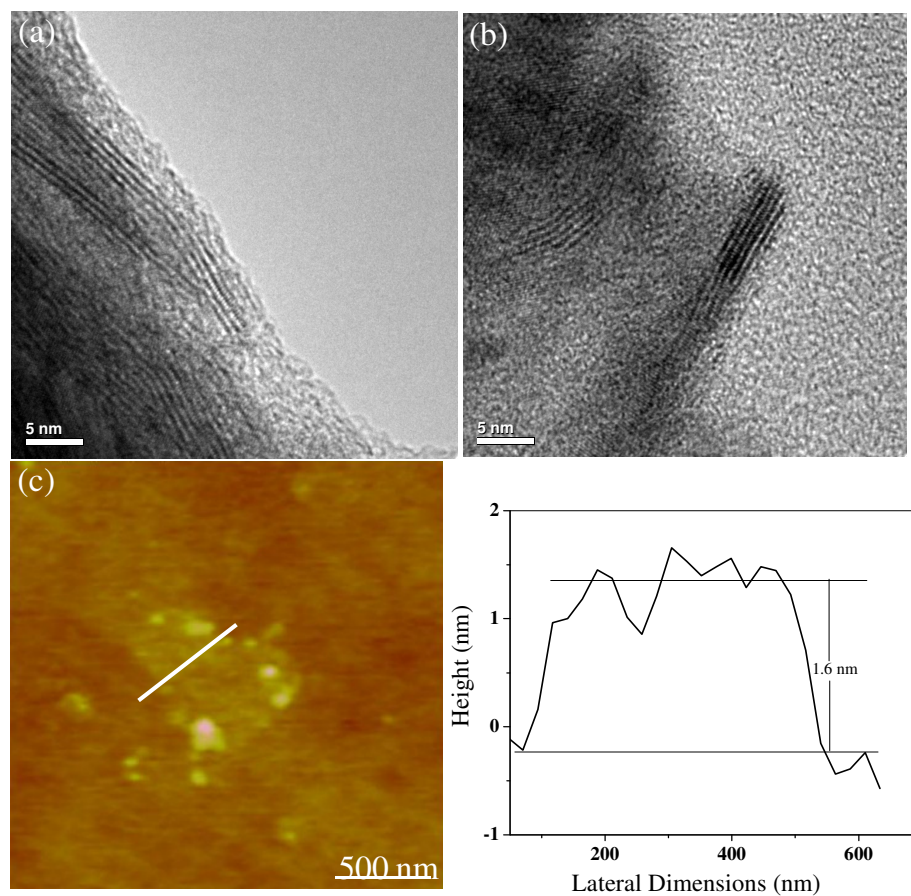

Figure 2: (a) and (b) TEM images of (c) AFM image and the associated height profile of NbSe$_2$.

consistent with that of the NbSe$_2$ (100) plane. We have carried out magnetic measurements with a Squid magnetometer at 20 Oe for both bulk and the few-layered samples to find if

2.7: Superconductivity of few-layer NbSe$_2$
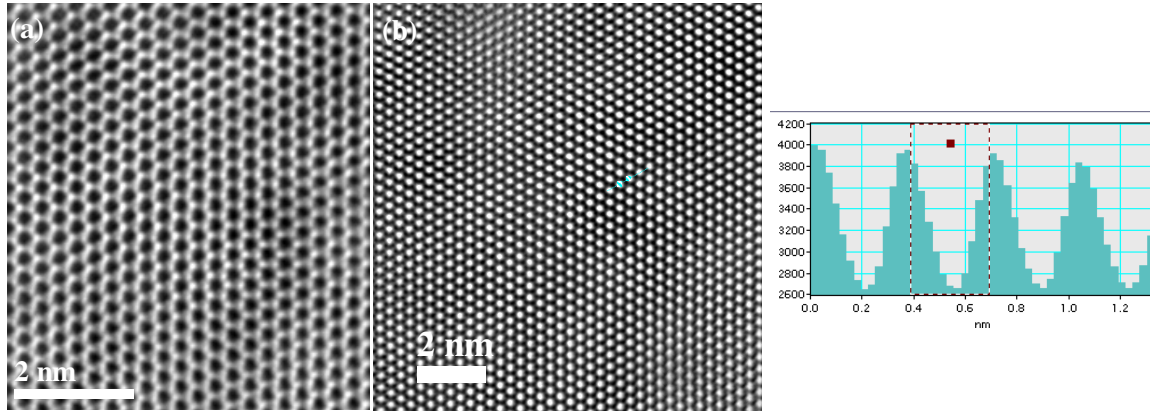
Figure 3: (a), (b) are HREM images NbSe$_2$ and (c) corresponding distance profile

there are any changes at the superconducting transition temperature. From the Figure 4(a), we see that the bulk sample shows a T$_c$ of 8.3 K as expected. The graphene analogue shows transistion temperature of 3.6 K close to that expected for single-layer.[6] On careful examination, we see that the transition starts around 6.5 K and shows a break at 3.6 K. This behavior would be expected if the sample has the mixture of single- and few-layer NbSe$_2$. The lower T$_c$ of few-layer NbSe$_2$ suggests that electron–phonon coupling and the electron density of states at the Fermi level changes significantly in the few-layer sample causing a decrease in the T$_c$.[2]
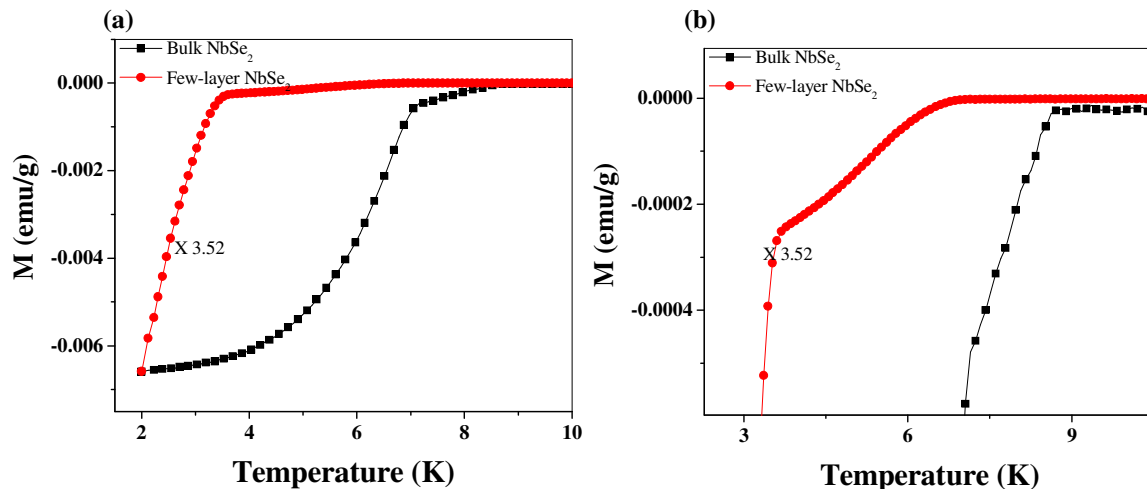
Figure 4: (a) Temperature dependent magnetization of bulk NbSe$_2$ and few-layer NbSe$_2$ at H=20 Oe, (b) zoomed portion between 3 to 10 K (few-layer NbSe$_2$ data multiplied by 3.52 to compare with the bulk data).

2.7.5: Conclusions

We have successfully prepared few-layer NbSe$_2$ using a sealed tube reaction at high temperatures. It is interesting to see that the transition temperature for the few-layer NbSe$_2$ is lower than its bulk counterpart. There is a need to prepare better samples of single-layer and few-layer NbSe$_2$ to determine the variation of T$_c$ with number of layers.

2.5.6: References

[1]   D. H. Galvan, J.-H. Kim, M. B. Maple, M. Avalos-Borja, E. Adem, *Fullerene Sci. Technol.* **2000**, *8*, 143.

[2]   M. Nath, S. Kar, A. K. Raychaudhuri, C. N. R. Rao, *Chem. Phys. Lett.* **2003**, *368*, 690.

[3]   T. Tsuneta, T. Toshima, K. Inagaki, T. Shibayama, S. Tanda, S. Uji, M. Ahlskog, P. Hakonen, M. Paalanen, *Curr. Appl. Phys.* **2003**, *3*, 473.

[4]   S. F. Meyer, R. E. Howard, G. R. Stewart, J. V. Acrivos, T. H. Geballe, *J. Chem. Phys.* **1975**, *62*, 4411.

[5]   P. Sekar, E. C. Greyson, J. E. Barton, T. W. Odom, *J. Amer. Chem. Soc.* **2005**, *127*, 2054.

[6]   R. F. Frindt, *Phys. Rev. Lett.* **1972**, *28*, 299.

Appendix[*]

Summary of the M. S. degree thesis on metal-organic frameworks

1. **Two- and three-dimensional hybrid compounds formed by 1,2-, 1,3- and 1,4-cyclohexanedicarboxylates of Zinc.**

We have investigated the structural features of hybrid dicarboxylate frameworks in terms of dimensionality and extended inorganic and organic connectivity. We have employed the three isomeric (1,2-, 1,3- and 1,4-) flexible (conformational) cyclohexanedicarboxylic acids to synthesize hybrid frameworks of Zn with or without chelating amines. Six hybrid inorganic-organic cyclohexanedicarboxylates have been synthesized under hydrothermal conditions and their structures established by X-ray crystallography. Compound **I** is a molecular structure while **II**, **IV** and **VI** have two-dimensional layered structures. Compounds **III** and **V** have closely related three-dimensional structures. In all these compounds, the CHDC anions are in the (e,e) conformation except in **II** where it has the (a,e) conformation.

2. **Inorganic-Organic hybrid compounds exhibiting both magnetic order and non-linear optical properties or dielectric properties.**

We have investigated the paired properties of hybrid organic-inorganic compounds having non-linear optical properties and dielectric properties which are exhibiting interesting magnetic properties. We have also investigated the multiferroic properties as well as magnetocapacitance in hybrid compounds having perovskite structure.

---

[*]Papers based on this work have been published in Z. Anorg. Allg. Chem. (2009) (Special issue dedicated to Prof. Martin Jansen) and Solid State Comm. (2009).